Novel Concepts and Theoretical Studies for High-Quality Plasma-Based Accelerators

Dissertation
zur Erlangung des Doktorgrades
an der Fakultät für Mathematik, Informatik und Naturwissenschaften
Fachbereich Physik
der Universität Hamburg

vorgelegt von

Ángel Ferran Pousa

Hamburg

2019

Betreuer der Dissertation:	Dr. Ralph W. Aßmann Prof. Dr. Florian Grüner Dr. Alberto Martinez de la Ossa
Gutachter der Dissertation:	Dr. Ralph W. Aßmann Prof. Dr. Florian Grüner
Zusammensetzung der Prüfungskommission:	Dr. Ralph W. Aßmann Prof. Dr. Florian Grüner Prof. Dr. Wolfgang Hillert Dr. Alberto Martinez de la Ossa Prof. Dr. Daniela Pfannkuche
Vorsitzende/r der Prüfungskommission:	Prof. Dr. Daniela Pfannkuche
Datum der Disputation:	29.06.2020
Vorsitzender Fach-Promotionsausschusses PHYSIK:	Prof. Dr. Günter Hans Walter Sigl
Leiter des Fachbereichs PHYSIK:	Prof. Dr. Wolfgang Hansen
Dekan der Fakultät MIN:	Prof. Dr. Heinrich Graener

To my parents and brother,
for always supporting me on my way.

Abstract

In this work, new concepts for solving some of the current challenges of plasma-based acceleration are proposed and explored. These concepts, which rely on a combination of plasma-acceleration stages with a magnetic chicane, show that GeV-range beams with sub-percent energy stability and an unprecedented sub-per-mille energy spread could be produced. Achieving such a low energy spread, which is at least an order of magnitude below current state-of-the-art, has only been possible thanks to an improved understanding of the beam dynamics in this type of accelerators and the subsequent analytical modelling of previously unaccounted sources of energy spread. In addition to proof-of-principle simulations and conceptual designs, a comprehensive study of sensitivity and tolerances of the acceleration concept is included here. This systematic study has only been possible thanks to a fast particle tracking code which has been integrally developed within this work. The positive findings presented here provide a new way towards the realization of reliable and high-quality plasma-based accelerators with a broad range of applications. Among these, the outstanding beam properties that can be reached with the presented schemes would allow for the demonstration of compact plasma-driven free-electron lasers. Thanks to these good prospects, the conceptual design of a 6 GeV accelerator based on the presented methods, which has been realized as part of this work, has been selected as a baseline option for the international EuPRAXIA project. Several of the ideas and studies carried out within this thesis have been published in peer-reviewed journals including *Physical Review Letters* and *Scientific Reports*.

Zusammenfassung

In dieser Arbeit werden neue Konzepte vorgestellt, mit denen derzeitige Probleme von plasmabasierten Beschleunigern adressiert werden. Diese Konzepte beruhen auf einer Kombination von Plasmabeschleunigerstufen mit einer magnetischen Schikane. Sie zeigen, dass Strahlen im GeV-Bereich mit einer Energiestabilität im Sub-Prozentbereich und bisher nicht erreichter Energieunschärfe im Sub-Promillebereich produziert werden können. Eine so geringe Energieunschärfe, die mindestens eine Größenordnung unter dem derzeitigen Stand der Technik liegt, konnte durch ein besseres Verständnis der Strahldynamik solcher Beschleunigertypen erreicht werden. Dieses basiert auf der Entwicklung eines neuen, den Beschleunigertypen entsprechenden, analytischen Modells, das bislang unberücksichtigte Energieunschärfequellen mit betrachtet. Diese Arbeit enthält zusätzlich zu Machbarkeitssimulationsstudien und konzeptionellen Designs eine umfassende Toleranz- und Empfindlichkeitsstudie des Beschleunigerkonzepts. Diese systematische Studie war nur durch einen schnellen Teilchen-Tracking Code möglich, welcher innerhalb dieser Arbeit entwickelt und integriert wurde. Die hier vorgestellten positiven Ergebnisse zeigen einen neuen Weg auf zur Realisierung von zuverlässigen, plasmabasierten Beschleunigern von hoher Qualität mit einer Vielzahl von Anwendungen. Zu diesen zählt die Entwicklungsmöglichkeit von kompakten plasmabasierten Freien-Elektronen-Lasern, welche durch die herausragenden Strahleigenschaften der hier vorgestellten Schemata möglich wird. Dank dieser vielversprechenden Aussichten wurde ein in dieser Arbeitet entwickelter und auf den präsentierten Methoden basierender 6 GeV-Beschleuniger als eine Basisoption für das internationale EuPRAXIA Projekt ausgewählt. Zusätzlich sind mehrere Ideen und Studien aus dieser Arbeit in Peer-Review Zeitschriften wie *Physical Review Letters* und *Scientific Reports* veröffentlicht worden.

Contents

1. Introduction

Since their invention in the early 1900s, particle accelerators have become essential tools for the study of the structure of matter and its most fundamental components. Their use as particle colliders to achieve energies up to the TeV range has been of central importance to particle physics [Shi12]. In addition, synchrotron light sources, including storage rings and free-electron lasers (FELs), have a great demand from fields such as chemistry, biology, material science or condensed matter physics [WD12]. However, due to the multi-GeV to TeV energy requirements and the gradient limitations of current radio-frequency (RF) technology ($\lesssim$100 MeV/m) [Dob04], these machines are typically large facilities with a footprint on the kilometre scale which require billion-dollar investments [Shi14].

Due to this, there has been a growing interest over the past decades in the development of novel technologies which could overcome these gradient limitations and, thus, could offer a path towards accelerators of reduced size and cost. Going beyond the current limits is of particular importance for the realization of future compact colliders [Zim18]. Similarly, a great interest exists in the development of compact, or table-top, FELs and radiation sources which could be afforded by universities, research labs, medical institutes or hospitals around the world [Mal+08].

With the purpose of achieving accelerating gradients above the GeV/m-range, different novel concepts have been proposed. For the case of electron acceleration, these are generally classified as terahertz (THz) accelerators [Nan+15], dielectric laser accelerators (DLAs) [Eng+14] or plasma-based accelerators (PBAs) [ESL09]. From these different options, although all of them face certain practical challenges, plasma-based accelerators appear to be the most mature technology, owing to their fast growth and development over the past decades.

In these accelerators, an intense high-energy charged particle beam [plasma wakefield acceleration (PWFA)] [Che+85] or laser pulse [laser wakefield acceleration (LWFA)] [TD79] is used to drive an electron density wave in a gaseous plasma in which strong wakefields containing accelerating gradients of up to $\sim$100 GeV/m can be sustained. This is three orders of magnitude higher than with current RF technology and could therefore allow for a vast reduction of the accelerator size. Both LWFAs and PWFAs have demonstrated GeV energy gain in centimetre to metre scales [Blu+07; Gon+19], and each driver technology has its own set of advantages and disadvantages. However, since PWFAs already require a large RF linac as the source for the drive beams, they are generally a less attractive option than LWFAs towards the realization of ultra-compact accelerators.

Since the development of chirped-pulse amplification (CPA) [SM85], outstanding progress has been made over the past decades in the field of LWFA. Among different milestones, some of particular importance were the demonstration of so-called *quasi-monoenergetic* beams [Man+04; Ged+04; Fau+04], the achievement of energies of up to 8 GeV in only centimeter scales [Gon+19] or the production of bunches with femtosecond-scale duration and kiloampere current [Lun+11] as well as micron-level emittance [Bru+10]. All of these advances are necessary steps towards the demonstration of FEL applications [Grü+07] and, perhaps eventually, of a laser-driven collider [LE09]. However, despite this major progress, several challenges have yet to be addressed before LWFAs can be considered as a viable alternative to RF acceleration. Among these, some of the most pressing issues include a low wall-plug efficiency, a low repetition rate (and thus low average power), low beam stability, and a characteristically large beam energy spread on the 1 % to 10 % range. In addition, there is also the need to demonstrate an effective staging of several LWFAs towards the realization of high-energy applications.

Many of these issues are directly linked to the driver technology, i.e., the laser system. For example, the wall-plug efficiency and repetition rate of current high-power Ti:Sa lasers are typically on the 1 % and 1 Hz range, respectively. These are constraints which are therefore not fundamental limits of plasma acceleration, and are instead expected to gradually improve as the laser technology is further developed. It is also well known that one of the major sources of energy and charge jitter in LWFAs, which has been measured to be in the percent range [Gon+11], are the shot-to-shot fluctuations of the laser pulse. This is due to the unstable nature of many mechanisms for electron injection into the plasma wake, which are strongly coupled to the laser pulse properties and are thus sensitive to any fluctuations. Finally, the large energy spread, which can arise from a variety of sources, is known to be typically correlated due to the large slope of the accelerating fields, which appears as a result of the large gradients and small wavelength. The issues which can therefore be tackled from an accelerator physics point of view, i.e., those not uniquely determined from the laser driver technology, are the development of more robust injection and acceleration schemes and new ideas for achieving higher quality beams. This is particularly important with regards to the energy spread, which also requires a better understanding of the beam dynamics and the different sources that lead to its growth.

A possible path towards this improvement in quality and stability is the acceleration of an electron beam which has been externally prepared in an RF linac, instead of trapping electrons from the background plasma. This effectively decouples the electron injection from fluctuations in the laser properties. Therefore, it could allow for a higher control and stability of the injected beam parameters, which can then be optimized to minimize the energy spread by means of beam loading or other alternative methods. External injection introduces, however, additional complexity, and can be considered in itself as a staging experiment, with the inherent challenges that this carries. Of particular importance are

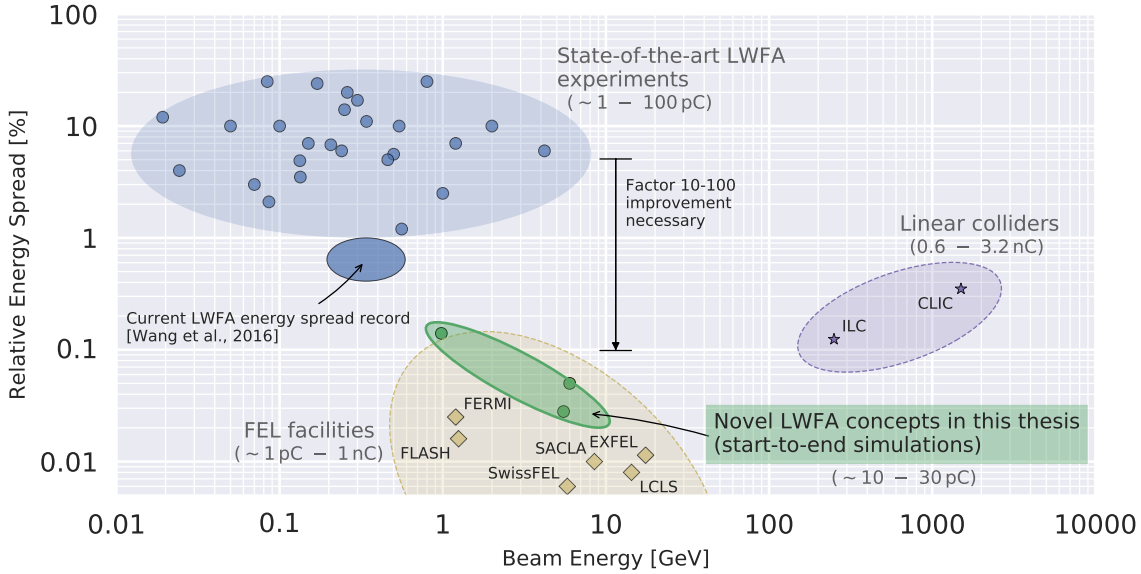

Figure 1.1.: General overview of the energy and energy spread performance of state-of-the-art LWFAs. As it can be observed, typical values range between 1 % and 10 %, which is a factor of 10 to 100 away from current FEL facilities. This is a gap which EuPRAXIA aims to close and which could be achievable with the novel concepts developed in this thesis. Note that the data points for experimental LWFAs correspond to the total beam energy spread (no slice measurements available), while the rest, except for colliders, are slice values. The typical range of bunch charge in each group is also included. Data of LWFA experiments taken from [Man+04; Ged+04; Fau+04; Lee+06; Kar+07; Haf+08; Kam+08; Buc+11; Wan+13; Lee+14; Liu+11; Pol+11; Mir+15; Gol+15; Cou+17; Fau+10; Sch+10a; Gon+11; Buc+13; Fau+06; Rec+09; Kot+09; Lun+11; Wan+16; Li+18]. Data of FEL facilities obtained from [Pen+12; SF15; SY11; Gan10; Art+02; Ish+12]. Data of linear colliders obtained from [Beh+13; Bur+18]. The energy value displayed for the colliders is the one at the end of the linac and not the center of mass energy.

the arrival time jitter between the laser driver and the electron beam, which should be synchronized to the sub-femtosecond level to prevent large energy fluctuations, and the matching of the transverse beam size to the focusing fields in the plasma, so that the emittance can be preserved. Although the matching is by now well understood and solutions exist, there is still no proven concept that can achieve the required level of synchronization. External injection is also in principle a less compact option that a purely laser-driven accelerator. However, state-of-the-art ∼20 m RF linacs such as ARES at DESY [Mar+17] can be used for external injection into plasma cells and still offer a major size reduction compared to conventional FEL facilities.

In this work, the use of external injection to produce high-quality beams in the GeV range is explored. For this, new ideas that could solve the synchronization and energy spread challenges are proposed and studied in detail. A novel analytical theory, which describes previously unaccounted sources of energy spread and thus provides new insights for producing low-energy-spread beams, is also presented. In addition, a particle tracking code for ultra-fast simulations of plasma-based accelerators has been developed. This code has allowed, for the first time, to carry out systematic sensitivity and tolerance studies of some of the presented accelerator concepts. Also as part of this work, a set of tools for data analysis and visualization with unique capabilities has been developed and is reported here.

All of these activities can be framed within the bigger context of the EuPRAXIA project [Wal+17], a large international collaboration started in 2015 with the aim of demonstrating the usability of plasma-based accelerators. Bringing together 16 European laboratories, laser industry and multiple international partners, this collaboration delivered towards the end of 2019 a conceptual design report [Ass+19] for a high-quality plasma accelerator which includes the ideas integrally developed within this thesis. A visual representation of the energy spread performance achieved through start-to-end simulations of these novel concepts is shown in Figure 1.1, where a general overview of the current state-of-the-art in LWFA and conventional RF accelerators is included.

Following the introduction, this thesis begins in Chapter 2 with a general overview of the current state and challenges in the field of plasma-based acceleration. Then, the theoretical background of the work is laid out in Chapter 3. This is followed by a description of the newly-developed particle-tracking code in Chapter 4 and of the data-analysis and visualization tools in Chapter 5. The description of the main physical studies begins then in Chapter 6, where a new concept for timing jitter correction between laser driver and witness beam is presented. Having demonstrated the possible feasibility of this solution for external injection, the focus of this work then shifts towards addressing the energy spread issue. In first place, beam dynamics studies on understanding previously unaccounted sources of energy spread in plasma-based accelerators are presented in Chapter 7. Then, in Chapter 8, a novel plasma-acceleration scheme for achieving ultra-low energy spread beams is introduced. Several conceptual beamline designs based on this method

are here proposed and studied, including detailed tolerance studies. To finalize, the main conclusions drawn from this work are summarized in Chapter 9.

2. Current state and challenges of plasma-based acceleration

It has now been 40 years since Tajima and Dawson first proposed the idea of using a laser pulse to accelerate electrons in a plasma medium [TD79]. In their seminal paper, which eventually gave rise to a whole new field of plasma and accelerator physics, they demonstrated that a plasma medium can be effectively used to convert the strong transverse fields of a laser pulse into large-amplitude plasma waves (see Figure 2.1) able to sustain extremely high longitudinal fields (up to $\sim 100\,\mathrm{GeV\,m^{-1}}$ [Fau+06]) which can be used for particle acceleration. This new technique, nowadays generally known as laser wakefield acceleration (LWFA), promised the generation of GeV electron beams in only centimetre scales. Thus, it gained interest as a possible path for overcoming the limitations of RF technology, in which the maximum gradient is limited to $\sim 100\,\mathrm{MV\,m^{-1}}$ due to breakdown and field emission in the metallic walls of the cavities [WL96]. Such a technology could lead to future accelerator facilities of reduced size and cost, such as compact free-electron lasers (FELs) [Grü+07] or particle colliders [LE09; Sch+10b].

At the time in which this technique was initially proposed, due to the unavailability of ultrashort ($\sim$30 fs) laser pulses with intensities above $10^{18}\,\mathrm{W\,cm^{-2}}$, the use of two co-propagating laser pulses of different frequency was needed to excite a plasma wave, as initially proposed in [RL72]. The first experimental demonstration of wakefield generation with this so-called plasma beat wave accelerator (PBWA) was realized in [Cla+85]. Since then, rapid progress in laser technology after the invention of chirped pulse amplification (CPA) [SM85] led also to fast developments in LWFA. These include the demonstration of $\gtrsim 100\,\mathrm{GeV\,m^{-1}}$ gradients and the acceleration of electron beams to energies above 100 MeV with charges up to the nanocoulomb range [ESL09]. The quality of the produced beams was, however, insufficient for any kind of practical applications. This was mainly due to the fact that the energy distribution of the beams exhibited a broad and continuous spectra [Mal+02]. Fortunately, this situation changed in 2004, when three different groups demonstrated almost simultaneously the production of so-called *quasi-monoenergetic* beams with $\sim$100 MeV energies and clear, few-percent energy spread peaks [Man+04; Ged+04; Fau+04].

In the 15 years since this milestone was reached, further progress in laser technology, added to the development of controlled electron injection techniques and a better understanding of the underlying physics have allowed for outstanding progress in the field. Among the achieved milestones, of particular relevance are the demonstration of electron

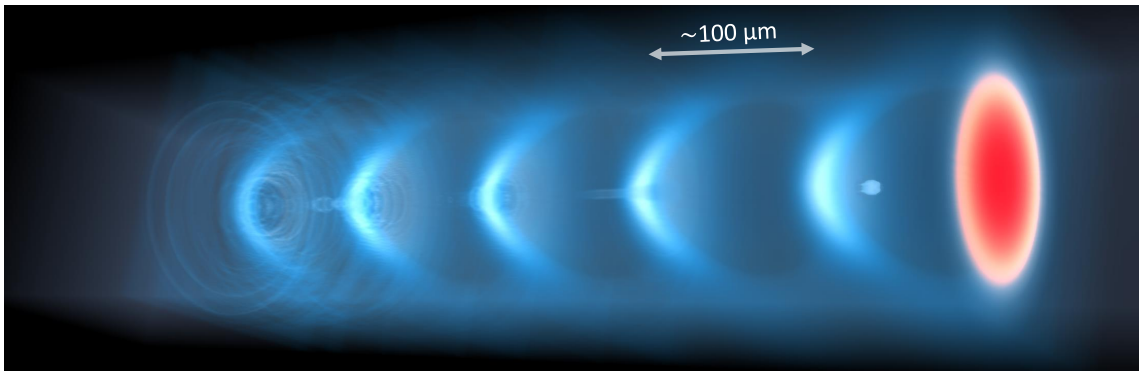

Figure 2.1.: 3D visualization of a plasma wave (blue) excited by a high-intesity laser pulse (red) and accelerating an electron beam. Image generated with VisualPIC (see Chapter 5 for details).

bunches with multi-GeV energy [Lee+06; Wan+13; Lee+14; Mir+15; Gon+19], micron-level emittance [Fri+04; Bru+10] and kiloampere current [Lun+11; Cou+17]. However, despite these major advances, a number of challenges still remain which prevent the use of plasma-based accelerators as a viable alternative to conventional RF technology.

One of the current most pressing issues regarding the beam quality is achieving an energy spectrum beyond the *quasi-monoenergetic* limit, that is, beams with sub-percent energy spread. Typical values still range between 1 % to 10 %, as seen previously in Figure 1.1, which is higher than required for most applications. This is particularly limiting for free-electron lasers, where an energy spread between 0.1 % to 0.01 % is typically needed [Cor+13]. One of the main reasons for this high energy spread is the insufficient control of the properties of the injected beams when using internal injection methods. Thus, a possible alternative to this is the external injection of a beam which has been generated in an RF linac and whose properties can be tailored to maintain a small emittance and energy spread within the plasma accelerator [Wei+17; Svy+18]. An issue raised by this, however, is that an excellent synchronization (fs to sub-fs) between the driver and witness is needed in order to achieve sufficient energy stability [Fer+17]. This is particularly challenging, and beyond current state-of-the-art, when driver and witness are generated from different sources, as it is the case in an LWFA.

Another important issue faced nowadays by plasma-based accelerators is the shot-to-shot stability of the produced beams. In terms of charge, energy and emittance, the fluctuations have been reported to be on the percent range [Gon+11] and should therefore be improved for a reliable operation. Other key parameters which are also hindering the use of LWFAs with respect to RF technology are the average power delivered by the beam and the efficiency of the accelerator. Both issues arise from limitations of current high-power laser systems, whose repetition rate and wall-plug efficiency typically range around 1 Hz and 0.1 %, respectively [Zou+15; Adl+19]. To this low efficiency one has to add the laser-to-beam efficiency, which is typically between 1 % to 10 % depending on the degree of beam loading and the depletion of the laser driver, thus leading to a

wall-plug-to-beam efficiency below 0.01 %. This is in strong contrast to current RF linacs and synchrotrons, which can operate at kHz or even MHz repetition rates and whose wall-plug-to-beam efficiency is generally on the 10 % range. Maximizing the efficiency of LWFAs requires not only improvements in the laser system, but also maximizing the effective acceleration length. For this, further advances in laser guiding in preformed plasma channels are needed, particularly at low ($\sim 10^{17}$ cm^{-3}) densities and in the case of realistic laser pulses.

In addition to these general requirements towards usable and efficient LWFAs, some other challenges become relevant in the quest for higher energies, particularly for an eventual plasma-based collider. These are issues related to positron acceleration, which is more problematic in this type of accelerators [Cor+15], and the staging of several LWFA modules. This includes the laser coupling and removal for each stage as well as the beam transport and matching between them such that emittance growth is avoided.

An alternative approach to plasma-based acceleration which avoids some of the issues listed above consists of using, instead of a laser pulse, a high-energy and dense electron beam as the wakefield driver [Che+85]. This technique, now generally referred to as beam-driven plasma wakefield acceleration and abbreviated simply as PWFA, offers a higher efficiency and repetition rate than LWFAs thanks to the high-quality RF accelerators used to produce the drive bunches. An obvious drawback is, however, the large size and cost of the accelerator required to generate the drivers, which makes this option less attractive than LWFA in terms of compactness. This technique brings nonetheless the possibility of studying and developing plasma-based accelerators in a regime which is inaccessible by current lasers, and which offers other interesting properties such as no dephasing nor need for external guiding of the driver. Apart from this classic PWFA approach, there is a growing interest in the development of so-called *hybrid* plasma accelerators [Hid+10; Mar+19a] in which the PWFA driver is generated by an LWFA stage instead of an RF linac. This has again the benefits of a compact setup and allows the study of PWFAs without the need for an RF linac. This type of hybrid accelerators promise the production of electron beams in the PWFA stage which have a significantly improved quality with respect to the original LWFA beam (thus, they are sometimes referred to as *beam brightness transformers* [Mar+19a]) but, since they rely on an first LWFA stage suffer from the same (or even worse) low average power and efficiency issues.

Major efforts are now being dedicated worldwide by independent research groups, national institutions and large international collaborations towards solving the challenges posed by these different approaches, all with the common goal of demonstrating usable plasma-based accelerators. Many ideas have, for example, been proposed in recent years which aim at solving the energy spread issue and producing usable beams. These include, apart from the well-known use of beam loading [Kat+87; Tzo+09], modulating [Bri+17] or tailoring [Döp+18] the plasma density profile, injecting a secondary bunch [Man+17] or taking advantage of the beam-induced wakefields [BS12; Ant+14; DAr+19;

Shp+19; Wu+19a; Wu+19b]. In this regard, the use of external injection is also being considered as a viable option for achieving high-quality acceleration, specially thanks to progress in producing beams which can be matched to the plasma requirements in compact RF linacs [Ros+14; Mar+16; Zei].

In the case of LWFAs, there is now a particular push towards the development of high average power laser systems which can operate at kHz repetition rate, such as the new KALDERA (kilowatt lasers at DESY for revolutionary accelerators) project at DESY [Lee+19]. The realization of such a laser system would not only lead to an average beam power closer to that of RF technology, but would also result in an improvement of the beam quality and stability thanks to the possibility of implementing effective feedback loops [Str+18]. In addition, there are also potential solutions based on diode-pumped lasers with direct CPA for achieving not only a high average power, but also a wall-plug efficiency on the few-percent or even above the 10 % range [Sis+19]. There has also been a great progress regarding the guiding of high-power lasers through long (up to 20 cm) plasma channels, either generated by a single pre-pulse [Sha+18; Sha+19] or by a combination of a discharge and a so-called *heater* laser [Gon+19]. This culminated with the production of electrons with a worldwide record 8 GeV energy in a single LWFA stage [Gon+19]. The coupling of two LWFA stages has also been demonstrated, albeit with a low capture efficiency in the second stage [Ste+16], by using plasma mirrors and plasma lenses. These two devices, which are key towards compact multistage LWFAs, have also undergone major developments in recent years with the rise of thin, liquid-crystal mirrors [Poo+16], and by solving the issues with chromatic aberrations in plasma lenses [Lin+18].

Apart from laser-driven acceleration, many PWFA projects have also been established to push the boundaries of this technology. Examples of this are the FLASHForward facility at DESY [Asc+16], where plasma experiments with multi-kW average power can be carried out, the SPARC_LAB test facility [Fer+13], where novel PWFA techniques can be studied, the AWAKE experiment at CERN [Gsc+16], where 400 GeV proton beams are used as drivers, or the FACET II test facility at SLAC [Jos+18], where the production of high-quality beams, novel injection techniques or positron acceleration could be explored. With regards to hybrid accelerators, a collaboration between German institutes has also been recently established and has already produced the first experimental results [Kur+19].

Great progress in all major fronts has therefore been achieved in recent years throughout the world. For the particular case of Europe, where many independent groups exist, a large international collaboration was established in 2015 to join the efforts of the large, but spread, plasma acceleration community towards a common goal. This collaboration, known as EuPRAXIA (European Plasma Research Accelerator with eXcellence In Applications) [Wal+17], was joined by 16 European laboratories and 25 additional associated partners from Europe, Asia and the USA. The common objective of this joint effort

Table 2.1.: Target beam parameter requirements for the 5 GeV EuPRAXIA accelerator.

Parameter	**Symbol**	**Units**	**Value**
Beam energy	E_b	GeV	5
Relative energy spread	σ_δ	%	1
Relative energy spread (slice)	$\sigma_{\delta,\mathrm{sl}}$	%	0.1
Normalized emittance	$\epsilon_{n,x\|y}$	µm	1
Normalized emittance (slice)	$\epsilon_{n,x\|y,sl}$	µm	1
Bunch charge	Q	pC	30
Bunch duration (FWHM)	τ_{FWHM}	fs	10
Peak current	I_{peak}	kA	3
Repetition rate	f_{rep}	Hz	10

was to produce a conceptual design report (CDR) for the worldwide first plasma-based accelerator usable for applications. In particular, for a 5 GeV plasma-based FEL user facility. The focus was therefore not on reaching record-breaking energies, but rather on exploring all possibilities offered by LWFA, PWFA and hybrid options for improving the beam quality, detecting key challenges and proposing new solutions towards the realization of such a facility. In the final CDR [Ass+19], finished at the end of 2019, several options were identified as potential candidates able to deliver the beam quality requirements specified in Table 2.1. These are 5 different accelerator proposals based on single- and multistage LWFA, PWFA, and with both internal and external injection methods. One of these 5 options was developed within this thesis and is presented later in Chapter 8. A conceptual design of this beamline, which is composed by a combination of LWFA stages and magnetic chicanes, is shown in Figure 2.2.

On a national level, Germany, as well as other countries, is also showing a strong commitment to the development of laser-plasma accelerators with the ATHENA (Accelerator Technology HElmholtz iNfrAstructure) project [AS+18]. This project builds up infrastructure for implementing two flagship sub-projects: one for electron (ATHENA_e) and another for hadron (ATHENA_h) acceleration. The ATHENA_e project, hosted by DESY, will be partly located at SINBAD, a dedicated accelerator research facility in which the KALDERA laser will be integrated (see Figure 2.3). One of the core elements of this facility is the ARES linac [Mar+17], a normal-conducting S-band accelerator able to deliver ultrashort (fs to sub-fs) bunches with energies of up to 150 MeV. Thanks to these ultrashort bunches, whose parameters are included in Table 2.2, ARES is ideally suited for performing external injection experiments into novel accelerators, such as LWFAs or DLAs (dielectric laser accelerators), which are characterized by small wavelengths. At the time of writing, it is currently foreseen that, in addition to internal injection LWFA experiments with the KALDERA laser, external injection into an LWFA and acceleration of up to 1 GeV will be tested at SINBAD with the ARES linac as part of the ATHENA_e

Figure 2.2.: 3D render of the 6 GeV conceptual multistage accelerator beamline for EuPRAXIA. This accelerator concept, which offers an unprecedented energy spread performance, was developed within this thesis and is included in Chapter 8. Image from [Ass+19]

efforts. The preliminary parameters of KALDERA are listed in Table 2.3.

The work presented in this thesis was performed within the framework of ATHENA/SINBAD and, mainly, the EuPRAXIA collaboration. The use of externally-injected beams, based on the parameter range of ARES, into an LWFA has been explored as a potential solution for achieving high-quality, GeV-class, plasma-accelerated beams. As previously mentioned, novel solutions for achieving an ultra-low energy spread and sufficient synchronization for effectively realizing external injection have been proposed and studied. Within the general context of current challenges in plasma-based acceleration, this thesis therefore contributes directly towards solving the energy spread and stability issues. It also contributes, perhaps more indirectly, to the realization of multistage LWFAs. This is because all the concepts presented here rely on the staging of several laser-driven plasma modules, and various alternatives on how such multistage schemes might be implemented are proposed and studied through detailed start-to-end simulations.

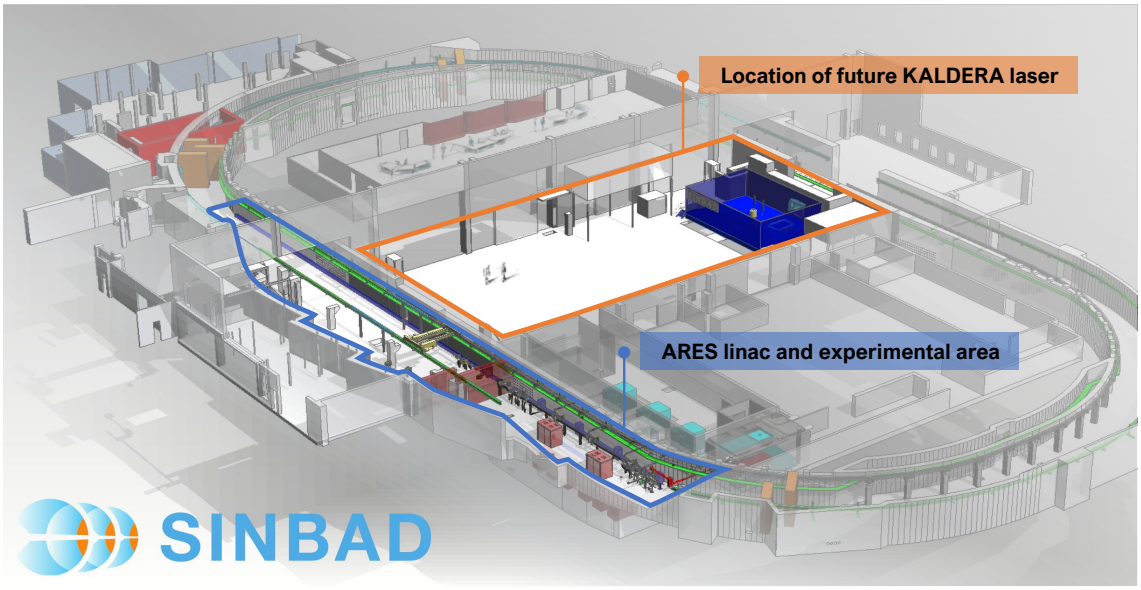

Figure 2.3.: Overview of the SINBAD accelerator research facility at DESY, where part of the plasma-acceleration research within the ATHENA_e project will be carried out. Image adapted from [Dor+18].

Table 2.2.: Beam parameter of the ARES linac at SINBAD based on currently designed working points. Data obtained from [Zhu17].

Parameter	**Symbol**	**Units**	**Value**
Beam energy	E_b	MeV	50 to 150
Relative energy spread	σ_δ	%	∼0.1
Relative energy spread (slice)	$\sigma_{\delta,\mathrm{sl}}$	%	∼0.1
Normalized emittance	$\epsilon_{n,x\|y}$	µm	$\lesssim$0.5
Normalized emittance (slice)	$\epsilon_{n,x\|y,sl}$	µm	∼0.1
Bunch charge	Q	pC	0.5 to 30
Bunch duration (RMS)	τ_{FWHM}	fs	0.5 to 30
Peak current	I_{peak}	kA	0.5 to 1.5
Repetition rate	f_{rep}	Hz	10 to 50
RMS arrival time jitter	$\mathcal{T}$	fs	$\leq$ 10

Table 2.3.: Current preliminary parameters for the KALDERA laser [Lee+19].

Parameter	**Symbol**	**Units**	**Value**
Wavelength	λ_l	nm	800
Pulse energy	E_l	J	3
Pulse duration (FWHM)	$\tau_{\mathrm{FWHM},l}$	fs	30
Peak power	$P_{\mathrm{peak},l}$	TW	100
Repetition rate	$f_{\mathrm{rep},l}$	kHz	1
Average power	$P_{\mathrm{avg},l}$	kW	3

3. Theoretical framework

In this chapter, the general theoretical background of this thesis is laid out. To begin, some fundamental concepts of accelerator physics regarding single-particle and beam dynamics are presented. The basic theory of plasma-based acceleration is then introduced, starting first with general concepts about lasers and plasmas and eventually diving in more detail into the physics of wakefield generation with a special focus on laser drivers. Certain particularities of beam dynamics in plasma-based accelerators are also discussed, such as matching, electron injection techniques or sources of energy spread. Afterwards, the basic theory of free-electron lasers is presented, since they are the main target application of the plasma-acceleration concepts presented in this thesis. To finalize, a summary of all the accelerator and plasma simulation codes which have been used throughout this thesis is included.

3.1. Dynamics of charged particles

3.1.1. Fundamental equations and coordinate system

Particle accelerators use electromagnetic fields to accelerate charged particles. As such, the basic model which governs the acceleration process is the well known set of Maxwell's equations. In their differential form, these can be expressed as

$$\nabla \cdot \boldsymbol{E} = \frac{\rho}{\epsilon_0} \,, \tag{3.1}$$

$$\nabla \cdot \boldsymbol{B} = 0 \,, \tag{3.2}$$

$$\nabla \times \boldsymbol{E} = -\frac{\partial \boldsymbol{B}}{\partial t} \,, \tag{3.3}$$

$$\nabla \times \boldsymbol{B} = \mu_0 \left(\boldsymbol{J} + \epsilon_0 \frac{\partial \boldsymbol{E}}{\partial t} \right) \,, \tag{3.4}$$

which describe the source of, and the relationship between, the electric and magnetic fields $\boldsymbol{E}$ and $\boldsymbol{B}$. In this equations, ρ and $\boldsymbol{J}$ represent the charge and current density, while the constants ϵ_0 and μ_0 correspond to the electric permittivity and permeability of free space. The action of these electromagnetic fields on a particle with charge q and velocity $\boldsymbol{v}$ is given by the Lorentz force:

$$\boldsymbol{F} = q \left(\boldsymbol{E} + \boldsymbol{v} \times \boldsymbol{B} \right) \,. \tag{3.5}$$

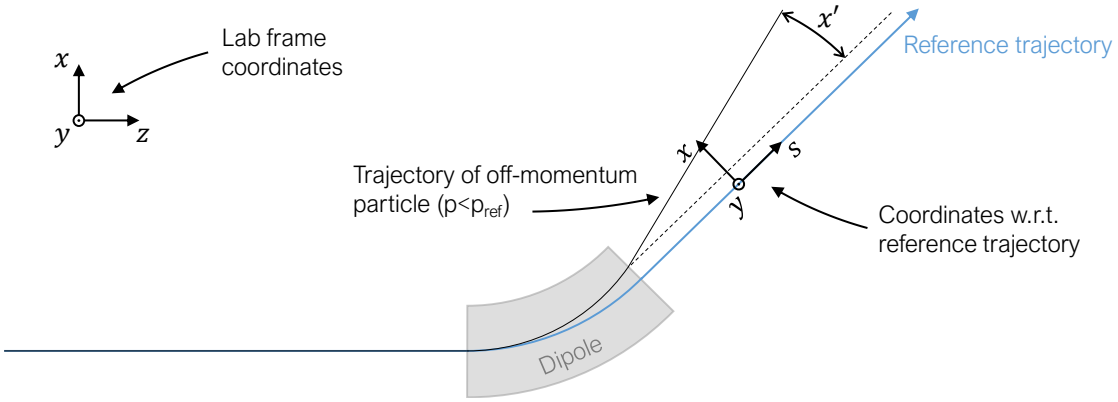

Figure 3.1.: Overview of the coordinate systems in the lab frame and with respect to the reference trajectory. A sample particle trajectory in a bending section is shown.

Throughout this thesis, a basic set of coordinates will be used to describe the position in space and time of particles within an accelerator. For this task, two main reference frames can generally be used. On one side there is the set of laboratory-frame spatial coordinates x, y, z as well as the time t. In this case, as linear accelerators (linacs) will be considered, the z coordinate will refer to the longitudinal, or parallel, direction along the linac, while the x and y components will refer to the horizontal and vertical transverse directions. Alternatively, to describe the evolution of particles and particle beams along the accelerator it is also useful to define a set of coordinates with respect to a reference trajectory along the linac elements, which normally corresponds to the ideal trajectory of particle with a certain reference energy. In this reference frame, the coordinate s refers to the longitudinal position along the reference trajectory, and the transverse coordinates x and y are instead defined as perpendicular to the propagation along s. This reference frame is particularly useful when the reference trajectory is not straight (otherwise s and z are equivalent), as seen in Figure 3.1, where an overview of these two coordinate systems is shown. For simplicity, the transverse coordinates are denoted as x and y in both reference frames.

In addition to the set of spatial coordinates $\boldsymbol{r} = (x, y, z)$ in both reference frames, the 6D phase-space of the particles is completed with the momentum $\boldsymbol{p} = m_0 \gamma \dot{\boldsymbol{v}}$, where $\boldsymbol{v} = d\boldsymbol{r}/dt$ is the particle velocity, m_0 is the rest mass of the particle and $\gamma = 1/\sqrt{1-\beta^2}$ is the relativistic Lorentz factor, in which $\beta = v/c$ is the particle speed $v = |\boldsymbol{v}|$ normalized to the speed of light c. Using these parameters, the energy and momentum of a relativistic particle can be expressed as

$$E_p = \gamma m_0 c^2 \,, \tag{3.6}$$

$$p = \beta \gamma m_0 c \,. \tag{3.7}$$

As the motion of particles in an accelerator becomes relativistic ($v \simeq c$), the factor $\beta \simeq 1$ is normally neglected and $\gamma \gg 1$. In addition, since the longitudinal motion is typic-

ally the dominant component, i.e., $p_x \sim p_y \ll p_z$, it can be considered that the particle momentum is simply $p \simeq p_z \simeq m_0 c\gamma$. The 6D phase-space of a particle can be described in the lab frame by the position and momentum variables as (x, p_x, y, p_y, z, p_z). Another widely used option, however, is to describe it with respect to the trajectory of a reference particle along the accelerator. In this case, the set of variables (x, x', y, y', s, δ) is used, where $x' = dx/ds \simeq p_x/p_{\text{ref}}$ and $y' = dy/ds \simeq p_y/p_{\text{ref}}$ are the transverse slopes of the particle trajectory with respect to that of the reference particle and $\delta = (p - p_{\text{ref}})/p_{\text{ref}} \simeq (\gamma - \gamma_{\text{ref}})/\gamma_{\text{ref}}$ is the fractional momentum deviation with respect to the reference momentum, $p_{\text{ref}} \simeq \gamma_{\text{ref}} m_0 c$ [CM08]. Finally, since the focus of this thesis is exclusively on electron acceleration, the particle charge and rest mass will generally be regarded as $q = -e$ and $m_0 = m$, which correspond, respectively, to the elementary charge and rest mass of an electron.

3.1.2. Particle acceleration and transport with electromagnetic fields

Particle accelerators, in order to be useful, should not only provide an energy boost to charged particles, but should do so while properly guiding them throughout the device such that they are contained in well defined streams, called particle beams. The Lorentz force in Equation (3.5) provides the basic information in how to achieve both acceleration and guiding while decoupling these two processes. From this equation it can be seen that the magnetic force, $\boldsymbol{F}_m = q(\boldsymbol{v} \times \boldsymbol{B})$, cannot be used to change the energy of the particles, i.e, it cannot perform work, W, on them:

$$W_m = \int \boldsymbol{F}_m \boldsymbol{v} dt = \int q(\boldsymbol{v} \times \boldsymbol{B}) \boldsymbol{v} dt = 0\,, \tag{3.8}$$

due to $(\boldsymbol{v} \times \boldsymbol{B}) \perp \boldsymbol{v}$. Thus, the acceleration of particles has to be instead carried out by longitudinal electric fields, E_z, while the guiding and confinement of the particles in x and y can be performed by magnetic fields, which only deviate their trajectory. This functional separation allows the design and optimization of dedicated devices specialized on each task: while particle acceleration in conventional machines is typically carried out by metallic cavities filled with radiofrequency (RF) electric fields, the beam transport is performed by elements with optimized magnetic fields.

The decoupling of acceleration and guiding also allows the longitudinal and transverse particle dynamics to be independently treated. In the longitudinal plane, where the acceleration takes place, the energy gain of electrons within an accelerating module is obtained by integrating Equation (3.5) as:

$$\Delta E_p = \int_0^t \boldsymbol{F} \boldsymbol{v} dt = \int_0^t -eE_z v_z dt = -eE_z L_{\text{acc}}\,, \tag{3.9}$$

where no magnetic fields and a constant $\boldsymbol{E} = (0, 0, E_z)$ are assumed, and L_{acc} is the total acceleration length.

In regards to the transport and guiding, the transverse particle dynamics will be controlled by external magnetic fields which bend their direction of propagation. A key parameter to describe this is the so-called magnetic rigidity [Wie15], $B\rho$, defined as:

$$B\rho = \frac{p}{q}\,, \tag{3.10}$$

where ρ is the bending radius experienced by a particle with momentum p and charge q under a uniform magnetic field B. The applied magnetic fields can be optimized to achieve different effects over the particle motion. In order to see this, it is useful to perform a Taylor expansion of the field along the transverse planes. In particular, for a simple 1D case along the x direction it is obtained that the y component of the magnetic field can be expressed as

$$B_y(x) = B_{y,0} + \frac{\partial B_y}{\partial x}x + \frac{1}{2}\frac{\partial^2 B_y}{\partial x^2}x^2 + \dots\,, \tag{3.11}$$

where one can differentiate, in order of appearance, between the dipolar, quadrupolar, sextupolar and higher order components of the field, which have different effects on the particle dynamics. For example, a constant magnetic field $B_{y,0}$ will lead to a bend in the particle trajectory according to Equation (3.10), while a positive gradient $\partial B_y/\partial x$ will focus the particle towards the axis an induce an oscillatory motion, as explained in the following section. By normalizing Equation (3.11) with with respect to the magnetic rigidity, the following expression is found [Wie15]:

$$\frac{B_y(x)}{p/q} = \frac{B_{y,0}}{p/q} + \frac{g_1}{p/q}x + \frac{1}{2}\frac{g_2}{p/q}x^2 + \cdots = \frac{1}{\rho} + k_1 x + \frac{1}{2}k_2 x^2 + \dots\,, \tag{3.12}$$

where the normalized quadrupole and sextupole gradients, $k_1 = g_1/(p/q)$ and $k_2 = g_2/(p/q)$, have been defined, with $g_1 = \partial B_y/\partial x$ and $g_2 = \partial^2 B_y/\partial x^2$. The different effect on the particle dynamics of each of the terms in this expansion allows the development of specialized magnetic devices which have, in an ideal case, only one of these components. As such, these magnetic elements are known as dipoles, quadrupoles, sextupoles, etc.

3.1.3. Particle motion in a focusing field

Of particular importance is the use of focusing devices, typically quadrupoles (only k_1 component is non-zero), to transport and guide the particle beams along the accelerator. This is a fundamental component of any accelerator and, as such, it is of high interest to determine the particle dynamics in the presence of focusing fields. This can be obtained from Equation (3.5), which, in the absence of accelerating fields, allows the transverse dynamics of a charged particle along a focusing channel with gradient $k(s)$ to be written as:

$$x''(s) + k(s)x(s) = 0\,, \tag{3.13}$$

where the subindex in k_1 has been dropped for simplicity.

In the case of constant focusing, i.e. $k(s) = k$, this expression is simply the equation of motion of a harmonic oscillator. However, a more general solution can be obtained when $k(s)$ is an arbitrary function of s describing the focusing fields along the accelerator. In this case, the solution can be found to be [Wie15]:

$$x(s) = A\sqrt{\beta(s)}\cos\left(\psi(s) + \psi_0\right) \,, \tag{3.14}$$

$$x'(s) = -A\sqrt{\frac{1}{\beta(s)}}\left[\alpha(s)\cos\left(\psi(s) + \psi_0\right) + \sin\left(\psi(s) + \psi_0\right)\right] \,, \tag{3.15}$$

where a set of new functions and parameters have been introduced for convenience, but whose significance will soon become apparent. These are the amplitude factor A, the β and α parameters, where

$$\alpha(s) = -\frac{1}{2}\frac{d\beta(s)}{ds} \,, \tag{3.16}$$

the initial phase ψ_0 and the phase advance, which is given by

$$\psi(s) = \int_0^s \frac{ds}{\beta(s)} \,. \tag{3.17}$$

From Equations (3.14) and (3.15) it can be found that there is a constant of motion

$$A^2 = \gamma(s)x(s)^2 + 2\alpha(s)x(s)x'(s) + \beta(s)x'(s) \,, \tag{3.18}$$

also known as the Courant-Snyder invariant [CS00]. This expression corresponds to the equation of an ellipse of area πA^2 whose shape is determined by the parameters β, α and γ, which, at the same time, are related to each other through

$$\beta\gamma - \alpha^2 = 1 \,. \tag{3.19}$$

Equation (3.18) is indeed, as illustrated in Figure 3.2, the equation of the ellipse described by the particle as it moves in phase-space. The parameters of this ellipse, β, α and γ, are generally known as Courant-Snyder or Twiss parameters. Since they depend on s, the shape of this ellipse will also be changing along the accelerator. Its area, however, will remain constant.

The Twiss parameters should not be confused with the relativistic parameters β and γ introduced in Section 3.1.1. In the following, it will always be explicitly stated to which parameters they refer to, and a subindex might be added to differentiate them.

3.1.4. Transfer matrix formalism

Instead of directly solving the equations of motion, a particularly effective method for determining the particle evolution along the accelerator is through the use of transfer matrices. In this case, the particle position in phase-space $\boldsymbol{u} = (x, x', y, y', s, \delta)^T$, can be

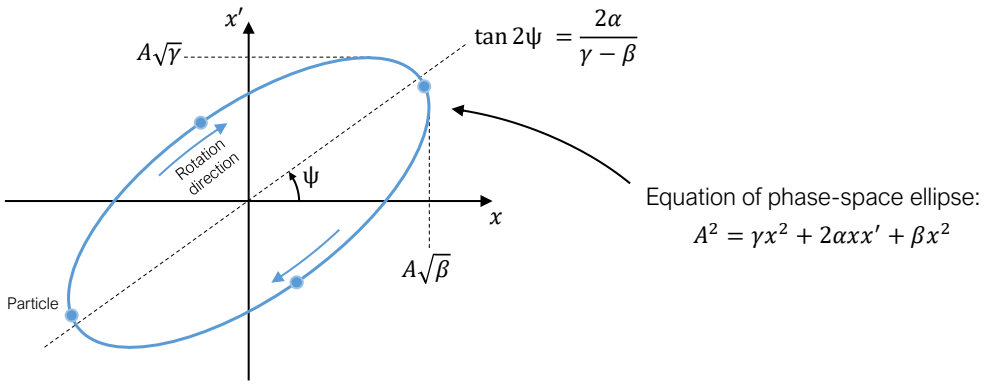

Figure 3.2.: Phase-space ellipse along which a single particle moves. Since the ellipse parameters β, α and γ change along the accelerator, the shape of this ellipse is also continuously changing. Some key parameters such as the maximum x and x' of the trajectory as well as the inclination angle of the ellipse are indicated.

evolved to its final state after a beamline element, $\boldsymbol{u}^f$, by applying a 6×6 transfer matrix $\boldsymbol{R}$ to the initial coordinates of the particle, $\boldsymbol{u}^0$, as

$$\boldsymbol{u}^f = \boldsymbol{R}\boldsymbol{u}^0 \,. \tag{3.20}$$

This matrix, which can be expressed as

$$\boldsymbol{R} = \begin{bmatrix} \boldsymbol{R}_{XX} & \boldsymbol{R}_{XY} & \boldsymbol{R}_{XZ} \\ \boldsymbol{R}_{YX} & \boldsymbol{R}_{YY} & \boldsymbol{R}_{YZ} \\ \boldsymbol{R}_{ZX} & \boldsymbol{R}_{ZY} & \boldsymbol{R}_{ZZ} \end{bmatrix} \tag{3.21}$$

is composed by three 2×2 sub-matrices in the diagonal which describe the evolution of the horizontal, vertical and longitudinal coordinates independently from each other. In addition, the six 2×2 sub-matrices outside of the diagonal describe the possible couplings between the different planes. The elements R_{16} to R_{56} are referred to as dispersion and describe how the single-particle trajectories change when $\delta \neq 0$.

Each beamline element is characterized by a certain transfer matrix. For example, for a quadrupole with constant focusing ($k(z) = k$) and length L, the solution to Equation (3.13) can be easily found and expressed as [Wie15]

$$\begin{bmatrix} x_f \\ x'_f \end{bmatrix} = \begin{bmatrix} \cos\sqrt{k}L & \frac{1}{\sqrt{k}}\sin\sqrt{k}L \\ -\sqrt{k}\sin\sqrt{k}L & \cos\sqrt{k}L \end{bmatrix} \begin{bmatrix} x_0 \\ x'_0 \end{bmatrix} , \tag{3.22}$$

where the 2×2 matrix would correspond to the $\boldsymbol{R}_{XX}$ transfer matrix of the quadrupole. With this approach, the particle propagation through several consecutive beamline elements can be simply obtained by repeatedly multiplying the transfer matrices of each

element.

It should be noted, however, that Equation (3.20) is only a first-order approximation for small deviations from the phase-space trajectory of the reference particle. Thus, it contains only the first term of a Taylor expansion which can be more generally written as [BS85]

$$u_i^f = \sum_j R_{ij} u_k^0 + \sum_{j,k} T_{ijk} u_j^0 u_k^0 + \dots \,, \tag{3.23}$$

where transport matrices of first ($\boldsymbol{R}$), second ($\boldsymbol{T}$), and higher order can be individually identified. With this expansion, each element in an accelerator can be modelled with different degrees of accuracy.

3.2. Dynamics of particle beams

When dealing with large particle ensembles (beams), a statistical description of the system is needed. This is done through the beam matrix $\boldsymbol{\Sigma}$, which corresponds to the covariance matrix of the particle positions in phase-space, $\boldsymbol{u} = (x, x', y, y', s, \delta)^T$:

$$\boldsymbol{\Sigma} = \mathrm{Cov}(\boldsymbol{u}, \boldsymbol{u}) = \begin{bmatrix} \langle x^2 \rangle & \langle x x' \rangle & \langle x y \rangle & \langle x y' \rangle & \langle x s \rangle & \langle x \delta \rangle \\ \langle x' x \rangle & \langle x'^2 \rangle & \langle x' y \rangle & \langle x' y' \rangle & \langle x' s \rangle & \langle x' \delta \rangle \\ \langle y x \rangle & \langle y x' \rangle & \langle y^2 \rangle & \langle y y' \rangle & \langle y s \rangle & \langle y \delta \rangle \\ \langle y' x \rangle & \langle y' x' \rangle & \langle y' y \rangle & \langle y'^2 \rangle & \langle y' s \rangle & \langle y' \delta \rangle \\ \langle s x \rangle & \langle s x' \rangle & \langle s y \rangle & \langle s y' \rangle & \langle s^2 \rangle & \langle s \delta \rangle \\ \langle \delta x \rangle & \langle \delta x' \rangle & \langle \delta y \rangle & \langle \delta y' \rangle & \langle \delta s \rangle & \langle \delta^2 \rangle \end{bmatrix} . \tag{3.24}$$

The notation $\langle u_i u_j \rangle$ has been defined here to represent the covariance between the two variables in brackets. That is, for a particle beam characterized by a distribution function $f(x, \dots, \delta)$:

$$\langle u_i u_j \rangle = \int u_i u_j f(x, \dots, \delta) \, \mathrm{d}V - \left(\int u_i f(x, \dots, \delta) \, \mathrm{d}V \int u_j f(x, \dots, \delta) \, \mathrm{d}V \right) , \tag{3.25}$$

where $\mathrm{d}V = \mathrm{d}x \, \mathrm{d}x' \, \mathrm{d}y \, \mathrm{d}y' \, \mathrm{d}s \, \mathrm{d}\delta$ is the 6D differential phase-space volume and the distribution function is assumed to be normalized, i.e., $\int f(x, \dots, \delta) \, \mathrm{d}V = 1$. From this definition, it is clear that $\langle u_i u_i \rangle = \langle u_i^2 \rangle$ is the variance or second central moment of the u_i variable. Thus, the RMS beam parameters such as the transverse size (σ_x, σ_y), divergence (σ_x', σ_y'), length (σ_z) and energy spread (σ_δ) can be directly obtained as

$$\sigma_{u_i} = \sqrt{\langle u_i^2 \rangle}. \tag{3.26}$$

3.2.1. Transverse dynamics

As described in Section 3.1.3, the position of a single particle in transverse phase-space evolves following an ellipse whose shape can change along the accelerator. When considering a whole particle beam, the description of its transverse phase-space can also be simplified by enclosing it within an ellipse. A common choice for this is the so-called RMS ellipse, which is directly given by the beam matrix in Equation (3.24). In particular, for the coordinates $\boldsymbol{X} = [x \; x']^T$ in the horizontal plane, the phase-space ellipse is given by

$$\boldsymbol{X}^T \boldsymbol{\Sigma}_{XX}^{-1} \boldsymbol{X} = 1 \,, \tag{3.27}$$

where $\boldsymbol{\Sigma}_{XX} = \mathrm{Cov}(\boldsymbol{X}, \boldsymbol{X})$ is the 2D beam matrix, which corresponds to the first symmetric 2×2 sub-matrix in the diagonal of $\boldsymbol{\Sigma}$. By performing the matrix multiplication, this equation turns into

$$\left\langle x'^2 \right\rangle x^2 - 2 \left\langle x x' \right\rangle x x' + \left\langle x^2 \right\rangle x'^2 = \epsilon \,, \tag{3.28}$$

where a new parameter

$$\epsilon_{\mathrm{tr,\,rms}} = \det \boldsymbol{\Sigma}_{XX} \,, \tag{3.29}$$

known as the RMS trace-space emittance has been defined. This parameters characterizes the area of the ellipse, which is then given by $\pi \epsilon_{\mathrm{tr,\,rms}}$.

This phase-space ellipse can be associated with that described by a single particle which has an oscillation amplitude given by $A = \sqrt{\epsilon}$. In this case, by comparing Equations (3.18) and (3.28), the following identities are obtained:

$$\beta = \frac{\left\langle x^2 \right\rangle}{\epsilon}, \quad \gamma = \frac{\left\langle x'^2 \right\rangle}{\epsilon}, \quad \alpha = -\frac{\left\langle x x' \right\rangle}{\epsilon}. \tag{3.30}$$

By doing so, the description of a whole particle beam is reduced to that of a single particle since, from Liouville's theorem, all the particles initially contained within this ellipse will remain inside it [Wie15]. This association between the Twiss parameters of the single-particle ellipse, which are determined from the focusing system, and those of the beam ellipse, which are determined from the statistical moments of particle distribution, is commonly used in periodic focusing systems such as in circular accelerators, but it might not be generally true. When the single-particle and the beam ellipses are not identical, the beam is said to be mismatched to the focusing lattice [Wan08]. Thus, in general, the expressions in Equation (3.30) should be taken as the definition of the Twiss parameters of the beam and not as an identity with the single-particle ellipse.

The RMS trace-space emittance defined in 3.29 is, according to Liouville's theorem, a constant property of the beam in the absence of acceleration and non-linear transverse forces. However, when the beam is accelerated, this quantity will decrease proportional to p^{-1} since $x' =\simeq p_x/p$. Thus, it is useful to introduce the normalized trace-space emittance [Flo03], defined as

$$\epsilon_{\mathrm{n,\,tr,\,rms}} = \beta_r \gamma_r \epsilon_{\mathrm{tr,\,rms}} \,, \tag{3.31}$$

where β_r and γ_r are now the average relativistic parameters of the beam. This normalized emittance remains constant also during acceleration and is generally used as a figure of merit of the transverse beam quality.

Alternative definitions of the emittance can be introduced by considering the phase-space (x, p_x) instead of the trace-space (x, x'). In this case, the RMS normalized (phase-space) emittance is given by

$$\epsilon_{\mathrm{n,\,rms}} = \frac{1}{mc}\sqrt{\langle x^2\rangle \langle p_x^2\rangle - \langle x p_x\rangle}\,, \tag{3.32}$$

and a so-called geometric emittance, in analogy to the unnormalized trace-space emittance, is defined as

$$\epsilon_{\mathrm{rms}} = \epsilon_{\mathrm{n,\,rms}}/\beta_r\gamma_r\,. \tag{3.33}$$

These two sets of expressions (Equation (3.29) and Equation (3.33)) and (Equation (3.31) and Equation (3.32)) can be considered as equivalent when the energy spread of the beam is sufficiently small, i.e., $\epsilon_{\mathrm{n,rms}} \simeq \langle\gamma\rangle\epsilon_{\mathrm{tr,rms}}$, for $\beta \sim 1$. However, when this is not the case, as it is often in plasma-based accelerators, the full expression

$$\epsilon_{\mathrm{n,rms}}^2 = \langle\gamma\rangle^2(\sigma_\delta^2\sigma_x^2\sigma_{x'}^2 + \epsilon_{\mathrm{tr,rms}}^2)\,. \tag{3.34}$$

must be used [Flo03; Mig+13], where σ_δ, σ_x and $\sigma_{x'}$ are, respectively, the relative energy spread, transverse size and divergence of the beam.

The statistical description of a particle beam given by the Twiss parameters is particularly useful for describing the beam transport along the accelerator. Instead of tracking every single beam particle, it is enough to determine the evolution of these three parameters to describe the transverse properties of the beam. Considering $\boldsymbol{R}$ to be the first-order transport matrix of a beamline section as defined in Equation (3.23), the final Twiss parameters of the beam in the horizontal plane after this section (subindex f) will be given, in terms of the initial parameters (subindex 0), by [Wie15]

$$\begin{bmatrix}\beta_f\\ \alpha_f\\ \gamma_f\end{bmatrix} = \begin{bmatrix} R_{11}^2 & -2R_{11}R_{12} & R_{12}^2\\ -R_{11}R_{12} & R_{11}R_{22}+R_{12}R_{21} & R_{12}R_{22}\\ R_{21}^2 & -2R_{21}R_{22} & R_{22}^2\end{bmatrix}\begin{bmatrix}\beta_0\\ \alpha_0\\ \gamma_0\end{bmatrix}\,. \tag{3.35}$$

3.2.2. Longitudinal dynamics

The longitudinal phase-space of the beam (coordinates $\boldsymbol{Z} = (s, \delta)$) is characterized by the matrix $\boldsymbol{\Sigma}_{ZZ} = \mathrm{Cov}(\boldsymbol{Z}, \boldsymbol{Z})$ and can therefore also be described by an ellipse, as seen in Figure 3.3. Thus, in analogy to the transverse plane, a longitudinal emittance can also be defined as

$$\epsilon_{\mathrm{L}} = \det\boldsymbol{\Sigma}_{ZZ} = \sqrt{\langle s^2\rangle \langle\delta^2\rangle - \langle s\delta\rangle}\,, \tag{3.36}$$

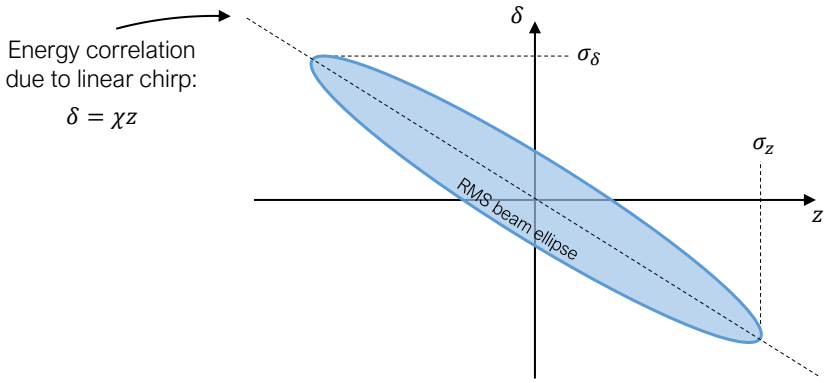

Figure 3.3.: Longitudinal phase-space of a particle beam showing its RMS ellipse. Some key parameters such as the bunch length, energy spread and the correlation due to a linear chirp are included.

and a normalized equivalent, which does not decrease when the beam is accelerated, can also be introduced as

$$\epsilon_{\mathrm{L,n}} = \sqrt{\langle s^2 \rangle \langle \gamma^2 \rangle - \langle s\gamma \rangle}\,, \tag{3.37}$$

where γ is the energy (Lorentz factor) of each particle

The projection of the phase-space ellipse on the δ axis determines the width of the beam in energy, i.e., its relative RMS energy spread $\sigma_\delta = \sqrt{\langle \delta^2 \rangle}$, while the projection along the longitudinal coordinate corresponds to the RMS bunch length $\sigma_z = \sqrt{\langle s^2 \rangle}$. The energy spread of the beam is typically given not only as a relative value but also as an absolute energy spread $\sigma_\gamma = \sqrt{\langle \gamma^2 \rangle}$.

The energy spread of a beam is typically separated into a correlated and an uncorrelated component. The first one refers to the longitudinal energy correlation along the particle beam. The slope (or chirp) of this correlation is given by

$$\chi = \frac{\langle s\delta \rangle}{\langle s^2 \rangle}\,. \tag{3.38}$$

This correlated component typically arises from different energy gain rates along the beam due to a non-uniform longitudinal electric field. In conventional accelerators this occurs due to the sinusoidal shape of the accelerating fields in the RF cavities ($E_z = E_{z,0} \cos\phi$, where ϕ is the acceleration phase), which can imprint a linear correlation in longitudinal phase-space when the beam is not accelerated on crest [Wan08]. This is also the case in plasma accelerators, where E_z can both vary linearly or sinusoidally along z depending on the acceleration regime, as discussed later in Section 3.4. From Equations (3.36) and (3.38) it can be shown that this chirp does not lead to an increase of the longitudinal beam emittance and, thus, it can in principle be reverted at a later stage without affecting the beam quality, as explored later in Chapter 8.

On the other hand, the uncorrelated energy spread increases the size of the beam ellipse in δ without inducing a correlation, therefore leading to longitudinal emittance growth.

Sources of uncorrelated energy spread are multiple, starting already with a finite value at the photocathode in RF accelerators [Orl+04], and increasing, among others, due to space-charge forces, synchrotron radiation [Mic+06], or the betatron motion of particles in plasma accelerators, as introduced later in Chapter 7.

Having a non-zero energy spread also implies that, as mentioned previously in Section 3.1.4, the dispersion terms in the transport matrices will play a role in the beam dynamics. Thus, after a dispersive beamline section, the longitudinal position of a particle in the reference frame of the beam will be given, as obtained from Equation (3.23), by

$$s_f = s_0 + R_{56}\delta + T_{566}\delta^2 + \mathcal{O}(\delta^3) \,, \tag{3.39}$$

where s_0 is the initial position of the particle. This correlation between particle energy and final position implies that the insertion of dispersive media in the beamline can be used for performing longitudinal phase-space manipulations. In particular, this brings the possibility of compressing the electron bunches to achieve a higher peak current, as done, for example, in free-electron lasers (FELs) [Lim+96].

To obtain an expression on the bunch length after a dispersive element, it will be considered that the particle energy within the bunch is given by $\delta = \chi s_0 + \delta_u$, i.e., there is a linear chirp χ plus a random energy deviation δ_u due to a non-zero uncorrelated energy spread. Substituting this into Equation (3.39) yields, to first order:

$$s_f \simeq (1 + \chi R_{56}) s_0 + R_{56}\delta_u \,, \tag{3.40}$$

from which the final bunch length can be obtained by computing its standard deviation [Cha+13]:

$$\sigma_{z,f} \simeq \sqrt{(1 + \chi R_{56})^2 \sigma_{z,0}^2 + R_{56}^2 \sigma_{\delta,u}^2} \,. \tag{3.41}$$

From this expression it can be seen that the minimum bunch length, i.e., full compression, is achieved when $R_{56} = -1/\chi$. Conversely, when $1 + \chi R_{56} > 0$ the bunch is instead said to be under-compressed and when $1 + \chi R_{56} < 0$ the bunch has been over-compressed. All these expressions assume that the particle energy does not change during the dispersive region. This, however, might not be the case, as seen later in Section 3.2.3.

Of special interest for bunch compression, as well as for the new plasma accelerator concepts presented in Chapters 6 and 8, is the use of magnetic chicanes. As illustrated in Figure 3.4, this device consists on an array of 4 dipole magnets in which the particles experience an energy-dependent path length, as given by Equation (3.39). For a small bending angle in the dipoles, the first- and second-order dispersion in a chicane can be simply found to be [Cha+13]

$$R_{56} \simeq 2\theta^2 (L_d + 2L_m/3) \,, \tag{3.42}$$

$$T_{566} \simeq -3/2 R_{56} \,. \tag{3.43}$$

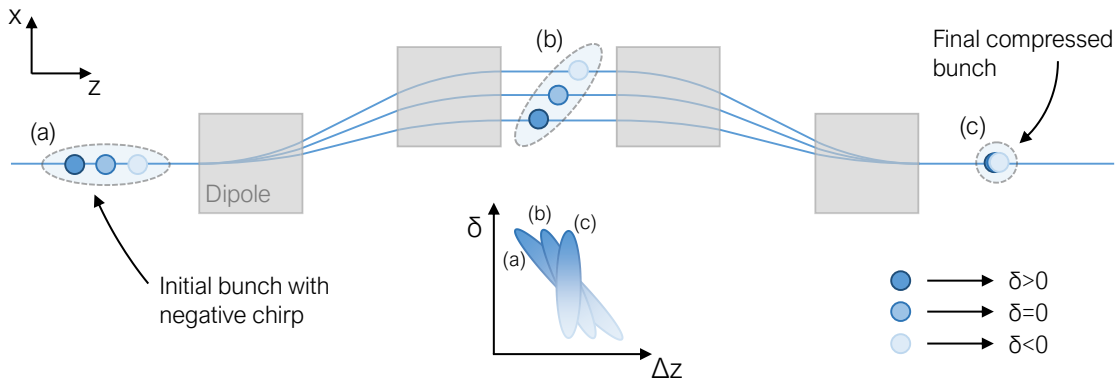

Figure 3.4.: Working principle of a magnetic chicane operating at full compression.

3.2.3. Collective effects

So far the dynamics of particle beams has been treated from a single-particle approach, i.e., only as the statistical averages over the motion of independent particles, without taking into account the interactions between them. The different mechanisms through which particles can interact with each other are typically referred to as collective effects. Two of the most important ones, space-charge and coherent synchrotron radiation (CSR), are reviewed in this section.

Space-charge forces

The space-charge forces refer to those which arise from the electromagnetic fields generated by the charge distribution of the beam itself. These forces act in addition to those externally applied by the individual components of the accelerator and can severely disturb the dynamics of the beam.

The transverse space-charge force of a relativistic beam can be obtained by applying Gauss' law (Equation (3.1)) to the charge distribution. For the case of a cylindrically symmetric Gaussian beam (both in longitudinal and transverse planes) with size σ_r, length σ_z and total charge Q, if cylindrical coordinates (r, ϕ, z) are considered, the radial electric field can be found to be [FMP14]

$$E_r^{\mathrm{sc}}(r,z) = \frac{1}{(2\pi)^{3/2}\epsilon_0}\frac{Q}{\sigma_z}e^{-\frac{z^2}{2\sigma_z^2}}\left[\frac{1-e^{-\frac{r^2}{2\sigma_r^2}}}{r}\right]. \tag{3.44}$$

In addition, for a relativistic particle with charge q moving along z within the space-charge field of the beam, the azimuthal magnetic, B_ϕ^{sc}, experienced by the particle can be obtained as $B_\phi^{\mathrm{sc}} = (\beta/c)E_r^{\mathrm{sc}}$ [FMP14]. Thus, the total space-charge force acting on this particle can be calculated from the Lorentz force (Equation (3.5)) as $F_r^{\mathrm{sc}} = q(E_r^{\mathrm{sc}} - vB_\phi^{\mathrm{sc}})$.

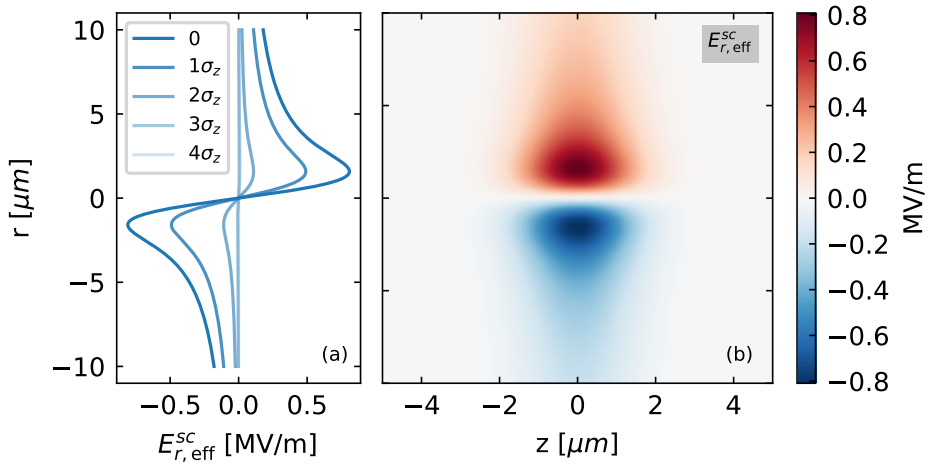

Figure 3.5.: Effective radial electric field due to space-charge for a beam with $\sigma_r = \sigma_z = 1$ µm, $Q = 10$ pC and $\gamma = 200$. A lineout of the field at different longitudinal positions is shown in (a), while the 2D field can be seen in (b).

This leads to the expression

$$F_r^{\mathrm{sc}}(r,z) = q(1-\beta^2)E_r^{\mathrm{sc}} = \frac{q}{(2\pi)^{3/2}\epsilon_0\gamma^2}\frac{Q}{\sigma_z}e^{-\frac{z^2}{2\sigma_z^2}}\left[\frac{1-e^{-\frac{r^2}{2\sigma_r^2}}}{r}\right]. \tag{3.45}$$

From Equation (3.45) it can be seen that the transverse space-charge force vanishes with γ^{-2} and its effect is therefore quickly suppressed as $\gamma \to \infty$. However, it can have a strong impact at lower energies and/or very dense beams. The suppression of the transverse space charge forces at higher energies arises from the compensation of the defocusing and focusing effects of E_r^{sc} and B_ϕ^{sc}, respectively. Thus, an effective electric field is sometimes defined as $E_{\mathrm{r,eff}}^{\mathrm{sc}} = (1-\beta^2)E_r^{\mathrm{sc}} = E_r^{\mathrm{sc}}/\gamma^2$. A particular example of this effective field can be seen in Figure 3.5 for a beam with $\sigma_r = \sigma_z = 1$ µm, $Q = 10$ pC and $\gamma = 200$. It can clearly be seen that this transverse effective field is linear only for $r < \sigma_r$ and can therefore lead to emittance growth.

The space-charge effects can also be significant in the longitudinal plane, where the repulsive forces between beam particles can have an impact on the beam length and energy profile. A simple formula for the longitudinal space-charge forces which contains the most relevant effects can be found for the case of a cylindrical beam with radius r_b propagating coaxially in a perfectly conducting beam pipe with radius r_p. Assuming a uniform transverse charge distribution but allowing for an arbitrary longitudinal profile $\lambda(z)$, with $\int_z \lambda(z)dz = Q$, leads to the expression [FMP14]

$$F_z^{\mathrm{sc}}(r,z) = \frac{q}{4\pi\epsilon_0\gamma^2}\left[1 - \frac{r^2}{r_b^2} + 2\ln\frac{r_p}{r_b}\right]\frac{\partial\lambda(z)}{\partial z}. \tag{3.46}$$

From Equation (3.46) it can be seen that the longitudinal forces are also damped with γ^{-2} and can mostly be neglected for ultra-relativistic beams. Another feature that can

be seen in this equation is that the sign of the force acting on a particle is determined by the sign of $\delta\lambda(z)/\delta z$. Therefore, regions with positive density variation will lead to a positive force, and vice-versa. This is an important effect which can lead to modulations in the longitudinal energy profile when the sign of $\delta\lambda(z)/\delta z$ varies along z and, as a consequence, trigger a (possibly undesired) microbunching of the beam [SSY04].

Coherent Synchrotron Radiation

Synchrotron radiation is the emission of electromagnetic radiation when the trajectory of charged particles is bent. In an accelerator beamline this typically occurs in dipole magnets, where the trajectory of particles is circular with a bending radius ρ. For a bunch with N particles, three main regimes of synchrotron radiation can be distinguished depending on the coherence of the emitted photons. If the distance between individual bunch particles is sufficiently large, each particle radiates independently (or incoherently) and the total radiated power in a dipole is simply N times the power emitted by a single particle

$$P_{\text{in}} = N\frac{e^2c}{6\pi\epsilon_0}\frac{\gamma^4}{\rho^2}\,. \tag{3.47}$$

On the other extreme, when the particle separation is reduced below the wavelength of the emitted radiation, the radiation can become fully coherent and increase the total radiated power by a factor N [DLE05]:

$$P_{\text{fc}} = N^2\frac{e^2c}{6\pi\epsilon_0}\frac{\gamma^4}{\rho^2} = NP_{\text{in}}\,. \tag{3.48}$$

Between these two cases there is an additional regime where the radiation is still coherent, but where the radiated power is proportional to the bunch length instead of the particle energy. This regime of coherent synchrotron radiation (CSR) is the most relevant in linear accelerators, as it is the one in which bunch compressors typically operate [DLE05]. Calculating the radiated power in this case is highly non-trivial and might require expensive 3D simulations [DKL00]. However, a simple expression can be found when the so-called Derbenev criterion [Der+95] is satisfied. That is, when

$$\frac{\sigma_r}{\sigma_z} \ll \left(\frac{\rho}{\sigma_z}\right)^{1/3}\,. \tag{3.49}$$

Under this condition the bunch can be treated as a line charge and the following expression is obtained [DLE05]

$$P_{\text{csr}} \simeq 0.0279\frac{e^2c}{\epsilon_0}\frac{N^2}{\rho^{2/3}\sigma_z^{4/3}}\,. \tag{3.50}$$

The transition between these three regimes can be obtained by comparing Equations (3.47) and (3.48) with Equation (3.50). From this comparison it is found that $P_{\text{csr}}/P_{\text{in}} \sim N(\sigma_z/\sigma_0)^{-4/3}$ and $P_{\text{csr}}/P_{\text{fc}} \sim (\sigma_z/\sigma_0)^{-4/3}$, where the normalization factor $\sigma_0 = \rho/\gamma^3$ has

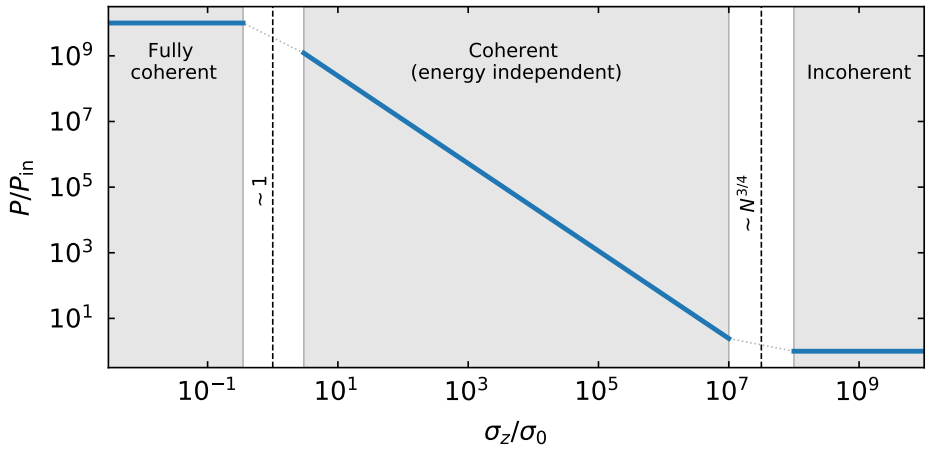

Figure 3.6.: Radiated power in a dipole due to the emission of synchrotron radiation for a bunch with $N = 10^9$ particles. The three different regimes and the transitions between them are shown. Figure inspired from [DLE05].

been introduced. From these expression it can be seen that the transition from incoherent to coherent radiation occurs when $\sigma_z/\sigma_0 \sim N^{3/4}$ and from coherent to fully coherent when $\sigma_z/\sigma_0 \sim 1$. The range of these three regimes and the transitions between them can be seen in Figure 3.6.

One of the main problems of CSR is that the radiated power is not uniform along the bunch [DL97], and that the interaction with the emitted radiation can also result in energy gain or loss at different locations within the bunch. This leads not only to an increased energy spread but also to transverse centroid deviations after a dispersive section which, in turn, can give rise to emittance growth. For a beam with an initial emittance of $\epsilon_{n,x,0}$, the final emittance after a 4-dipole chicane can be estimated in terms of the generated energy spread, $\sigma_{\delta,\mathrm{CSR}}$, as [Zhu17]

$$\epsilon_{n,x,f} \simeq \left(1 + \frac{\beta_x \theta^2 \sigma_{\delta,\mathrm{CSR}}^2}{\epsilon_{n,x,0}}\right)^{1/2} \epsilon_{n,x,0} \,, \tag{3.51}$$

where θ is the bending angle of the dipoles and β_x is the horizontal beta function at the last dipole.

3.3. Fundamental concepts for plasma-based acceleration

In this section, a review of basic concepts about electromagnetic waves and plasmas which are relevant for the physics of plasma-based acceleration is presented. The content is based on multiple references in the literature [FLS11; Jac98; Nic83; Gib16] as well as previous comprehensive summaries of relevant theory for plasma-based acceleration [Ost09; Meh14]. Other used references are also indicated along the text.

3.3.1. Electromagnetic waves

The wavelike nature of electromagnetic radiation, or light, is a property that can be directly deduced from the system of Maxwell's equations (see Equations (3.1) to (3.4)). In the simple case in which no charge or current sources are present ($\rho = 0$, $\boldsymbol{J} = \boldsymbol{0}$), it can be obtained that the fields $\boldsymbol{E}$ and $\boldsymbol{B}$ obey the well know wave equation, $\Box \boldsymbol{E} = 0$ and $\Box \boldsymbol{B} = 0$, where the operator $\Box = \nabla^2 - (1/c^2)\partial^2/\partial t^2$ is introduced. The solution to this equation, apart from the trivial $\boldsymbol{E} = \boldsymbol{0}$ and $\boldsymbol{B} = \boldsymbol{0}$, is then found to be

$$\boldsymbol{E} = \boldsymbol{E}_0 \sin(\omega t - kz) \,, \tag{3.52}$$

$$\boldsymbol{B} = \boldsymbol{B}_0 \sin(\omega t - kz) \,, \tag{3.53}$$

for the particular case of plane monochromatic waves, i.e., waves propagating along a single direction z whose value does not depend on the transverse position (x and y) and which have only a single frequency ω. These expressions are a wave both in space and time, meaning that for a frozen time they can be seen as an oscillation in z while for a fixed position the oscillations occur in time. The rate of change of the phase with these two variables is given by the frequency (time) and the wave number k (space), which are related through the so-called dispersion relation. In vacuum, this relation is found to be

$$\omega = ck \,, \tag{3.54}$$

although more complex expressions appear once vacuum conditions cannot be assumed, as it will be seen later on. The amplitude of these waves is given by $\boldsymbol{E_0}$ and $\boldsymbol{B_0}$, which are vectors perpendicular to the direction of propagation and always verify $\boldsymbol{E_0} \perp \boldsymbol{B_0}$ and $\boldsymbol{E_0} = c\boldsymbol{B_0}$. The components of the amplitude determine the polarization of the wave. In this work only linear polarization will be considered, that is, when the field oscillations are contained in a single line in x and y, as this is generally the case for the laser systems of interest in plasma-based acceleration. However, when a phase difference exists between the oscillations in x and y, the wave amplitude describes instead an ellipse in the transverse plane. The field is then said to have elliptical (or circular, for the case of $\pi/2$ phase difference) polarization.

Although electromagnetic radiation is observed in reality through the fields $\boldsymbol{E}$ and $\boldsymbol{B}$, it is generally useful to describe it instead by means of the scalar and vector potentials Φ and $\boldsymbol{A}$, from which the real fields can be derived according to

$$\boldsymbol{E} = -\nabla\Phi - \frac{\partial \boldsymbol{A}}{\partial t} \,, \tag{3.55}$$

$$\boldsymbol{B} = \nabla \times \boldsymbol{A} \,. \tag{3.56}$$

This new set of variables allows for a more versatile mathematical description of electromagnetic phenomena, as these potentials are not uniquely defined and can thus be

modified to simplify the treatment of certain systems. In terms of these potentials, the solution of the wave equations can be written in a single expression

$$\boldsymbol{A} = \boldsymbol{A}_0 \cos(\omega t - kz) \,, \tag{3.57}$$

from which Equations (3.52) and (3.53) can be derived. From Equations (3.55) and (3.56) it is directly obtained that the amplitudes of these different quantities are related through $E_0 = \omega A_0 = cB_0$ and that $\boldsymbol{E} \parallel \boldsymbol{A} \perp \boldsymbol{B}$.

In contrast to the infinite waves described by Equation (3.57), the laser radiation, which is of central interest in this work, comes typically in well confined wave packets both in space and time. A direct implication of this is that laser pulses can never be fully monochromatic owing to the uncertainty principle, which in terms of spatial length Δz and bandwidth Δk can be expressed as $\Delta z \Delta k \leq 1/2$ [Jac98]. The coexistence of a finite number of frequencies in a light pulse gives rise to the appearance of two distinct velocities within the wave packet: the group and phase velocity. The former corresponds to the propagation velocity of the envelope of the wave packet itself, while the latter represents the rate at which the phase of the wave propagates within the envelope. The value of these two properties is derived from the dispersion relation of the wave as

$$v_g = \frac{dw}{dk} \,, \tag{3.58}$$

$$v_{ph} = \frac{w}{k} \,. \tag{3.59}$$

Thus, although $v_g = v_{ph} = c$ in vacuum (from Equation (3.54)), these two velocities may differ in other media.

Another important feature of electromagnetic waves, without which wakefield generation, for example, would not be possible, is their ability to transport energy. The main parameter to quantify this is the energy flux density given by the Poynting vector

$$\boldsymbol{S} = \epsilon_0 c^2 (\boldsymbol{E} \times \boldsymbol{B}) \,, \tag{3.60}$$

from which the intensity of a light wave can be obtained as

$$I = \langle |\boldsymbol{S}| \rangle = \epsilon_0 c \langle |\boldsymbol{E}|^2 \rangle = \frac{1}{2} \epsilon_0 c E_0^2 = \frac{1}{2} \epsilon_0 c w^2 A_0^2 \,, \tag{3.61}$$

where $\langle\rangle$ represents temporal averaging and linearly polarized fields are assumed.

3.3.2. High-power lasers

The advances in laser-based acceleration over the past decades have been possible thanks to the fast development of laser technology since the invention of the chirped pulse amplification (CPA) technique [SM85]. The advent of CPA has allowed the generation of ultra-short (fs- to ps-scale) laser pulses with TW to PW power and intensities above

10^{18} W/cm^2, properties which are necessary in order to drive plasma waves to accelerate particles.

In laser-plasma acceleration, these high-power pulses can be described in a simplified way as a monochromatic plane wave modulated by an envelope [MA97], and are usually expressed in terms of the normalized vector potential $\boldsymbol{a} = e\boldsymbol{A}/mc$. Thus, a laser pulse linearly polarized in the x direction with radially symmetric Gaussian envelope can be written as

$$\boldsymbol{a}(z,t) = a_0 \frac{w_0}{w(z)} \exp\left(\frac{-r^2}{w(z)^2}\right) \exp\left(-\frac{(z-z_c(t))^2}{2\sigma_z^2}\right) \cos(kz-\omega t)\hat{x}\,, \tag{3.62}$$

where a_0 is known as the peak normalized vector potential, $w(z)$ is the spot size and w_0 is its value at focus. This expression is only an approximation (for example, it does not take into account the wavefront curvature out of focus), but is generally used in the literature [ESL09]. In vacuum, the laser spot size evolves as $w(z) = w_0\sqrt{1+(z/Z_R)^2}$, where Z_R, defined as [Sie86]

$$Z_R = \frac{\pi w_0^2}{\lambda_l}\,, \tag{3.63}$$

is known as the Rayleigh length and corresponds to the distance at which $w = \sqrt{2}w_0$.

One of the most important properties of laser pulses, due to its relevance in plasma-based acceleration, is their ability exert a net force over charged particles. This force, known as ponderomotive force, arises due to the finite spatial extension of laser pulses and can be understood as a kind of radiation pressure which pushes particles away from regions of high intensity. In the limit $a_0 \ll 1$, this force can be expressed as [ESL09]

$$\boldsymbol{F}_p = -\frac{mc^2}{2}\nabla a^2\,, \tag{3.64}$$

and is the driving mechanism that allows laser pulses to generate plasma waves for particle acceleration.

3.3.3. Definition and basic properties of plasmas

A plasma can be generally described as one of the four fundamental states of matter, which arises when positive and negative charges become unbounded, as in an ionized gas. However, not every ionized gas is a plasma *per se*, as certain conditions must be satisfied. A more precise definition is given in [Che84], where a plasma is described as a "quasineutral gas of charged and neutral particles which exhibits collective behavior". The term quasineutral implies that the overall charge of the gas should be approximately neutral, which requires the system to have a large enough spatial extent such that local perturbations of the charge density do not affect the overall neutrality. In addition, it can be said that an ionized gas exhibits collective behavior if the long range Coulomb interactions dominate over particle-particle collisions, as it would be the case in a non-ionized

gas. All these conditions and definitions will become more precise in the following as the basic plasma properties are introduced.

Debye shielding and the plasma parameter

A key property of plasmas is their ability to shield out any electric potential applied to it. This property arises from the high mobility of charged particles in a plasma, which are attracted to (or repelled from) the applied potential and thus create a thick charge layer around it which effective isolates the rest of the plasma from its influence. The characteristic distance over which this shielding takes place is the so-called plasma Debye length, λ_D, defined as

$$\frac{1}{\lambda_D^2} = \frac{1}{\lambda_{D,e}^2} + \frac{1}{\lambda_{D,i}^2} \tag{3.65}$$

where

$$\lambda_{D,e} = \sqrt{\frac{\epsilon_0 k_B T_e}{e^2 n_e}}\,, \quad \lambda_{D,i} = \sqrt{\frac{\epsilon_0 k_B T_i}{q_i^2 n_i}} \tag{3.66}$$

are the Debye lengths of the plasma electrons and ions, respectively. In these equations ϵ_0 is the vacuum permittivity, k_B is Boltzmann's constant, e is the elementary electron charge, q_i is the net charge of the positive ions and T_s and n_s, for $s = e, i$, are the temperature and density of the electron and ion species. The Debye length of the plasma is typically dominated by that of the electrons, owing to their much higher mobility as a result of their reduced mass [Gib16; Ste+17], and thus $\lambda_D \simeq \lambda_{D,e}$ can be typically assumed.

From the Debye length a more precise condition for the quasineutrality of the plasma can be defined. In particular, it is required that the spatial scale of the plasma, L, is much larger than its Debye length, i.e., $L \gg \lambda_D$, so that the dimensions of charge perturbations in the plasma are much smaller than its extension, thus preserving an overall neutrality. In addition, the Debye length allows the definition of another important quantity called the plasma parameter, commonly defined as

$$\Lambda = \frac{4\pi}{3} n_e \lambda_D^3\,, \tag{3.67}$$

which represents the number of plasma particles contained in a Debye sphere (sphere with radius λ_D). A plasma satisfying $\Lambda \gg 1$ can be classified as an ideal plasma, in which the collective Coulomb interactions dominate over binary particle collisions. This simplifies the mathematical treatment of the plasma, as the particle collisions can be neglected. The plasmas of interest for this work, i.e., those used for plasma wakefield acceleration, fall also within the range of temperature and pressure [Gib16] and can therefore be treated as ideal plasmas. The scope of this theoretical introduction will thus be restricted to this case.

Plasma oscillations and response time

Another important parameter of plasmas is how fast they respond to an applied perturbation, such as the passage of a laser pulse or electron beam. This property can be obtained by considering a quasineutral region of the plasma where the electron layer is displaced by a certain distance with respect to the background ions, which are assumed to be fixed due to their higher inertia. The charge displacement results in a local loss of charge neutrality and thus gives rise to a restoring electrostatic force over the displaced electrons, which after the initial perturbation would perform harmonic oscillations with respect to their original position. The frequency of these oscillations is known as the plasma frequency

$$\omega_p = \sqrt{\frac{e^2 n_e}{\epsilon_0 m}}\,, \tag{3.68}$$

which defines the characteristic response time $t_D = \omega_p^{-1}$ of the plasma. Strictly speaking, Equation (3.68) is the frequency of the plasma electrons. However, due to the large mass of the ions, it can generally be assumed that $w_p^2 = \omega_{p,e}^2 + \omega_{p,i}^2 \simeq \omega_{p,e}^2$.

Propagation of electromagnetic waves in plasmas

The plasma frequency is also related to the ability of electromagnetic waves to propagate within the plasma. In particular, if the response time is faster than the period of an externally applied electromagnetic field, the plasma will be able to quickly recover from the perturbation and effectively shied the radiation, which will therefore be reflected. This heuristic explanation can be put more formally by considering the dispersion relation of electromagnetic waves in a plasma

$$\omega^2 = \omega_p^2 + c^2 k^2\,, \tag{3.69}$$

where an additional term ω_p^2 has appeared with respect to Equation (3.54). From this dispersion relation the phase and group velocity of the electromagnetic waves in a plasma (see Equations (3.58) and (3.59)) can be found to be

$$v_{ph} = \left(c^2 + \frac{w_p^2}{k^2}\right)^{1/2}\,, \tag{3.70}$$

$$v_g = \frac{c^2}{v_{ph}} = c\left(1 - \frac{\omega_p^2}{\omega^2}\right)^{1/2}\,, \tag{3.71}$$

which shows that $v_g < c < v_{ph}$. The group velocity of a light pulse becomes therefore slower for higher plasma densities (higher ω_p) until it reaches a point where $k = \sqrt{(\omega^2 - \omega_p^2)/c^2}$ becomes imaginary. When this occurs, Equation (3.57) loses its wave behavior in the plasma, where it is instead exponentially damped [Wie14]. The density at

which this happens, i.e., the density at which $\omega = \omega_p$, is known as the critical density

$$n_c = \frac{w^2 n_e}{4\pi e^2} \,, \tag{3.72}$$

and defines the maximum plasma density in which a light wave of frequency w can penetrate. The characteristic length over which the shielding of low frequency radiation ($\omega \to 0$) takes place is known as the skin depth [Ste+17] and defined as $k_p^{-1} = c/\omega_p$. In plasma-based accelerators, this quantity is generally used as the characteristic spatial scale of the acceleration process within the plasma.

3.3.4. Mathematical modelling of plasmas

The exact mathematical modelling of a plasma requires that the evolution of each of the particles which conform the system has to be known. Thus, all the microscopic interactions at the single-particle level, including collisions and long-range Coulomb interactions, have to be taken into account. Two alternative mathematical models, the Liouville equation and the Klimontovich equation, coupled with Maxwell's equations (Equations (3.1) to (3.4)), allow for this exact description of a plasma at a microscopic level (not including quantum-mechanical effects). However, using these models directly to determine the evolution of a plasma is of little practical use, as the computational power required to determine the motion of the large amount of particles in a typical plasma (order of the Avogadro number) would be far from realistic. Fortunately, in order to obtain an accurate representation of a plasma it is generally not needed to retain the exact microscopic description of the system, and simplified models which can be computationally solved with reasonable resources have been developed.

Kinetic model

One of these models is obtained by considering a statistical description of the plasma, where the microscopic single-particle nature of the system is substituted by statistical averages. From this point of view, the state of the each particle species, s, in the system is characterized by a probability distribution function $f_s(\boldsymbol{r}, \boldsymbol{v}, t)$ defined as

$$dN = N f_s(\boldsymbol{r}, \boldsymbol{v}, t) d\boldsymbol{r} d\boldsymbol{v} \,, \tag{3.73}$$

where dN represents the number of particles that can found in a phase-space volume $d\boldsymbol{r}d\boldsymbol{v}$ around $\boldsymbol{r}$ and $\boldsymbol{v}$ at time t for a species with N particles. In this so-called kinetic description of a particle ensemble, by taking into account that an ideal plasma is dominated by collective behavior over particle collisions, the well-known Vlasov equation which determines the evolution of the distribution function can be obtained:

$$\frac{\partial f_s}{\partial t} + \boldsymbol{v}\frac{\partial f_s}{\partial \boldsymbol{r}} + \frac{q_s}{m_s}(\boldsymbol{E} + \boldsymbol{v} \times \boldsymbol{B})\frac{\partial f_s}{\partial \boldsymbol{v}} = 0 \,, \tag{3.74}$$

where $\boldsymbol{E}$ and $\boldsymbol{B}$ are the electric and magnetic fields acting on the plasma, both due to internal and external sources. This equation can be derived both from the Liouville and Klimontovich models [Nic83] and can be related to Maxwell's equations by recovering the macroscopic quantities

$$\rho(\boldsymbol{r},t) = \sum_s q_s \int f_s(\boldsymbol{r},\boldsymbol{v},t)d\boldsymbol{v}\,, \tag{3.75}$$

$$\boldsymbol{J}(\boldsymbol{r},t) = \sum_s q_s \int \boldsymbol{v} f_s(\boldsymbol{r},\boldsymbol{v},t)d\boldsymbol{v}\,. \tag{3.76}$$

Equations (3.1) to (3.4) and (3.74) therefore form a closed system of equations which can be computationally solved. This set of equations is in fact the basis of many modern codes for plasma simulation based on the Particle-in-Cell (PIC) method [Daw83], particularly for the case of plasma-based acceleration.

Fluid model

Another approach to model a plasma, which can allow for more efficient computations and even analytical solutions in some particular cases, is to treat the plasma macroscopically as a fluid. This fluid approach, which can be derived from Vlasov's kinetic model, neglects the microscopic structure of the plasma and takes into account only the macroscopically observable variables, i.e., the fluid density and velocity, which are then coupled to Maxwell's equations.

A particularly useful approximation which is commonly used in this model is to consider the plasma as a cold electron fluid. In this approximation, the thermal motion of electrons is assumed to be negligible (hence cold fluid model). In addition, the plasma ions, which are much heavier than the plasma electrons, are treated as a static background. Thus, only the evolution of the electron fluid has to be computed. The governing equations of this model are the continuity equation of the electron plasma density, n,

$$\frac{\partial n}{\partial t} + \nabla(n\boldsymbol{v}) = 0\,, \tag{3.77}$$

and the fluid momentum equation ([Esa+93])

$$\frac{1}{c}\frac{\partial}{\partial t}(\boldsymbol{u}-\boldsymbol{a}) = \nabla(\phi-\gamma)\,, \tag{3.78}$$

where $\boldsymbol{u} = \boldsymbol{p}/mc$ is the normalized momentum of the electron fluid, $\boldsymbol{\phi} = e\boldsymbol{\Phi}/mc^2$ and $\boldsymbol{a} = e\boldsymbol{A}/mc$ are the normalized scalar and vector potentials, respectively, and γ is the relativistic Lorentz factor of the fluid. The term $\nabla\gamma$ represents the generalized non-linear ponderomotive force $\boldsymbol{F}_{p,n} = -mc^2\nabla\gamma$ [ESL09], as opposed to Equation (3.64), which was only valid for $a_0 \ll 1$. Equation (3.78) is an exact description of the cold fluid system as long as $\nabla\times(\boldsymbol{u}-\boldsymbol{a}) = 0$, which can be shown to hold for any time t as long as it is initially fulfilled [CS93]. In particular, this is the case for an initially unperturbed plasma

with no laser, such that $\boldsymbol{u} = \boldsymbol{a} = 0$.

The fluid density and velocity obtained from Equations (3.77) and (3.78) are then coupled to Maxwell's equations through $\rho = e(n_0 - n)$ and $\boldsymbol{J} = -en\boldsymbol{v}$, forming a closed system of equations.

3.4. Generation of plasma wakefields

Now that the basic equations governing the plasma evolution have been introduced, the generation of wakefields for particle acceleration will be explored. Both laser and particle beam drivers will be considered, and several acceleration regimes, depending on the driver properties, will be distinguished and separately discussed.

3.4.1. Cold electron fluid model in the quasi-static approximation

To introduce the basic physics of wakefield generation, a simplified cold fluid model will be introduced. This model assumes the transverse size of the driver to be much larger than the plasma wavelength, such that only the longitudinal spatial direction has to be considered [SET90a; ESL09]. The three momentum components of the fluid are however retained.

The description of the plasma evolution with this model will be carried out in the so-call co-moving frame, where the longitudinal component and time are given by

$$\xi = z - v_d t \,, \tag{3.79}$$

$$\tau = t \,, \tag{3.80}$$

with v_d corresponding to the propagation velocity of the driver, e.g., the group velocity, Equation (3.58), in case of a laser pulse. In addition, it will be assumed that the transit time of a plasma electron through the driver is much shorter than the characteristic evolution time of the driver. Thus, the laser or particle beam generating the wakefields can be considered as frozen during the characteristic response time of the plasma, corresponding to $\tau_p = w_p^{-1}$. This is known as the quasi-static approximation (QSA), and is commonly used in the mathematical treatment of plasma wakefields since it can greatly simplify the equations. It implies that

$$\frac{\partial}{\partial t} \simeq -v_d \frac{\partial}{\partial \xi} \,, \tag{3.81}$$

so that the time variation of a certain variable can instead be expressed as a spatial derivative.

Under the QSA, and assuming that $v_d \simeq c$ (speed-of-light frame), the continuity equa-

tion (3.77) in this 1D model can be expressed as [SET90a]

$$(1-\beta_z)n = n_0\,, \tag{3.82}$$

where $\beta_z = v_z/c$ is the normalized longitudinal fluid velocity. In addition, under the QSA, it is obtained from the longitudinal component of Equation (3.78) that $\gamma - u_z - \phi + a_z$ is an invariant which can therefore be set to unity [Esa+93], leading to the equality

$$u_z + \psi - \gamma = -1\,, \tag{3.83}$$

where $\psi = \phi - a_z$ is the so-called wakefield potential.

In this 1D model, if the field of the laser is contained in the transverse plane, i.e., $\boldsymbol{a} = \boldsymbol{a}_\perp$, conservation of transverse canonical momentum implies that $\boldsymbol{u}_\perp = \boldsymbol{a}_\perp = \boldsymbol{a}$ [ESL09]. As a consequence, the relativistic parameter of the electron fluid can be simply expressed as

$$\gamma = \sqrt{1 + u_z^2 + \boldsymbol{a}^2}\,. \tag{3.84}$$

From Gauss's law (3.1) and Equation (3.55) in the QSA, by taking into account Equations (3.82), (3.83) and (3.84), the following differential equation for the wakefield potential in the 1D model is obtained [BKS89; SET90a; ESL09; Meh14]:

$$\frac{1}{k_p^2}\frac{\partial^2\psi}{\partial\xi^2} = \frac{1+\boldsymbol{a}^2}{2(1+\psi)^2} + \frac{n_b}{n_0} - \frac{1}{2}\,, \tag{3.85}$$

where the charge density was considered to be $\rho = -e(n + n_b - n_0)$ in order to take into account the presence of an electron beam (either witness or driver) with density n_b. This equation determines the shape of the wakefield potential in an initially unperturbed plasma under the influence of a laser pulse and/or a particle beam. Solutions can be found numerically and, for some particular cases, even analytically.

Once the wakefield potential has been determined, the fluid variables can be recovered as

$$\frac{n}{n_0} = \frac{1+\boldsymbol{a}^2+(1+\psi)^2}{2(1+\psi)^2}\,, \tag{3.86}$$

$$u_z = \frac{1+\boldsymbol{a}^2-(1+\psi)^2}{2(1+\psi)}\,, \tag{3.87}$$

and the accelerating fields generated within the wakefield can be obtained as

$$\frac{E_z}{E_0} = -\frac{1}{k_p}\frac{\partial\psi}{\partial\xi}\,, \tag{3.88}$$

where $E_0 = (mc/e)w_p$ is a constant generally referred as the cold nonrelativistic wave breaking field [Daw59].

This set of equations gives an accurate description of wakefield generation in the 1D,

broad driver limit in the *linear* ($a^2 \ll 1, n_b/n_0 \ll 1$) and *non-linear* ($a^2 \sim 1, n_b/n_0 \sim 1$) regimes. This model can be extended to 3D [Esa+97b] to take into account the transverse distribution of the laser and electron beams and its influence on the plasma dynamics. However, for high-intensity lasers or very dense beams ($a^2 \gg 1, n_b/n_0 \gg 1$) using a fluid model is no longer strictly valid, as the driver might be strong enough to transversely expel all plasma electrons and generate a fully cavitated wake or *bubble*. This is the so-called *blowout* regime, whose accurate modelling requires a more general description of a plasma, such as Vlasov's kinetic model, although simpler analytical models for this regime have also been developed. A review of these different acceleration regimes is included next.

3.4.2. The linear regime

In the linear regime, which is generated by drivers with $a^2 \ll 1$ or $n_b/n_0 \ll 1$, the wakefield potential verifies $\psi \ll 1$. Thus, the Taylor expansion $(1+\psi)^{-2} \simeq 1 - 2\psi$ can be applied in Equation (3.85), which leads to the simplified expression

$$\left(\frac{\partial^2}{\partial \xi^2} + k_p^2\right)\psi = \frac{k_p^2}{2}\boldsymbol{a}^2 \,, \tag{3.89}$$

where, for simplicity, only the case of a laser driver has been considered ($n_b = 0$) and the term containing $\boldsymbol{a}^2\psi \ll \boldsymbol{a}^2$ has been neglected. This equation is that of a forced harmonic oscillator driven by the ponderomotive force of the laser, and analytical solutions can be obtained [GK87; Meh14] from which the expressions of the density perturbation and longitudinal electric field can be derived as [GK87; ESL09; Meh14]

$$\frac{n - n_0}{n_0} = \frac{1}{k_p}\int_\infty^\xi \sin(k_p(\xi - \xi'))\frac{\partial^2}{\partial \xi'^2}\left(\frac{\boldsymbol{a}^2}{2}\right)d\xi' \,, \tag{3.90}$$

$$\frac{E_z}{E_0} = -\int_\infty^\xi \sin(k_p(\xi - \xi'))\frac{\partial}{\partial \xi'}\left(\frac{\boldsymbol{a}^2}{2}\right)d\xi' \,. \tag{3.91}$$

The one-dimensional model given by Equation (3.89) and its solutions can be easily extended to three spatial dimensions as long as the generated plasma waves are purely longitudinal. This condition is satisfied for sufficiently wide drivers, such that the longitudinal ponderomotive force dominates. In this case, the transverse structure of the driver can be simply included in Equation (3.89), such that, for example, $\boldsymbol{a} = \boldsymbol{a}(\xi, r)$ in case of a cylindrically symmetric laser pulse. This approach therefore allows for the description of longitudinal plasma waves in three dimensions generated by drivers of finite transverse size. In particular, for the case of a linearly polarized and cylindrically symmetric Gaussian laser driver in which only the envelope is considered (fast oscillations are averaged out), i.e., a laser pulse given by

$$a_{\text{env}}^2 = \frac{a_0^2}{2}\exp\left(-\frac{(\xi - \xi_c)^2}{\sigma_z^2}\right)\exp\left(-\frac{r^2}{\sigma_r^2}\right) \,, \tag{3.92}$$

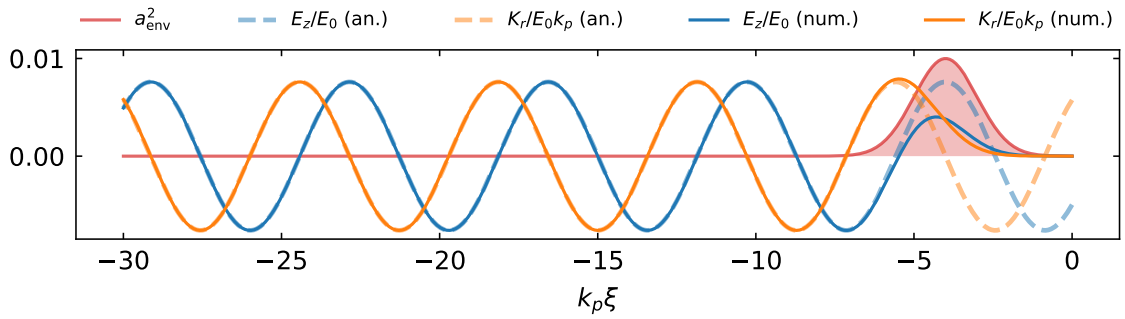

Figure 3.7.: Linear plasma wakefields generated by a linearly-polarized Gaussian laser driver with $a_0 = 0.02$, $k_p\sigma_z = \sqrt{2}$ and $k_p\sigma_r = \sqrt{2}$. The normalized accelerating and focusing fields on-axis are shown as obtained from the analytical expressions Equations (3.93) and (3.96) and from numerically solving Equation (3.89).

where ξ_c is its central position, the longitudinal field given by Equation (3.91) can be expressed, for positions sufficiently behind the driver, as [GK87; Spr+88]

$$\frac{E_z}{E_0} = \frac{\sqrt{\pi}}{4} a_0^2 k_p \sigma_z \exp\left(-\frac{(k_p\sigma_z)^2}{4}\right) \cos(k_p(\xi - \xi_c)) \exp\left(-\frac{r^2}{\sigma_r^2}\right) . \tag{3.93}$$

From this expression, the transverse wakefields, $W_r = E_r - cB_\phi$, and focusing gradient, $K_r = \partial W_r/\partial r$, that a relativistic particle with $v_z \simeq c$ travelling behind the driver would experience can be obtained from the Panofsky-Wenzel theorem [PW56; ESL09]

$$\frac{\partial E_z}{\partial r} = \frac{\partial W_r}{\partial \xi} , \tag{3.94}$$

from which it is found that

$$\frac{W_r}{E_0} = -\frac{\sqrt{\pi}}{2} a_0^2 k_p \sigma_z \exp\left(-\frac{(k_p\sigma_z)^2}{4}\right) \sin(k_p(\xi - \xi_c)) \frac{k_p r}{(k_p\sigma_r)^2} \exp\left(-\frac{r^2}{\sigma_r^2}\right) , \tag{3.95}$$

$$\frac{K_r}{E_0 k_p} = -\frac{\sqrt{\pi}}{2} a_0^2 k_p \sigma_z \exp\left(-\frac{(k_p\sigma_z)^2}{4}\right) \sin(k_p(\xi - \xi_c)) \frac{1}{(k_p\sigma_r)^2} \left(1 - \frac{2r^2}{\sigma_r^2}\right) \exp\left(-\frac{r^2}{\sigma_r^2}\right) . \tag{3.96}$$

Equations (3.93) to (3.96) show that, behind the driver, the plasma wakefields in the linear regime are sinusoidal with a wavelength corresponding to that of the plasma, and that the accelerating and focusing components have a $\pi/2$ phase shift, as seen in Figure 3.7. This is a characteristic feature of linear plasma waves, which implies that only half of the accelerating region is also focusing and thus well suited for particle acceleration. From Equation (3.93) it can also be obtained that, for a fixed a_0, the wakefield generation is most efficient, i.e., the amplitude of the accelerating fields is maximum, when $k_p\sigma_z = \sqrt{2}$.

3.4.3. The non-linear regime

For more intense drivers which reach the threshold of $a^2 \sim 1$ or $n_b/n_0 \sim 1$, the wakefield potential becomes also $\Psi \sim 1$ and thus the linear approximation is no longer valid. Instead, the full expression in Equation (3.85) must be considered. In addition, for intense drivers of finite size ($\sigma_r \lesssim k_p^{-1}$), the 1D model cannot be as easily extended to three dimensions as in the linear regime, since the transverse ponderomotive force becomes significant and the plasma waves are no longer purely longitudinal. Therefore, an accurate description of non-linear wakes typically requires the use of a 3D fluid model.

The transition from linear to non-linear wakefields is illustrated in Figure 3.8, where three different cases corresponding to a Gaussian laser driver with $k_p\sigma_z = \sqrt{2}$ and different a_0 are shown. In order for the 1D model to be strictly valid, the transverse size of the laser pulse is here assumed to be $\sigma_r \gg k_p^{-1}$. From the displayed cases, it can be seen that, as a_0^2 is increased, the purely sinusoidal shape that fields exhibited in the linear regime is progressively lost. Instead, the wakefield potential transitions into a periodic function with parabolic shape which in turn gives rise to strong density spikes and a sawtooth-shaped longitudinal fields. For $a_0^2 \lesssim 1$, the situation still does not strongly differ from the linear case and is thus generally referred as *quasi-linear* or weakly non-linear regime. However, as a_0^2 is further increased, sharp density spikes appear and the fields are no longer sinusoidal. In this extreme case, complete cavitation of plasma electrons and trajectory crossing behind the driver can occur once its transverse size can no longer be regarded as infinite. In this strongly non-linear case, generally known as the blowout regime, the fluid description of the plasma no longer applies and a different model is required, as reviewed in more detail in the following section.

Another distinct property of non-linear wakes is the progressive elongation of the wavelength as the driver intensity is increased [BKS89; BM90; SET90b; ESL09]. This can be explained as a consequence of the increased mass of the plasma electrons, which for high-intensity drivers can become relativistic and thus decrease their oscillation frequency according to Equation (3.68).

Furthermore, in addition to the different shape and elongation of the non-linear wakefields, the usable accelerating region is also increased with respect to the linear case. This useful property is a consequence of the focusing part of the wake, which covers only half of the accelerating phase in the linear regime but progressively lengthens as the fields become non-linear. An example of this is shown in Figure 3.9 for two particular cases with different a_0. It can be seen how in the non-linear case ($a_0^2 = 10$) the focusing region of the wake covers a significantly larger fraction of the accelerating part, and can even fully cover it for large enough a_0, as seen in Figure 3.9c. The results shown in this figure were obtained from numerical solutions of Equation (3.85) extended to three dimensions as performed in the linear case. Although, as explained before, this model is not strictly valid for intense narrow drivers, it still manages to reflect the increase of usable accelerating phase.

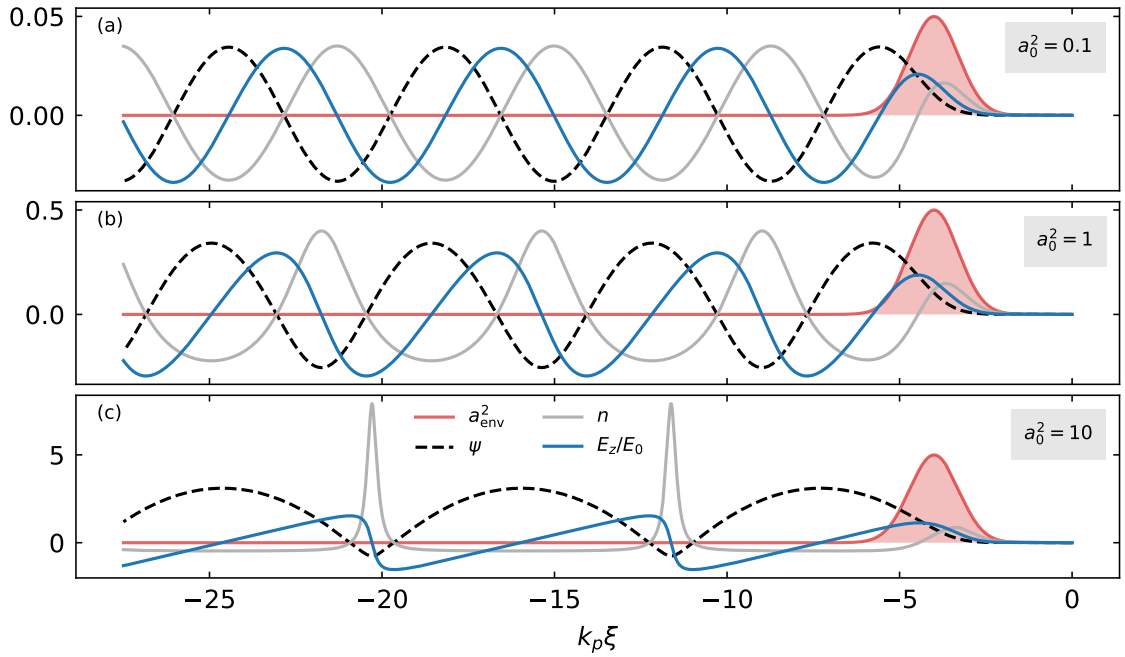

Figure 3.8.: Normalized wakefield potential, density variations and longitudinal fields generated by a linearly-polarized Gaussian laser driver with $k_p\sigma_z = \sqrt{2}$ and $a_0^2 = 0.1$ (a), $a_0^2 = 1$ (b), $a_0^2 = 10$ (c). Results obtained from numerical solutions of Equation (3.85). The transition from linear to non-linear wakefields, which feature an elongated wavelength and non-sinusoidal shape, can be clearly seen.

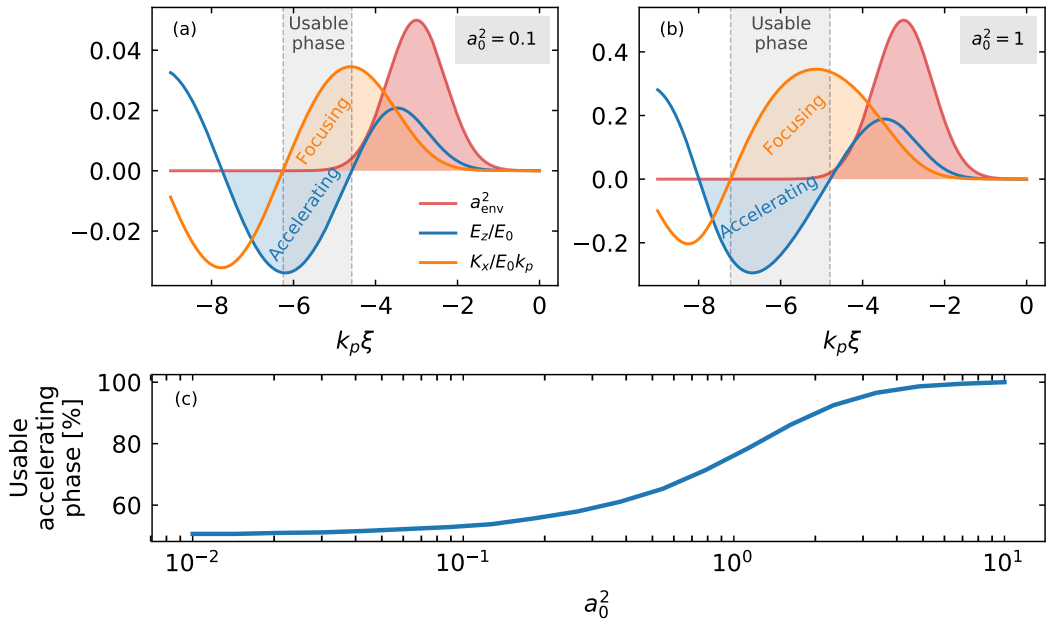

Figure 3.9.: Increase of the usable phase for particle acceleration when transitioning from the linear (a) to the non-linear regime (b). For higher a_0, the focusing region of the wake lengthens and can even cover the whole accelerating part, thus increasing its usable phase a s seen in (c). This results were obtained by numerically solving Equation (3.85) extended to 3D (thus only taking into account longitudinal plasma waves) for a laser driver with $k_p\sigma_z = k_p\sigma_r = \sqrt{2}$.

3.4.4. The blowout regime

As previously mentioned, for ultra-intense drivers ($a_0^2 \gg 1$ or $n_b/n_0 \gg 1$) which are tightly focused, the transverse push given to the plasma electrons becomes relevant and can lead to complete electron cavitation of the wake. Inside the cavitated region, neglecting the driver, only a constant background of plasma ions exists. This gives rise to a uniform focusing gradient $K_r = (m/2e)\omega_p^2$ within the wake whose strength depends only on the plasma density. Outside of this cavity, the plasma electrons expelled by the driver form a thin and dense sheath, as seen in Figure 3.10. This particular characteristic of the blowout regime [Ros+91; Lot04], i.e, a uniform and positively charged ion cavity surrounded by a thin electron sheath, has allowed the development of simplified analytical models from which the shape of the wakefield potential (and, thus, of the accelerating and focusing fields) within the blowout can be predicted.

One commonly used model [Lu+06b; Lu+06a], developed assuming quasi-static conditions, obtains that, for the simplified case of an electron sheath of width Δ_s starting at a radial position r_s and with uniform density $n_s = r_s^2/((r_s+\Delta_s)^2 - r_s^2)$ for $r_s \leq r \leq r_s + L$, the wakefield potential can be expressed as

$$\psi(r,\xi) = \frac{r_s^2(\xi)}{4}(1+\beta) - \frac{r^2}{4}\,, \tag{3.97}$$

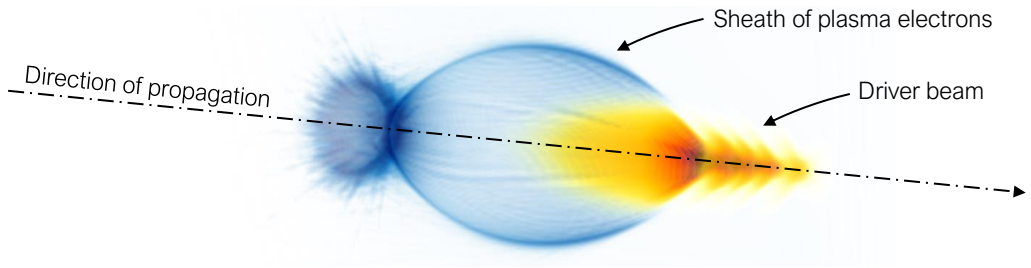

Figure 3.10.: Illustrative case of an electron driver generating a blowout. The formation of a thin sheath of expelled plasma electrons is clearly visible. This example was obtained from an OSIRIS simulation and the 3D render was generated with VisualPIC (see Chapter 5).

for $r \leq r_s$, where $\beta = \frac{(1+\alpha)^2 \ln(1+\alpha)^2}{(1+\alpha)^2-1} - 1$ and $\alpha = \Delta_s / r_s$. At the same time, the ξ-dependent radial position of the sheath is determined by numerically solving an inhomogeneous second-order differential equation. However, for sufficiently short and intense drivers such that the maximum radial extension of the sheath, r_m, reaches $r_m \gtrsim 4$, the following simplified equation can be found:

$$r_s \frac{d^2 r_s}{d\xi^2} + 2\left(\frac{dr_s}{d\xi}\right)^2 + 1 = -\frac{1}{4+\beta r_s^2}\frac{d|a|^2}{dr} \tag{3.98}$$

which is valid for a laser driver. All the radial variables in these expressions, i.e., r, r_s and r_m, are non-dimensional and normalized to k_p^{-1}.

Achieving this so-called ultra-relativistic scenario requires an $a_0 \gtrsim 4$. In this case, the longitudinal electric field, which is obtained by applying Equation (3.88), is found to be [Lu+06a]

$$\frac{E_z}{E_0} = \frac{k_p \xi}{2} \tag{3.99}$$

around the central position (longitudinally) of the blowout, which agrees with the predictions of earlier models [KPK04]. Further models for this regime have also been developed to take into account the effect of a witness beam on the fields, i.e., the beam-loading effect (see Section 3.4.6) [Tzo+08], to obtain the fields outside of the cavitated region [Yi+13] or to describe the case of radially inhomogeneous plasmas [Tho+16].

The blowout regime thus offers, in contrast to the linear and quasi-linear regimes, focusing and accelerating fields which are transversely (and even longitudinally in the case of K_r) uniform. This property makes the blowout regime specially attractive for particle acceleration, as it contributes towards preventing emittance and energy spread growth. This point will be discussed in more detail in Section 3.6.

3.4.5. Wave-breaking

As seen from the 1D non-linear fluid theory and in Figure 3.8, for higher driver intensities, the plasma waves become more peaked and the amplitude of the generated fields

increases. However, a finite limit exists for the maximum field amplitude that can be sustained by a plasma wave. In the linear regime approximation, the maximum field amplitude is found to be [Daw59]

$$E_0 = \frac{mc}{e}\omega_p \,, \tag{3.100}$$

which is commonly referred to as the cold nonrelativistic wave-breaking limit. For nonlinear waves, however, this value can be greatly surpassed and a higher limit can be found in the 1D limit as [AP56; EP95]

$$E_0^{\text{rel}} = \sqrt{2}(\gamma_p - 1)^{1/2} E_0 \,, \tag{3.101}$$

which is known as the cold relativistic wave-breaking limit. In this expression, γ_p is the relativistic factor corresponding to the phase velocity of the plasma wave, which for a laser driver in the 1D low-intensity limit can be simplified to $\gamma_p \simeq \omega/\omega_p$ [ESL09]. This limit arises as the longitudinal velocity of the plasma electrons becomes larger than the phase velocity of the plasma wave. When this happens, the plasma density peaks, where the electrons feature the highest longitudinal momentum, become faster than the wave, leading to its breakdown. In this situation, the electrons that have "fallen" forward into the wake can become trapped and accelerated, as seen later in section 3.5.3.

3.4.6. Beam loading

As seen in Equation (3.85), laser pulses and electron beams are both equally capable of generating a plasma wave. As such, electron beams trapped and accelerated in the wake of the driver can be equally capable of generating their own wake. The direct consequence of this is that the structure of the wakefield generated by the driver will be altered by the presence of the witness, as the dynamics of the plasma wave will now be driven by the action of both beams. If the witness beam is located in the accelerating region of the wakefield, its wake will be out of phase with that of the driver, which will lead to a reduction of the accelerating field at the location (and downstream) of the witness. This effect is known as beam loading, and has important consequences for the quality and properties of the accelerated beam, as well as for the efficiency of the acceleration process itself.

Several analytical models have been developed to take into account the effect of beam loading. In the linear regime, it was initially proposed that the beam loading field could be optimized to achieve a constant accelerating field along the beam (and thus not generate time-correlated energy spread) by shaping its longitudinal profile as a triangular distribution (higher charge on the front) [Mee85]. These studies were later extended to include also limits on the maximum number of electrons that can be accelerated in a linear plasma wave [Kat+87]. In the blowout regime, where a different theoretical approach is needed, more recent models beam loading effect have been developed which

also establish conditions on the maximum charge that can be accelerated and the required bunch shape to achieve a uniform accelerating field [Lot05; GP05; Lu+07; Tzo+08; Tzo+09]. In this regime, the optimal bunch profile for minimum energy spread is found to be trapezoidal.

3.5. Laser-driven wakefield acceleration

3.5.1. General acceleration limits

Several physical processes, arising from the nature of laser pulses and their interaction with plasmas, can limit the maximum accelerating distance in an LWFA. As such, these mechanisms, which are generally referred to as laser diffraction, electron dephasing and pump depletion [ESL09], limit the achievable energy gain.

Laser diffraction

The spot size of a Gaussian laser pulse in vacuum evolves as $w(z) = w_0\sqrt{1+(z/Z_R)^2}$, where z is the distance to the focal position in which $w = w_0$ and Z_R is the Rayleigh length defined in Equation (3.63). Due to the increase in spot size (diffraction), the peak amplitude of the laser decreases as $a_0 \propto (1+(z/Z_R)^2)^{-1/2}$. Thus, in an LWFA, if the laser pulse diffraction is not controlled, the reduced a_0 will limit the effective acceleration length to a few Z_R. As seen later in subsection 3.5.2, different mechanisms for laser guiding within the plasma can be used to overcome the limitations of diffraction.

Electron dephasing

In an LWFA, the group velocity of the laser pulse, v_g, (and thus the phase velocity of the plasma wake, v_p) is, as given by Equation (3.71), below the speed of light. However, a relativistic electron bunch in the accelerating region of the wake will asymptotically increase its velocity $v_b \to c$. Thus, if v_p is constant along the LWFA, the electron bunch will eventually outrun the wake and reach the decelerating region. This effectively limits the maximum achievable energy gain, and the distance needed for it to happen is generally known as the dephasing length, L_d. A simple estimate of this parameter can be obtained in the 1D limit for the case of linearly polarized square laser pulse as [ESL09]

$$L_d \simeq \frac{\lambda_p^3}{2\lambda_l^2} k_d \,, \tag{3.102}$$

for $\lambda_p/\lambda_l \gg 1$ and where $k_d = 1$ if $a_0^2 \ll 1$ or $k_d = \sqrt{2}a_0/\pi$ if $a_0^2 \gg 1$ (valid only for first plasma period behind the laser). Other analytical approximations of the dephasing length have also been found [Lu+07]. In order to overcome this limitation, certain solutions have been proposed to "phase-lock" the witness beam such that it does not run into the decelerating area. These include tapering the longitudinal plasma profile with a

slowly increasing density [Kat86; Spr+01], or externally applying a transverse magnetic field (the so-called *surfatron* concept) [KD83]. In addition, other techniques to increase the group velocity of the driver have also been proposed, such as the use of a so-called flying focus [Fro+19; Pal+20] or the overlap of two lasers [Deb+19].

Laser pump depletion

Another limitation on the maximum accelerating distance in an LWFA comes from the energy transfer of the laser pulse to the plasma as it drives a wake. As it loses energy, its pump depletes and the wakefield amplitude decreases. An estimate of the pump depletion length can again be obtained in the 1D case for a linearly polarized square pulse as [SSE09]

$$L_{pd} \simeq \frac{\lambda_p^3}{\lambda_l^2} k_{pd} \,, \tag{3.103}$$

where $k_{pd} = 2/a_0^2$ for $a_0^2 \ll 1$ and $k_{pd} = \sqrt{2}a_0/\pi$ for $a_0^2 \gg 1$. Other analytical expressions for the pump depletion also exist [Lu+07].

The relevance of these 3 different mechanisms depends on the acceleration regime. For example, in the linear regime, where $a_0^2 \ll 1$, it is generally the case that $Z_R \ll L_d \ll L_{pd}$ if laser guiding is performed, otherwise, the acceleration length will be limited by dephasing. On the contrary, in strongly non-linear wakes, $a_0^2 \gg 1$, pump depletion will typically occur before reaching dephasing [ESL09].

3.5.2. Laser guiding

As discussed in the previous section, laser diffraction is one of the main factors limiting the energy gain in an LWFA. In order to overcome this issue, several mechanisms can be exploited to generate a non-uniform index of refraction in the plasma such that the laser pulse can be guided over several Z_R. To achieve this, the radial profile of the index of refraction should be such that it exhibits a maximum on axis [Esa+96]. Although the index of refraction in a plasma is in principle uniform for an electromagnetic wave of frequency ω, $\eta_r = (1 - \omega_p^2/\omega^2)^{1/2}$, for large amplitude waves, relativistic motion of plasma electrons and density variations δn due to the ponderomotive force of the laser can lead to a non uniform η_r. In addition, a preformed density channel Δn_p can also be applied. For the case of $a_0^2 \ll 1$, $|\Delta n_p/n_0| \ll 1$ and $|\delta n/n_0| \ll 1$, the following expression for the index of refraction can be found:

$$\eta_r \simeq 1 - \frac{\omega_{p0}^2}{\omega^2}\left(1 + \frac{\Delta n_p}{n_0} + \frac{\delta n}{n_0} - \frac{a^2}{2}\right) \,, \tag{3.104}$$

where the last three terms account, respectively, for a preformed density channel, density variations due to the ponderomotive force of the laser, and relativistic effects.

From Equation (3.104) different strategies for performing laser guiding can be iden-

tified. On one side, the relativistic motion of plasma electrons induced by the laser increases the index of refraction towards the axis, where the laser intensity is higher. This can lead to what is known as relativistic self-focusing if the laser power reaches a critical value determined by the plasma density [STE87]. On the other side, the transverse ponderomotive force of the laser can expel electrons from the axis and generate a density channel. This enhances the effects of relativistic self-focusing and is generally known as ponderomotive self-channeling [Sun+87]. These two mechanisms, however, are not well suited for guiding short ($L \sim \lambda_p$) laser pulses [SET90a; Spr+92], such as those needed to resonantly driver a wake. Thus, the guiding technique that has been considered throughout the work presented later in this thesis is that of generating a preformed plasma channel before the arrival of the laser driver. Neglecting the two last terms in Equation (3.104), it can be found that the ideal radial profile for guiding a Gaussian laser pulse is given by

$$\frac{n}{n_0} = 1 + \frac{\Delta n_c \, r^2}{w_0^2} \,, \tag{3.105}$$

where $\Delta n_c = (\pi r_e w_0^2)^{-1}$ is the critical channel depth [Spr+92; SE92] and $r_e = e^2/mc^2$ is the classical electron radius. Different experimental techniques are available for generating this kind of channels. These include capillary discharges [Zig+96] or by hydrodynamic expansion of the plasma due to the action of a laser pre-pulse [DM93], a technique which has recently been used for plasma densities as low as $n_p \sim 10^{17}\,\mathrm{cm}^{-3}$ [Sha+18; Sha+19]. These two options can also be combined in order to guide PW-range laser beams without damage to the capillaries [Gon+19].

A preformed density channel is therefore an effective technique for laser guiding, and is well suited for short pulses in the linear and weakly non-linear regimes. In the blowout regime, however, relativistic and ponderomotive guiding become a feasible option thanks to the high laser intensity. Although no formal derivation is currently available, a phenomenological model has been developed [Lu+07] which establishes the following condition for a stable laser propagation in the blowout regime:

$$k_p w_0 \simeq 2\sqrt{a_0} \,. \tag{3.106}$$

3.5.3. Overview of injection techniques

Several methods for injecting electrons into the plasma wake have been developed over the years. The simplest one to realize experimentally, and which was the most common technique in the early laser acceleration experiments, is to take advantage of wave-breaking (see subsection 3.4.5) [Mod+95; Bul+97]. Several important milestones in the development of LWFA were achieved with this method, including the first demonstrations of beams with narrow energy bandwidth (percent-range) [Man+04; Ged+04; Fau+04], the first GeV-range beams [Lee+06] and the current electron beam energy record at around 8 GeV [Gon+19]. However, even though wave-breaking proved to be an effective method

for electron trapping, the insufficient quality and low shot-to-shot stability of the produced beams limited the usability of this technique. The underlying reason for this is the lack of control of the wave-breaking process, as it strongly depends on the profile and parameters of the laser driver, and these present strong shot-to-shot variations in current high-power systems.

In order to achieve a higher control of this process, different techniques considering the use of tailored density profiles have been proposed. These density variations affect the phase velocity of the plasma wave and can therefore be used to trigger wave-breaking in a controlled manner. The different techniques include the use of plasma downramps (a downward transition of plasma density) [Bul+98], which where shown to produce beams with low absolute energy spread [Ged+08], the use of sharp, localized density bumps [Buc+13; Too+17], and even triggering injection with plasma upramps [Li+13]. Apart from density transitions, it has also been shown that electron trapping can occur from the evolution of the plasma wake in the blowout regime [Kal+09] or by applying an external magnetic field [Vie+11].

In addition to this trapping concepts, other ideas for controlled electron injection have also been proposed which take advantage of the ionizing and ponderomotive properties of lasers. Some of these techniques consider the use of additional laser pulses to, by means of their ponderomotive force, push electrons into the wake generated by the main laser pulse. This injection can be triggered by a single pulse orthogonal to the driver [UKD96], or from the collision of two counter-propagating pulses [Esa+97a; Sch+99]. The production of electron bunches with improved reproducibility has been demonstrated with this so-called colliding pulse technique [Fau+06; Kot+08]. Apart from the ponderomotive force, the ionizing capabilities of lasers can also be used to release electrons into the wakefield. This was first proposed in already in [UKD96], where the use of a gas medium with multiple ionization levels is discussed, such that the plasma background is composed of electrons from outer shells, while inner shell electrons can be locally ionized and trapped only in regions where the driver has higher intensity. Combinations of this ionization method with the ponderomotive force of the laser where also initially investigated [Moo+99]. Since then, multiple ionization techniques have appeared [Che+06; Row+08; Pak+10; Liu+11; Pol+11; Zen+14; Yu+14] and are nowadays commonly used in experiments.

However, despite the plethora of injection techniques listed above, the beam quality of plasma-based accelerators is still far behind of what conventional radiofrequency technology can offer. In particular, meeting the requirements on stability and energy spread for applications such as FELs is one of the current major challenges in the field. A possible alternative to the ideas presented before, which could open a new path towards improved beam quality, is to inject into the wakefield an externally prepared beam which has been previously accelerated and optimized in a conventional RF linac. This concept, known as external injection, would allow for a higher degree of control over the accelerated beam,

whose properties could be tailored to the plasma accelerating stage to, for example, optimize beamloading and would benefit from the improved stability of RF technology. The external injection of an RF beam is, however, not a new proposal. This technique was already experimentally tested in the early days of plasma acceleration [Cla+93; Eve+94; Ami+98] to prove the accelerating capabilities of laser-driven plasma waves by boosting the energy of a fraction of the injected electrons. More advanced concepts have since then been proposed [Irm+07], but where complete trapping of the external beam could not yet be achieved. These difficulties arise from the tight requirements that the plasma-accelerating stages impose on the injected beams, i.e., a beta function on the order of $\beta \sim 1$ mm and a length on the femtosecond scale, which are challenging to achieve with conventional accelerators. However, near 100% capture efficiency has been recently demonstrated [HWL19], and multiple projects worldwide are now focusing on this technique with state-of-the-art RF linacs. These include the SPARC_LAB facilty at INFN, Italy, [Ros+14; Ros+18], the DESY projects REGAE [Zei] and SINBAD-ARES [Zhu+16; Wei+17; Mar+18], and the large european EuPRAXIA collaboration [Wal+17].

3.6. Beam dynamics in plasma-based accelerators

In this section, a brief overview of the particular characteristics of the beam dynamics in plasma-based accelerators is presented, in particular with regards to the energy spread and emittance.

3.6.1. Sources of energy spread

Outstanding progress in PBAs over the past decades has led to significant improvements in beam quality. Recent experimental work has achieved beams with micron to sub-micron emittance [Bar+17; Bru+10; Cur+17; Gol+16; Fri+04; Kne+12; Pla+12; Sea+10; Wei+12], peak current over tens of kiloamperes [Lun+11; Cou+17] and bunch duration as short as a few femtoseconds [Cou+17; Rec+10; Buc+11; Lun+11]. Still, the achievement of an energy spread below the percent level, as required by applications such as FELs, has remained an issue.

Prior to 2004, where three different groups demonstrated almost simultaneously the production of quasimonoenergetic (per-cent range energy spread) beams with $\sim$100 MeV energies [Man+04; Ged+04; Fau+04], electrons accelerated in PBAs exhibited broad and continuous energy spectra [Kit+92; Ums+96; Moo+97; Mal+01; Mal+02]. Since then, the rapid advances in laser technology as well as the development of new techniques for controlled injection, as described above, have led to the successful realization of multi-GeV beams with energy spreads as low as $\sim$ 1%. This progress can be observed in Figure 1.1, where an overview of the energy and energy spread performance og LWFA experiments over the past decades is shown compared with state-of-the-art FEL facilities and future proposed colliders.

The main source of this high energy spread in PBAs is typically the steep slope of the accelerating fields within the focusing region of the wake, which arises due to the short period and high amplitude of the fields, as seen in Section 3.4. This slope induces a longitudinal energy correlation or chirp, as defined in Equation (3.38), along the bunch which dominates its total energy spread. Other sources of energy spread include the transverse dependence of the accelerating fields in the linear and weakly non-linear regimes [LNM18], the emission of so-called betatron radiation [Wan+02; Esa+02] or continuous electron trapping in internal injection schemes [Zen+14]. In addition, within this work, another source of energy spread which had been previously unaccounted for is introduced in Chapter 7. This energy spread source arises from the longitudinal slippage of particles due to betatron motion, and can have a significant impact on the beam quality.

Due to its importance for applications such as FELs, and to avoid other issues such as emittance growth, as explained below, several concepts have been proposed to minimize the energy spread in PBAs. Most of them focus on mitigating the correlated energy spread, as it is typically the dominating contribution. These include the use of beam loading, as described in subsection 3.4.6, the injection of a secondary bunch to "overload" the wake [Man+17], the use of modulated [Bri+17] or tailored [Döp+18] plasma density profiles, or to take advantage of the beam-induced wakefields [BS12; Ant+14; DAr+19; Shp+19; Wu+19a; Wu+19b]. Other concepts deal with beams with a large uncorrelated energy spread, which is then stretched in a chicane to minimize the slice energy spread for FEL applications [Mai+12; Lou+15; And+18]. While some of this concepts have been experimentally proven, the energy spread of PBA-produced beams remains on the few-percent range. In Chapter 8, a new concept for correlated energy spread compensation is proposed which could lower this figure down to the sub-per-mille level.

3.6.2. Beam matching and emittance growth

Apart from being detrimental to the beam quality in itself, the large energy spread that typically develops in PBAs can also be a source of emittance growth. This is a well-known problem which can occur both during acceleration [AY98; Meh+12] as well as during beam transport downstream of the plasma stage [Flo03; Mig+13].

The basic beam dynamics leading to this emittance growth can be understood by considering the beam envelope equation in the simplified case of no acceleration and a uniform focusing field with gradient K [Fer16]:

$$\sigma_x'' + \left(k_\beta^2 - \frac{1}{\beta^2}\right)\sigma_x = 0\,, \tag{3.107}$$

where σ_x is the beam size, $k_\beta = \sqrt{(e/mc^2)K/\gamma}$ is the betatron wave number, $\beta = \sigma_x^2\gamma/\epsilon_n$ is the beam beta function, ϵ_n is the normalized emittance as defined in Equation (3.32) and γ is the relativistic factor of the beam. In general, the solution of this equation is an oscillatory behavior of the beam envelope where the beam ellipse rotates in phase

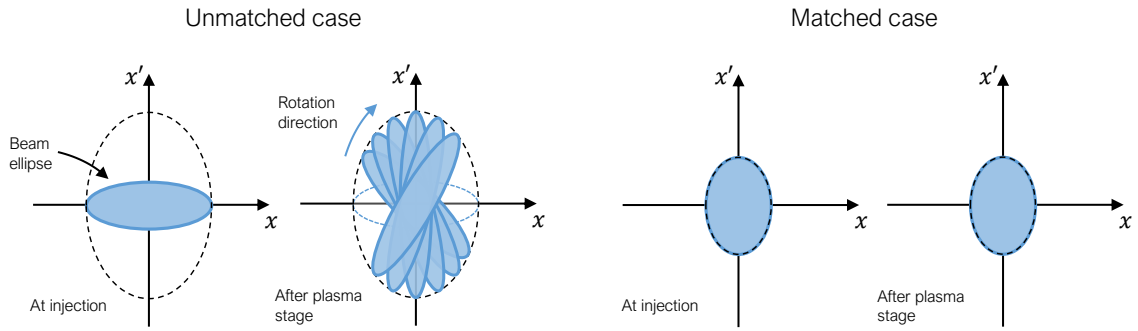

Figure 3.11.: Comparison of the phase-space evolution inside a plasma stage of an unmatched and matched externally injected beam with a large correlated energy spread. The different rotation rates of each slice in the unmatched case lead to projected emittance growth. This simplified view on the phase-space evolution neglects effects from the energy gain in the plasma stage.

space. Since the rotation frequency (known as betatron frequency) $\omega_\beta = k_\beta/c \propto \gamma^{-1/2}$ of each particle is energy-dependent, this can lead, in beams with large energy spread, to different single-particle ellipses rotating at different rates. This, as illustrated in Figure 3.11 for the case of a beam with a large correlated energy spread, can lead to a large growth of the projected beam emittance.

However, by looking at Equation (3.107), it can be seen that the beam envelope oscillations can be suppressed if $\beta = k_\beta^{-1}$, which, for a constant K, requires also $\alpha = -\beta'/2 = 0$. When these conditions are fulfilled the beam is said to be *matched* to the focusing fields in the plasma and the emittance growth is effectively suppressed, even when the energy spread is large. Although these requirements have been obtained for the particular case of constant K and γ, adiabatic changes to these variables, i.e., changes in time scales much larger than ω_β^{-1}, will not alter the matching conditions and thus not lead to emittance growth [Meh+12].

In addition to mitigating emittance growth during acceleration by properly matching the beam, it is equally important to prevent the beam emittance from increasing after exiting the plasma stage. As seen in Equation (3.34), this is bound to happen for beams with a large energy spread which are also strongly divergent, as it is often the case in PBAs due to the strong focusing fields. The emittance growth in a drift ($K = 0$) after the plasma stage can be obtained from Equations (3.34) and (3.107) as [Mig+13; Fer16]

$$\epsilon_n^2 = \langle\gamma\rangle^2 (z^2 \sigma_\delta^2 \sigma_{x'}^4 + \epsilon_{tr}^2) \,, \tag{3.108}$$

where z is the propagation distance in the drift. In this expression it can be seen that the strongest contribution to the emittance growth arises from the beam divergence. Thus, reducing this parameter is key for mitigating this issue. A method that has been shown to be an effective solution to reduce the beam divergence and suppress emittance growth is to take advantage of a properly tailored plasma-to-vacuum transition (or plasma down-

ramp) such that the focusing fields experienced by the beam are progressively diminished and its divergence reduced [Flo14b; DFM15; Xu+16]. Another option is to place a focusing element as close as possible to the plasma exit that can quickly reduce the beam divergence in both planes. This can be achieved with plasma lenses driven by a discharge [Che87; Lin+18] or which take advantage of the same laser driver used in the accelerating stage [Leh+14; Tha+15].

The concept of beam matching is particularly relevant for the case of external beam injection, as the strong focusing fields in the plasma place tight requirements on the beta function at injection. For example, at a plasma density of 10^{17} cm^{-3}, $\beta \simeq 0.3$ mm is required assuming a blowout and a beam energy of 100 MeV. This sub-mm-range values are very challenging to achieve with conventional focusing elements used in linacs, although new designs based on permanent quadrupoles could overcome this difficulty [Zhu+16]. In addition, these tight constraints can be significantly reduced by the use of plasma upramps, akin to how plasma downramps are used for reducing the beam divergence. With a properly-tailored density transition, these ramps can allow for a larger beta function at injection that is then gradually reduced by the slowly increasing focusing fields, which grow with the plasma density, until it reaches the desired value at the plateau.

3.7. Basic physics of free-electron lasers

The generation of synchrotron radiation, far from being only a residual product in accelerators and detrimental to the beam quality, is nowadays a powerful scientific tool with applications in a broad range of disciplines [WD12]. This includes research both in industry and science in areas such as physics, chemistry, material science or medicine.

The production of X-ray synchrotron radiation with particle accelerators started as by-product of the bending magnets in storage rings, and its use was simply "parasitic" as these accelerator facilities were built for high-energy physics experiments. These are generally referred to as *first-generation* synchrotron light sources. However, due to the high interest in this technique, storage rings dedicated to the production of synchrotron light were developed. These *second-generation* sources featured an optimized design to increase the production of synchrotron light [RM73]. Later on, in the 1990s, a *third generation* emerged which was characterized by the use of insertion devices like wigglers and undulators, which allow for a much higher photon yield than simple dipoles [BEW05]. The latest addition to this family, considered as *fourth-generation* generation synchrotron light source[1], is the Free-Electron Laser (FEL) [Mad71; BPN84]. This device relies also on magnetic undulators, but uses a linear accelerator instead of a storage ring as the source of electrons (e.g [Tie+09; Emm+10]) due to the large kA-range peak current that is typically required, as explained below. FELs are characterized by the production of ultra-short

[1]The title of *fourth-generation* synchrotron light sources is technically shared with ultra-low emittance or *diffraction-limited* storage rings [Win97; Bor14].

(up to fs-scale) and coherent radiation pulses, achieving a peak brilliance several orders of magnitude higher than storage rings [RGM10].

As seen in Figure 3.12, an undulator consists on a periodic arrangement of permanent dipole magnets of alternating polarity which is inserted in the path of the electron beam. In this magnetic array, the beam electrons are forced to perform a sinusoidal trajectory and continuously emit radiation in a narrow angular cone with an opening angle of $1/\gamma$. On axis, the emitted radiation has a wavelength [HK07]

$$\lambda_{ph} = \frac{\lambda_u}{2\gamma^2}\left(1 + \frac{K^2}{2}\right) , \tag{3.109}$$

where λ_u is the undulator period (period of the magnetic array) and K is the undulator strength, which is given by

$$K = \frac{e}{2\pi mc} B_u \lambda_u , \tag{3.110}$$

where B_u is the amplitude of the magnetic field. Due to the sinusoidal motion, the path length of the electrons is increased along the undulator. This induces a slippage between the beam electrons and the emitted photons of one radiation wavelength per undulator period. As a consequence, the electrons continuously interact and exchange energy with the emitted radiation, gaining or losing energy depending on their longitudinal position along the plane wave of the electromagnetic radiation. Given enough undulator periods, this positive and negative energy exchange can lead to a significant energy modulation along the beam, which eventually gives rise to a sub-structure of micro-bunches shorter than λ_{ph}. The radiation emitted by these sub-bunches will therefore be coherent and therefore, as seen in Equation (3.48), will scale with N^2. This dramatically increases the radiated power, which grows exponentially as the micro-bunching develops and eventually reaches saturation. This process, in which coherent radiation is produced due to micro-bunching from the interaction with the initially incoherent, or spontaneous, radiation is known as Self-Amplified Spontaneous Emission (SASE) [KS80], and is the working principle behind many current FEL facilities.

A key parameter which contains all the relevant variables in an FEL is the so-call Pierce or FEL parameter. In the one-dimensional (along z) FEL theory, in which the energy spread and emittance of electron beam as well as the diffraction of the radiation are neglected, this parameter is given by [BPN84; HK07]

$$\rho_{\text{FEL}} = \left(\frac{1}{64\pi^2 I_A}\frac{\lambda_u^2 I_p K^2 [JJ]^2}{\gamma^3 \sigma_x \sigma_y}\right)^{1/3} , \tag{3.111}$$

where $I_A \simeq 17$ kA is the Alfvèn current, I_p is the peak current of the electron beam, σ_x and σ_y are the transverse beam size in both planes and $[JJ]$ is the Bessel function factor, a constant which depends on the undulator type (planar, helical...). The Pierce parameter

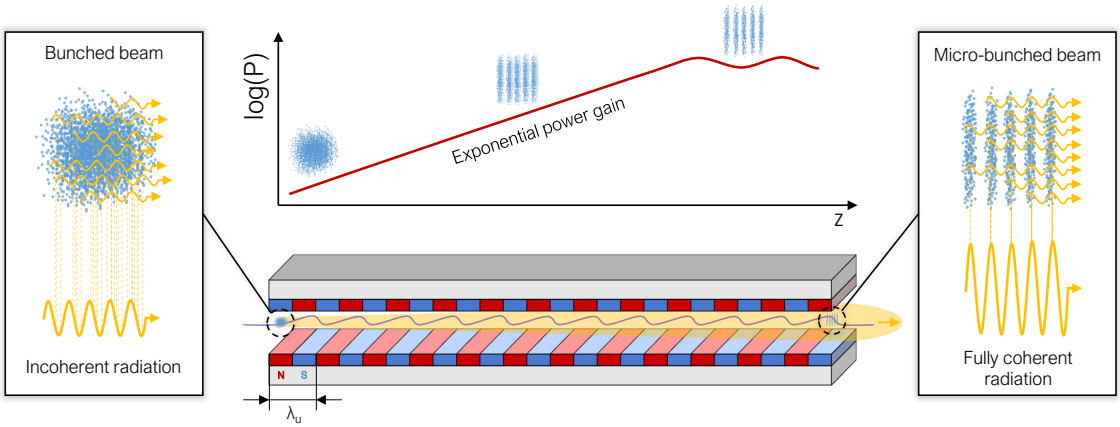

Figure 3.12.: General overview of the microbunching process in an undulator and the exponential power growth. In practice, much more undulator periods are needed to reach saturation. Figure based on a similar diagram in [Zhu16].

is related to other important FEL parameters, such as the gain length [HK07]

$$L_g \simeq \frac{1}{4\pi\sqrt{3}} \frac{\lambda_u}{\rho_{\text{FEL}}} , \tag{3.112}$$

which corresponds to the undulator length over which the radiated power increases by a factor $e \simeq 2.718$. This determines how fast the power grows while the microbunching develops, since $P(z) \propto e^{z/L_g}$ for $z \geq 3L_g$, as well as the saturation length, i.e the length to reach full saturation, which is obtained from $L_s \simeq \lambda_u/\rho_{\text{FEL}}$ [HK07]. The peak radiated power at saturation can be written in terms of the Pierce parameter as $P_{\text{sat}} \simeq 1.6\rho_{\text{FEL}}P_b$ [Xie95], where $P_b = (mc^2/e)I_p\gamma$ is the peak power of the electron beam. This expression is only valid if the gain length once 3D effects are taken into account does not significantly differ from Equation (3.112). Another important parameter is the slippage distance between the beam electrons and the emitted radiation over one gain length. This is called the cooperation length and can be obtained as [HK07]

$$L_c \simeq L_g \frac{\lambda_{ph}}{\lambda_u} . \tag{3.113}$$

This length is the longitudinal distance over which beam electrons can effectively interact with each other via the emitted radiation. Thus, this is also the distance over which the radiation pulse is coherent.

In order for an electron beam to achieve microbunching and emit coherent radiation in a SASE FEL, some strict conditions on its quality have to be satisfied. Of particular importance are the slice emittance and slice energy spread, where the length of the slices is determined by L_c. On one side, the geometric emittance should be smaller than the emittance of the radiated photon beam [PMR16]

$$\epsilon \lesssim \frac{\lambda_{ph}}{4\pi} , \tag{3.114}$$

so that all beam electrons can interact with the radiation. On the other side, the slice energy spread should be smaller than the velocity spread of the electrons over one gain length. This is the case when [PMR16]

$$\sigma_\delta < \rho_{\mathrm{FEL}} \, . \tag{3.115}$$

In general, from these two conditions and Equation (3.112) it can be seen that a large ρ_{FEL} is beneficial, as it shortens the saturation length, increases the peak power at saturation and eases the condition on the slice energy spread. Thus, from Equation (3.111) it is clear that the electron density of the beam should be maximized by increasing its peak current and reducing the transverse size. For current FEL facilities, typical values of ρ_{FEL} are in the range of 10^{-3} to 10^{-4} depending on the beam energy ($\rho_{\mathrm{FEL}} \propto \gamma^{-1}$).

3.8. Summary of simulation codes used

To finalize the theoretical background of this thesis, a summary of the main features and characteristics of the simulations codes used in the following chapters is included here.

WinAGILE

AGILE (or WinAGILE) [Bry00] is a code dedicated to the interactive design of alternating-gradient latices for synchrotrons and transfer lines. Among other features, it contains fitting and matching routines to optimize the arrangement, geometry and strength of magnets to satisfy certain user-defined conditions on the Twiss parameters. It has been largely used throughout this thesis to perform the initial design of the transfer lines between plasma stages.

Elegant

Elegant, which stands for 'ELEctron Generation ANd Tracking' [Bor00], is a code entirely written in C for particle tracking in circular and linear accelerators. The evolution of the 6D phase-space of the particle beams along the accelerator is calculated by means of transfer matrices of up to third order. This approach allows for highly-efficient simulations, which can be completed in a matter of seconds. In addition, it includes models for collective effects such as 1D CSR, longitudinal space-charge, wakefields, intra-beam scattering, etc. However, due to the lack of transverse space-charge, this program is better suited for high energies significantly above 100 MeV or other cases where no significant space-charge forces are expected. Apart from particle tracking, Elegant offers additional capabilities such as accelerator optimization, parameter scans, error and tolerance studies, and more.

ASTRA

ASTRA (A Space-charge TRacking Algorithm) [Flo17] is, as the name implies, a particle-tracking code with a focus on accurately simulating space-charge forces. It is written in Fortran 90 and has both a serial and a parallel version which are independently maintained. In this code, instead of using transfer matrices, the 6D phase-space of the particles is evolved by numerically solving the equations of motion of charged particles under the influence of externally-defined fields. This is performed by means of a Runge-Kutta solver of fourth order. The fields in which the particles move are a combination of those from the beamline elements (dipoles, quadrupoles, RF cavities, etc.) with the space-charge fields obtained from the particle distribution itself. The calculation of this space-charge fields is performed with a Poisson solver in the rest frame of the beam by applying a Lorentz transformation. In this rest frame, the particles are assumed to have no transverse momentum and no longitudinal velocity spread. Once the fields are computed, they are transformed back into the laboratory frame, where they can now be applied to the particle motion. The space-charge fields are scaled when the beam dimensions change and are fully updated either after a certain scaling threshold is reached or in predefined intervals of time steps. The space-charge fields can be computed either with an efficient 2D cylindrical-symmetric algorithm or with a full 3D cartesian mesh. The simulations with ASTRA can take significantly longer than with ELEGANT, particularly when the 3D solver is used. For the cases simulated in this thesis, typical simulation times with the parallel version of ASTRA ranged from several minutes to several hours using a single node in the DESY Maxwell cluster. ASTRA is mainly meant as a tool for simulating straight accelerator sections in linear accelerators. It also supports plasma-accelerating stages, but only with the linear fields described in Section 3.4.2.

CSRtrack

CSRtrack [DL04] is a particle-tracking code written in Fortran 77 which is specialized in the simulation of CSR effects on the beam dynamics. Several CSR models of different accuracy and computational cost are available. On one side, a simple and efficient 1D model can be used in which the bunch charge is projected into the trajectory of a reference particle, thus obtaining a line charge distribution which is longitudinally binned into 1D Gaussian sub-bunches. This approach neglects all transverse dimensions and forces, as well as space-charge effects. Alternatively, a more rigorous (and computationally expensive) 3D calculation is also possible in which the particle distribution is divided into three-dimensional Gaussian sub-bunches of identical dimensions. This approach, however, neglects vertical self-fields. The force of each sub-bunch on each of the surrounding particles is then taken into account by the numerical algorithm integrating the single-particle equations of motion. CSRtrack can handle dipole, quadrupole and multipole magnets. Typical 3D simulations for the cases simulated during this thesis can be

computationally costly, taking up to several days in a single node in the DESY Maxwell cluster.

OCELOT

OCELOT [Aga+14] is a multiphysics simulation toolkit including particle tracking and optimization for linear and circular accelerators, the calculation of spontaneous radiation and FEL calculations. The relevant part for this thesis is however its use as a particle tracker. In this regard, it is based on a transfer matrix approach (up to second order) which is complemented with the addition of 3D space-charge effects (same model as in ASTRA) and a 1D CSR model (same as in CSRtrack). In order to take these self-fields into account, the propagation along the beamline is divided into steps of specified length. After each of these steps, the forces arising from them are applied as additional kicks to the particle trajectory. The code is fully written in Python and can therefore be easily coupled with available data analysis and visualization libraries, or interfaced with other Python codes such as Wake-T. This allows for full start-to-end simulations, including space-charge and CSR effects, of beamlines which combine plasma and conventional elements.

OSIRIS

OSIRIS [Fon+02] is a massively-parallelized, fully-relativistic PIC code written in Fortran 90 which is mainly aimed at simulating plasma-based accelerators. As a general PIC code, it supports both laser- and beams-driven cases. The simulations can be performed in a full 3D cartesian grid or in 2D with either cylindrical or vertical (along y) symmetry. Full 3D simulations of laser-driven cases can be however highly demanding in terms of computing power due to the large resolution required, and 2D simulations do not accurately describe some important physics. Therefore, simplified laser models such as the PCG (ponderomotive guiding centre) algorithm have also been implemented [Hel+16; GMA00]. Alternative field solvers and numerical methods have been also recently added [Dav+15] in order to speed up the simulations and offer alternatives which do not suffer from the numerical Cherenkov instability (NCI) [God74], which can otherwise lead to unphysical results with typical electromagnetic solvers [Kan66].

FBPIC

FBPIC (Fourier-Bessel Particle-In-Cell) [Leh+16] is a PIC code specially designed for the simulation of plasma-based accelerators. This code, which is entirely written in Python, takes advantage of the near-cylindrical symmetry typically observed in this type of accelerators and makes use of a spectral cylindrical representation of the fields. In this way, while the particle trajectories are fully tracked in 3D, the fields are instead solved in a set of 2D radial grids. This allows for a vast reduction of the computing resources required,

performing 3D simulations at basically 2D cost. An additional advantage of this spectral solver is that it is intrinsically free from the NCI. On top of this, FBPIC can further reduce the computing time by performing simulations in the so-called boosted frame [Vay07], a Lorentz transformation into the optical frame of reference. As an example, simulations performed in this thesis of $\sim$10 cm-long plasma cells could be carried out with FBPIC in a matter of hours. With a full 3D code like OSIRIS, this would have instead required several days and a larger amount of computing resources (several high-performance CPU nodes vs a single GPU with FBPIC).

HiPACE

HiPACE (Highly efficient Plasma Accelerator Emulation) [Meh+14] is another PIC code based on reduced physical models to offer faster simulations. In this case, it makes use of the quasi-static approximation to strongly reduce the number of time steps in the simulation. This takes advantage of the fact that the driver evolution takes place typically in much longer time scales than the plasma and can therefore be assumed to be frozen while calculating the plasma response. HiPACE currently supports only beam-driven acceleration.

Wake-T

Wake-T (Wakefield particle Tracker) [FAM19] is a particle-tracking code for plasma accelerators based on reduced wakefield models which was developed as part of this thesis. Its purpose was to close the gap between codes for conventional and plasma-based accelerators, offering the possibility of performing full start-to-end simulations of the complex beamlines presented in this work. Another major reason for its development was the ability to perform these simulations in a matter of seconds instead of hours or days, thus allowing for large parameter scans. The full details of this code are presented in Chapter 4.

4. Development of a fast particle-tracking code for plasma-based accelerators

Associated publication

A. Ferran Pousa, R. Assmann and A. Martinez de la Ossa. "Wake-T: a fast particle tracking code for plasma-based accelerators". In: *J. Phys. Conf. Ser.* 1350 (Nov. 2019), p. 012056. DOI: 10.1088/1742-6596/1350/1/012056

4.1. Introduction

One of the current challenges in the design and optimization of plasma-based accelerators is that the numerical codes required to accurately simulate these devices can be highly demanding in terms of computing time and resources. Correctly modelling the complex laser-plasma and beam-plasma interactions in the accelerator in a general way requires the use of 3-dimensional Particle-in-Cell (PIC) codes such as OSIRIS [Fon+02]. These general-purpose codes for plasma simulations tend, however, to be computationally demanding. As an example, typical 3D simulations of an LWFA stage can take up to several days even in highly-parallelized supercomputers.

To improve this, a number of simplified (but more efficient) codes and algorithms have been developed which make use of certain approximations and assumptions that are usually valid when describing PBAs. This is the case, for example, of FBPIC [Leh+16], a PIC code which takes advantage of the (typically) quasi-cylindrical symmetry of laser-plasma and beam-plasma interactions to reduce the computing time from days to a matter of hours. Although this is a large boost in speed, it still implies that performing large parameter scans to, for example, determine the sensitivity and tolerances of an LWFA (as routinely done for RF accelerators) would be prohibitively expensive. For this type of studies, where thousands of simulations might be needed, a different type of code which could perform simulations in minutes (or seconds) instead of hours would be of high interest, even if the increase in speed comes at a cost in accuracy.

With this purpose in mind, a new fast particle tracking code named Wake-T (Wakefield particle Tracker) which is specially designed for PBAs has been developed as part of this thesis. In this code, the plasma wakefields are calculated according to simplified physical models and not by a general PIC algorithm. The key idea is that instead of having a single general PIC solver, several computationally-light wakefield models which are tailored to a particular interaction regime could be available. The user would then

have to chose the appropriate wakefield model for the case under study. Once the fields in the plasma are computed, the evolution of the beam particles in them is determined with either a numerical Runge-Kutta solver of fourth order or by means of the analytical model derived later in Chapter 7. This approach to particle-tracking is similar to that of codes for conventional accelerators (such as ASTRA, which also uses a Runge-Kutta solver) and allows for a drastic speed-up of the simulations, which can now potentially be performed in a matter of seconds.

In addition to plasma-accelerating stages, other elements such as plasma lenses, drifts, dipoles, quadrupoles and sextupoles have been implemented. This therefore allows for complete start-to-end simulations of complex beamlines such as those in the multistage concepts presented later in Chapters 6 and 8. Thanks to the fast, although potentially less accurate, simulations, this tool is well suited for the initial design of PBAs as well as for performing large parameter scans, tolerance studies or optimization of whole beamlines including plasma elements.

Wake-T is an open-source project available at

`https://github.com/AngelFP/Wake-T`

and entirely written in Python.

4.2. Implementation of particle tracking in Wake-T

As illustrated in Figure 4.1, the core idea behind Wake-T is to track the evolution of charged particles in the presence of external electromagnetic fields, i.e., the plasma wakefields, which are determined though simplified models instead of full PIC simulations. After the fields have been computed, the 6D phase-space evolution of the beam particles is then obtained by means of either analytical or numerical solutions of the equations of motion

$$\frac{d\boldsymbol{p}}{dt}(t) = -e\boldsymbol{W}(t)\,, \tag{4.1}$$

$$\frac{d\boldsymbol{r}}{dt}(t) = \frac{\boldsymbol{p}(t)}{m\gamma(t)}\,, \tag{4.2}$$

where t is the time, $\boldsymbol{p} = (p_x, p_y, p_z)$ and $\boldsymbol{r} = (x, y, z)$ are the particle momentum and position, e and m are the electron charge and mass and $\gamma = 1/\sqrt{1-(v/c)^2}$ is the relativistic Lorentz factor of the particles, with v and c being respectively the particle and light speed. The quantity $\boldsymbol{W}$ represents the wakefields, which for a relativistic particle ($v \simeq c$) can be expressed as $\boldsymbol{W} = (E_x - cB_y, E_y + cB_x, E_z)$, where E_i and B_i, for $i = x, y, z$, are the different components of the electric and magnetic fields.

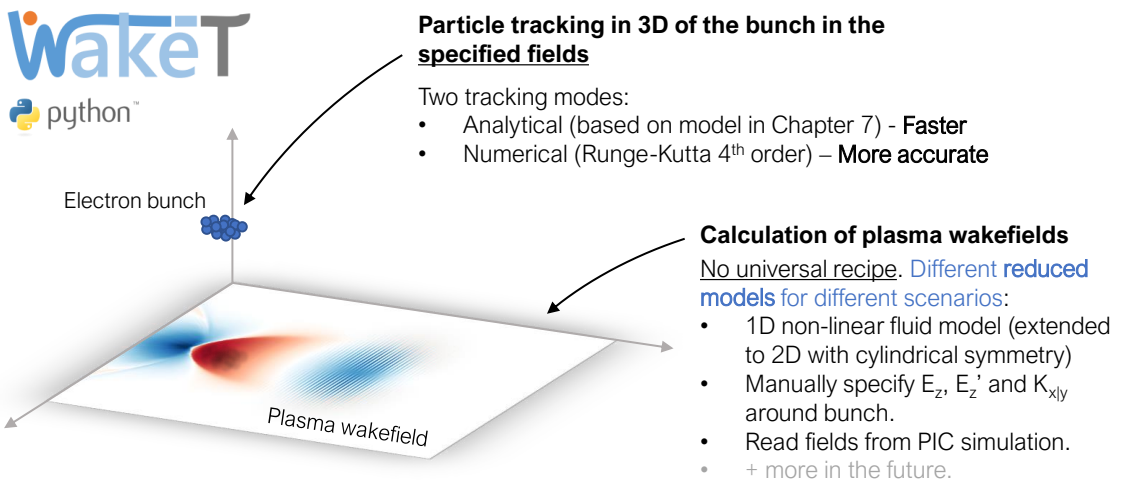

Figure 4.1.: Basic representation of the Wake-T tracking algorithm in plasma stages. The wakefields are first determined from a user-selected reduced model, specified manually, or from data from an actual PIC simulation. The particle beam is then evolved in the specified fields using an analytical or numerical solver. The current Wake-T logo is included in the upper left corner.

4.2.1. Calculation of plasma wakefields

In the current state of development, three different options for specifying the fields in the plasma are available. However, any method for calculating them can in principle be implemented, so the modelling capabilities of the code can be further expanded in the future.

In the currently available options, one possibility for computing the wakefields is to use the 1D non-linear fluid model (extended to 2D with cylindrical symmetry) presented in Section 3.4.1, which is characterized by Equation (3.85). This is a computationally-efficient method which is valid when the plasma waves are predominantly longitudinal, i.e., for wide drivers and/or $a_0 \lesssim 1$. Beam-loading effects are currently not implemented and the laser is modelled as a Gaussian envelope like in Equation (3.62). The transverse evolution of this envelope is then assumed to either evolve as in vacuum or simply to not evolve. A comparison of the wakefields computed with this method compared to the same case with FBPIC can be seen in Figure 4.2.

For more intense drivers capable of generating a blowout, a different reduced model such as the ones presented in [Lu+06a] or [Stu18] would be more adequate. At the time of writing, however, none of these models is implemented in Wake-T. Instead, a different simplified approach is currently used to simulate a blowout. This consists of manually specifying the values of the electric field slope $E_z' = \partial E_z/\partial z$ and the focusing gradient $g = \partial W_x/c\partial x = \partial W_y/c\partial y$ inside the blowout, which are then assumed to be constant. In addition, the value of E_z at a particular position along ξ has to be provided. This is an adequate model to use when the plasma wakefields do not significantly change along the plasma stage (for example, for a guided driver far from depletion) and when beam-

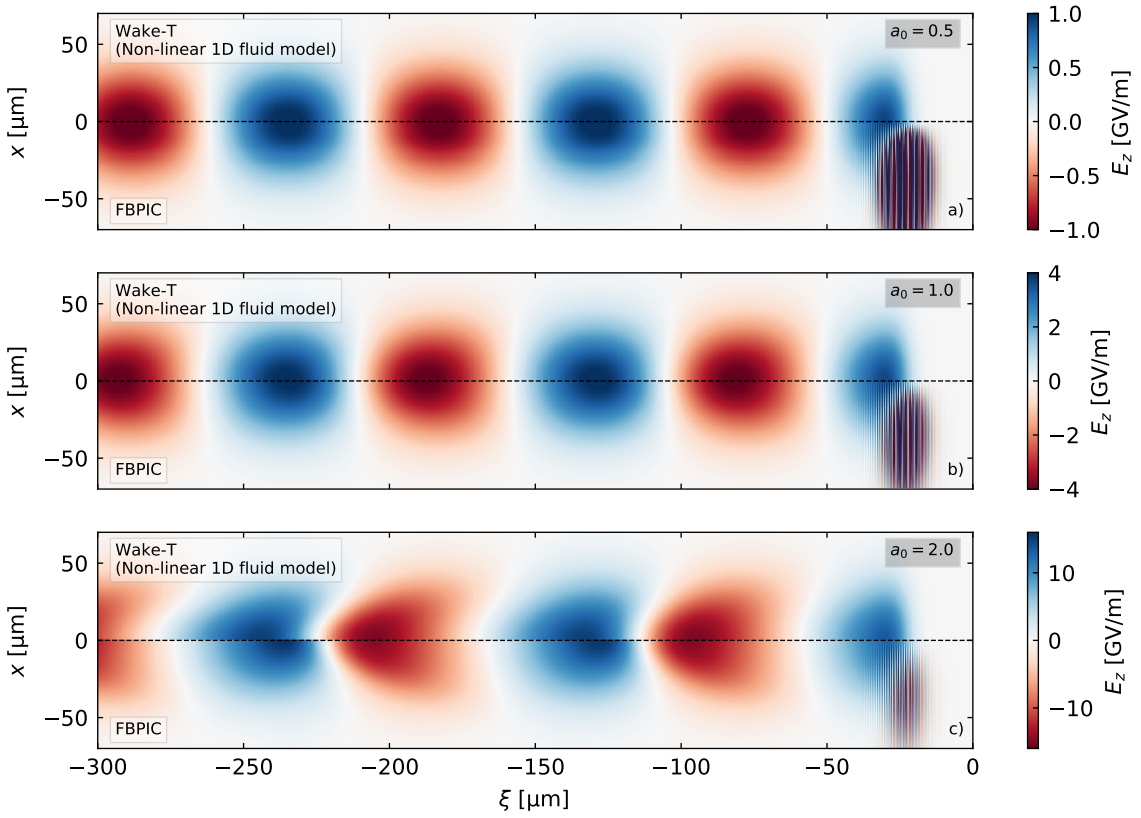

Figure 4.2.: Comparison of the plasma wakefields as calculated by the 1D fluid model in Wake-T with the results obtained from an FBPIC simulation. All cases correspond to a uniform plasma profile with a density of $10^{17}\,\mathrm{cm}^{-3}$ and a laser driver with a FWHM duration (in intensity) of 30 fs and a $w_0 = 50\,\mu\mathrm{m}$. A different a_0 has been used in each simulation. This comparison shows that the 1D fluid model in Wake-T is accurate for $a_0 \lesssim 1$.

loading effects can be neglected. It requires, however, a previous knowledge of the fields that will be generated in the plasma.

Since these two wakefield models cannot cover all possible use cases, a third option has been implemented which consists of reading the plasma wakefields from an actual PIC simulation. This can be done thanks to the the VisualPIC libraries (presented later in Chapter 5), which have compatibility for data from codes such as OSIRIS, HiPACE and any code using the openPMD standard [Hue+18] (such as FBPIC). This option allows, for example, to perform a single PIC simulation with a certain driver which can then be reused multiple times to compute the evolution of different witness beams in a fast way. In this modality, the plasma wakefields can be either read from a single time step and then assumed constant in time or, if multiple time steps from the PIC simulation are available, the fields will be automatically updated at the corresponding times.

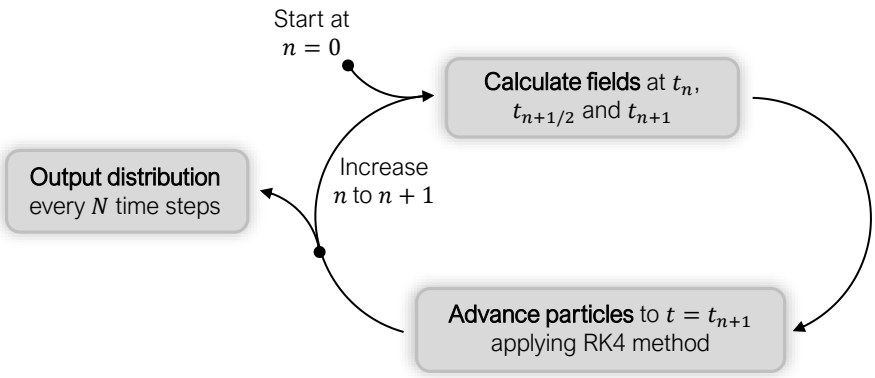

Figure 4.3.: Simple schematic representation of the numerical algorithm based on the RK4 method. The time at the iteration n is defined as $t_n = t_0 + n\Delta t$, where t_0 is the initial time at the beginning of the computation and Δt is the time step.

4.2.2. Particle tracking in plasma stages

After the fields have been specified, the particle evolution is obtained by solving the equations of motion (Equations (4.1) and (4.2)) either by using a fast analytical model or with a more general numerical algorithm. The analytical model is based on the single-particle model presented later in Chapter 7, which takes into account the coupling of longitudinal and transverse particle dynamics. This set of analytical expressions allows for a fast computation of the 6D particle distribution at any time $t = t_f$ simply from the initial conditions at $t = t_0$, and provides accurate solutions as long as the particle motion is relativistic and the fields have not significantly evolved between t_0 and t_f. More accurate solutions can be obtained if the numerical model is used. This is a more general model which solves the equations of motion with a Runge-Kutta method of 4^{th} order (RK4) and is not limited by the approximations of the analytical model. A simple diagram of the basic implementation of this method can be seen in Figure 4.3.

4.2.3. Particle tracking in other beamline elements

In addition to the plasma acceleration stages, Wake-T can simulate the beam evolution in other elements such as plasma up- and downramps (which are treated separately from the plasma stage itself), plasma lenses, drifts and conventional magnets, including dipoles, quadrupoles and sextupoles. This allows the simulation of complex beamlines for PBAs, which can include multiple plasma stages and beam transport elements such as in the concepts presented in Chapters 6 and 8. The particle tracking algorithm in these elements is however different than the one used in the plasma-accelerating stages.

For the plasma ramps, which are currently treated as a separate beamline element, the same numerical RK4 method is used, but no analytical solver is available. In addition, while the same 1D fluid wakefield model is available, the blowout model, instead of allowing a manual specification of the fields, assumes always that $g(z) = (e/2c^2\epsilon_0)n_{p,\mathrm{r}}(z)$,

where $n_{p,r}(z)$ is the plasma density profile of the ramp, and that the longitudinal fields can be neglected. This is generally a good approximation as long as the driver is able to generate a blowout throughout the whole plasma ramp. Different density profiles are currently available, including linear, exponential, Gaussian and inverse quadratic shapes.

The active plasma lenses also make use of the same RK4 particle-tracking solver, but no wakefield models are present. Instead, the focusing gradient provided by the lens is manually specified by the used.

Finally, the particle tracking in drifts, dipoles, quadrupoles and sextupoles is performed by means of second order transport matrices, as introduced in Section 3.1.4, and not by a numerical RK4 solver. The implementation of these elements is based on the Ocelot code [Aga+14]. At the moment, no collective effects such as space-charge or CSR are included.

4.3. Sample studies and validation against PIC simulations

The simplified physical models in Wake-T allow for extremely fast simulations with respect to conventional PIC codes, with typical computation times on a standard PC ranging from a few seconds up to a few minutes depending on the number of beamline elements and particles. This code is therefore well suited for large parameter scans which can be used for the optimization and initial simulation of PBAs as well as for performing tolerance studies. In this regard, two relevant case studies are presented in this section and validated against PIC simulations performed with FBPIC. The first case considers the optimization of the plasma upramp for matching an externally-injected electron beam and minimizing its emittance growth during acceleration. The second case studies the sensitivity of the final beam emittance to transverse beam offsets at injection. In both cases the same electron beam is used, which corresponds to a simulated working point of the ARES linac. The transverse phase-space of this beam at the beginning of the plasma can be seen in Figure 4.4. This particle distribution has a total charge of 5.7 pC, an energy of 100 MeV with 0.5 % spread, a duration $\tau_{\mathrm{FWHM}} = 5.0$ fs, a peak current $I_p = 1.1$ kA, a normalized emittance $\epsilon_{n,x} = 0.52$ µm and $\epsilon_{n,y} = 0.44$ µm, and Twiss parameters $\beta_x = 1.7$ mm, $\beta_y = 1.9$ mm, $\alpha_x = 0.67$ and $\alpha_y = -0.72$. The beam distribution has been centered so that $\langle x \rangle = \langle y \rangle = \langle p_x \rangle = \langle p_y \rangle = 0$ at injection, where $\langle\rangle$ represents the average of the distribution.

4.3.1. Plasma upramp optimization

Properly tailoring the vacuum-to-plasma transition (or upramp) is essential for coupling an external electron beam into a plasma acceleration module without emittance degradation [Flo14b; DFM15; Xu+16]. This upramp acts as a focusing element which, in an optimal case, matches the Twiss parameters of the beam to the focusing fields in the plasma stage [Meh+12; AY98]. Properly optimizing the length and shape of this ramp is essential

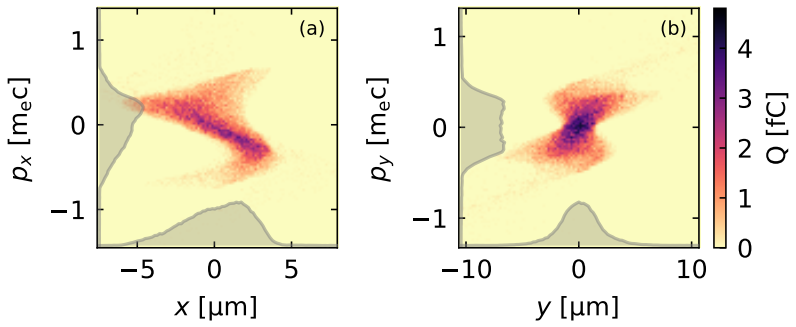

Figure 4.4.: Transverse phase-space in the x and y planes of the electron beam at injection with $\langle x \rangle = \langle y \rangle = \langle p_x \rangle = \langle p_y \rangle = 0$.

for achieving this objective.

The sample case presented here consists of using Wake-T to find the optimal ramp length which minimizes the emittance growth during acceleration. The plasma stage has a plateau density $n_p = 10^{17}\,\mathrm{cm}^{-3}$ and an upramp of length L_{ramp} which, for simplicity, is assumed to have an initial density $n_{p,0} = 5 \times 10^{15}\,\mathrm{cm}^{-3}$ and grows exponentially as $n_{p,\mathrm{up}}(z) = n_p e^{-a(1-z/L_{\mathrm{ramp}})}$, where $a = \ln(n_p/n_{p,0})$. The stage is driven by a 40 fs laser pulse with a peak normalized vector potential $a_0 = 3$, a beam waist $w_0 = 40\,\mu\mathrm{m}$ and a wavelength $\lambda_l = 0.8\,\mu\mathrm{m}$, which corresponds to a peak power of 480 TW and a 20 J energy. This parameters are in the range of those considered in the EuPRAXIA project [Wal+17]. PIC simulations with FBPIC predict that such a laser generates a blowout in the plasma stage with focusing fields $g \simeq 2.6\,\mathrm{MT\,m}^{-1}$, which correspond to a matched beta function $\beta_m = 0.36\,\mathrm{mm}$. This is ~ 5 times smaller than that of the witness beam under consideration, so optimizing the upramp is therefore essential to mitigate the mismatch.

Using Wake-T, a set of 30 simulations have been carried out considering different ramp lengths ranging from 0 (no ramp) to 1 cm, as seen in Figure 4.5a. In these simulations, which were performed with the numerical RK4 algorithm, it was assumed that the focusing fields along the upramp correspond to a blowout and that the longitudinal fields can be neglected, as explained before in Section 4.2.3. Inside the plasma stage, it was simply assumed that $g = 2.6\,\mathrm{MT/m}$, $E_z = -33\,\mathrm{GV/m}$ and $E_z' = 1.4 \times 10^{15}\,\mathrm{V/m}^2$ at the beam position, as expected from PIC simulations. The results can be seen in Figure 4.5b, where they are also validated against FBPIC simulations. In the FBPIC simulations the laser focus was set at the beginning of the plateau and a transverse parabolic density profile is used to guide the laser. This can be seen schematically in Figure 4.5a, where the laser envelope $L_{\mathrm{env}}(z) = \pm w(z)$, with $w(z)$ being the spot size, is represented.

The emittance values shown in Figure 4.5b are measured after a propagation distance of 2 cm inside the plateau. The agreement between Wake-T and FBPIC simulations is excellent (1 % to 10 % difference in this particular study), showing how this tool is well suited for fast parameter scans. As a comparison, the total computing time for each Wake-T simulation was less than 1 minute using 2 cores in a conventional PC, while each FBPIC simulation required $\sim$ 4 hours in a dedicated GPU node in a high-performance

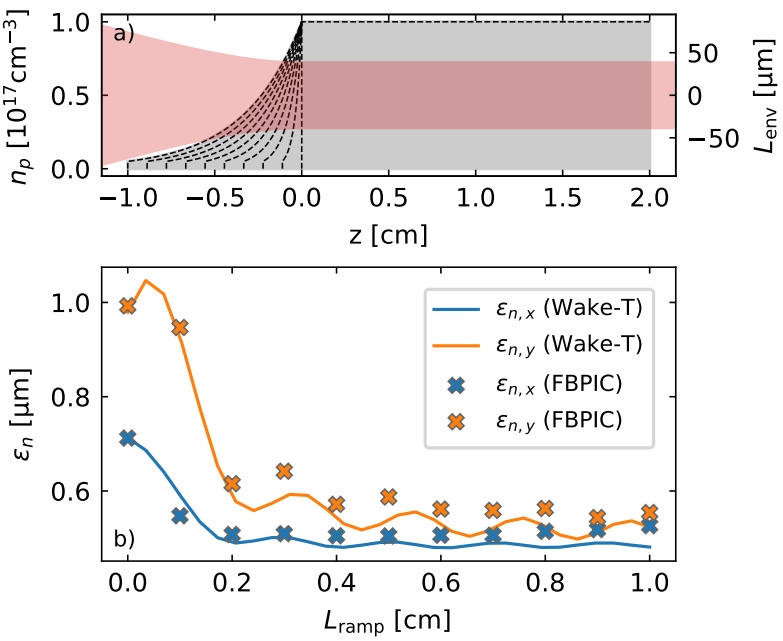

Figure 4.5.: (a) On-axis plasma density profile showcasing the different ramps used. The approximate evolution of the laser envelope, L_{env}, in the FBPIC simulations is also included. (b) Normalized emittance of the beam in both transverse planes measured at $z = 2$ cm for different choices of ramp length.

computing cluster. The results also show that the emittance growth can be effectively mitigated by tuning the ramp length and that, in this case, it quickly converges to a minimum for $L_{\text{ramp}} \gtrsim 0.2$ cm.

4.3.2. Analysis of sensitivity to injection offsets

In addition to beam matching, another critical aspect of external injection into PBAs is that the beams should be ideally injected on-axis, i.e., with $\langle x \rangle = \langle y \rangle = 0$, as well as with $\langle p_x \rangle = \langle p_y \rangle = 0$ in order to prevent, among other problems, emittance growth during acceleration. When designing a PBA it is therefore of key importance to determine the sensitivity to transverse injection offsets and establish a range of tolerances. However, performing this kind of studies only with PIC simulations can be prohibitively expensive.

In this section, the validity of Wake-T for performing certain sensitivity studies is tested. The same setup as in the previous case is used, considering an upramp length of 0.4 cm. In each simulation the initial centroid position of the beam is displaced by a certain offset, $\langle x \rangle = x_{\text{off}}$, with respect to the laser propagation axis and the final emittance in both planes is measured again at $z = 2$ cm. Injection offsets between -10 and 10 µm have been tested. The results, displayed in Figure 4.6, show again very good agreement (1 % to 10 % differences) between the Wake-T and FBPIC simulations and predict a quadratic dependence of the final emittance on the initial transverse offset. It is also interesting to note that the minimum emittance is achieved for a non-zero offset. This is due to the asymmetric profile of the beam in the x plane, in which although $\langle x \rangle = \langle p_x \rangle = 0$ in

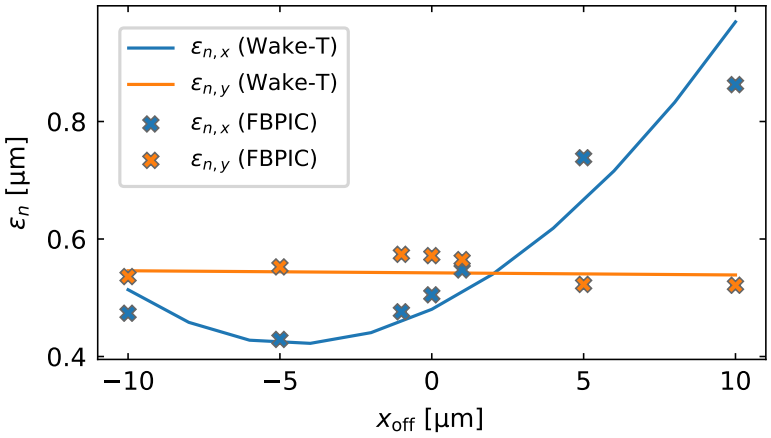

Figure 4.6.: Normalized emittance of the beam in both transverse planes measured at $z = 2$ cm for different transverse offsets at injection. An asymmetric behavior can be observed which arises from phase-space asymmetries in the distribution of the input beam, as explained in the text.

the case with no offset, the peak of the distribution both in position and momentum is not centered, as seen in Figure 4.4. Instead, an offset $x_{\text{off}} \simeq 4\,\mu\text{m}$ seems to minimize the misalignment of the peak and reduce the emittance growth.

4.4. Conclusion

In this chapter, a new particle tracking code for fast simulations of PBAs has been presented. The main working principle of Wake-T and its basic functionality have been described. The results of two particular case studies, which showcase the potential of the code for fast parameter scans, have been shown and validated against full PIC simulations with the FBPIC code. The good agreement between Wake-T and FBPIC simulations, coupled with the vast reduction in computing time and resources ($\sim$1 min per Wake-T simulation in a regular PC versus $\sim$4 hours per FBPIC simulation in a high-performance computing cluster) make this code an attractive option for fast parameter scans of PBAs. These scans, specially when extended to more variables, could then be used for the initial optimization of these devices (before having to perform full PIC simulations) as well as for carrying out sensitivity and tolerance studies, which would otherwise be too computationally demanding with conventional PIC codes.

5. Development of software for data analysis, visualization and other utilities

Associated publication

A. Ferran Pousa, R. W. Assmann and A. Martinez de la Ossa. "VisualPIC: A New Data Visualizer and Post-Processor for Particle-in-Cell Codes". In: *Proc. of 8th International Particle Accelerator Conference (IPAC'17)* (Copenhagen, Denmark). May 2017, pp. 1696–1698. DOI: 10.18429/JACoW-IPAC2017-TUPIK007

5.1. Introduction

Apart from the fast simulation code presented in the previous chapter, another pair of computational tools with unique capabilities has been developed as part of this thesis. These tools are mainly dedicated to the visualization and analysis of data from simulations and provide a set of unique features.

5.2. VisualPIC: a data visualizer and post-processor for PIC codes

5.2.1. Overview of main capabilities

VisualPIC is a new tool for the visualization, analysis and post-processing of data produced by particle-in-cell codes. In particular, it is specially tailored for simulations of plasma wakefield acceleration. The main purpose of this code is to provide a flexible and easy-to-use graphical interface for accessing the simulation data which the user can handle without having to write any code. Through this interface, the fields and particle distributions in the simulation, as well as any quantities derived from those, can be easily visualized at any time step. In addition to basic 1D and 2D visualization, the code offers a dedicated interface for particle tracking (available when the particle distributions have individual tags assigned) and a dedicated visualizer for generating 3D renders of the fields in the simulation. VisualPIC is fully developed in Python and most of the available functionality can also be easily accessed through written code instead of the graphical interface. A quick overview of the main features included in this code is shown in Figure 5.1.

The basis of VisualPIC is a set of libraries for accessing and handling the simulation data which is common for all simulation codes. Currently, data from OSIRIS, HiPACE and from any code using the openPMD standard is supported, but further compatibility

Figure 5.1.: Overview of the main capabilities of VisualPIC.

with other simulation tools can be easily added. This basic layer for data reading and handling supports multiple field geometries and includes common operations such as unit conversion or field slicing. In addition, it provides particle variables or fields, such as the laser normalized vector potential or intensity, which are derived from (but not present in) the original simulation data. This data-handling library provides the foundation on top of which the other modules for data visualization, particle tracking and 3D rendering are built. The graphical interface then provides an easy way of accessing to all of this functionality.

The main window of VisualPIC, as shown in Figure 5.2, presents an entry point to the simulation data located in a specified folder. It allows for the simultaneous visualization of any available fields and particle data, which can be displayed at any time step. The units, color schemes, labels and many other graph properties can be manually modified. It also provides access to tools for creating animations and to all other capabilities of the code.

One of the distinguishing features of VisualPIC is the built-in 3D renderer shown in Figure 5.3. This tool offers a convenient way of quickly visualizing the fields in the simulation and provides customization options for generating attractive renders and animations. Even fields from 2D simulations can be reconstructed and visualized in 3D by assuming cylindrical symmetry. The implementation of this renderer relies on the VTK software for 3D visualization [SAH00] and was initially based on PIC-VTK functions [Mar18].

Apart from data visualization, a dedicated tool for particle tracking is also included. This is useful, for example, for detailed studies of beam dynamics, laser-plasma interactions or internal electron injection. For this, many PIC codes have the capability of assigning individual tags to the particles in the simulation so that their evolution between time steps can be tracked. VisualPIC automatically detects whether these particle tags are

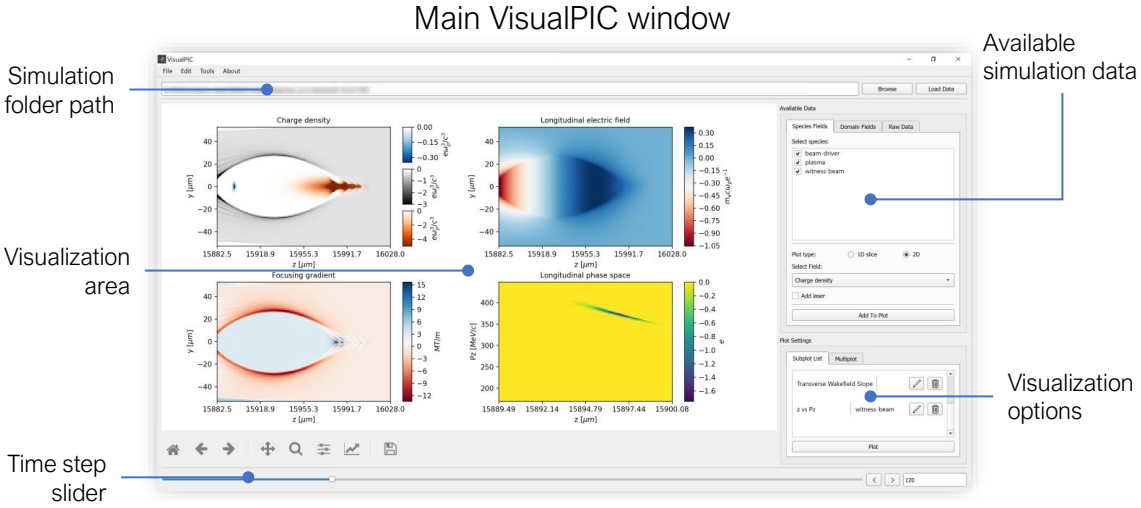

Figure 5.2.: Main window of the graphical interface of VisualPIC. The purpose of the most relevant interaction areas is indicated.

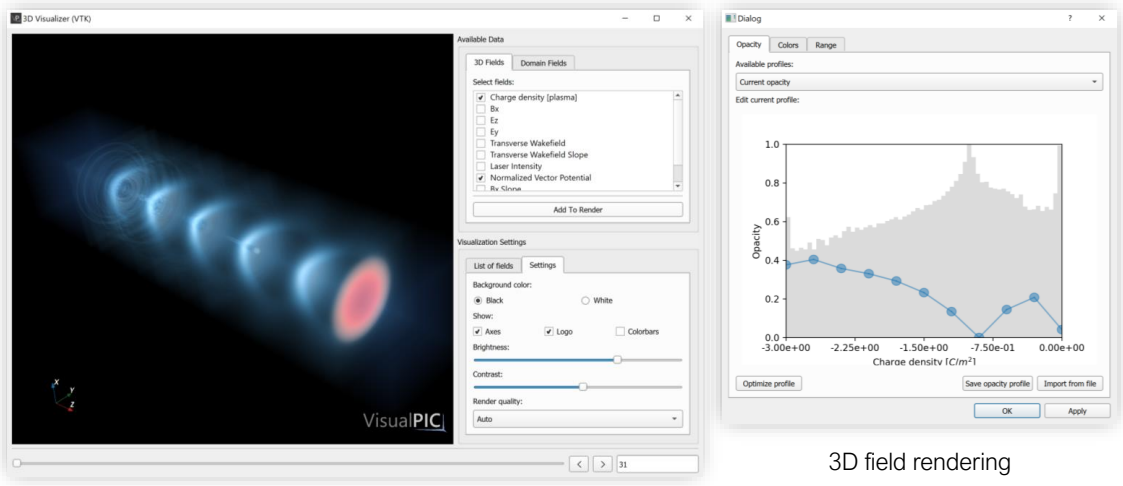

Figure 5.3.: View of the interface for 3D field rendering. The main window (left) allows for an interactive visualization of the selected fields. The visual properties of each field, such as the color and opacity levels can be adjusted to obtain the desired appearance (right).

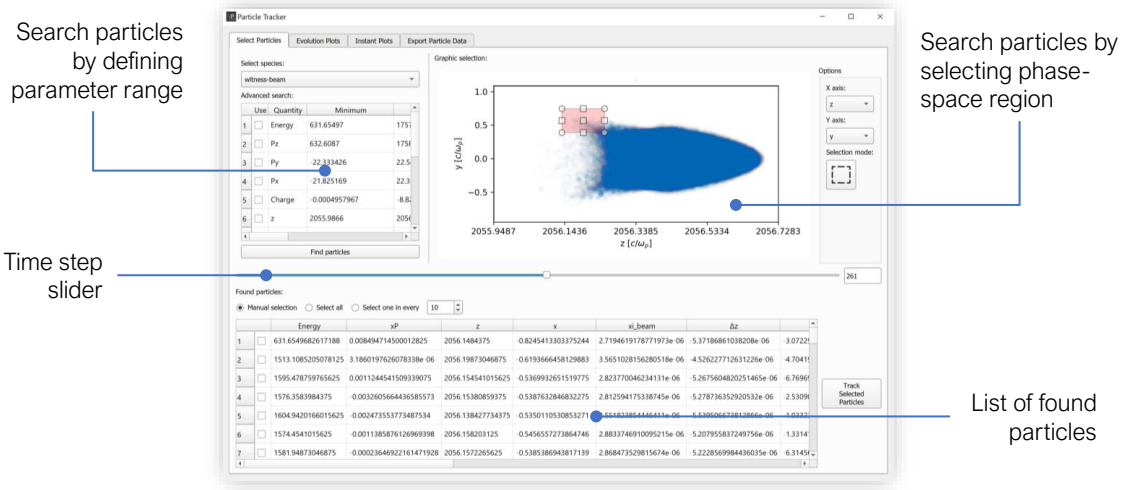

Figure 5.4.: Graphical interface of the particle-tracking tools in VisualPIC. The main interaction areas are highlighted.

available in the data and, if so, offers the particle-tracking functionality. This tool has its own graphical interface, where the phase-space of the particle species can be visualized at any time step and particles to track can be selected. This can be done either by manually specifying a range of parameters within which, at a certain time step, the particles have to be, or by directly selecting a region of the displayed phase-space of the distribution. With either of these two methods, a list of particles fulfilling the range conditions will be populated. Then, from this list, all or just some of the particles can be selected for tracking. After performing the tracking, the data of each particle can be visualized and/or saved to a file. A general view of the tracking interface is included in Figure 5.4.

5.2.2. Details about implementation and dependencies

At the time of writing, VisualPIC is fully written in Python and is designed to run in versions $\geq$ 3.5. The main libraries on which this project depends are `numpy` for handling the data arrays and `scipy` for additional functionality, `matplotlib` for graphing, `H5Py` for reading data files, `vtk` for 3D visualization, `openPMD-viewer` for compatibility with openPMD data, and the imaging library `pillow`. The graphical user interface has been developed with Qt (versions $\geq$ 5.7) using the `PyQt5` bindings.

The code is fully open source and available at

`https://github.com/AngelFP/VisualPIC`,

where installation instructions and further documentation is available.

5.3. APtools: a collection of tools for accelerator physics

In addition to PIC simulations and their produced data, designing and simulating complex accelerator beamlines involves performing simulations with multiple particle track-

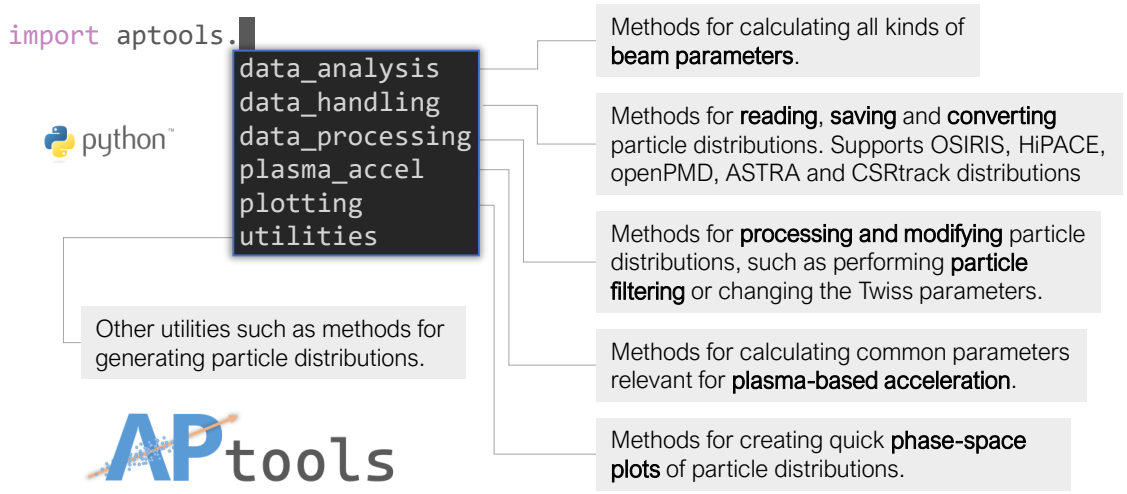

Figure 5.5.: Overview of the functionality provided by the Python modules included in APtools.

ing codes and continuously analyzing beam particle distributions. Due to this, there is a common set of operations, such as reading beam files from different codes, converting them to other formats to transfer them to other codes, or analyzing and visualizing the properties of particle bunches, among others. APtools is a Python library containing several modules populated with methods and utilities to easily perform all these common tasks. An overview of all the built-in functionality at the time of writing is shown in Figure 5.5, and a more detailed description of each module is included in the following.

`data_analysis` At the moment, this module contains only a single `beam_diagnostics` submodule in which all sorts of methods for calculating the properties of particle distributions are available. This includes all the common parameters such as the transverse emittance, energy spread, bunch length, peak current, etc. Many of these parameters can be calculated both for the projected distribution as well as for beam slices.

`data_handling` Contains three submodules named `reading`, `saving` and `conversion`. These modules define multiple methods for easily reading and saving particle distributions from and for different simulation codes. The `conversion` module then uses the other two to provide a simple interface for converting particle data from one code to another. At the moment, data from ASTRA, CSRtrack, OSIRIS, HiPACE and from openPMD codes is supported.

`data_processing` This module is meant for methods which act on the particle distribution. It currently includes a submodule named `beam_filtering`, which provides methods for filtering particle distributions according to some input parameters, and a module called `beam_operations`, which at the moment contains methods for modifying the Twiss parameters of particle distributions to the specified values.

`plasma_accel` In addition to the modules for dealing with particle distributions, this module aims instead at providing a set of common parameters, relations, conditions which are particularly relevant for plasma acceleration. This includes, for example, methods for calculating plasma and laser properties, obtaining beam matching and laser guiding conditions, computing beam wakefields in plasma lenses, etc.

`plotting` This module makes use of the data-reading, handling and processing modules to provide a simple set of functions for the visualization of particle distributions and their properties.

`utilities` This module is meant to provide other useful functionality. At the moment, it contains a `beam_generation` submodule where multiple methods for generating particle distributions are available.

This set of modules provides a comprehensive toolkit for easily carrying out some of the most common tasks related to the design and simulation of particle accelerators. Being a Python library, it can be easily incorporated to data-analysis scripts and other Python projects. This is for example the case of Wake-T, described previously in Chapter 4, which extensively uses the functionality provided by APtools. As the other software projects developed during this thesis, this code is open source and available at

`https://github.com/AngelFP/APtools`.

5.4. Conclusion

The codes presented in this chapter have a unique set of features which makes them ideal companion tools for performing theoretical and simulation studies of plasma-based accelerators. They have been entirely developed during this thesis and have been extensively used while carrying out the physical studies presented in the following chapters. VisualPIC has been proven to be a useful tool for quickly and easily visualizing simulation data, generating attractive 3D renders, and as a Python library for universal access to data from different simulation codes. On the other side, APtools provides a useful set of methods for handling, analyzing and processing particle distributions that no other Python library offers. It has also been widely used for the analysis of the simulations performed in this work and has greatly simplified many common tasks such as the data reading and conversion between codes. Both of these tools are open source and publicly available with the hope that they will also be useful to the general plasma-acceleration community.

6. External injection with sub-fs timing jitter into a plasma-based accelerator

Associated publication

A. Ferran Pousa, R. W. Assmann, R. Brinkmann and A. Martinez de la Ossa. "External injection into a laser-driven plasma accelerator with sub-femtosecond timing jitter". In: *J. Phys.: Conf. Ser.* 874.1 (2017), p. 012032. DOI: 10.1088/1742-6596/874/1/012032

6.1. Introduction

One of the main challenges of external injection into an LWFA is the synchronization between the laser driver and the witness electron beam. This is because, due to the short wavelength ($\sim$100 µm) and high amplitude ($\sim$10 GV m^{-1}) of the accelerating fields in the plasma, small differences in the injection phase can lead to large variations in the final beam energy. As an example, achieving an energy stability of $\sim$0.1 % requires, for a plasma density of 10^{17} cm^{-3} and a typical blowout with $E_z = (mc/e)\omega_p$ and $E_z' = (m/e)\omega_p^2/2$, a stability on the injection phase of $\sim$0.1 fs, well below current state-of-the-art.

This strong requirement, together with other difficulties such as producing bunches which are significantly shorter than the plasma wavelength and are matched to the focusing forces of the wakefield, are some of the reasons why external injection is not a common choice for plasma acceleration experiments. However, recent progress towards the generation of femtosecond to sub-femtosecond bunches with conventional RF technology, such as at REGAE [Flo14a] and ARES [Mar+18] at DESY, has made this a viable option for producing high quality beams and has thus placed a new interest in overcoming the synchronization issue. In order to achieve this, it is of particular importance to reduce the shot-to-shot arrival time fluctuations, or timing jitter, between laser driver and witness beam. Recent experimental work has shown that this driver-to-witness timing jitter could in principle be reduced to the $\sim$10 fs range (RMS) [Tit+17; Tit]. In addition, the ARES linac has also been designed to provide an RMS arrival time jitter $\lesssim$10 fs [Zhu+16], not considering the timing jitter of the laser driver.

In this chapter, a plasma-acceleration concept based on a similar working principle as the old 'plasma klystron' concept [Kat+96; CS96; Fer+00] is proposed as a way of strongly reducing the relative arrival time jitter between driver and witness down to an unprecedented sub-femtosecond range. The proposed method, as seen in Figure 6.1,

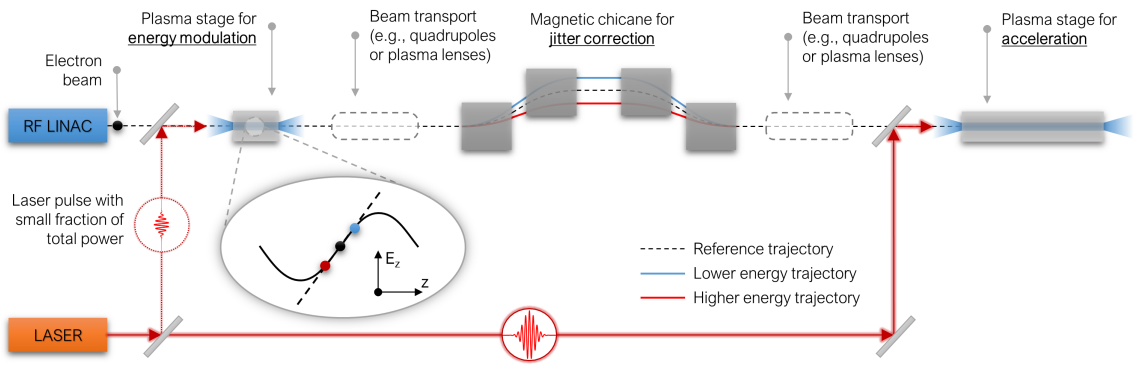

Figure 6.1.: General overview of the proposed accelerator concept for timing jitter correction.

consists in including an additional plasma stage before the main LWFA in which the beam energy is linearly correlated to its relative arrival time with respect to the driver. Then, by means of a magnetic chicane, the initial arrival time jitter is corrected thanks to the dependence between path length and beam energy.

A detailed review of the working principle of this concept is included below in Section 6.2, which is followed in Section 6.3 by analytical studies of the expected performance as well as certain design considerations. Proof-of-principle studies with start-to-end simulations are then included in Section 6.4, where the performance of the scheme for timing jitter correction and the subsequent energy stability improvement is studied. The impact of beam-loading effects in the first stage is also investigated, and the potential of the scheme to act both as a bunch compressor and jitter corrector is explored.

An important remark about this two-stage concept with an intermediate magnetic chicane is that it was the trigger which eventually inspired the acceleration concept for low energy spread beams which is later presented in Chapter 8. This idea for correlated energy spread compensation, which in principle also features less sensitivity to timing jitter, quickly became the main focus of this thesis. Thus, due to the limited available time, the studies presented in the current chapter are limited only to first proof-of-principle performance tests.

6.2. Working principle

As seen in Figure 6.1, this two-stage scheme begins by splitting the initial laser pulse in two. One of these two pulses, containing only a small fraction of the total power, will be used as the driver in the first plasma stage. The other one, having most of the original power, will then drive the main plasma stage used for acceleration.

In the first stage, the electron beam, which is assumed to be much shorter than the plasma wavelength, will experience a different energy gain depending on its relative arrival time with respect to the driver. Assuming a linear plasma wave, the accelerating field experienced by an electron beam placed a distance ξ_l behind a linearly-polarized

Gaussian laser driver can be expressed, from Equation (3.93), as

$$E_z = \frac{\sqrt{\pi}}{4}\frac{mc}{e}a_0^2 k_p^2 \sigma_{z,l} \exp\left(-\frac{(k_p\sigma_{z,l})^2}{4}\right)\cos(k_p\xi_l) + E_{z,bl}\,, \tag{6.1}$$

where $\sigma_{z,l}$ is the RMS laser length, as defined in Equation (3.62), and $E_{z,bl}$ is introduced as a modification to the experienced field due to beam loading. In the focusing region of this wave, which should be long enough to accommodate for the expected timing jitter of the electron beams, the slope of the accelerating field at the zero-crossing, ξ_0, is given by

$$E'_{z,0} = \frac{\sqrt{\pi}}{4}\frac{mc}{e}a_0^2 k_p^3 \sigma_{z,l} \exp\left(-\frac{(k_p\sigma_{z,l})^2}{4}\right)\,, \tag{6.2}$$

and can be considered constant for a region of $\sim \pm\lambda_p/8$ around ξ_0, where the electric field can then be approximated as

$$E_z \simeq E_{z,bl} + E'_{z,0}\Delta\xi\,, \tag{6.3}$$

with $\Delta\xi = \xi - \xi_0$.

Assuming that $E_{z,bl}$ is independent of the injection phase, Equation (6.3) implies that a linear correlation between arrival time and energy will be generated. This correlation is given by

$$\gamma = \gamma_0 + \frac{e}{mc^2}E_z L_p \simeq \gamma_{\text{ref}} - \frac{e}{mc^2}E'_{z,0}L_p\Delta\xi\,, \tag{6.4}$$

where L_p is the length of the plasma stage and $\gamma_{\text{ref}} = \gamma_0 - (e/mc^2)E_{z,bl}L_p$ is defined as the reference energy, which is the energy of a beam arriving with $\Delta\xi = 0$. Since $E'_z > 0$, the correlation given by Eq (6.4) will be negative, implying that beams arriving later than the reference beam will have an energy $\gamma > \gamma_{\text{ref}}$, while for those arriving earlier will instead feature $\gamma < \gamma_{\text{ref}}$. This correlation, which can be interpreted as a 'multi-bunch' chirp χ_{mb} defined as

$$\delta = \frac{\gamma - \gamma_{\text{ref}}}{\gamma_{\text{ref}}} = -\frac{e}{mc^2}\frac{E'_{z,0}L_p}{\gamma_{\text{ref}}}\Delta\xi = \chi_{mb}\Delta\xi\,, \tag{6.5}$$

can then be used by a magnetic chicane to correct the timing jitter of the incoming beams. As given by Equation (3.40), a chicane operating at full compression with respect to this multi-bunch chirp, i.e., with an R_{56} satisfying

$$R_{56} = -\frac{1}{\chi_{mb}} = \frac{mc^2}{e}\frac{\gamma_{\text{ref}}}{E'_{z,0}L_p} \simeq \frac{4}{\sqrt{\pi}}\frac{\gamma_{\text{ref}}}{a_0^2 k_p^3 \sigma_{z,l} L_p}\exp\left(\frac{(k_p\sigma_{z,l})^2}{4}\right)\,, \tag{6.6}$$

where Equation (6.1) has been used, would remove the initial arrival time jitter. Therefore, since both laser drivers are intrinsically synchronized, the timing jitter with respect to the second pulse has also been corrected. The injection phase of the electron beam in the second stage could then be precisely chosen by controlling the delay between the two pulses.

6.3. Design and performance considerations

The theoretical working principle of this scheme has been presented so far by considering only first-order dispersion in the chicane. However, in practice, the performance of the jitter correction will be affected by higher-order contributions when the energy difference with respect to the reference beam reaches the few-percent range. In addition, when designing a particular implementation of this concept, it should be taken into account that the chicane can also have an impact on the bunch length depending the energy spread of the beams. In this section, both of these issues are explored and analytical conditions are derived.

6.3.1. Jitter correction performance with second-order dispersion

As seen in Equation (3.39), the final position of an electron beam after a magnetic chicane is, to second order, and assuming $T_{566} \simeq -3/2R_{56}$ (see Equation (3.43)), given by

$$\xi_f \simeq \xi_i + R_{56}\delta - \frac{3}{2}R_{56}\delta^2 \,, \tag{6.7}$$

where both ξ_f and the initial position ξ_i are defined with respect to the position of the reference beam, i.e., with respect to the beam with $\gamma = \gamma_{\text{ref}}$. This allows the relative beam energy difference to be written as $\delta = \xi_i \chi_{mb}$, where χ_{mb} is again the multi-bunch chirp generated in the first plasma stage. By inserting this into Equation (6.7), and remembering that $R_{56} = -1/\chi_{mb}$, it is finally found that

$$\xi_f \simeq \xi_i - \frac{\delta}{\chi_{mb}} + \frac{3\delta^2}{2\chi_{mb}} = \frac{3}{2}\xi_i^2 \chi_{mb} \,. \tag{6.8}$$

By calculating the standard deviation of this expression, represented as $\sigma(\xi_f)$, the final timing jitter $\mathcal{T}_f$ after the chicane due to second-order effects can be obtained in terms of the initial jitter $\mathcal{T}_i$ as

$$\mathcal{T}_f = \frac{\sigma(\xi_f)}{c} \simeq \frac{3c}{\sqrt{2}}\chi_{mb}\mathcal{T}_i^2 \,. \tag{6.9}$$

This expression implies that achieving a significant jitter reduction so that $\mathcal{T}_f \ll \mathcal{T}_i$ requires

$$\frac{3c}{\sqrt{2}}\chi_{mb}\mathcal{T}_i \ll 1 \,. \tag{6.10}$$

6.3.2. Impact on bunch length

In addition to correcting the initial timing jitter, a side effect of sending a beam through a magnetic chicane is that its length might be affected. This brings in new possibilities, such as performing bunch compression or decompression before injection into the main plasma stage, but can also be a negative effect if the longitudinal shape of the bunch was not intended to be modified.

From Equation (3.41), the ratio between the initial and final bunch length, $\sigma_{z,f}$ and $\sigma_{z,i}$, is given, to first order, by

$$\frac{\sigma_{z,f}^2}{\sigma_{z,i}^2} = (1 + \chi R_{56})^2 + \frac{R_{56}^2 \sigma_{\delta,u}^2}{\sigma_{z,i}^2} \,, \tag{6.11}$$

where χ is here the bunch chirp after the first plasma (which does not have to the same as χ_{mb}) and $\sigma_{\delta,u}$ is the uncorrelated relative energy spread.

Assuming that the energy spread of the bunch is only uncorrelated ($\sigma_\delta = \sigma_{\delta,u}$), it is found from Equation (6.11) that

$$\frac{\sigma_{z,f}}{\sigma_{z,i}} = \sqrt{1 + \left(\frac{R_{56}\sigma_\delta}{\sigma_{z,i}}\right)^2} \simeq 1 + \frac{R_{56}^2 \sigma_\delta^2}{2\sigma_{z,i}^2} \tag{6.12}$$

where the second equality is obtained by performing a first-order Taylor expansion. This expression implies that maintaining $\sigma_{z,f} \simeq \sigma_{z,i}$ requires the chicane R_{56} or, alternatively, the multi-bunch chirp, to satisfy

$$R_{56}^2 = \frac{1}{\chi_{mb}^2} \ll 2\left(\frac{\sigma_{z,i}}{\sigma_\delta}\right)^2 . \tag{6.13}$$

If, however, the bunch has a certain chirp, it is still possible to obtain a condition for preserving the bunch length after the chicane. From Equation (6.11), if $\chi \neq 0$, it can be obtained that $\sigma_{z,f} = \sigma_{z,i}$ if the chirp satisfies the following equation:

$$\chi^2 + \frac{2}{R_{56}}\chi + \frac{\sigma_{\delta,u}^2}{\sigma_{z,i}^2} = 0 \,, \tag{6.14}$$

from which two possible solutions are obtained:

$$\chi_+ = -\frac{2}{R_{56}} + \frac{R_{56}\sigma_{\delta,u}^2}{2\sigma_{z,i}^2} \,, \tag{6.15}$$

$$\chi_- = -\frac{R_{56}\sigma_{\delta,u}^2}{2\sigma_{z,i}^2} \,. \tag{6.16}$$

The first one implies, however, that even though the final bunch length is unchanged, the beam has undergone over-compression in the chicane, i.e., it has been longitudinally inverted, which might not be desirable.

6.4. Proof-of-principle simulation studies

In this section, the performance of the concept is studied by means of detailed start-to-end simulations including the plasma stages and the beam transport through the magnetic chicane. The objective of these simulations was to perform some first proof-of-principle

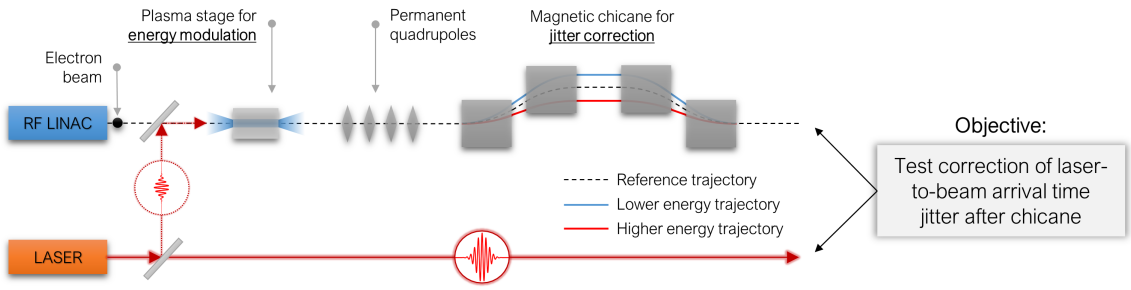

Figure 6.2.: Schematic view of the beamline used to test the performance of the scheme for correcting the laser-to-beam arrival time jitter.

studies on the potential of this scheme for reducing the timing jitter and improving the energy stability of the accelerator. In addition, dedicated studies for determining the impact of beam-loading effects in the first stage have been performed, and the potential of the scheme for serving also as a bunch compressor is explored. Depending on the case, different simulation codes have been used, including OSIRIS and FBPIC for the plasma-accelerating stages and Wake-T, Ocelot and Elegant for the transport line.

6.4.1. Achieving sub-femtosecond timing jitter

The first proof-of-principle study of this scheme, which was published in [Fer+17], was aimed at demonstrating the reduction of an initial ∼10 fs laser-to-beam arrival time jitter down to the sub-femtosecond range. For this, only simulations until the end of the chicane were performed and no injection into the second LWFA was considered yet.

A sketch of the beamline used for this study can be seen in Figure 6.2. The Ti:Sa laser system was assumed to produce a 100 J pulse which, at the time, was being considered as the baseline option for EuPRAXIA. From this initial pulse, a 3.5 % of the energy was reserved to generate a driver for the first plasma stage with an $a_0 = 0.6$, a spot size $w_0 = 54\,\mu\text{m}$, a length $\tau_{\text{FWHM},I} = 93\,\text{fs}$ (FWHM in intensity) and a peak power of 35 TW. The first plasma stage had a length of only 2 mm and was assumed to have a flat-top density profile of $10^{17}\,\text{cm}^{-3}$. The choice of such a short plasma stage was motivated due to numerical instabilities which, at the time, appeared after a certain propagation distance when using the ponderomotive guiding center (PGC) algorithm [GMA00] in the 3D simulations with OSIRIS. This short length also meant that a relatively powerful driver was needed to imprint a significant energy change in the electron beams.

In this first case study, the witness beam was assumed to be Gaussian and have an energy of 100 MeV with a 0.1 % energy spread, a 1 fs duration, a normalized emittance $\epsilon_{n,x|y} = 0.3\,\mu\text{m}$ and a charge of only 0.1 pC, as summarized in Table 6.1. These parameters were chosen in order to avoid significantly perturbing the plasma wakefield due to beam-loading effects (see Figure 6.3) and are similar to the ARES WP1 but with less charge. The transverse size of the bunch was assumed to be matched at the entrance of the plasma. This implies, for the current choice of laser and plasma parameters, a $\sigma_{x|y} = 1.3\,\mu\text{m}$ for

Table 6.1.: Initial parameters of the witness bunch used in the first proof-of-priciple studies.

Parameter	Q [pC]	I_{peak} [A]	σ_t [fs]	γ_0	σ_δ [%]	$\epsilon_{n,x\|y}$ [µm]
Value	0.1	40	1	200	0.1	0.3

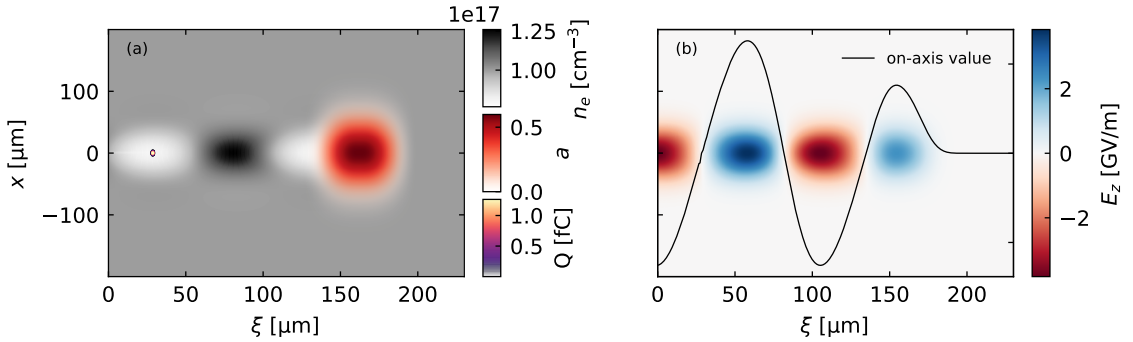

Figure 6.3.: (a) View of the laser driver, the plasma density and the witness beam after a propagation distance of 1.2 mm through the first plasma stage. (b) Longitudinal electric field at the same time step. Only a weak perturbation due to beam loading can be seen in the on-axis value around the zero-crossing.

the focusing fields around ξ_0. A total of 7 different cases have been simulated with initial arrival time offsets between -20 fs and 20 fs with respect to the reference case.

As seen in Figure 6.2, the capturing of the beam after the plasma stage is performed by a set of 4 permanent quadrupoles (PMQ) with a length of 1 cm. They are located only 4 cm after the plasma and are separated by drifts of 4 cm, 6 cm and 4 cm. Their focusing strength was optimized in order to achieve a beam waist at the center of the chicane, leading to a normalized gradient of $-878\,\text{m}^{-2}$, $1406\,\text{m}^{-2}$, $-1497\,\text{m}^{-2}$ and $823\,\text{m}^{-2}$. For the beam energy under consideration, this translates into field gradients of up to $\sim 500\,\text{T m}^{-1}$, requiring tight apertures.

Regarding the magnetic chicane, Equation (6.6) predicts an $R_{56} = 0.222$ mm for the laser and plasma parameters in this case. However, for higher accuracy, the R_{56} of the chicane was directly determined from the multi-bunch chirp measured after the plasma stage, obtaining a value of $R_{56} = 0.267$ mm. This difference with respect to the theoretical value could be due to the laser a_0 being 0.6, which is slightly high for the linear theory ($a_0^2 \ll 1$ is assumed). The bending angle of the dipoles was then determined from Equation (3.42) by assuming a magnet length $L_m = 10$ cm and a drift length $L_d = 2.5$ cm, obtaining an angle $\theta = 2.19°$.

As already mentioned, the simulations of the plasma stage were performed in 3D with OSIRIS using the PGC algorithm. The optimization of the quadrupole section was carried out with WinAGILE while the tracking of the electron beam from the plasma exit until the end of the chicane was performed with ELEGANT. Effects derived from CSR at the chicane were taken into account using a 1D model, but no space-charge forces were con-

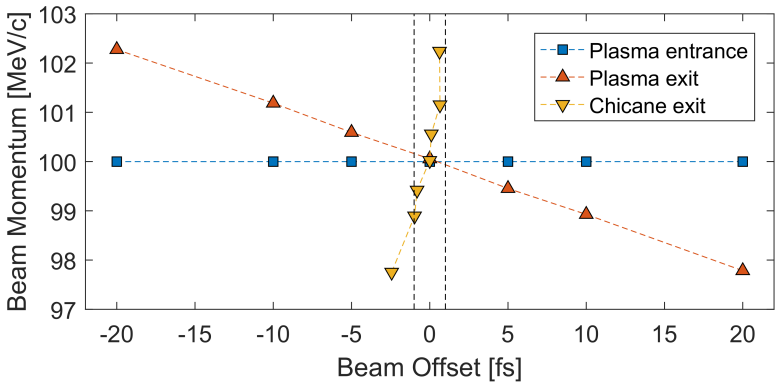

Figure 6.4.: Jitter correction thanks to plasma stage and chicane. The vertical lines delimit a ± 1 fs range. Negative values indicate here a later arrival time. Image from [Fer+17].

sidered as they are not included in ELEGANT. However, due to the low charge density of the beam and its relativistic energy, strong effects from space charge are not expected.

From the simulation results shown in Figure 6.4 it can be seen that, as predicted, the plasma stage imprints a linear energy-to-arrival time correlation on the incoming beams. This correlation then allows the magnetic chicane to successfully correct the initial timing offsets. All beam offsets between ± 10 fs have been reduced to sub-fs level, showcasing the potential of this method. It can also be observed that there seems to be a final positive multi-bunch chirp, implying that the chicane is over-correcting the initial offsets. This is likely arising from the R_{56} of the $\sim$1 m drift (given by $R_{56} = L_{\mathrm{dr}}/\gamma_{\mathrm{ref}}^2$, where L_{dr} is the drift length [Cha+13]) between the end of the plasma and the end of the chicane, which at this energy can still be significant and is not taken into account by Equation (3.42).

The evolution of the beam after the plasma stage is displayed in Figure 6.5. An emittance growth of 10 % to 20 % can be observed due to the strong divergence of the beam and chromatic effects in the quadrupoles. This could in principle be greatly improved if the presence of plasma density ramps is taken into account, as it was done in the studies presented in the following sections. In addition to the emittance growth, it can be observed that beams with $\Delta\xi_i \neq 0$ present a different evolution of the beta function owing to their different energy. This could be an important issue for the beam transport after the chicane, particularly for matching into a second plasma stage. A possible solution for improving this would be the use of plasma lenses instead of a set of quadrupoles, as they present reduced sensitivity to chromatic effects.

6.4.2. Achieving sub-percent energy jitter after accelerating stage

Having demonstrated that sub-femtosecond timing jitter can in principle be achieved, the next step is to use this scheme to inject into a second plasma stage and show that the energy stability can in fact be improved. To study this, a new set of simulations has been performed with the beamline outlined in Figure 6.6. In addition to including a second

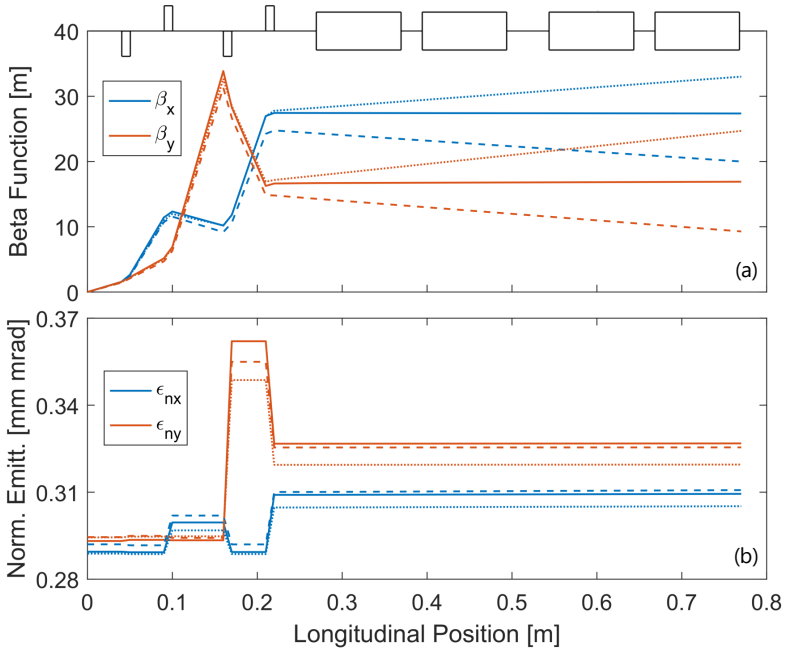

Figure 6.5.: (a) Beta function and (b) normalized emittance evolution for beams with different arrival time offsets. The solid line corresponds to $\Delta\xi_i = 0$, while the dashed and dotted lines represent offsets of 20 fs and -20 fs, respectively. Image from [Fer+17].

LWFA, this beamline features a number of improvements that mitigate some of the issues which were observed in the previous section.

The first change with respect to the previous case is on the laser parameters, which are now much more conservative and in the range of what can be achieved by current laser systems. Instead of a total energy of 100 J, a 3 J system, such as that expected for KALDERA (see Table 2.3), is now considered. From this energy, 0.5 J are used for the driver in the first plasma stage for jitter correction, while the remaining 2.5 J are reserved for the driver in the main accelerating stage. The complete set of parameters of these two Gaussian laser pulses is included in Table 6.2. With regards to the electron bunch, the same parameters as in the previous case have been used (see Table 6.1). This was

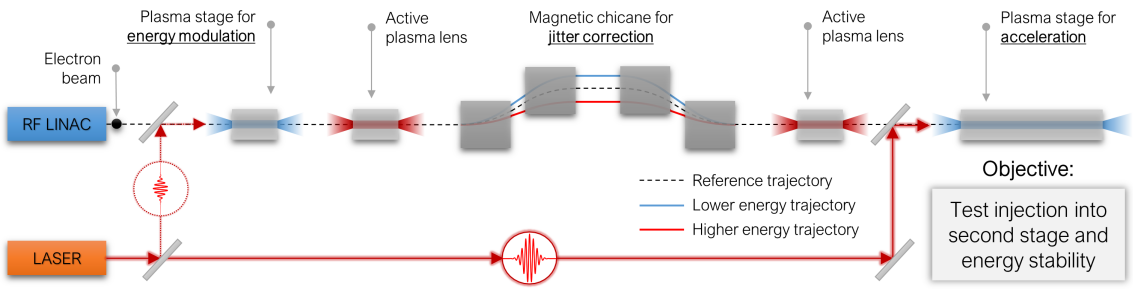

Figure 6.6.: Schematic view of the beamline used to test the performance of the scheme for correcting the arrival time jitter and improving the final energy stability.

Table 6.2.: Parameters of the laser drivers used in the synchronizing and accelerating plasma stages in the weakly beam-loaded case.

Parameter	E_l [J]	$P_{\text{peak},l}$ [TW]	$\tau_{\text{FWHM},l}$ [fs]	a_0	w_0 [µm]	λ_l [nm]
First LWFA	0.5	15.7	30	0.4	54	800
Second LWFA	2.5	77.4	30	1.2	40	800

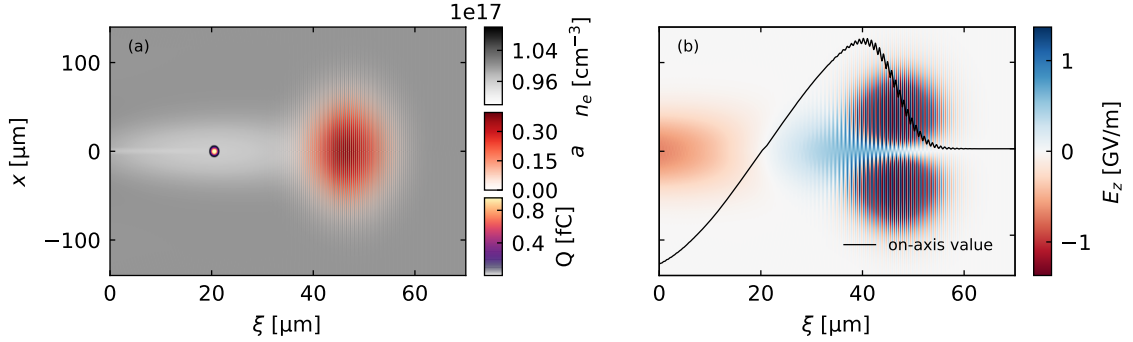

Figure 6.7.: (a) View of the laser driver, the plasma density and the witness beam after a propagation distance of 4 mm through the flat-top of the first plasma stage. (b) Longitudinal electric field at the same time step. Only a weak perturbation due to beam loading can be seen in the on-axis value around the zero-crossing.

done again to be able to neglect strong beam-loading effects, which are instead studied separately later in Section 6.4.3.

With regards to the plasma targets, a longitudinal density profile with a plateau density of $n_{p,0} = 10^{17}\,\text{cm}^{-3}$ has been used in both stages. However, unlike in the previous case, the presence of plasma up- and downramps has now been taken into account. The density profile of these ramps is given by $n_{p,r}(z) = n_{p,0}/(1 + z/L_r)^2$, where z represents the distance to the beginning or end of the flat-top, depending on the case, and L_r is the characteristic length of the ramp, which controls how fast the density changes along z. In both stages, a value of $L_r = 2\,\text{mm}$ has been considered for all ramps, similar to the values from fluid simulations included in Appendix C. The total length of the ramps in all cases was of 2 cm. The plateau length of each LWFA is of 1 cm for the first stage and 10 cm for the second. Both of them feature a transverse parabolic density profile $n_p(r) = n_{p,0} + r^2/\pi r_e w_0^4$ for laser guiding, as given by Equation 3.105.

In this study, a total of 19 cases featuring different arrival times have been simulated. These range from $-30\,\text{fs}$ to 30 fs with respect to the reference injection phase, which in the first stage is defined as the zero-crossing of the longitudinal electric field in the first accelerating bucket. An overview of the fields in this stage is shown in Figure 6.7, where it can be seen that they slightly deviate from the purely linear regime and provide a longer region with close-to-constant slope around the zero-crossing. As a result from this slope, a multi-bunch linear chirp of $\chi_{mb} \simeq -4800\,\text{m}^{-1}$ is generated after the first stage.

The beam capturing after the first LWFA, its transport through the chicane, and the final focusing into the accelerating stage is now carried out by two active plasma lenses (APLs) instead of PMQs. This choice was motivated by the smaller chromaticity of these devices, as already noted in the previous section, and was essential to successfully inject the beams into the second plasma stage. This is because, due to the percent-range energy differences between beams during the transport line, strong variations of the Twiss parameters were observed at the entrance of the second LWFA when PMQs were used. This would then lead to strongly mismatched (or even not fully captured) beams in the accelerating stage. The use of APLs was therefore required and greatly minimized this issue. The two APLs considered have a length of 2.7 cm and a focusing gradient of $100\,\mathrm{T\,m^{-1}}$ and $98\,\mathrm{T\,m^{-1}}$, respectively. This gradient is also smaller than in the PMQs used in the previous section thanks to the effect of the plasma ramps in the LWFA stages, which greatly minimize the beam divergence after the first stage and relax the matching requirements in the second.

In addition to the APLs, which are placed 12 cm away from the plasma stages (ignoring the plasma ramps), the $\simeq$3.2 m-long transport line is composed by a 4-dipole chicane. The magnets in this case have a length of 10 cm and are separated by drifts of 90 cm, 10 cm and 90 cm, with the first and the last dipole located 35 cm away from the APLs. The field strength in the magnets is only of 25.6 mT for achieving a bending angle of 7.8 mrad (0.45°). From Equation (3.42), this would imply a total $R_{56} = 117\,\mu\mathrm{m}$, which is almost a factor of 2 smaller than what the relation $R_{56} = -1/\chi_{mb}$ would yield. This is because at the 100 MeV energy range under consideration, the contribution of the drifts to the R_{56} is still significant, as observed in the previous study, and thus Equation (3.42) is no longer strictly valid. Instead, the drifts also contribute to reducing the arrival time jitter and relax the requirements on the dipole magnets.

The simulations of the plasma stages in this case were carried out with FBPIC, while the transport line was simulated with a combination of Wake-T for the plasma lenses and Ocelot for all the other elements. In the Ocelot simulations, both 3D space-charge and 1D CSR effects have been taken into account. The obtained evolution of the energy and arrival time of the different beams up to the end of the chicane is shown in Figure 6.8(a). The linear correlation between arrival time and beam energy imprinted by the first plasma stage can be clearly seen, as well as the subsequent arrival time correction performed by the chicane. The final position of the beams, as predicted by the analytical theory, is not perfectly aligned with respect to the reference case but exhibits some second-order contributions from the chicane. In addition, some differences with respect to the analytical prediction appear in the lower energy beams. This might be because the energy correlation given in the first stage is not perfectly linear and instead imprints a slight curvature from the sinusoidal fields far from the zero-crossing. To help visualize this, a straight line with the slope of the correlation at the zero-crossing is shown on top of the individual beams.

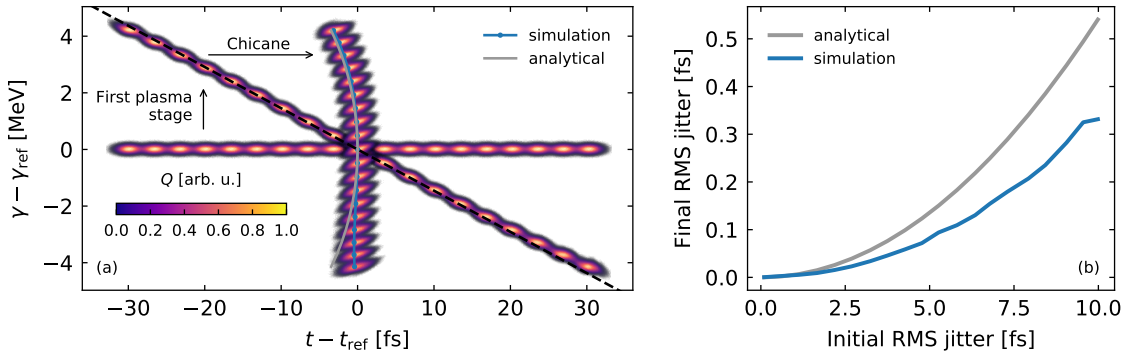

Figure 6.8.: (a) Evolution of the arrival time and energy of all simulated beams with respect to the reference case. The first plasma stage imprints a linear correlation between arrival time and energy which is then used by the chicane to correct the initial arrival time offsets. The analytical prediction for the final beam positions after the chicane is also displayed. A straight line with the slope at the zero-crossing is included to better highlight the slightly sinusoidal energy correlation given by the first stage. (b) Comparison between the theory and simulation results for the final RMS timing jitter after the chicane for different initial jitters. For the case of an initial 10 fs RMS jitter, a reduction by a factor of ~ 30 can be observed.

From the 19 simulated cases, which are all evenly spaced in 3 fs intervals, a direct relation between the initial injection phase and the final position after the chicane can be obtained. This correlation therefore allows the final position of any beam to be determined from its initial arrival time, as long as this arrival time is within the range scanned in the simulations, i.e., between -30 fs and 30 fs. Thanks to this, the jitter correction performance of the scheme can be tested for different possible values of the incoming RMS jitter by randomly generating initial beam positions according to a normal distribution. The results from this analysis, in which an RMS timing jitter at injection up to 10 fs has been tested, can be seen in Figure 6.8(b). In this figure, each data point in the *simulation* line has been obtained by calculating the RMS value of the final arrival time after the chicane for 10000 randomly generated initial arrival times. On the other hand, the analytical curve represents the prediction from Equation (6.9) by using the R_{56} value obtained from Equation (3.42). As it can be observed, the curve from the simulations shows a better performance than the analytical estimate. This is due to the deviation of the lower energy beams towards the right seen in Figure 6.8(a), which might occur as a result of the slightly sinusoidal correlation imprinted by the linear wakefield in the first stage. This then partially compensates the second-order effects in the chicane. Overall, for all the initial timing jitter values tested, an improvement of a factor $\gtrsim 30$ can be seen, showcasing again the potential of the presented concept.

Thanks to this strong reduction in timing jitter, the energy stability of the beams after acceleration in the second plasma stage is also greatly improved. As seen in Figure 6.9(a), if no jitter correction was applied to the 19 simulated cases, a large spread of energies

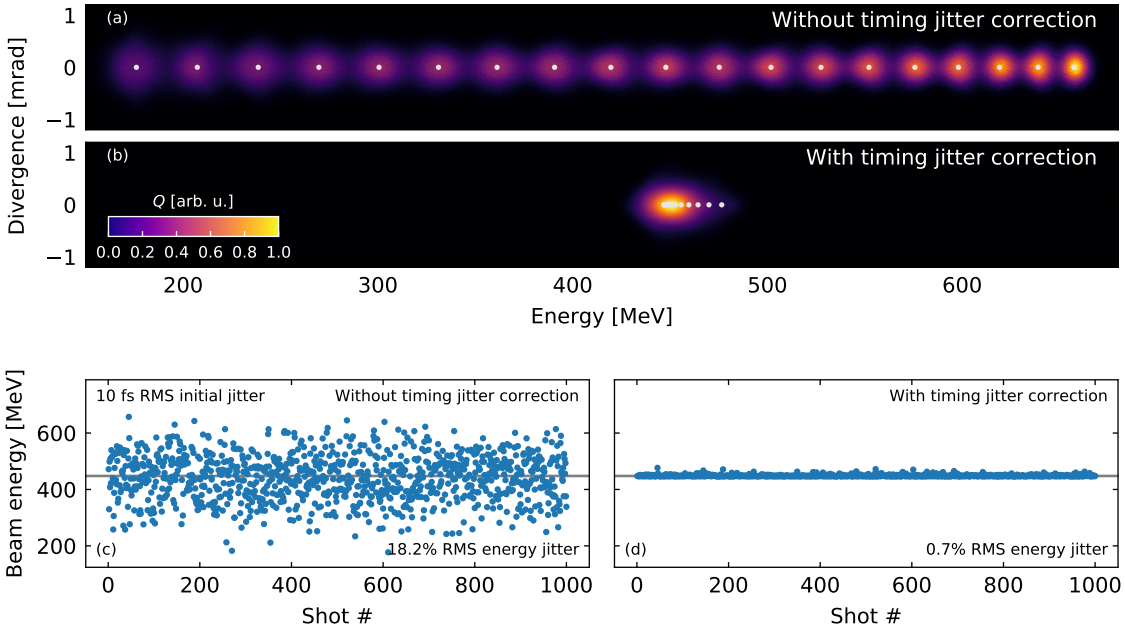

Figure 6.9.: (a) Simulated spectrometer image of the beam energy distribution of the 19 simulated cases when no jitter correction is applied, i.e., when the beam is directly injected into the accelerating stage. (b) Simulated spectrometer image of the same 19 cases when the timing jitter correction scheme is used, i.e., when the beam is sent through a first plasma stage and chicane previous to its injection in the plasma-accelerating stage. (c) Beam energy fluctuations for 1000 randomly generated initial arrival times with a 10 fs RMS jitter when not jitter correction is applied. (d) Same as (c) but after applying jitter correction.

from 200 MeV to 600 MeV would be obtained at the plasma exit. Instead, when the jitter correction scheme is used, this large variation of energies is greatly suppressed and all beams converge towards the same final energy. From these simulations, a direct correlation between the initial arrival time and the final beam energy can be established for both cases (with and without jitter correction). This allows the RMS energy jitter to be calculated for a random sample of initial arrival times. In particular, the case of a 10 fs RMS arrival time jitter is shown in Figures 6.9(c) and (d) for a sample of 1000 randomly generated shots. A clear improvement in the energy stability can be observed when the jitter correction scheme is used, reducing the RMS fluctuations by a factor of ∼20 from 18.2 % to only 0.7 %.

Apart from the final beam energy, the evolution of the beam parameters along the simulated beamline is included in Figure 6.10, where also a layout of the transport line and the plasma density profiles is shown. In this figure, it can be seen that the relative energy differences between beams imprinted in the first stage, which reach the ∼ 5 % level, lead to a different evolution of the beta function along the transport line. As a result, some beams will be over- or underfocused at the entrance of the second plasma, leading to emittance growth. Still, a sub-micron emittance is preserved in all cases, much better

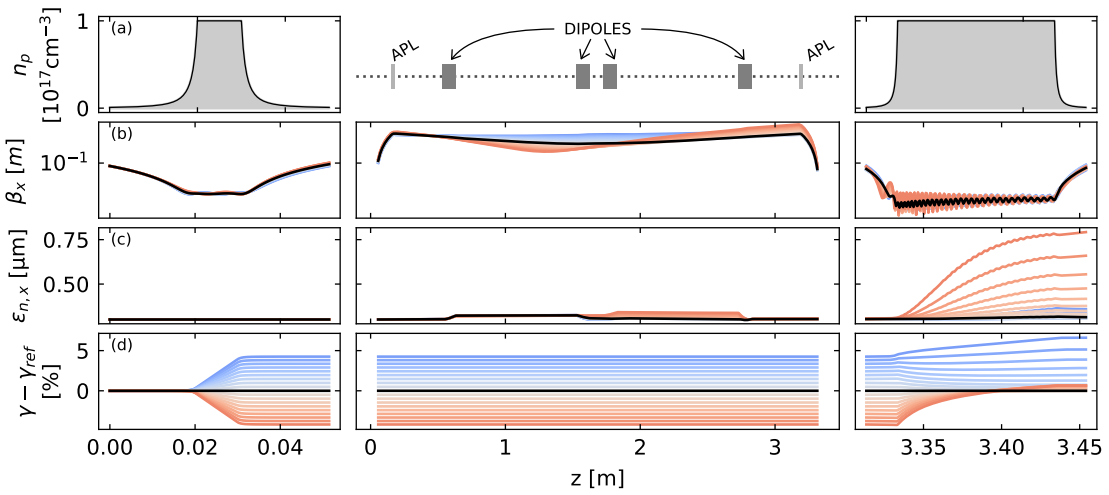

Figure 6.10.: (a) View of the plasma density profiles used in both stages and the arrangement of the elements in the transport line. (b) Evolution of the beta function along the beamline of all simulated cases. The reference case is shown in black, while beams with lower and higher energy are shown in a gradient of color from blue to red, respectively. (c) Evolution of the normalized horizontal emittance. (d) Evolution of the beam energy relative to that of the reference case.

than what the situation would be if quadrupoles were being used instead of the APLs. In a way, this emittance growth implies that the presented scheme partly translates the initial arrival time jitter into an emittance jitter. Therefore, for optimal performance, this is an issue which could ideally be minimized. A way of achieving this could be, for example, to design a properly tailored plasma upramp which is less sensitive to variations in the incoming Twiss parameters of the beams. It should also be noted that the second stage turned out to be better matched for beams with a slightly higher energy than that of the reference case, as it can be observed from the asymmetric behavior of the emittance. This is something that could be easily improved by better optimizing the transfer line. As a result, the spread in the final emittance values after the second stage still offers room for improvement in the presented setup.

6.4.3. Impact of beam-loading effects in the first plasma stage

Up until now, all the cases studied have considered a witness beam with a peak current that is low enough to neglect beam-loading effects. In order to independently evaluate the potential impact of beam loading on the performance of the scheme, a dedicated simulation study has been carried out. In this case, the charge of the witness bunch has been increased by a factor of 10 up to 1 pC while retaining the other parameters, which can be seen in Table 6.3. The laser driver also preserves the same parameters as in the previous case, which are included in Table 6.2, and the same transport line and chicane have been used.

Table 6.3.: Initial parameters of the witness bunch used in the strongly beam-loaded case.

Parameter	Q [pC]	I_{peak} [A]	σ_t [fs]	γ_0	σ_δ [%]	ϵ_n [µm]
Value	1	400	1	200	0.1	0.3

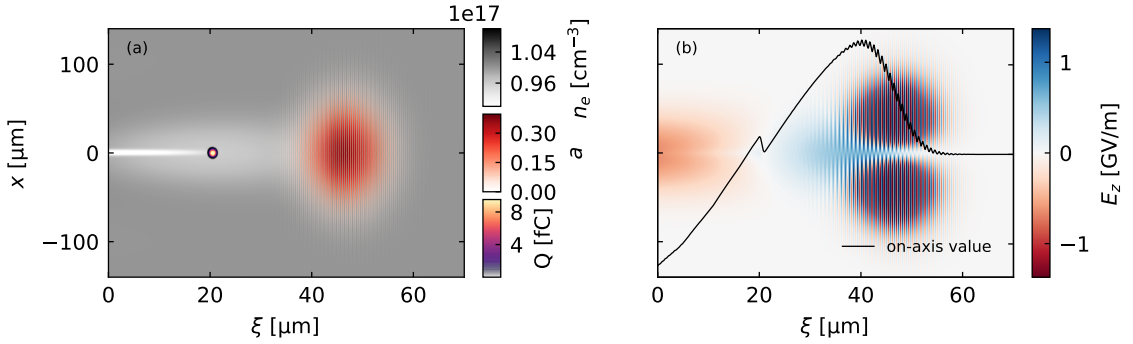

Figure 6.11.: (a) View of the laser driver, the plasma density and the witness beam after a propagation distance of 4 mm through the flat-top of the first plasma stage. (b) Longitudinal electric field at the same time step. A significant perturbation due to beam loading can be seen in the on-axis value around the position of the bunch.

As seen in Figure 6.11, for the laser driver used in the first stage, the peak current in this new case is large enough to invert the slope of the accelerating fields around the bunch. Compared to the previous case, this leads to the development of a large correlated energy spread within the bunch comparable to the bunch-to-bunch energy differences imprinted by the first stage. Thus, the condition in Equation (6.13) is no longer satisfied and a significant bunch lengthening, with its subsequent loss in peak current, occurs after the chicane. This effect can be seen in Figure 6.12, where the evolution of the longitudinal phase-space of the beams is displayed. As a result of the induced energy spread, the bunch length increases from 1 fs to $\gtrsim$ 4 fs after passing through the chicane and the peak current is therefore reduced from 400 A to $\lesssim$ 70 A.

These simulations show that although the initial arrival time offsets are still effectively corrected, strong beam-loading effects lead to a potentially severe, and undesired, bunch lengthening. To preserve the longitudinal properties of the bunch, these effects should therefore be minimized. For large peak currents, this requires a stronger wakefield excitation, that is, a laser driver with a larger a_0. This can be achieved either by focusing the laser more tightly, i.e., reducing w_0, or by increasing its peak power. In the ideal case, the beam-loading effects should be such that the accelerating field is flattened around the bunch and the induced energy spread is therefore minimum. Another possibility would be to start with a particle bunch that initially has a chirp which is opposite to the one imprinted by beam loading. In this way, both chirps would cancel each other by the end of the plasma stage and the bunch length would therefore be preserved after the chicane.

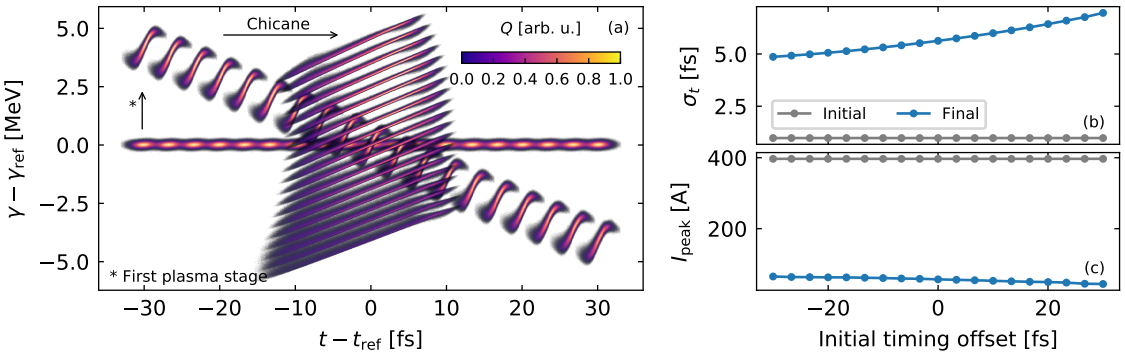

Figure 6.12.: (a) Longitudinal phase-space evolution of the simulated beams. Although the initial arrival time offsets are effectively corrected, a significant bunch lengthening occurs due to the induced energy spread in the first plasma stage. (b) Comparison between the initial (at injection) and final (after the chicane) bunch length. (c) Comparison between the initial and final peak current of the bunches.

Table 6.4.: Initial parameters of the witness bunch used to test compression and timing jitter correction.

Parameter	Q [pC]	I_{peak} [A]	σ_t [fs]	γ_0	σ_δ [%]	ϵ_n [µm]
Value	1	40	10	200	0.1	0.3

6.4.4. Dual use as bunch compressor and jitter corrector

An alternative approach for achieving short bunches while taking advantage of the jitter correction is, instead of providing an already compressed bunch at the entrance of the first plasma, to provide a beam which is initially longer and has a low-enough peak current so that it can develop a negative chirp. Therefore, when the beam is sent through the chicane, in addition to correcting any possible arrival time jitter, its length will be compressed.

In order to test this dual use of the presented scheme (jitter correction and bunch compression), another series of simulations has been performed. In this case, a longer 10 fs beam with a total charge of 1 pC has been used while keeping the same remaining parameters as in the previous cases. With regards to the laser driver in the first stage, in order to imprint a larger chirp on the witness beam, a larger $a_0 = 0.55$ has been used, thus increasing the total pulse energy to 1 J. An overview of all the electron beam and laser parameter is included in Tables 6.4 and 6.5. In addition, due to the increase in a_0 by a factor of $\sqrt{2}$ with respect to the previous cases, the length of the plateau of the first plasma stage has been halved to only 0.5 mm. This was done in order to compensate for the increase in field amplitude, which grows by a factor of 2 according to Equation (3.93), so that the multi-bunch chirp and the beam-to-beam energy differences are kept approximately constant.

Table 6.5.: Parameters of the laser driver used in the first plasma stage for the case of dual use of the scheme for compression and jitter correction.

Parameter	E_l [J]	$P_{\text{peak},l}$ [TW]	$\tau_{\text{FWHM},l}$ [fs]	a_0	w_0 [µm]	λ_l [nm]
Value	1	30	30	0.55	54	800

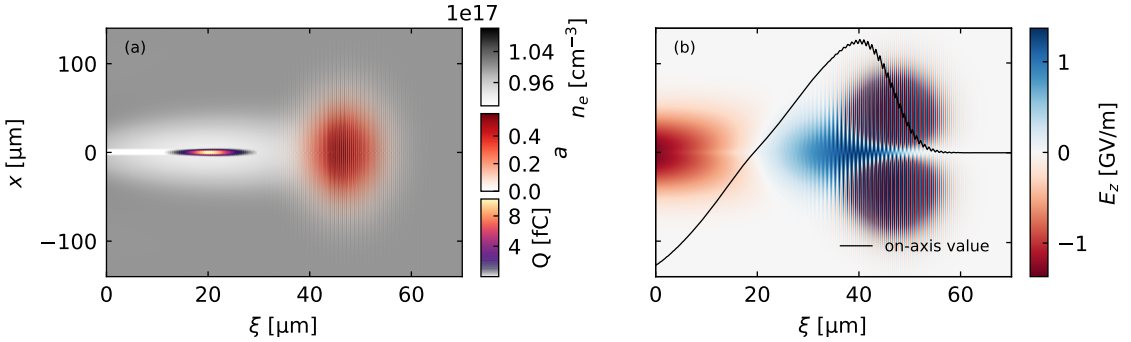

Figure 6.13.: (a) View of the laser driver, the plasma density and the witness beam after a propagation distance of 4 mm through the flat-top of the first plasma stage. (b) Longitudinal electric field at the same time step. Only small beam-loading effects can be seen in the on-axis value around the position of the bunch.

With this set of driver and witness parameters, the beam-loading effects on the wake-field are small, as seen in Figure 6.13. Therefore, the bunch is able to develop a chirp similar to the multi-bunch chirp, which increases its compression in the chicane. This can be observed in Figure 6.14, where only 3 out of the 19 simulated cases are shown in order not to overload the plot. The bunch length is clearly reduced at the same time that the arrival time offsets are corrected. It is also interesting to note that a slight energy modulation due to interaction with the laser driver appears in the rightmost bunch, leading to a slightly distorted shape after compression. This could be avoided by using the second accelerating bucket instead of the first one.

The final bunch length and peak current after passing through the magnetic chicane can be seen in Figures 6.14(b) and 6.14(c) for all the simulated cases. A bunch compression of a factor of $\sim$4 is achieved for the beams close to reference energy, leading to a final bunch length of 2.6 fs. For beams far from the reference case, the performance drops due to second-order contributions in the chicane. As a consequence of the reduction in bunch length, the peak current is equally increased from the initial 40 A to a final value of 150 A in the best case.

This set of simulations therefore shows that the combination of a preliminary plasma stage and a magnetic chicane can be effectively used not only to strongly reduce the arrival time jitter of the incoming beams but also as a bunch compressor. Therefore, it is possible to inject relatively long beams with lower peak current and still achieve a short bunch duration at the entrance of the main accelerating stage. Due to the lower peak

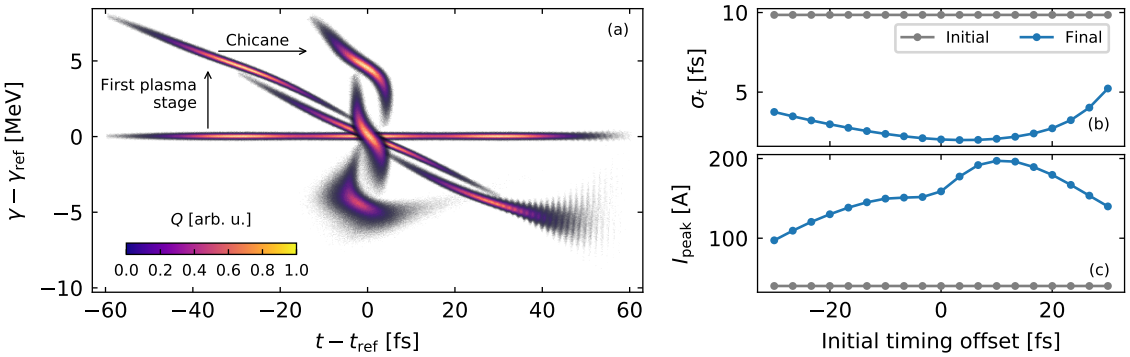

Figure 6.14.: (a) Longitudinal phase-space evolution of the simulated beams. Due to the length of the bunches in these simulations, only three of the cases are shown here which correspond to the reference beam and the earliest and latest arriving beams. In addition to correcting the initial arrival time offsets, the bunches are significantly compressed in the chicane. (b) Comparison between the initial (at injection) and final (after the chicane) bunch length. (c) Comparison between the initial and final peak current of the bunches.

current in this case, the laser requirements for the first stage are potentially reduced with respect to an already fully-compressed witness, since a more powerful driver would be needed to avoid detrimental beam-loading effects, as described in Section 6.4.3. Although the performance of the compression, in the same way as the jitter correction, is affected by second-order effects, these could in principle be compensated for by introducing sextupole magnets in the chicane. This would therefore be an interesting option to explore in future studies.

6.5. Conclusion

In this chapter, a plasma-acceleration concept for reducing the arrival time jitter between a laser driver and an RF-generated electron beam has been proposed. Detailed start-to-end simulations of this scheme have shown that an initial timing jitter on the ∼10 fs range can be effectively reduced to a sub-femtosecond value. This is of key importance for a successful realization of a LWFA with external injection. Thanks to this improvement, the beam energy fluctuations after a plasma-accelerating stage have been reduced by a factor of ∼30, leading to a sub-percent energy stability. Analytical conditions to obtain a good performance have been derived, and dedicated studies have shown that strong beam-loading effects in the first plasma stage should be avoided. Otherwise, severe beam lengthening in the chicane might occur. A possible way of overcoming this issue and still obtaining high-current beams at the entrance of the accelerating stage has also been proposed. This option considers injecting relatively long beams with low peak current in the first stage, which then acquire a chirp and can be compressed in the chicane while also correcting for the initial timing jitter.

The presented scheme could therefore be a solution to the critical timing-jitter issue of external injection into an LWFA. As such, further studies of this technique should be performed in the future. Among these, of particular interest would be to carry out sensitivity and tolerance studies, specially to fluctuations of the laser parameters, which could negatively impact on the performance of the timing-jitter correction. Of key importance would be also to design working points for higher charge beams at least on the 10 pC-range, since only up to 1 pC beams have been considered so far. This could be achieved through a combination of stronger lasers, pre-chirped beams to compensate for beam loading, and initially under-compressed bunches, as mentioned before. In addition, due to the reliance of this concept on plasma lenses and its multistage nature, further dedicated simulations of APLs including any possible beam-induced wakefields should be performed. Possible experimental setups for the laser in- and out-coupling between stages, such as those proposed later in Chapter 8, should also be explored. Finally, ways of minimizing the second-order dispersion in the chicane, such as including sextupole magnets in the transfer line, could be tested to improve the overall performance of the scheme.

7. Energy spread growth due to betatron motion in plasma-based accelerators

Associated publication

A. Ferran Pousa, A. Martinez de la Ossa and R. W. Assmann. "Intrinsic energy spread and bunch length growth in plasma-based accelerators due to betatron motion". In: *Scientific Reports* 9.1 (2019), pp. 1–11. DOI: doi:10.1038/s41598-019-53887-8

7.1. Introduction

Having developed a potential solution to the timing jitter challenge of external injection, the focus of the work shifts now towards the achievement of high-quality electron beams. As discussed in Chapter 2, a major problem in this regard for plasma-based accelerators is the large energy spread, which typically ranges between 1 % to 10 %. This forbids applications such as free-electron lasers and is one of the main current limitations of this technology. A typical reason for the high energy spread is the large energy chirp that the plasma wakefields can imprint on the witness beam, and for which several solutions have been proposed. This is described in more detail in Chapter 6. There can be also other relevant sources such as the emission of betatron radiation [Mic+06] or transverse inhomogeneities in the wakefields [LNM18].

In this chapter, additional important contributions to the energy spread in PBAs are described. In particular, it is shown that the transverse oscillations of beam electrons (known as betatron motion), which are induced by the strong focusing fields in the plasma wake, can be a significant source of uncorrelated (or slice) energy spread as well as increased bunch length. This arises due to the coupling of the longitudinal and transverse dynamics, which leads to path length and longitudinal velocity differences between particles with different oscillation amplitude. Although the effects of this coupling were already known [RJ04; Xu+14], no model exists to date for their impact on the beam parameters. As part of this thesis, a novel analytical theory which accurately describes these phenomena in the assumption of relativistic electrons in a non-evolving wake has been developed and is presented here. The predictions of this model have been validated against numerical simulations with the PIC codes OSIRIS and HiPACE, showing excellent agreement. The analytical expressions derived therefore allow for the definition of general guidelines for minimizing the impact of these phenomena and achieving high-quality electron beams. In addition, the effects on the bunch length predicted by this

model explain previously observed limitations, such as a finite energy spread even when the initial bunch length at injection approaches zero [Gre+14].

7.2. Development of an analytical single-particle model

As a first step, a single-particle model capable of describing the coupling of the transverse oscillations into the longitudinal motion is needed. Then, from this model, statistical averages over a particle beam can be analytically obtained in order to determine the impact of this coupling on parameters such as the energy spread and bunch length.

7.2.1. Calculation of the 6D equations of motion

For a relativistic particle moving close to the speed of light c, the longitudinal component of its velocity is given by

$$v_z = (v^2 - v_x^2 - v_y^2)^{1/2} \simeq c\left(1 - \frac{v_x^2 + v_y^2}{c^2}\right)^{1/2}, \tag{7.1}$$

where $v = |\boldsymbol{v}|$ is the magnitude of the particle velocity $\boldsymbol{v}$. This expression shows that v_z is limited to c and can be decreased due to motion in the transverse planes, i.e, if $v_x, v_y \neq 0$. Thus, in the speed-of-light frame $\xi = z - ct$, where z is the longitudinal coordinate in the laboratory frame and t is the time, a particle performing betatron oscillations will experience a slippage towards the back which, at a time t, will be given by

$$\Delta\xi(t) = \xi(t) - \xi_0 = \int_0^t v_\xi(t)dt\,, \tag{7.2}$$

where ξ_0 is the initial position of the particle and $v_\xi = v_z - c$ is the longitudinal velocity in the speed of light frame.

Determining the particle slippage thus requires obtaining an expression for $v_\xi(t)$, which, in turn, depends on the evolution of the transverse components v_x and v_y. In order to find these expressions, the equations of motion of a relativistic electron in a plasma wakefield have to be solved. These are given by

$$\dot{\boldsymbol{p}} = -e\boldsymbol{W}\,, \tag{7.3}$$

where $\boldsymbol{p} = m\gamma\boldsymbol{v}$ is the particle momentum, m is the electron mass, $\gamma = 1/\sqrt{1-(v/c)^2}$ is the relativistic Lorentz factor of the particle, e is the elementary charge and $\boldsymbol{W} = \left(E_x - cB_y, E_y + cB_x, E_z\right)$ is the wakefield. In this expression, E_i and B_i (for $i = x, y, z$) are the different components of the electric and magnetic fields. Analytical expressions of the wakefields can be found for the linear regime [GK87; Spr+88], and several models have been developed for non-linear wakes in the blowout regime [Lot04; Lu+06b]. In what follows, the wakefield gradients around the particle, $K_x = \partial_x W_x$, $K_y = \partial_y W_y$ and

$E_z' = \partial_z W_z$, will be assumed constant and $\partial_i W_j = 0$ for $i \neq j$. This is especially well-suited for the blowout regime, where the driver expels all plasma electrons and leaves behind an ion cavity with uniform focusing fields $K_x = K_y = m\omega_p^2/2e$ and an approximately constant E_z' in a wide range of the accelerating phase. The plasma frequency is defined as $\omega_p = \sqrt{n_p e^2/m\epsilon_0}$, where ϵ_0 is the vacuum permittivity and n_p is the unperturbed plasma density. For linear wakes, although these gradients are not uniform, this model can be applied for regions sufficiently close to the propagation axis, where K_x and K_y can be regarded as constant, and if $\Delta\xi \ll c/\omega_p$, so that the longitudinal change in K_x, K_y and E_z' can be neglected.

Under these conditions, the longitudinal and transverse components of the equations of motion in Equation (7.3) can be written as

$$\dot{\gamma}(t) = \mathcal{E}(t), \tag{7.4}$$

$$\ddot{p}_x(t) + \omega_x(t)^2\, p_x(t) = 0, \tag{7.5}$$

for a beam electron in a non-evolving wake moving with a phase velocity v_w given by the propagation velocity of the driver. In this expression, the normalized longitudinal electric field is introduced as $\mathcal{E} = -eE_z/mc$, which corresponds to the energy gain rate, and $\omega_x(t) = \sqrt{\mathcal{K}_x/\gamma(t)}$ is the betatron frequency of the accelerated electron, where $\mathcal{K}_x = eK_x/m$ is the normalized focusing gradient. Since $\mathcal{E}' = -eE_z'/mc$ is assumed constant, the evolution of the accelerating field experienced by the particle as it slips back due to betatron oscillations and dephasing with the wake [Sch+11] can be expressed as

$$\mathcal{E}(t) = \mathcal{E}_0 + \mathcal{E}'\left[\Delta\xi(t) + (c - v_w)t\right] , \tag{7.6}$$

where $\mathcal{E}_0 = \mathcal{E}(0)$ is the initial electric field experienced by the particle. Inserting Equation (7.6) into Equation (7.4) allows one to find a solution for the particle energy evolution given by

$$\gamma(t) = \gamma_0 + \mathcal{E}_0 t + \int_0^t \mathcal{E}'\left[\Delta\xi(t') + (c - v_w)t'\right] dt = \gamma^{(0)}(t) + \gamma^{(1)}(t) , \tag{7.7}$$

where γ_0 is the initial particle energy. In this expression, the terms $\gamma^{(0)}(t) = \gamma_0 + \mathcal{E}_0 t$ and $\gamma^{(1)}(t) = \int_0^t \mathcal{E}'\left[\Delta\xi(t') + (c - v_w)t'\right] dt'$ have been introduced and correspond, respectively, to the energy evolution assuming constant acceleration and to the contributions of slippage and dephasing to the energy gain. If $\gamma^{(1)}/\gamma^{(0)} \ll 1$, then $\gamma \simeq \gamma^{(0)}$ can be assumed in order to solve Equation (7.5), for which analytical solutions can be found if $\omega_x(t)$ is a slowly varying function [KPK04], i.e, if $\dot{\omega}_x/\omega_x^2 = \mathcal{E}_0/2\sqrt{\gamma\mathcal{K}_x} \ll 1$. This yields the following expressions for the transverse particle position and velocity:

$$x(t) \simeq A_{x,0}\Gamma(t)^{-1/4}\cos\left(\phi_x(t) + \phi_{x,0}\right), \tag{7.8}$$

$$v_x(t) \simeq -A_{x,0}\omega_{x,0}\Gamma(t)^{-3/4}\sin\left(\phi_x(t) + \phi_{x,0}\right), \tag{7.9}$$

where $A_{x,0} = \sqrt{x_0^2 + (v_{x,0}/\omega_{x,0})^2}$ is the initial transverse oscillation amplitude, in which x_0, $v_{x,0}$ and $\omega_{x,0}$ correspond to the initial transverse position, velocity and betatron frequency. The factor $\Gamma(t) = \gamma^{(0)}(t)/\gamma_0 = 1 + \mathcal{E}_0 t/\gamma_0$ is the relative energy evolution, which damps or enhances the oscillation amplitude of both x and v_x depending on whether the particle gains or loses energy, and $\phi_{x,0} = -\arctan(v_{x,0}/x_0\omega_{x,0})$ is the initial phase of the particle oscillation, which evolves with a phase advance $\phi_x(t)$ given by

$$\phi_x(t) = \int_0^t \omega_x(t')\,\mathrm{d}t' \simeq 2\frac{\sqrt{\mathcal{K}_x\gamma_0}}{\mathcal{E}_0}\left(\Gamma(t)^{1/2} - 1\right) . \tag{7.10}$$

Equations (7.8) to (7.10) determine the particle evolution in the x plane, and analogous expressions, which are not included here for simplicity, can be found for the y direction.

The solutions to the transverse electron motion given by Equations (7.8), (7.9) and their y-plane counterparts can now be inserted into Equation (7.2) to obtain the longitudinal slippage by considering $v_z = (v^2 - v_x^2 - v_y^2)^{1/2} \simeq v - (v_x^2 + v_y^2)/2v$ and $v - c \simeq -c/2\gamma^2$ for a relativistic electron. Since the time scale of the oscillation amplitude damping, $\Gamma^{-3/4}(t)$, in Equation (7.9) is much longer than the betatron period, the time-average of this expression can be used for the electron transverse velocity. This results in the expression

$$\Delta\xi(t) \simeq \frac{c}{2\mathcal{E}_0\gamma_0}\left(\Gamma(t)^{-1} - 1\right) + \frac{A_0^2\mathcal{K}}{2c\mathcal{E}_0}\left(\Gamma(t)^{-1/2} - 1\right), \tag{7.11}$$

where $A_0^2 = A_{x,0}^2 + A_{y,0}^2$ and the focusing gradient is assumed to be the same in both planes, i.e $\mathcal{K}_x = \mathcal{K}_y = \mathcal{K}$. A more detailed derivation of this expression is included in Appendix A.1. The two terms in Equation (7.11) account, respectively, for the slippage due to $v < c$ and the slippage caused by betatron motion. Most of $\Delta\xi$ occurs initially (at lower energies) and reaches a limit $\Delta\xi_{\max}$ as $\Gamma \to \infty$ given by

$$\Delta\xi_{\max} = -\frac{1}{2\mathcal{E}_0}\left(\frac{c}{\gamma_0} + \frac{A_0^2\mathcal{K}}{c}\right). \tag{7.12}$$

Finally, Equation (7.11) can now be inserted in Equation (7.7) in order to find an expression for the particle energy which takes into account the influence of slippage effects. This yields

$$\gamma(t) \simeq \gamma_0 + \mathcal{E}_0 t + \mathcal{E}'\Delta\xi_{\max} t + \frac{\mathcal{E}'}{2}(c - v_w)\,t^2 + \frac{c\mathcal{E}'}{2\mathcal{E}_0^2}\ln\Gamma(t) + \frac{\mathcal{E}' A_0^2\mathcal{K}\gamma_0}{c\mathcal{E}_0^2}\left(\Gamma(t)^{1/2} - 1\right), \tag{7.13}$$

where the third term is a correction to the linear energy gain, which is modified due to slippage, and the fourth one accounts for the influence of dephasing with the wake when $v_w < c$ in laser-driven cases. The following terms are higher order corrections which account, respectively, for slippage due to $|v| < c$ and slippage due to betatron motion.

Equations (7.8), (7.9), (7.11) and (7.13) allow for a complete description of the 6D phase-

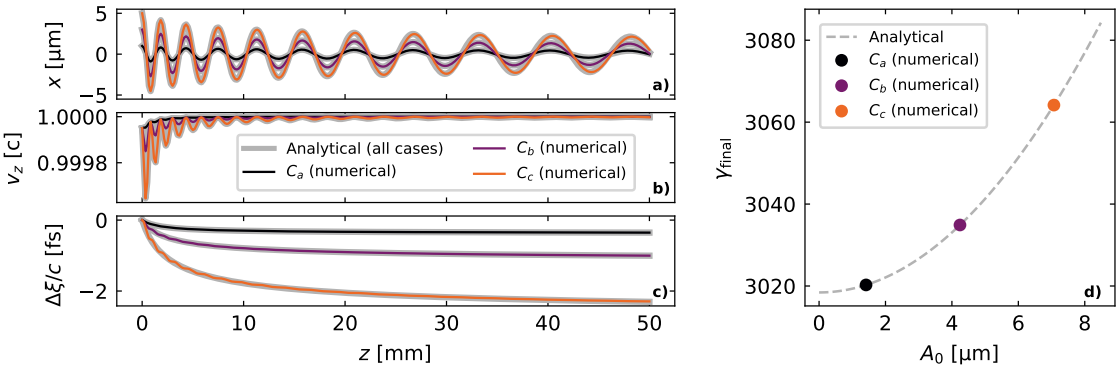

Figure 7.1.: Comparison of the analytical and numerical results for three test particles with different oscillation amplitude in a 5 cm plasma stage: **(a)** betatron oscillations in x, **(b)** longitudinal velocity, **(c)** longitudinal slippage, and **(d)** the final energy after acceleration. The analytical predictions are all shown in grey, while the numerical solutions have a different color for each particle. Image from [FMA19].

space evolution of relativistic electrons in a non-evolving plasma wake. This is the first analytical model which, for the first time (to the knowledge of the author), describes the coupling between transverse and longitudinal dynamics of particles in a focusing channel which, at the same time, are being accelerated by a longitudinally-varying field. As such, it describes the longitudinal slippage arising from the reduced v_z due to transverse oscillations as well as the impact of this slippage on the particle energy when the accelerating fields are not uniform along z. This single-particle model will be the basis for calculating the impact of betatron-induced slippage on the overall parameters of a whole particle bunch, as presented in the following sections.

7.2.2. Validation against numerical solutions

In order to test the validity of the presented model, the obtained analytical expressions have been compared with numerical solutions of Equations (7.4) and (7.5). Three test cases corresponding to single electrons with different initial transverse offsets are shown in Figure 7.1. The electrons in these three cases (C_a, C_b and C_c) have, respectively, $x_0 = y_0 = 1, 3, 5$ μm and $v_{x,0} = v_{y,0} = 0$. They are injected with $\gamma_0 = 100$ and propagate 5 cm within a plasma stage with $n_p = 10^{17}\,\mathrm{cm}^{-3}$ assuming a blowout with $\mathcal{E}' = -\omega_p^2/2c$, $\mathcal{E}_0 = \omega_p$ and $\mathcal{K} = \omega_p^2/2$. The wake velocity is directly determined from the group velocity of a laser driver (see Equation (3.71)) assuming a wavelength $\lambda_l = 800\,\mathrm{nm}$ as in typical Ti:Sa lasers.

The agreement between numerical and analytical solutions is excellent, showing that this single-particle model accurately describes the coupling between longitudinal and transverse dynamics. From these test cases it can also be seen that betatron oscillations with micron-level amplitude can lead to femtosecond-level slippage and energy differences on the percent range. Thus, when considering a whole particle bunch, it is expected

that these differences in slippage and energy gain between individual electrons will have an impact on parameters such as the bunch length and energy spread.

7.3. Impact of betatron slippage on beam parameters

An immediate consequence of particle slippage due to betatron motion will be an increase of the bunch length. This will be especially relevant in bunches where the initial length is comparable or shorter than the average slippage experienced by the particles. In this case, the bunch lengthening will also result in an increase of the correlated energy spread if $\mathcal{E}' \neq 0$. Another implication, more critical for FEL applications, is that the intra-bunch slice mixing arising from the different slippage rates between particles will lead to a growth of the slice energy spread. In this section, these two issues are investigated theoretically and analytical expressions describing the impact on the beam parameters are derived.

7.3.1. Slice energy spread growth

In order to obtain an expression for the induced slice energy spread, Equations (7.11) and (7.13) can be used to calculate the energy difference $\Delta\gamma$ between two beam particles, p_1 and p_2, with the same γ_0 but different oscillation amplitude, $A_{0,p_1} = 0$ and $A_{0,p_2} \neq 0$, which at some time t are in the same infinitesimally-long beam slice at ξ_s due to the experienced slippage. If $\mathcal{E}'$ and $\mathcal{K}$ are constant along the bunch, then $\mathcal{E}_{0,p_i} = \mathcal{E}_{0,s} - \mathcal{E}'\Delta\xi_{p_i}$ for $i = 1, 2$, where $\mathcal{E}_{0,s}$ is measured at ξ_s. This allows the particle energy evolution, $\gamma_{p_i}(t)$, to be written in terms of the fields at the current slice. Additionally, if $\mathcal{E}'\Delta\xi_{p_i}(t)/\mathcal{E}_{0,s} \ll 1$, then $\mathcal{E}_{0,p_i} \simeq \mathcal{E}_{0,s}$ can be assumed for the higher-order terms in $\gamma_{p_i}(t)$ while maintaining the full expression in the leading linear term. This also means that $\Delta\xi_{p_2}(t) - \Delta\xi_{p_1}(t) \simeq A_{0,p_2}^2 \mathcal{K}(\Gamma_s^{-1/2}(t) - 1)/2c\mathcal{E}_{0,s}$, which, added to the previous considerations, leads to

$$\Delta\gamma(t) = \gamma_{p_2}(t) - \gamma_{p_1}(t) \simeq \frac{\gamma_0 \mathcal{E}' \mathcal{K} A_{0,p_2}^2}{2c\mathcal{E}_{0,s}^2} \frac{\left(\Gamma_s(t)^{1/2} - 1\right)^2}{\Gamma_s(t)^{1/2}}, \tag{7.14}$$

where $\Gamma_s(t) = 1 + \mathcal{E}_{0,s}t/\gamma_0$. The correlation $\Delta\gamma \propto -A_0^2$ (if $\mathcal{E}' < 0$) within a beam slice arises because, due to slippage, particles with a higher A_0 originally come from positions ahead of their current slice. Since $\mathcal{E}' < 0$, the accelerating fields they have experienced as they slip towards the back are smaller than at their current position, thus leading to a lower net energy gain. Equation (7.14) therefore shows that although a positive correlation $\Delta\gamma \propto A_0^2$ exists for particles *starting* at the same slice, as given by Equation (7.13), this correlation is actually negative when looking at particles which have *ended up* in the same slice due to slippage. The induced relative slice energy spread due to this effect can be found from the standard deviation of $\Delta\gamma/\bar{\gamma}_s$ if the mean slice energy is

assumed to evolve as $\bar{\gamma}_s(t) \simeq \bar{\gamma}_{0,s} + \mathcal{E}_{0,s}t$, from what it is found that

$$\frac{\sigma_{\gamma_s}^{\Delta\xi}}{\bar{\gamma}_s}(t) \simeq \frac{\mathcal{E}'\mathcal{K}\sigma_{A^2}}{2c\mathcal{E}_0^2}\frac{\left(\bar{\Gamma}_s(t)^{1/2}-1\right)^2}{\bar{\Gamma}_s(t)^{3/2}} \simeq \sqrt{\frac{2\mathcal{K}}{\bar{\gamma}_{0,s}}}\frac{\mathcal{E}'\mathcal{F}_m\epsilon_n}{\mathcal{E}_0^2}\frac{\left(\bar{\Gamma}_s(t)^{1/2}-1\right)^2}{\bar{\Gamma}_s(t)^{3/2}}\,, \tag{7.15}$$

where $\bar{\Gamma}_s = \bar{\gamma}_s/\bar{\gamma}_{0,s}$, σ_{A^2} is the standard deviation of A_0^2 for the particles within the slice and $\mathcal{E}_0$ is taken at the slice position. For an on-axis Gaussian bunch with zero average transverse momentum ($\bar{x} = \bar{y} = 0$ and $\bar{p}_x = \bar{p}_y = 0$), it can be obtained that $\sigma_{A^2} \simeq \sqrt{8c^2\mathcal{A}^2/\mathcal{K}\bar{\gamma}_{0,s}}$, where $\mathcal{A}^2 = \frac{1}{4}\sum_{i=x,y}\epsilon_{n,i}^2\left(\beta_i^4+\beta_m^4\right)/\beta_i^2\beta_m^2$. The variables $\epsilon_{n,i}$, $\beta_i = \sigma_i^2\bar{\gamma}_0/\epsilon_{n,i}$ and σ_i are, respectively, the beam's normalized emittance [Flo03], beta function and rms size in both transverse planes, while $\beta_m = c/\omega_0$, with $\omega_0 = \omega_{x,0} = \omega_{y,0}$, is the matched beta function [AY98] defined by the focusing fields within the plasma. For a cylindrically-symmetric bunch, i.e, if $\epsilon_{n,i} = \epsilon_n$ and $\beta_i = \beta$, a "mismatch factor" $\mathcal{F}_m = \left((M^4+1)/2M^2\right)^{1/2}$ can be defined, where $M = \beta/\beta_m$, such that $\mathcal{A} = \mathcal{F}_m\epsilon_n$, which leads to the last expression in Equation (7.15). For a matched beam ($M = 1$) the mismatch factor is $\mathcal{F}_m = 1$, which also corresponds to its minimum value. The impact of betatron slippage on the slice energy spread will therefore be stronger on mismatched beams. A detailed derivation of Equations (7.14) and (7.15) is included in Appendix A.2.

Analyzing Equation (7.15) it can be seen that the induced slice energy spread has a fast initial growth until it reaches a maximum when the bunch energy has increased exactly by a factor of 9, that is,

$$\max\left(\frac{\sigma_{\gamma_s}^{\Delta\xi}}{\bar{\gamma}_s}\right) \simeq \frac{4}{27}\frac{\mathcal{E}'\mathcal{K}\sigma_{A^2}}{2c\mathcal{E}_0^2} \simeq \frac{4}{27}\sqrt{\frac{2\mathcal{K}}{\bar{\gamma}_{0,s}}}\frac{\mathcal{E}'\mathcal{F}_m\epsilon_n}{\mathcal{E}_0^2}\,, \tag{7.16}$$

when

$$\Gamma_s = 9\,. \tag{7.17}$$

For higher energies, the slice energy spread slowly decreases proportional to $\bar{\Gamma}_s^{-1/2}$. This behaviour arises from $\sigma_{\gamma_s}^{\Delta\xi}$, whose growth rate is initially faster than $\bar{\gamma}_s$ but gradually slows down due to the reduced slippage at higher energies.

An effective way of mitigating the slippage-induced energy spread would be to beam-load the wake such that $\mathcal{E}' \to 0$, thus suppressing the energy spread growth as given by Equation 7.15. However, since this condition is difficult to achieve, especially along the whole bunch, other strategies can be derived from this equation. Regarding the accelerating structures, possible strategies include reducing plasma density, since the ratio $\mathcal{K}^{1/2}\mathcal{E}'/\mathcal{E}_0^2 \propto n_p^{1/2}$, or using hollow plasma channels [Chi+95], so that $\mathcal{K} \to 0$. In regard to the accelerated beam, minimizing the emittance, increasing the initial energy and fulfilling matching conditions ($\mathcal{F}_m = 1$) would be beneficial, with these two last points being especially relevant for externally-injected beams.

Minimizing this slice energy spread is especially important for PBAs based on chirp compensation schemes [Man+17; Bri+17; Fer+19]. This is because although the average

$\mathcal{E}'$ experienced by the beam after acceleration might be 0, its value at any point of the accelerator is not, thus giving rise to the development of a slice energy spread which will remain in the de-chirped beam. It is possible, however, that the alternation between positive and negative $\mathcal{E}'$ in these schemes might partially mitigate the correlation $\Delta\gamma \propto A_0^2$ from Equation (7.14) and thus the slice energy spread. As an additional remark, it should also be noted that this correlation between oscillation amplitude and energy caused by betatron slippage has been proposed as a way of performing beam conditioning for FELs [SWY92] by means of a magnetic chicane [PSW07]. Thus, it might also be beneficial in some cases.

7.3.2. Comparison with the effect of betatron radiation

The energy spread due to particle slippage will act in addition to that due to betatron radiation (BR) [Wan+02; Esa+02], which has also been shown to induce a correlation $\Delta\gamma \propto -A_0^2$ within a bunch slice and generate a slice energy spread given by [Mic+06]

$$\frac{\sigma_{\gamma_s}^{\mathrm{BR}}}{\bar{\gamma}_s} \simeq \frac{2r_e}{15c^3}\frac{\mathcal{K}^2\sigma_{A^2}\bar{\gamma}_{0,s}^2}{\mathcal{E}_0}\frac{(\bar{\Gamma}_s^{5/2}-1)}{\bar{\Gamma}_s}\,, \tag{7.18}$$

where $r_e = e^2/4\pi\epsilon_0 mc^2$ is the classical electron radius. A detailed explanation on how this formula has been obtained can be seen in Appendix A.3. As both effects are induced by the same underlying cause (the betatron motion of particles), it is of interest to compare and determine their relative relevance. This can be done by obtaining the intersection points of Equation (7.15) with the (7.18), for which perturbation theory is needed. Defining $C_{\mathrm{BR}} = (2r_e/15c^3)\mathcal{K}^2\sigma_{A^2}\bar{\gamma}_{0,s}^2/\mathcal{E}_0$ and $C_{\Delta\xi} = \mathcal{E}'\mathcal{K}\sigma_{A^2}/2c\mathcal{E}_0^2$, this method yields that the slippage-induced energy spread will initially dominate over betatron radiation if the ratio

$$\mathcal{R} = C_{\mathrm{BR}}/C_{\Delta\xi} \ll 0.1\,. \tag{7.19}$$

When this is the case, a transition into a BR-dominated regime occurs at an energy $\bar{\Gamma}_s = \bar{\Gamma}_t$ which, to first order, can be obtained as

$$\bar{\Gamma}_t \simeq \mathcal{R}^{-1/2}\,. \tag{7.20}$$

A detailed derivation of all these expressions can also be found in Appendix A.3.

An illustration of both regimes can be seen in Figure 7.2 for a particular set of parameters. As a general rule, although this will vary from case to case, the energy spread due to slippage will typically dominate over BR up to energies on the order of $\sim$10 GeV. This is the energy range in which FELs operate, implying that betatron slippage is the source of slice energy spread that should be minimized for these applications.

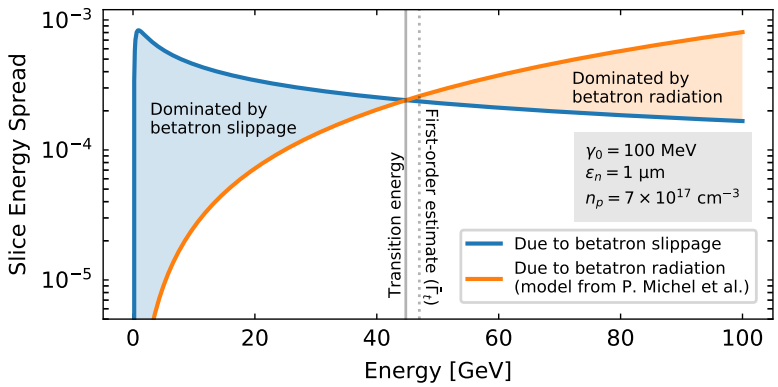

Figure 7.2.: Comparison of the slice energy spread due to slippage (from Equation (7.15)) and betatron radiation (from model by P. Michel *et al.* [Mic+06]) for the particular case of a 100 MeV bunch with 1 µm normalized emittance injected with matched beta function into a plasma with $n_p = 7 \times 10^{17}\,\mathrm{cm}^{-3}$ assuming a wakefield in the blowout regime ($\mathcal{E}' = -\omega_p^2/2c$, $\mathcal{E}_0 = \omega_p$, $\mathcal{K} = \omega_p^2/2$). Betatron slippage is found to be the dominant effect up to an energy of 44.8 GeV, which is accurately estimated by the ∼47 GeV value given by the first order approximation $\bar{\Gamma}_t \simeq \mathcal{R}^{-1/2}$. Image from [FMA19].

7.3.3. Bunch length and energy spread growth in ultra-short bunches

In addition to its impact on the slice energy spread, another immediate consequence of the betatron-induced slippage will be a growth of the bunch length. This is especially relevant for ultra-short bunches where the slippage experienced by the particles is comparable to or bigger than the initial bunch length $\sigma_{z,0}$. The contribution of the single-particle slippage to σ_z can be directly obtained from the standard deviation of Equation (7.11) by assuming an initially monoenergetic bunch with $\sigma_{z,0} = 0$. The bunch lengthening is then found to be

$$\sigma_{\Delta\xi}(t) \simeq \frac{\mathcal{K}\sigma_{A^2}}{2c\mathcal{E}_0}\left(1 - \bar{\Gamma}(t)^{-1/2}\right) \simeq \sqrt{\frac{2\mathcal{K}}{\bar{\gamma}_0}}\frac{\mathcal{F}_m\epsilon_n}{\mathcal{E}_0}\left(1 - \bar{\Gamma}(t)^{-1/2}\right), \tag{7.21}$$

where $\bar{\Gamma} = \bar{\gamma}/\bar{\gamma}_0 \simeq 1 + \mathcal{E}_0 t/\bar{\gamma}_0$. The last expression on the right is again obtained for the case of a cylindrically-symmetric Gaussian bunch. The bunch length evolution, when taking into account the impact of slippage, is thus given by $\sigma_z(t) = (\sigma_{z,0}^2 + \sigma_{\Delta\xi}^2(t))^{1/2}$ for initially Gaussian bunches. When this is the case, this expression therefore establishes a limitation on the minimum bunch length achievable in a PBA. This could have a strong impact on the production of high-energy, sub-femtosecond bunches, because although certain techniques to inject such ultra-short bunches into the plasma wake have been proposed [Li+13; Wei+16; Too+17; Mar+15], their sub-femtosecond duration could be lost when further accelerating them. Possible ways of mitigating this lengthening can be found by looking at Equation (7.21), which yields the same conditions on the beam emittance, matching and initial energy found for Equation (7.15). In this case, however,

no benefits from beam-loading or reduced plasma density are expected because $\mathcal{E}'$ does not play a role in the lengthening and the ratio $\mathcal{K}^{1/2}/\mathcal{E}_0$ does not depend on the plasma density. Another remark that can be extracted from Equation (7.21) is that, as expected from Equation (7.12), the lengthening has a finite upper limit when $\bar{\Gamma} \to \infty$ given by

$$\max\left(\sigma_{\Delta\xi}\right) \simeq \frac{\mathcal{K}\sigma_{A^2}}{2c\mathcal{E}_0} \simeq \sqrt{\frac{2\mathcal{K}}{\bar{\gamma}_0}}\frac{\mathcal{F}_m\epsilon_n}{\mathcal{E}_0}\,. \tag{7.22}$$

As a consequence of the bunch lengthening, in cases where $\mathcal{E}' \neq 0$, the correlated energy spread of the bunch will also increase. This explains previously observed limitations, where convergence to a finite energy spread was found as $\sigma_{z,0} \to 0$ [Gre+14]. This limit on the minimum energy spread as the initial bunch length is reduced can be calculated for an initially monoenergetic beam with $\sigma_{z,0} = 0$ from the standard deviation of Equation (7.13). This leads to

$$\left.\frac{\sigma_\gamma^{\Delta\xi}}{\bar{\gamma}}(t)\right|_{\sigma_{z,0}\to 0} \simeq \frac{\mathcal{E}'\mathcal{K}\sigma_{A^2}}{2c\mathcal{E}_0^2}\frac{\left(\bar{\Gamma}(t)^{1/2}-1\right)^2}{\bar{\Gamma}(t)} \simeq \sqrt{\frac{2\mathcal{K}}{\bar{\gamma}_0}}\frac{\mathcal{E}'\mathcal{F}_m\epsilon_n}{\mathcal{E}_0^2}\frac{\left(\bar{\Gamma}(t)^{1/2}-1\right)^2}{\bar{\Gamma}(t)}\,, \tag{7.23}$$

which, in the same way as Equation (7.21), also tends to a finite value as $\bar{\Gamma} \to \infty$. The last expression on the right corresponds again to the case of a cylindrically-symmetric Gaussian bunch.

An illustrative example of the phenomena described in this section can be seen in Figure 7.3, where an externally injected witness beam is shown at the entry and after 1 cm of plasma, as obtained from an OSIRIS 2D simulation. The induced lengthening as well as the development of a quadratic correlation between energy and oscillation amplitude can be clearly seen. As predicted by Equations (7.13) and (7.14), this correlation is positive for the overall bunch (Figure 7.3b) but negative at the slice level (Figure 7.3c).

7.4. Validation against 3D PIC simulations

In order to validate and illustrate the significance of the expressions for the slice energy spread and bunch lengthening, a series of 3D simulations with the PIC codes OSIRIS and HiPACE have been performed. The studied cases consisted on a beam-driven plasma stage providing a 1 GeV net energy gain to an externally injected witness beam, as it would be interesting for FEL applications or multi-staged acceleration. In the OSIRIS simulations, the impact of the slippage effects has been tested for different witness beam parameters and plasma densities, and in all cases beam loading effects could always be neglected due to the low peak current. On the contrary, the HiPACE simulations where performed to study the possible mitigating effects of beam loading for a fixed set of plasma and beam parameters, where only the total beam charge was varied. Although only beam-driven cases have been simulated, similar results should apply for a laser

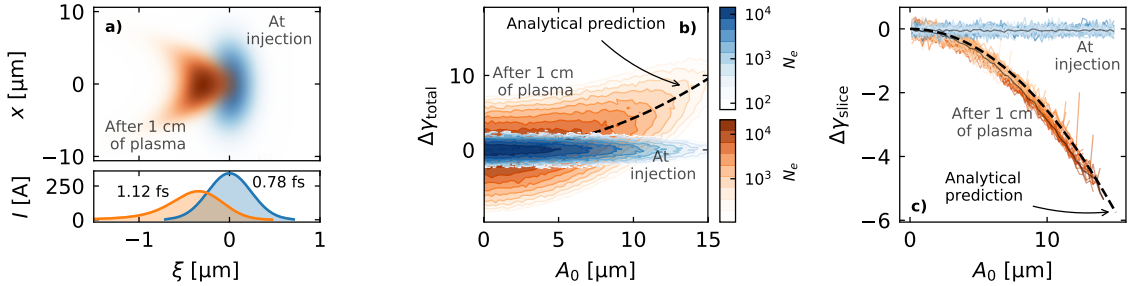

Figure 7.3.: Results from an illustrative 2D OSIRIS simulation of a 100 MeV, 0.7 pC and initially sub-femtosecond Gaussian electron bunch externally injected into the blowout of a laser driver in a plasma with $n_p = 10^{17}\,\mathrm{cm}^{-3}$. **(a)** Spatial distribution and current profile of the electron beam at injection and after 1 cm of propagation in the plasma. The development of a curved shape and increased length, as expected from the particle slippage, are clearly visible. **(b)** Beam energy distribution with respect to the initial oscillation amplitude of the particles. As expected from Equation (7.13), those with higher A_0 experience a higher energy gain. The analytical prediction of the energy-amplitude correlation as given by this equation is shown by a dashed black line. This curve was computed from the value of the fields in the simulation at the central position of the bunch, i.e., $\mathcal{E}_0 \simeq 0.60\,\omega_p$, $\mathcal{E}' \simeq -0.27\,\omega_p^2/c$ and $\mathcal{K} \simeq 0.36\,\omega_p^2$. The energy difference $\Delta\gamma_{\mathrm{total}}$ was calculated with respect to the average energy of the particles with $A_0 \simeq 0$ μm. **(c)** Distribution of the particle energy with respect to the initial oscillation amplitude within each beam slice. The coloured lines correspond to the distribution within each 20-nm-long slice, while the thin dark lines represent the average. As expected from Equation (7.14), the energy-amplitude correlation at the slice level is negative. The analytical prediction was again computed for the central beam slice using the same field values as before. The energy difference within the slice, $\Delta\gamma_{\mathrm{slice}}$, was calculated with respect to the average energy of the particles with $A_0 \simeq 0$ μm after removing the longitudinal energy correlation (chirp) along the beam. Image from [FMA19].

driver as long as dephasing effects in the mean beam energy can be neglected, as they are not included in Equations (7.15) to (7.23).

In all simulated cases, a Gaussian driver with an energy of 1 GeV and a 0.1% spread has been considered. Its dimensions and charge have been defined in terms of the plasma density so that the generated blowout can be scaled with n_p. For the baseline case in which $n_p = 7 \times 10^{17}\,\mathrm{cm}^{-3}$, as used in previous experiments [Lee+14], this means a transverse size $\sigma_x = \sigma_y = 0.4\,c/\omega_p \simeq 2.5\,\mu\mathrm{m}$, a length $\sigma_z = c/\omega_p \simeq 6.4\,\mu\mathrm{m}$, a normalized emittance $\epsilon_n = 0.4\,\sigma_x \simeq 1\,\mu\mathrm{m}$ and a peak electron density $n_b \simeq 3.78\,n_p$ for a total charge $Q \simeq 265$ pC and a peak current $I_p \simeq 5$ kA. The plasma target has a flat-top longitudinal profile and is transversely uniform.

For the studies made with OSIRIS, a Gaussian witness beam is injected on-axis at $\xi_w \simeq \xi_d - 4.5\,c/\omega_p$, where ξ_d is the driver centre. Different emittance values ($\epsilon_n = 0.1\,\mu\mathrm{m}$, $1\,\mu\mathrm{m}$ and $10\,\mu\mathrm{m}$) as well as injection energies between 10 MeV and 1 GeV have been tested. The transverse size is matched to the focusing fields so that $\mathcal{F}_m = 1$. With regard to the bunch charge and duration, two different sets of parameters have been considered: $\sigma_z/c = 3$ fs with 1 pC for the studies on the slice energy spread, as it could be obtained in the SINBAD facility at DESY [Ass+14; Zhu+16], while a shorter bunch with $\sigma_z/c = 0.1$ fs with 0.1 pC was used for the bunch lengthening studies. This shorter bunch duration was chosen to better highlight the impact of lengthening due to slippage on sub-femtosecond bunches. The peak current in both cases is too low to significantly modify $\mathcal{E}'$ along the bunch, therefore allowing beam loading effects to be neglected. The slice energy spread in all tested beams is dominated by slippage, because $\mathcal{R} \ll 0.1$ and $\bar{\Gamma} \ll \mathcal{R}^{-1/2}$. Also, in order to isolate the plasma stage as the only source of energy spread, a zero longitudinal momentum spread at injection has been considered.

In order to compare the simulation results with the analytical theory, the field values in Equations (7.15) and (7.21) need to be provided. While these could be estimated from analytical models [Lu+06b; Yi+13], they were measured directly at ξ_w from a single simulation with no witness beam, obtaining $\mathcal{E}_0 \simeq 0.53\,\omega_p$, $\mathcal{E}' \simeq -0.37\,\omega_p^2/c$ and $\mathcal{K} \simeq 0.5\,\omega_p^2$. This allows for a more accurate validation of the model. A view of the plasma wakefields in one of the OSIRIS simulations is shown in Figure 7.4. As assumed by the analytical model, a constant $\mathcal{K}$ within the blowout and a transversely homogeneous $\mathcal{E}$ with uniform $\mathcal{E}'$ along the witness bunch can be seen.

The final simulation results, displayed in Figure 7.5, show a strong dependence of the generated slice energy spread on the plasma density and initial beam parameters, reaching values in excess of 10^{-2} (or 1%) for certain configurations, way above typical FEL requirements. Similarly, the increase in bunch length can be on the femtosecond level for typical emittance and energy values, showcasing the difficulty of achieving GeV-class, sub-femtosecond bunches. No variation of the bunch length with the plasma density is observed, as expected from Equation (7.21). The analytical model shows excellent agreement with the simulations over several orders of magnitude, with expected discrepancies

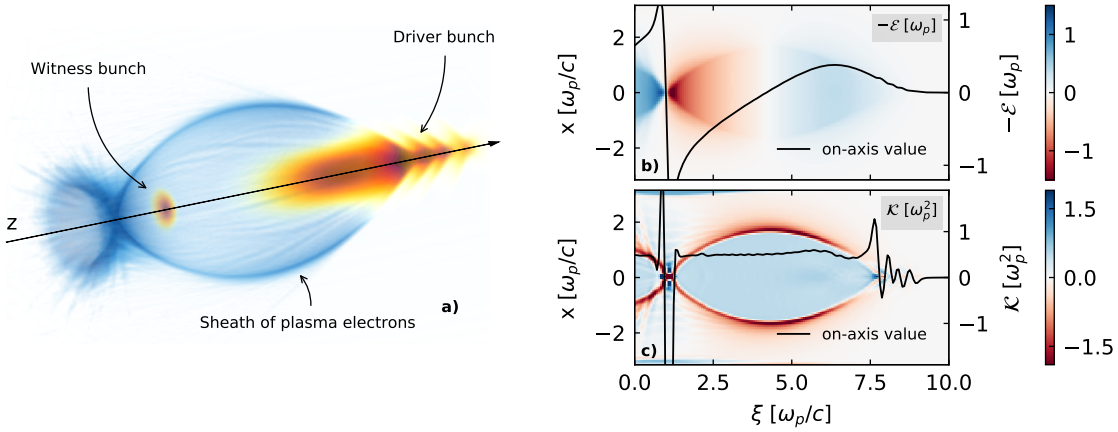

Figure 7.4.: **(a)** 3D visualization made with VisualPIC one of the OSIRIS simulations. The case shown is that of a witness beam with $\epsilon_n = 10\,\mu\text{m}$ and $n_p = 10^{17}\,\text{cm}^{-3}$, taken at a time $t \simeq 816/\omega_p$. **(b)** and **(c)** show the longitudinal field $\mathcal{E}$ and focusing gradient $\mathcal{K}$ of the same simulated case along the central slice ($y = 0$) and on axis (black line). Image from [FMA19].

in some of the higher emittance cases. The differences in Figure 7.5(b) arise from the large slippage experienced by particles with higher oscillation amplitude, which causes the transverse distribution of many beam slices to be a truncated Gaussian and thus leads to a smaller energy spread than predicted. The discrepancies in Figures 7.5(c) and (d) arise from the longitudinal energy correlation, neglected by Equation (7.21), which induces a slight longitudinal bunch compression due to velocity differences between head and tail. In addition to the final slice energy spread and bunch length values, the analytical model also accurately predicts the evolution of these parameters during propagation within the PBA, as shown in Figure 7.6. The discrepancies in the energy spread evolution in Figure 7.6(a) arise from the initial dephasing between the bunch and plasma wakefield due to the low initial energy (10 MeV), which leads to an experienced accelerating field $\mathcal{E} > \mathcal{E}_0$ and, thus, a lower energy spread than predicted by Equation (7.15). Furthermore, the initial oscillations on the slice energy spread at the beginning of the simulation correspond to the betatron oscillations of the witness beam, which lead to an oscillation in v_z, as seen previously in Figure 7.1(b). When v_z is minimum (maximum), more slippage occurs and the energy spread growth is faster (slower). This also leads to small oscillations on the bunch length, as seen in Figure 7.6(b). The impact of the v_z oscillations on the particle slippage had to be neglected in the theoretical model in order to obtain the analytical expression in Equation 7.11. Thus, this effect is not reproduced by the analytical curves shown in Figure 7.6.

In order to explore the potential of beam loading for mitigating the generated slice energy spread, an additional set of simulations was performed with HiPACE. The same driver parameters as in the OSIRIS simulations and a plasma density of $7 \times 10^{17}\,\text{cm}^{-3}$ were used. The witness beam parameters were fixed to an initial energy of 100 MeV, $\epsilon_n = 1\,\mu\text{m}$ and $\sigma_z/c = 3$ fs, while its total charge was varied from 1 to 100 pC. The final

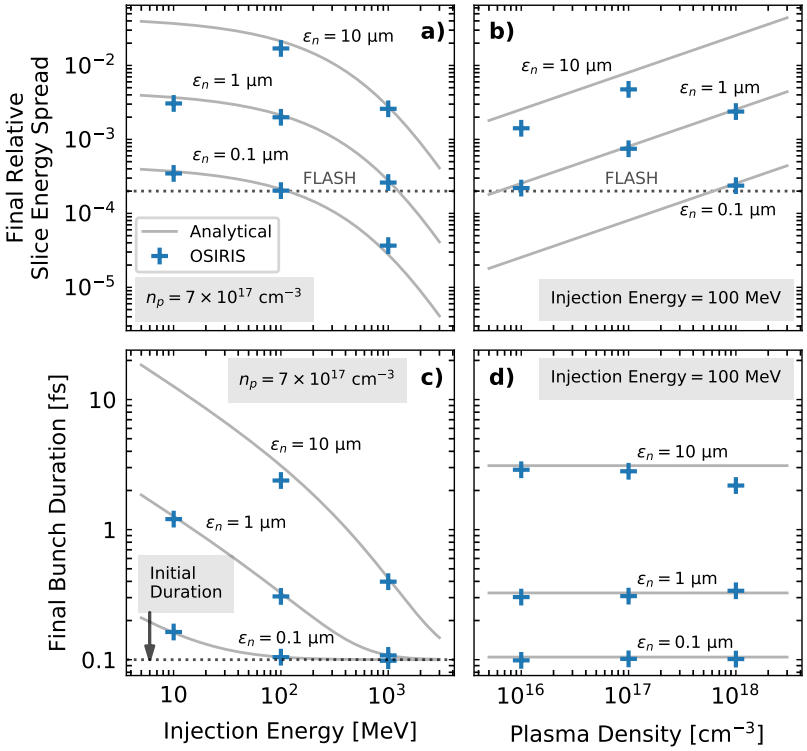

Figure 7.5.: Comparison between simulation results and the analytical curves from Equations (7.15) and (7.21) for a 1 GeV plasma stage, corresponding to an acceleration length of $\sim 3240\omega_p/c$ in all cases. The influence of injection energy, **(a)** and **(c)**, and plasma density, **(b)** and **(d)**, on the generated slice energy spread and bunch lengthening is displayed. The energy spread of the FLASH FEL at DESY ($\sim 2 \times 10^{-4}$) [SF15] is shown for reference. Only results from simulations with no significant numerical noise and in which the witness beam was sufficiently narrow to fit within the wake have been included. Image from [FMA19].

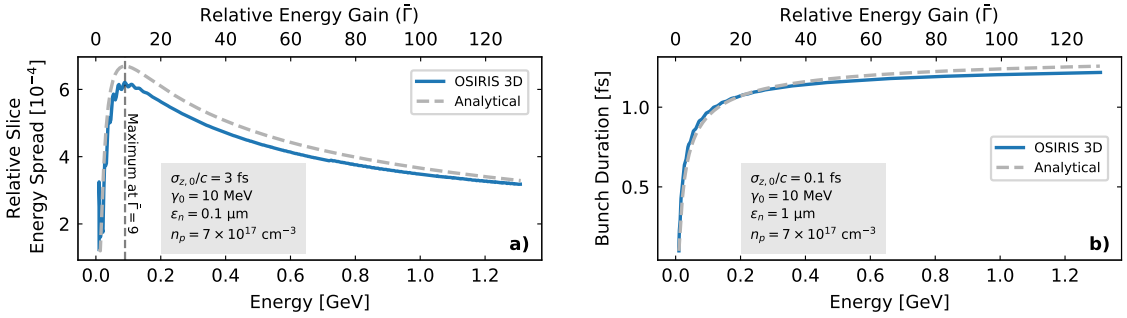

Figure 7.6.: Evolution of the relative slice energy spread **(a)** and bunch duration **(b)** on two of the simulated cases. Excellent agreement between analytical model and simulations is shown, including the predicted energy spread maximum at $\bar{\Gamma} = 9$. Image from [FMA19].

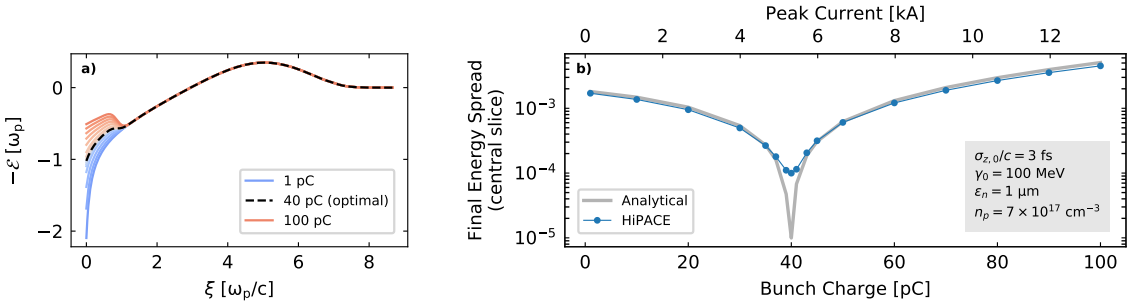

Figure 7.7.: **(a)** Effect of beam loading on the on-axis longitudinal electric field in all simulated cases for different total bunch charge. The ideal case which minimizes $\mathcal{E}'$ is shown in black, while those in which $\mathcal{E}' < 0$ are shown in blue tones and those in which beam loading inverts the slope ($\mathcal{E}' > 0$) are displayed in red. The fields are shown at $t = 500/\omega_p$. **(b)** Final central slice energy spread of the bunch with respect to its total charge as obtained from the HiPACE simulations. The value of the energy spread is calculated after a 1 GeV energy gain in the plasma. The effect of beam loading is clear, providing a minimum energy spread for a charge of 40 pC, which corresponds to a peak current of $\sim$ 5.3 kA. Image from [FMA19].

energy spread of the central bunch slice after a 1 GeV energy gain is shown in Figure 7.7 for the different bunch charges. Only the central slice energy spread is displayed in this case because the effect of beam loading on $\mathcal{E}$ varies along the bunch. The analytical points were calculated from the average value during acceleration of the fields at the center of the bunch.

The results show again good agreement between theory and simulations, and that beam loading can significantly reduce the development of slice energy spread (up to a factor of $\sim$ 20 in this case). For the particular set of parameters under consideration, the energy spread minimum is achieved for a total bunch charge of 40 pC (corresponding to a peak current of $\sim$ 5.3 kA) and grows again for higher charges because beam loading overcompensates $\mathcal{E}'$, which becomes positive. Peak currents in this range of parameters have been experimentally demonstrated [Lun+11; Cou+17] and, if optimized, could therefore provide an effective way of mitigating the slice energy spread growth. Discrepancies between the analytical curve and the simulations appear, however, around the energy spread minimum. This is because, in theory, the slice energy spread due to slippage could be completely suppressed for an ideally beam-loaded case in which $\mathcal{E}' = 0$ along the whole bunch. This, however, requires an optimized trapezoidal current profile [Tzo+08] , while the bunch in the simulated case is Gaussian and therefore does not experience a uniform $\mathcal{E}'$. Thus, even if $\mathcal{E}' = 0$ at the center, a certain energy spread will develop in the central slice due to the slippage of particles originally coming from slices ahead, where $\mathcal{E}' \neq 0$. In addition, other effects apart from particle slippage can lead to increased slice energy spread in beam-loaded cases, such as transverse variations of the accelerating fields in the linear and weakly non-linear regimes [LNM18].

7.5. Conclusion

In this chapter, new insights into the dynamics of betatron motion and its impact on beam parameters such as the energy spread and bunch length have been presented. To study this effect, a novel single-particle analytical model has been developed which, for the first time, describes the longitudinal slippage arising from the coupling of longitudinal and transverse dynamics as well as its subsequent impact on the particle energy when the accelerating fields vary longitudinally. From this single-particle model, analytical expressions for the impact of betatron slippage on the energy spread and bunch length have been derived and validated against 2D and 3D particle-in-cell simulations.

The performed simulations show that the effects of particle slippage can be very significant, inducing a slice energy spread of up to $\sim$1 % and a bunch lengthening on the femtosecond range. The slice energy spread growth could have strong implications for FEL applications, as a value $\lesssim 0.1\,\%$ is generally required. On the other side, the bunch lengthening is particularly relevant for the production of ultra-short bunches on the sub-femtosecond range, as proposed by certain schemes [Li+13; Wei+16; Too+17] , because it implies that this ultra-short duration could be lost when accelerating the bunches.

Fortunately, having an analytical theory that can accurately describe these phenomena also allows certain strategies for mitigating these issues to be defined. In particular, both theory and simulations show that beam loading would be an effective method for preventing the slice energy spread growth due to slippage. Similarly, the use of hollow plasma channels, such that the focusing fields vanish, would also suppress this issue. In case that these two options are not feasible, other mitigating strategies include reducing the plasma density and, regarding the beam parameters, reducing the emittance, increasing the initial energy and properly matching the beam to the plasma focusing fields. The conditions on the beam parameters are especially relevant for external injection. As an example, the simulations show that obtaining an energy spread $< 10^{-3}$, as typically needed for FELs, would require a plasma density $\lesssim 10^{17}\,\mathrm{cm}^{-3}$, a normalized emittance $\lesssim 1\,\mu\mathrm{m}$ as well as an initial energy $\gtrsim 100$ MeV.

In addition to these considerations, the relevance of the slippage effects on the slice energy spread has been compared with the impact of betatron radiation, which has also been shown to be detrimental to the energy spread [Mic+06]. The presented study shows that particle slippage will generally be the dominant contribution to the slice energy spread up to energies above tens of GeV and is therefore the effect that should be minimized for FELs, as they typically operate in the few-GeV range. Betatron radiation would, however, become the dominating contribution in high-energy ($\gtrsim 10\,\mathrm{GeV}$) accelerators such as particle colliders.

8. A multistage plasma-acceleration concept for ultra-low energy spread beams

Associated publication

A. Ferran Pousa, A. Martinez de la Ossa, R. Brinkmann and R. W. Assmann. "Compact Multistage Plasma-Based Accelerator Design for Correlated Energy Spread Compensation". In: *Phys. Rev. Lett.* 123 (5 July 2019), p. 054801. DOI: 10.1103/PhysRevLett.123.054801

8.1. Introduction

Since the first experimental demonstration of so-called quasi-monoenergetic beams (1 % to 10 % energy spread) from a plasma accelerator [Man+04; Ged+04; Fau+04], steady progress in the field has led to the successful demonstration of electron bunches with multi-GeV energy [Lee+06; Wan+13; Lee+14; Mir+15; Gon+19], micron-level emittance [Fri+04; Bru+10] and kiloampere current [Lun+11; Cou+17]. However, despite these major advances, reliably achieving an energy spread below the 1 %-range has remained an issue and is one of the critical challenges currently limiting the usability of these devices.

A typical cause of this high energy spread is the short wavelength ($\sim$100 µm) and high amplitude ($\sim$10 GV m^{-1}) of the accelerating fields in the plasma, which, combined, naturally imprint a longitudinal energy correlation (or chirp) along the accelerated bunch. This large energy spread, apart from being detrimental to the beam quality in itself, can also lead to a large emittance growth after the plasma stage due to the large divergence of the beams, as explained in Section 3.6.2.

Achieving a small emittance and energy spread is however essential for demonstrating the usability of PBAs. This is particularly relevant for applications such as FELs [Grü+07; Fuc+09; HDS12; Lou+15] where an energy spread below 0.1 % is typically required [Cor+13]. As such, several solutions have been proposed in order to solve or mitigate this issue. A well known concept for reducing (or even suppressing) the correlated energy spread is that of beam loading, in which, as seen in Section 3.4.6, the witness bunch itself is used to flatten the slope of the accelerating fields. This, however, relies on a very precise shaping of the current profile of the witness and has yet to be demonstrated with the desired performance. Furthermore, since the optimal profile depends on the wakefield structure, a certain energy spread will always develop in LWFAs, where the wakefields experienced by the bunch change in time due to the laser evolution [Kal+11;

ESL09] as well as dephasing [Sch+11]. Alternative ideas have also been proposed in order to achieve, in average, a flat accelerating gradient. These include modulating [Bri+17] or tailoring [Döp+18] the plasma density profile as well as injecting a secondary bunch [Man+17], but they show limited success or remain to be experimentally realized. Other dechirping techniques based on beam-induced wakefields have been proposed [Wu+19b] and even demonstrated experimentally [BS12; Ant+14; DAr+19; Shp+19; Wu+19a], although not for the extreme chirps imprinted by PBAs. In addition to these concepts for energy spread reduction, a different approach proposes instead a way of circumventing this issue by decompressing the bunches after acceleration [Mai+12]. In this way, the slice energy spread can be reduced to fulfill FEL requirements, although the total energy spread of the bunch still remains unchanged.

In this chapter, a novel concept for compensating for the correlated energy spread in PBAs and achieving a low energy spread (both slice and total) is presented. This concept, illustrated in Figure 8.1, takes advantage of the naturally occurring energy chirp in PBAs by performing the acceleration process in two identical plasma stages which are then joined by a magnetic chicane. In this way, the energy chirp generated in the first plasma stage can be inverted in the chicane and, thus, be fully compensated for in the second. As a result, a higher energy beam with low energy spread can be finally obtained.

A more detailed explanation of the working principle behind this method is given in Section 8.2. Afterwards, in Section 8.3, the results of start-to-end simulations of a first proof-of-principle implementation are presented. These show that 5 GeV beams with an energy spread on the range of $\sim$0.1 % (total) and $\sim$0.01 % (slice) could be produced with this scheme. Thanks to these positive results, a conceptual design for a 6 GeV EuPRAXIA accelerator based on this multistage scheme has also been realized and simulated. This design, which was finally chosen as a baseline option for EuPRAXIA, is presented in Section 8.4. In addition to these two high-energy cases, another conceptual design for a 1 GeV beamline which could be realized with more commonly available laser systems is later presented in Section 8.5. All these beamline simulations, which have been performed in ideal conditions, are then complemented with a detailed study of sensitivity and tolerances in Section 8.6. Finally, since all the studied cases have been carried out with externally-injected beams, a general discussion about a possible implementation and advantages of this scheme for LWFAs with internal injection is included in Section 8.7.

8.2. Working principle

In order to introduce the working principle of this concept, the blowout regime of plasma acceleration will be considered. In this case, as explained in Section 3.4.4, the laser or beam driver is able to expel all background plasma electrons, leaving behind an ion cavity with a uniform focusing gradient, $K = (m/2ec)\omega_p^2$, and an approximately constant

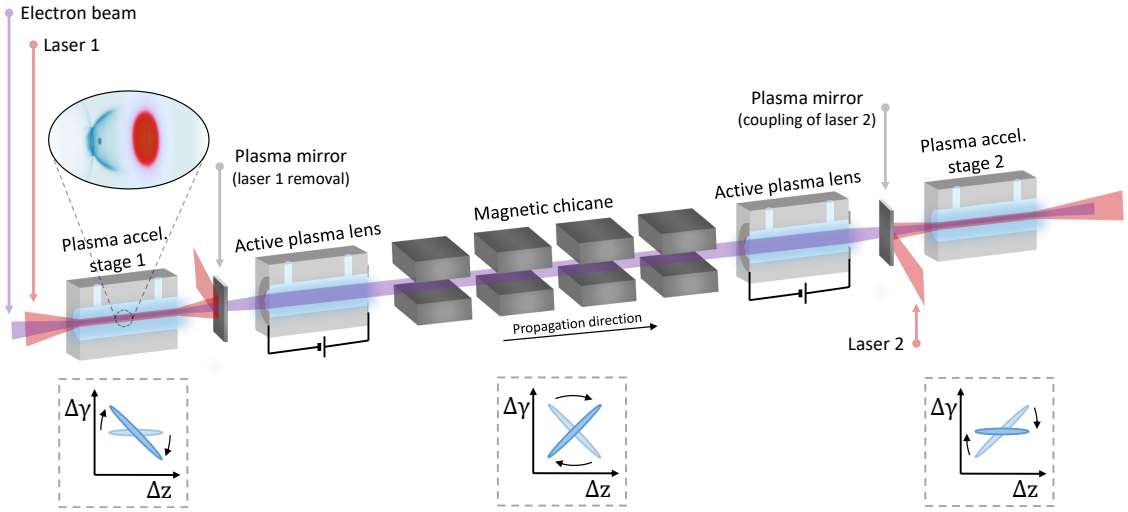

Figure 8.1.: Schematic view of a possible implementation of the energy chirp compensation concept. An externally-injected beam is accelerated in a first LWFA, where it acquires a strong negative chirp. The beam is then captured by an active plasma lens and transported through a chicane, where its energy chirp is inverted. By injecting it again in a second LWFA, the beam is further accelerated while the initial energy chirp is compensated for. Image adapted from [Fer+19].

longitudinal electric field slope, $E_z' \equiv \partial_z E_z \simeq (m/2e)\omega_p^2$, along most of the accelerating phase. Within this cavity, electrons perform transverse oscillations (betatron motion) with a frequency $\omega_\beta(t) = \sqrt{eK/m\gamma(t)}$, while their energy evolves as $\gamma(t) = \gamma_0 - (e/mc)E_z t$.

For a particle bunch with average energy $\bar{\gamma}(t) = \langle\gamma(t)\rangle$ centered at a longitudinal position $\bar{\xi}$ in the plasma wake, the longitudinal energy chirp can be generally expressed at any time as $\chi(t) = \langle\Delta\xi\Delta\gamma(t)\rangle \,/\, \langle\Delta\xi^2\rangle\, \bar{\gamma}(t)$, where $\Delta\gamma(t) = \gamma(t) - \bar{\gamma}(t)$ and $\Delta\xi = \xi - \bar{\xi}$. A simple expression for the chirp evolution within a plasma stage can then be obtained if a constant E_z' is assumed. This yields

$$\chi(t) = \left(\chi_0\bar{\gamma}_0 - \frac{e}{mc}E_z' t\right)\bar{\gamma}(t)^{-1}\,, \tag{8.1}$$

which tends asymptotically to $\chi = E_z'/E_z$ and where χ_0 and $\bar{\gamma}_0$ are the initial bunch chirp and energy at the beginning of the plasma. If the bunch length is $\sigma_z = \sqrt{\langle\Delta\xi^2\rangle}$, the correlated energy spread induced by this chirp can be simply written as $\sigma_\gamma^{\mathrm{corr}}(t)/\bar{\gamma}(t) = \chi(t)\sigma_z$. In a two-stage accelerator as in Figure 8.1, the accumulated chirp after a first plasma stage of length $L_{p,1}$ for an initially unchirped bunch ($\chi_0 = 0$) is given by $\chi_1 = -(e/mc^2)E_{z,1}'L_{p,1}/\bar{\gamma}_1$. Therefore, if the longitudinal phase space of the bunch is inverted at this point in order to obtain a chirp $\chi_{1,\mathrm{inv}} = -(\sigma_{z,1}/\sigma_{z,2})\chi_1$, the correlated energy spread could be compensated for in a second plasma stage if the field slope $E_{z,2}'$ and

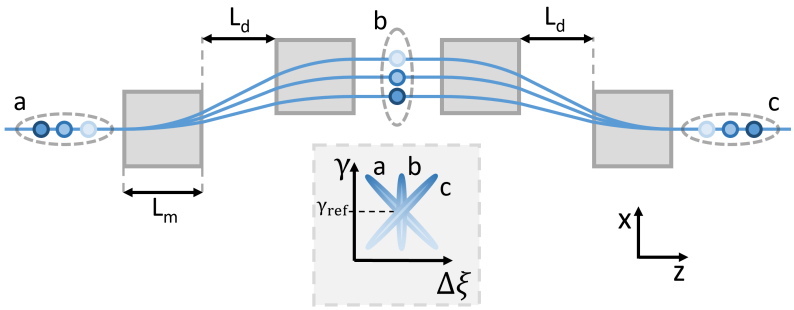

Figure 8.2.: Working principle of a magnetic chicane with $R_{56} = -2/\chi_1$. The bunch longitudinal phase space is shown at the chicane entrance (a), middle (b) and exit (c). Darker color implies higher energy. Image from [Fer+19].

length $L_{p,2}$ fulfill the condition

$$E'_{z,2} L_{p,2} = \frac{mc^2}{e} \chi_{1,\mathrm{inv}} \bar{\gamma}_1 = \frac{\sigma_{z,1}}{\sigma_{z,2}} E'_{z,1} L_{p,1} \,. \tag{8.2}$$

Thus, if the chirp inversion is symmetric, i.e, if $\sigma_{z,1} = \sigma_{z,2}$, using two identical plasma stages ($E_{z,2} = E_{z,1}$ and $L_{p,2} = L_{p,1}$) would be the simplest setup. Other combinations of accelerating stages with different densities and length could, however, also be possible.

Performing such a longitudinal phase-space inversion could be achieved, as seen in Section 3.2.2, with a conventional magnetic chicane operating with an $R_{56} < -1/\chi_1$. In particular, for a symmetric chirp inversion, an $R_{56} = -2/\chi_1$ is required. A representation of the effect of such a chicane on the longitudinal phase-space of a chirped bunch can be seen in Figure 8.2.

This technique is therefore ideally suited for bunches dominated by a linear chirp, as is often the case in PBAs, and thus particularly for the case of weakly beam-loaded wakefields, where a constant E'_z is not perturbed by the bunch, or where the beam-loading effect linearly modifies E_z [Tzo+08]. When this is not the case, the scheme can still be optimized to correct the chirp along the bunch core. The performance of this concept will also be better when the higher-order dispersion in the chicane, i.e. the terms with T_{566} and above in Equation (3.39), can be neglected, since these non-linear contributions cannot be compensated for in the second plasma stage. As a result, the energy spread of the bunch in the chicane should in principle not exceed the few-percent range, although this condition could be relaxed by including sextupole magnets to minimize the second-order dispersion [Eng+05].

Once the chicane R_{56} is determined, the magnet length L_m and bending angle θ experienced by the reference particle can be directly determined from $R_{56} = -2\theta^2(L_d + 2L_m/3)$ [Cha+13], where L_d, as defined in Figure 8.2, is the length of the drift space between the first and second as well as the third and fourth dipoles. The magnetic field strength can then be obtained as $B = (mc/e)\theta\gamma_{\mathrm{ref}}/L_m$, where γ_{ref} is the reference energy in the chicane. As an example, assuming a bunch with $\chi = E'_z/E_z$ and typical blowout fields, it

can be obtained that $R_{56} \simeq -4c/\omega_p$, which results in an $R_{56} \ll 1\,\mathrm{mm}$ for $n_p \gtrsim 10^{16}\,\mathrm{cm}^{-3}$. Thus, considering $L_m \sim L_d \sim 0.1\,\mathrm{m}$, the small R_{56} leads to $\theta \ll 0.1\,\mathrm{rad}$. The characteristically high chirp of PBAs therefore allows for a very compact chicane design ($\sim$1 m) while requiring a very small bending angle. This greatly minimizes the impact of CSR on the beam parameters, which could otherwise be a critical issue for this concept.

A possible layout of how this scheme could be implemented is shown in Figure 8.1, where an externally-injected electron beam is accelerated by two LWFA stages joined by a magnetic chicane. A combination of active plasma lenses (APLs) [Til+15] and plasma mirrors [Tha+07] is considered there for the electron beam transport and laser pulse coupling, respectively, although other configurations are also possible. The drivers for each LWFA stage should ideally be perfectly synchronized. Thus, as in Chapter 6, they could originate from splitting a single initial laser pulse.

In addition to offering an improvement on the energy spread, this multistage scheme could also mitigate other critical issues such as the sensitivity to timing jitter between laser driver and witness bunch, as explored in Chapter 6, or the development of the hosing instability [Whi+91]. The sensitivity to timing jitter could be reduced because, thanks to the chicane in this scheme, a temporal injection offset with respect to the ideal phase in the first LWFA would translate, to first order in Equation (3.39), into the opposite offset at the entrance of the second LWFA. Thus, in average, a stable average accelerating field and energy output would be obtained. This potential improvement is explored later in Section 8.6.1 taking also into account second-order effects. Regarding the hosing instability in the witness bunch, it has been shown that performing the acceleration with a large energy chirp, as it occurs in this scheme, can greatly mitigate it or prevent its onset [Leh+17; Meh+17].

8.3. Proof-of-principle simulations for a 5 GeV accelerator

In order to test the performance of this scheme, a first proof-of-principle beamline based on the layout shown in Figure 8.1 has been designed and studied with detailed start-to-end simulations. The LWFA stages and APLs have been simulated using FBPIC, while the tracking code ASTRA has been used for the remaining beamline elements taking into account 3D space-charge fields. In addition, the magnetic chicane has also been simulated with CSRtrack in order to correctly account for any possible CSR effects.

8.3.1. Beamline design

This first beamline heavily relies on the use of APLs for the beam transport. These consist on circular, gas-filled capillaries with typically $\lesssim$1 mm radius on which a multi-kV discharge is applied by electrodes at both ends, causing a breakdown of the gas. A current is then driven through the ionized plasma, generating radially symmetric focusing fields with up to kilotesla-per-meter gradients [Til+15]. Although these devices have been ob-

served to suffer from aberrations [Til+15; Pom+17; Til+18], a solution to this issue has recently been demonstrated [Lin+18]. Thanks to the strong and linear focusing fields, APLs are ideal for transporting the highly divergent and high-energy-spread bunches coming out of the first LWFA, as they can be placed sufficiently close to it and thus mitigate the emittance growth in the drift [Mig+13]. Futhermore, they show significantly reduced chromaticity with respect to other focusing systems [Til+15]. In practice, APLs could be combined with magnetic quadrupoles to achieve independent control of the focusing in the x and y planes.

Apart from the APLs, the use of plasma mirrors for the laser coupling would also allow for particularly compact setups. This is because conventional mirrors would require a separation of several metres from the plasma stages in order to avoid damage from the laser (see later in Section 8.5). On the contrary, plasma mirrors, such as those based on tape drives, can be placed right next to LWFA stages and be renovated from shot-to-shot. These type of mirrors have in fact already been successfully used for the experimental demonstration of the coupling of two successive LWFAs [Ste+16]. However, they can also have a negative impact on the beam quality and lead to emittance growth. This can occur due to multiple scattering with the tape material [Rei91] as well as due to Weibel-like instabilities induced by the incident laser [Raj+20]. A promising alternative are liquid crystal films [Poo+16], which, due to their nanometer-level thickness, are expected to have negligible impact on the multi-GeV beams considered. Conventional mirrors with a hole for the electron beam could also be used, albeit of course at a cost in compactness, and mirror-less alternatives have also been proposed, such as the use of curved plasma channels [Luo+18]. No specific laser coupling implementation has been considered in this first simulation study.

Motivated by the parameters from the EuPRAXIA design study [Wal+17], the simulated setup aims at providing 5 GeV electron beams suitable for FEL applications, i.e., a peak current in the kA range, sub-micron emittance and, specially, an energy spread $\lesssim$0.1 %. For this purpose, an externally injected Gaussian electron bunch with an initial energy of 250 MeV, a 0.5 % energy spread with no chirp, a normalized transverse emittance $\epsilon_{n,x} = 0.5\,\mu\text{m}$, 10 pC of charge, a duration $\tau_{\text{FWHM}} = 5\,\text{fs}$ and a peak current $I_{\text{peak}} \simeq 2\,\text{kA}$ has been considered. The bunch transverse size, σ_x, is matched to the plasma focusing fields in order to prevent emittance growth. This therefore requires the beam beta function to satisfy $\beta_x = c/\omega_\beta$ at the LWFA entrance. Electron beams within this range of parameters can be produced with conventional accelerators [Zhu+18; Mar+18; Zhu+16], and diagnostic devices for these ultra-short bunches are under active development [Cra+18; Mar+19b; Mar19].

The two identical LWFAs have a length $L_p = 8\,\text{cm}$ and a parabolic transverse density profile for laser pulse guiding $n_p = n_{p,0} + r^2/\pi r_e w_0^4$, as given by Equation 3.105, where $n_{p,0} = 10^{17}\,\text{cm}^{-3}$ is the on-axis plasma density. Plasma cells in this range of parameters, able to provide guiding for lasers with a w_0 between 30 µm and 60 µm, have been recently

demonstrated [Sha+18; Sha+19]. For simplicity, a longitudinal flat-top plasma density profile has been considered in this first study. However, the presence of smooth plasma-to-vacuum transitions (plasma ramps) would be beneficial for electron beam matching [Flo14b] and emittance growth minimization [DFM15].

This choice of electron beam and plasma parameters was motivated from the lessons learned in Chapter 7 for mitigating the relative energy spread generated due to betatron motion. Having an emittance under 1 µm and a plasma density of $10^{17}\,\mathrm{cm}^{-3}$ allowed this source of slice energy spread to be kept below the 10^{-4} range, which is the target performance of this beamline.

Each LWFA stage is driven by a 40 J, 0.75 PW laser pulse with a peak normalized vector potential $a_0 = 3$, a spot size $w_0 = 50\,\mu\mathrm{m}$ and a FWHM duration $\tau_{\mathrm{FWHM},l} = 50\,\mathrm{fs}$. This laser can be successfully guided throughout the LWFAs, which provide an energy gain of ∼2.6 GeV each. The APLs are placed 3 cm away from the LWFAs and provide a focusing gradient of $3\,\mathrm{kT\,m}^{-1}$, as demonstrated experimentally [Til+15]. They have a length of 6.6 cm, which is optimized to achieve a beam waist at the chicane center. The plasma density in these APLs was chosen to be $n_p^{\mathrm{APL}} = 10^{15}\,\mathrm{cm}^{-3}$ in order to minimize the impact of beam-driven wakefields [LA18]. The chicane has a total length of 1.2 m, with $L_d = 12.5\,\mathrm{cm}$ and dipoles with $L_m = 20\,\mathrm{cm}$ and $B = 0.54\,\mathrm{T}$ for a bending angle of $\theta = 0.011\,\mathrm{rad}$.

8.3.2. Start-to-end simulations

An overview of the results from the simulations of this beamline can be seen in Figure 8.3. The electron bunch leaves the first LWFA with preserved emittance, an energy of ∼2.9 GeV and a chirp $\chi \simeq -0.031\,\mu\mathrm{m}^{-1}$ (equivalent to $\sim 90\,\mathrm{MeV\,\mu m}^{-1}$ in absolute units), which induces a total relative energy spread of ∼2 %. As a consequence, the projected emittance grows after the accelerating stage until the beam divergence is controlled by the APL. Along this lens, the maximum beam size is $\sigma_r \simeq 15\,\mu\mathrm{m}$, much smaller than that of typical capillaries. Both ASTRA and CSRtrack simulations show that the influence of space-charge and CSR on the beam parameters is negligible thanks to its GeV energy and the small bending angle. For more details about this, a thorough overview of these simulations and of the space-charge and CSR effects in the chicane is included in Appendix B.1. After the chicane, the beam is focused by the following APL and injected into the second LWFA. In this stage, the beam energy is further increased up to a final value of ∼5.5 GeV while, at the same time, the energy chirp acquired in the first stage is compensated for.

As seen in Figure 8.4, the total energy spread after the second LWFA has been reduced by a factor of ∼20 down to 0.12 % with respect to a case with no chirp compensation, i.e., with respect to a case with acceleration in only a single plasma stage. This corresponds to a dechirping strength of 1.1 GeV/µm/m in the second stage, orders of magnitude higher than that achieved with other schemes [BS12; Ant+14; DAr+19; Shp+19; Wu+19a]. The slice energy spread has also been reduced to just 2.8×10^{-4} (0.028 %), when considering

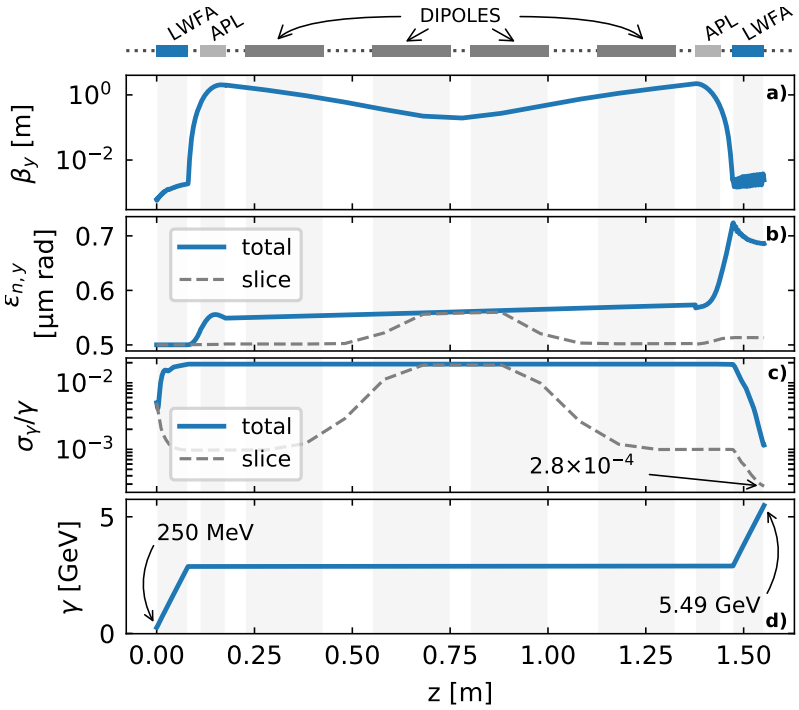

Figure 8.3.: Evolution of beam parameters along the accelerator: (a) beta function, (b) normalized emittance, (c) energy spread, and (d) energy. Transverse parameters are shown for the y plane, which is not affected by dispersion in the chicane. Final values in x and y planes are virtually identical (difference of $\ll 1\%$). Slice parameters grow in the chicane center due to shorter bunch duration because the slice length (0.1 µm) is kept constant. Image from [Fer+19].

0.1 µm-long slices. These values are at least one order of magnitude below state-of-art LWFAs and would satisfy the requirements of X-ray FELs [Cor+13]. The discrepancy between the total and slice energy spread arises mostly from the second order dispersion in the chicane, which induces the slight parabolic bunch shape seen in Figure 8.5.

The emittance evolution in the drifts and APLs is well controlled, achieving a final value of 0.69 µm (total) and 0.51 µm (slice). The projected emittance growth arises due to chromatic effects from the large energy chirp along the bunch, which causes individual slices to diverge (or converge) at different rates in the drifts and to have a different betatron frequency in the APLs. It should be noted, however, that the emittance growth is not the same in both APLs. Instead, it appears to be more moderate in the first one. This is due to the beam-induced focusing wakefields, which, for a short bunch, grow linearly towards the tail [LA18]. Therefore, for a case like this one in which $\chi < 0$, these linearly growing wakefields can mitigate the projected emittance growth by equalizing ω_β along the bunch. This suggests that wakefields in APLs, which are typically regarded as a key limitation of these devices [LA18], can also be useful and could be optimized for emittance preservation in bunches with a large negative energy chirp. Another consequence of this slice decoherence is that the beta function will evolve differently along the bunch. Therefore, not all slices will be matched to the focusing fields in the second LWFA, causing the oscillations seen in Figure 8.3a.

8.3.3. Discussion

The detailed start-to-end simulations of this first proof-of-principle beamline show that the presented scheme can offer a new path towards GeV-range beams with ultra-low energy spread ($\sim 10^{-4}$). Comprehensive studies of space-charge and CSR effects in the chicane have shown that none of these potential issues have a significant impact on the final beam parameters (see Appendix B.1 for details). Compared to other dechirping schemes proposed [BS12; Ant+14; DAr+19; Shp+19; Wu+19a], this multistage concept can offer a dechirping strength orders of magnitude higher and, in addition, it allows for dechirping while further accelerating the beam. The concept is ideally suited for PBAs with weakly or linearly beam-loaded wakefields where the beam develops a negative chirp before the magnetic chicane. It has been seen, however, that this chirp should not result in an energy spread above the few-percent-range. Otherwise non-linear dispersion in the chicane can become relevant and lead to sub-optimal performance in terms of the projected energy spread.

As a result of the excellent beam parameters which can be obtained, plasma accelerators based on this multistage setup could enable groundbreaking applications such as compact FELs. Higher energies beyond the GeV-range, which are interesting for collider applications, could also in principle be achieved either by introducing additional plasma stages while keeping a single central chicane, or by repeating multiple sections of one chicane every two plasma accelerating modules.

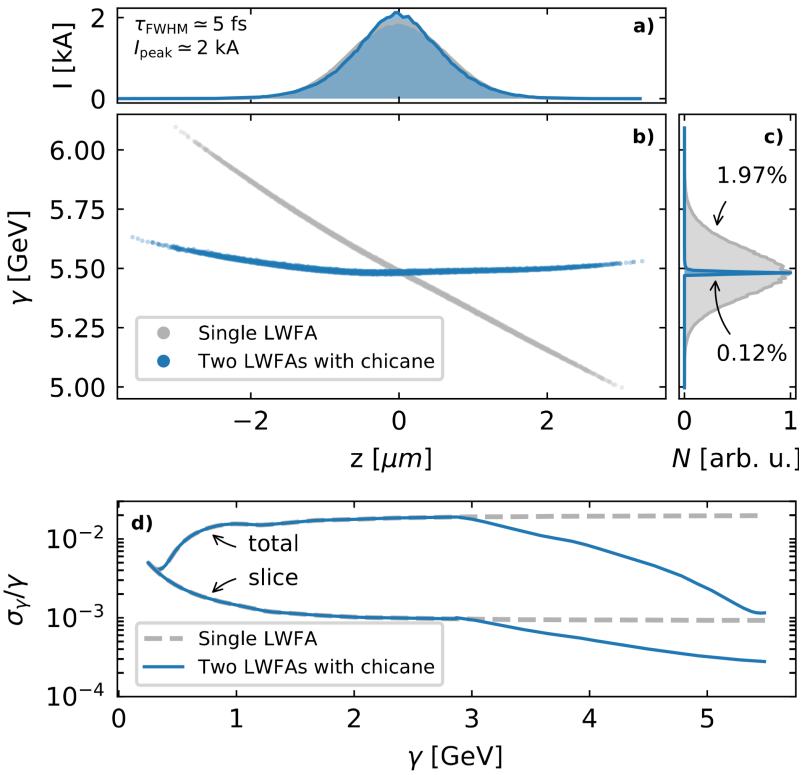

Figure 8.4.: Comparison of the final bunch properties with respect to a case with acceleration in a single LWFA (same driver and plasma profile but $\sim$ 20 cm long). The bunch current (a), longitudinal phase space (b) and energy profile (c) normalized to the peak number of counts, N, are shown. The energy spread evolution during acceleration can be seen in (d). Image from [Fer+19].

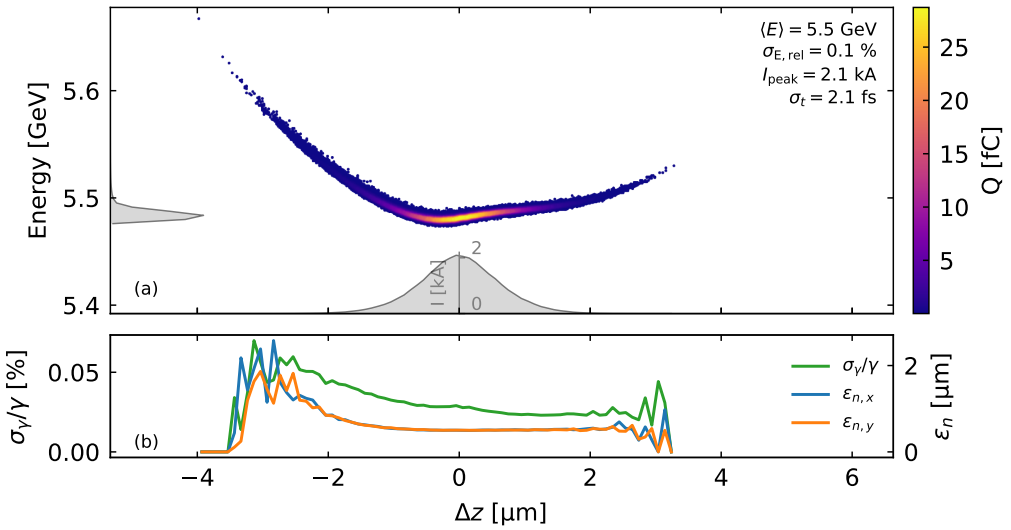

Figure 8.5.: (a) Detailed view of the final longitudinal phase-space of the beam after the second LWFA. (b) Slice emittance and energy spread along the bunch for a slice length of 0.1 μm.

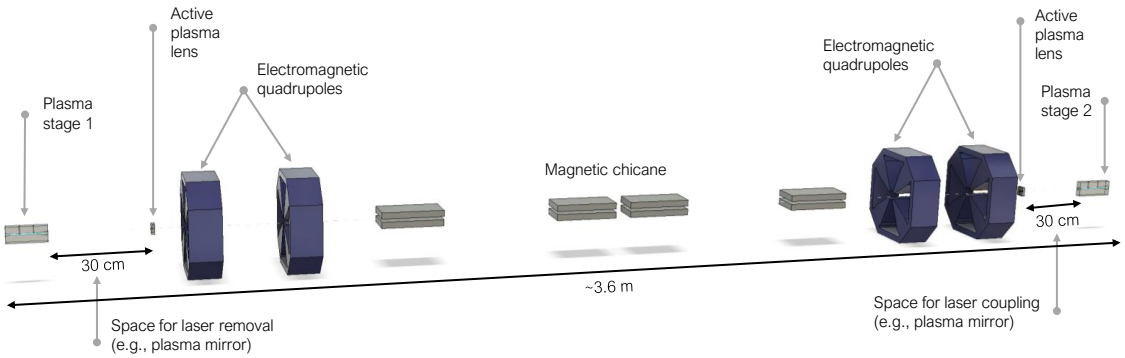

Figure 8.6.: Overview of the two-stage accelerator beamline for EuPRAXIA.

8.4. Conceptual design of a 6 GeV accelerator for EuPRAXIA

The first proof-of-principle implementation of the scheme presented in the previous section showed that beams of excellent quality fulfilling the EuPRAXIA requirements could be produced. Thanks to these promising results, a dedicated beamline for EuPRAXIA based on this concept has been designed as part of this thesis. This design successfully accelerates beams up to a final energy of 6 GeV, which is above the original 5 GeV target of EuPRAXIA. The full layout of the beamline as well as detailed start-to-end simulations with a realistic beam distribution are presented in this section.

8.4.1. Beamline design

The design of the EuPRAXIA beamline differs in several aspects with respect to the one considered before. This is because the beamline in Section 8.3, which has a total length of only 1.5 m, was only meant for a first proof-of-principle simulation study and it didn't take into account certain important aspects such as space for diagnostics or for the laser in- and outcoupling. In addition, the plasma-to-vacuum transitions (or ramps) were not considered and the beam transport between accelerating stages relied solely on active plasma lenses. For this reason, an improved conceptual design of this scheme for EuPRAXIA has been developed which goes a step further towards a realistic implementation by taking all these issues into account. A simplified view of this new accelerator layout can be seen in Figure 8.6. In the following, the details about each beamline section are given.

Plasma-accelerating stages

As in the case presented in Section 8.3, the two plasma-accelerating stages have a length of 8 cm and operate with an on-axis plasma density at the plateau of $n_{p,0} = 10^{17}\,\mathrm{cm}^{-3}$ with a parabolic transverse profile $n_p(r) = n_{p,0} + r^2/\pi r_e w_0^4$ for laser guiding. However, the plasma ramps have now been taken into account and optimized for beam matching at the plasma entrance and for divergence minimization at the exit. No transverse guiding

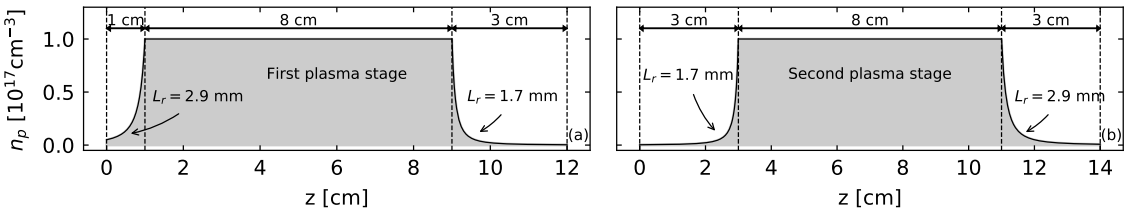

Figure 8.7.: On-axis plasma density profile of the first (a) and second (b) plasma stages in the EuPRAXIA beamline.

profile was assumed in the plasma ramps, while their longitudinal shape was assumed to follow the expression $n_{p,ramp}(z) = n_{p,0}/(1 + z/L_r)^2$. This ramp shape was found to provide good performance for matching and emittance preservation [Xu+16] and shows good agreement with realistic density profiles obtained from numerical simulations (see Appendix C). The total ramp length and the decay parameter L_r were optimized to offer the best possible matching at injection (minimize emittance growth) and minimize the beam divergence at extraction. The values of these two parameters and of the on-axis density profile in both plasma cells can be seen in Figure 8.7. The optimization of the length and shape of the plasma ramps was performed by means of Wake-T simulation scans of the whole accelerator beamline.

Regarding the laser driver, the same parameters as in the previous section have been considered. That is, a 40 J pulse per stage with a FWHM duration of 50 fs (peak power of 0.75 PW), a spot size of $w_0 = 50\,\mu$m, a wavelength of $\lambda_l = 800$ nm and a peak normalized vector potential of $a_0 = 3$. These parameters are, however, above what it is in principle required to achieve a $\sim$2.5 GeV energy gain per stage. In fact, preliminary simulation tests (which are not included in this work) already indicate that other designs based on 20 J of laser energy per stage could also be realized. Thus, further improvements and optimizations are possible in this regard.

Space for laser removal

Thanks to the plasma downramp in the first stage, the divergence of the beam can be significantly reduced with respect to the original design in Section 8.3. This reduces the emittance growth rate after the plasma stage and allows the first plasma lens to be placed farther away. In this case, a separation distance of 30 cm was chosen (in comparison to only 3 cm in the original design). This provides additional space for placing a plasma mirror and allows the laser pulse to diverge more, reducing its peak intensity from $\sim 2 \times 10^{19}\,\mathrm{W\,cm^{-2}}$ to $\sim 3 \times 10^{16}\,\mathrm{W\,cm^{-2}}$ after 25 cm. This greatly minimizes the magnetic fields which would be generated by the laser on a plasma mirror [OO07] and thus the risk of emittance increase [Raj+20]. In this regard, the use of liquid crystal mirrors [Poo+16] instead of tapes would also be strongly beneficial to mitigate emittance growth due to multiple scattering [Rei91], as they can be much thinner (few-nm vs few-µm). The same considerations apply for the coupling of the second laser into the following plasma stage.

Table 8.1.: Parameters of the focusing elements in the transport line between LWFA stages.

Element	APL 1	APL 2	EMQ 1	EMQ 2	EMQ 3	EMQ 4
Length [cm]	1	1	20	20	20	20
Gradient [T m^{-1}]	3000	3000	-35.47	29.07	25.59	-32.46

Transport line between plasma stages

The transport line in this case has been designed to allow for a higher degree of tunability. Instead of relying only on two active plasma lenses, two pairs of electromagnetic quadrupoles (EMQs) have been added. In this way, although the plasma lenses still provide most of the focusing strength, their role is now limited to controlling the beam divergence after the plasma stage in order to suppress further emittance growth, and to providing the last focus for injection into the second stage. The tuning of the beam transport is now instead performed by the quadrupoles, which are optimized to achieve a beam waist ($\alpha_x = \alpha_y = 0$) at the center of the chicane. The EMQs also allow for an independent control of both transverse planes of the beam, which, for a realistic distribution, might feature different properties at the exit of the first plasma. In addition, it is now also easier to increase the length of the transport line to, for example, accommodate for diagnostic devices. This can be done simply by optimizing the quadrupole strength and position without having to re-optimize the plasma ramps in the LWFAs nor the plasma lenses. The parameters of the focusing elements in the transport line used for the simulations are shown in Table 8.1.

Regarding the magnetic chicane, a 4-dipole array has again been considered. In this case, the magnets have a length of 20 cm, a field of 0.39 T and a separation between them of 37.5 cm, 5 cm and 37.5 cm.

Initial electron beam

The electron beam in this beamline, which is also externally injected, has been taken from a simulation study performed by J. Zhu of an RF injector for EuPRAXIA. This study, which can be found in [Zhu+18], was based on a hypothetical upgrade of the ARES linac to provide beams with an energy of ∼250 MeV and a peak current above 3 kA, as required for EuPRAXIA.

The phase-space of the particle distribution as provided by the linac at the plasma entrance is shown in Figure 8.8. It should be however noted that this distribution has been centered in transverse phase-space to correct for position and momentum offsets so that it is injected into the first LWFA with $\langle x \rangle = \langle y \rangle = \langle p_x \rangle = \langle p_y \rangle = 0$. In addition, the number of particles in this distribution has been manually increased by a factor of 8 with respect to the original bunch from the linac simulations in [Zhu+18]. This increase was required

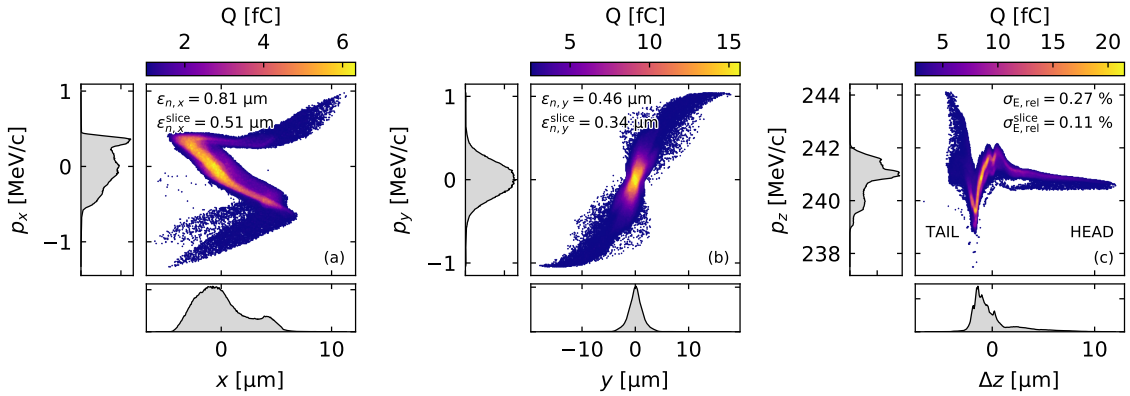

Figure 8.8.: (a) Horizontal, (b) vertical and (c) longitudinal phase-space of the RF-generated electron beam at the entrance of the first LWFA stage.

due to the fine longitudinal resolution ($\lambda_l/40$) in the FBPIC simulations, for which a sufficient number of particles per grid slice is needed in order to prevent artificial numerical noise. The addition of particles, up to a final number of ∼4.8 million, was performed by combining 8 identical copies of the original distribution and applying a random longitudinal displacement with a maximum amplitude of $\pm\lambda_l/40$ to each particle. In this way, the slice (and of course the projected) properties of the bunch, i.e, the emittance, energy spread, etc., are preserved for any slice significantly longer than the fine longitudinal grid resolution.

Another important remark regarding the externally-injected beam is that, as seen later in Section 8.4.2, the sharp peaks in its current profile (cf. Figure 8.8c) were found to induce an energy modulation in the first LWFA due to to longitudinal space-charge forces. This modulation then led to strong micro-bunching effects in the chicane which had a significant impact on the final beam quality. In order to mitigate this issue, a modified version of this beam with a smoothed current profile was created. This smoothing was performed by applying a random longitudinal displacement to each particle according to a normal distribution with a standard deviation of 0.3 µm, which was found to be sufficient to remove the sharp peaks in charge density. This smoothing, although artificial, was applied here to emulate the effect of a laser heater [SSY04] before the bunch compressor in the RF linac. This is a technique commonly used in FEL facilities (e.g. [Hua+04; Spa+14]) to mitigate the micro-bunching instability by increasing the slice energy spread. Such a laser heater could also be applied here to prevent the sharp peaks in the current profile [Zhu18]. The longitudinal phase-space of these two distributions (original and with smoothing) is compared in Figure 8.9, and the parameters of both are given in Table 8.2.

8.4.2. Start-to-end simulations

As in the previous case, the simulations of this beamline have been carried out with a combination of several numerical codes. The plasma elements, i.e, the accelerating stages and the active plasma lenses, have been simulated with FBPIC while the drifts between

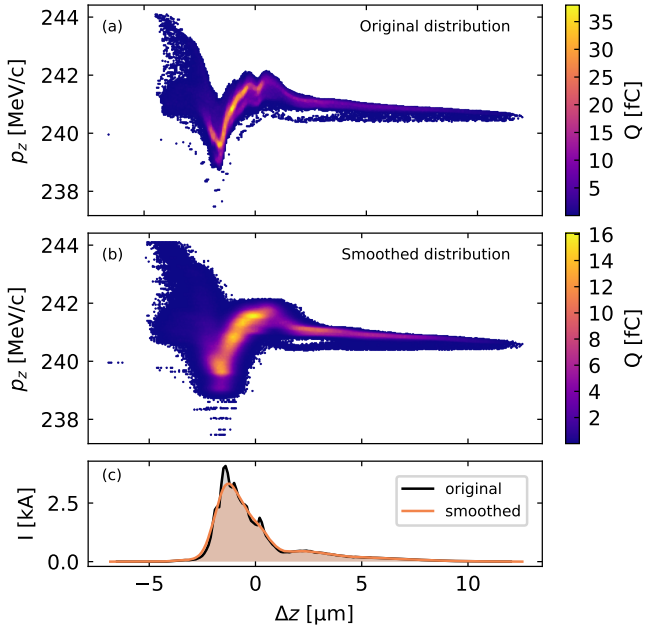

Figure 8.9.: Comparison of the original and smoothed beams at the entrance of the first LWFA: (a) Longitudinal phase-space of the original particle distribution, (b) longitudinal phase-space of the smoothed distribution and (c) current profile of both distributions. The smoothing applied is sufficient to remove the sharp density peaks observed in the original bunch.

Table 8.2.: Initial beam parameters of the original and the longitudinally-smoothed distributions at the entrance of the first LWFA. As expected, only the slice and longitudinal parameters (I_{peak} and τ_{FWHM}) present noticeable differences. The slice parameters correspond to the weighted average of the values computed for 0.1 μm-long slices.

Parameter	**Units**	**Value (original beam)**	**Value (smoothed beam)**
Q	pC	30	30
$\langle\gamma\rangle$	MeV	241	241
σ_δ	10^{-3}	2.74	2.74
I_{peak}	kA	4.08	3.33
τ_{FWHM}	fs	5.01	6.33
β_x | β_y	mm	3.08 | 3.04	3.08 | 3.04
α_x | α_y	-	1.12 | -1.28	1.12 | -1.28
$\epsilon_{\text{n,x}}$ | $\epsilon_{\text{n,y}}$	μm	0.81 | 0.46	0.81 | 0.46
$\epsilon_{\text{n,x,sl}}$ | $\epsilon_{\text{n,y,sl}}$	μm	0.51 | 0.34	0.54 | 0.36
$\sigma_{\delta,\text{sl}}$	10^{-3}	1.07	1.55

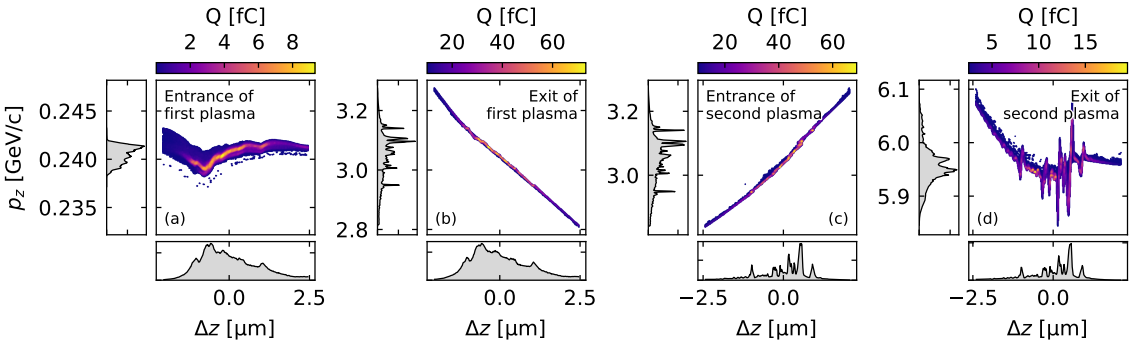

Figure 8.10.: Evolution of the longitudinal phase space of the beam along the accelerator for the case in which the original distribution is used. The phase-space is shown at (a) the entrance and (b) exit of the first plasma stage and at (c) the entrance and (d) exit of the second LWFA. The development of an energy modulation and the micro-bunching are clearly visible. For better visualization, only the central core of the beam along $\Delta z = z - \langle z \rangle$, which contains $\sim 80\%$ of the charge, is shown.

them as well as the transport line were simulated with ASTRA in order to account for 3D space-charge effects. Simulations with CSRtrack were also performed at a later stage to check for any possible CSR effects, as they were initially not expected to be of relevance. These CSR simulations, which don't foresee a detrimental impact on the beam quality, are not shown in this chapter and are instead included in Appendix B.2.

A first set of start-to-end simulations was performed using the original electron bunch shown in Figure 8.8. In this case, a boost of $\sim$2.9 GeV per plasma stage is obtained, reaching a final energy of $\sim$5.9 GeV at the end of the beamline. The energy chirp gained in the first LWFA is successfully inverted in the chicane and compensated for in the second plasma stage. However, as seen in Figure 8.10, a strong energy and charge density modulation seems to have developed along the accelerator. As a consequence, a high average slice energy spread of $\sim$0.3 % (for 0.1 μm-long slices) is observed, which is around one order of magnitude above the target requirements for an FEL.

The origin of this modulation can be traced back to the first LWFA. There, as seen in Figure 8.10(b), the beam develops not only a linear chirp but also a slight energy modulation which leads to a peaked energy profile. The reason for this appears to be the effect of longitudinal space-charge fields which, as illustrated by Equation (3.46), can give rise to positive or negative energy gain along the bunch depending on the longitudinal charge density gradient. For the beam under consideration, which features sharp peaks in its current profile, this gives rise to non-uniform longitudinal space-charge fields with an amplitude of up to $\sim 50\,\mathrm{MV\,m^{-1}}$ while propagating within the plasma[1]. This explains

[1]It is interesting to note here that the amplitude of these fields, which is taken from FBPIC simulations, is about a factor of 5 higher than the amplitude predicted by Poisson space-charge solvers such as those used by ASTRA or OCELOT. From several tests performed by the author, these differences seem to arise from the high transverse momentum that the beam particles have while being accelerated within the plasma as a result of the $\mathrm{MT\,m^{-1}}$ focusing fields. This transverse momentum, which can reach relativistic values significantly above 1 MeV/c, is neglected by Poisson solvers but not by the PIC algorithm, and

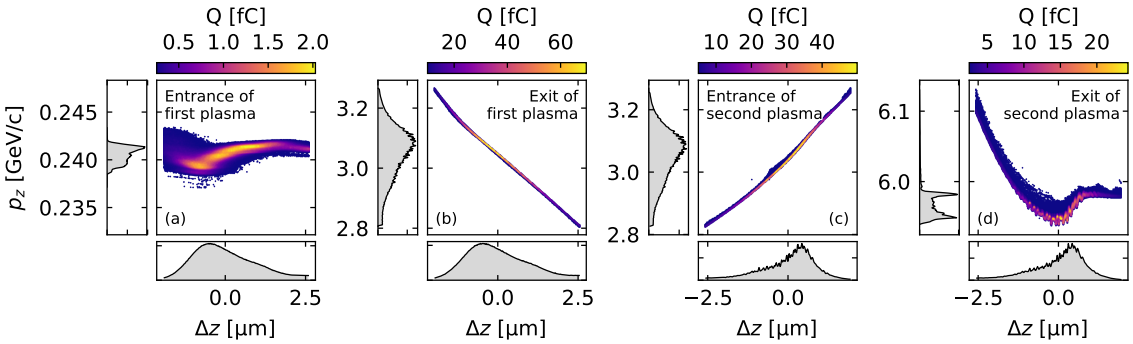

Figure 8.11.: Evolution of the longitudinal phase space of the beam along the accelerator for the case in which the smoothed distribution is used. The phase-space is shown at (a) the entrance and (b) exit of the first plasma stage and at (c) the entrance and (d) exit of the second LWFA. The final charge and energy modulation is significantly reduced with respect to the unsmoothed case. For better visualization, only the central core of the beam along $\Delta z = z - \langle z \rangle$, which contains $\sim$ 80% of the charge, is shown.

the energy modulations on the MeV-range which are observed after the first LWFA, and which are located at the position of the density peaks. Later on, in the chicane, these modulations in energy get translated into charge density modulations, as seen in Figure 8.10(c). These density modulations (or micro-bunches) are much more pronounced than the density peaks in the initial distribution. Thus, they give rise to even stronger longitudinal space-charge fields in the second LWFA, resulting in the final energy modulations seen in Figure 8.10(d).

In order to solve this issue, the initial density spikes in the beam must therefore be removed. While it is possible that these modulations are being overestimated in the linac simulations due to the limited amount of particles [Zhu18], a possible solution, if deemed necessary, would be to include a laser heater before the bunch compressor. As explained in the previous section, this possibility was explored here by creating a new distribution, shown in Figure 8.9(b), which features a smoothed longitudinal profile. Thanks to this smoothing, the energy and density modulations induced along beamline are greatly minimized, as seen in Figure 8.11, and a final average slice energy spread of $\sim$ 0.05% (for 0.1 μm-long slices) is achieved, fulfilling the EuPRAXIA requirements.

More details about the evolution of this improved particle distribution can be seen in Figure 8.12, where the beam parameters along both plasma stages are shown. In addition, the final transverse and longitudinal phase-space of the beam at the end of the second LWFA can be seen in Figure 8.13. It should be noted, however, that the parameters along the plasma stages as well as these phase-space plots correspond to those of the core part of the beam and not to the whole particle distribution. This core, which contains $\sim$80 % of the charge and is the relevant part for FEL applications, is defined as a range of $\sim$12 fs around the peak in the current profile and does not take into account a $\sim$ 3% of particles

can lead to an increase of the longitudinal component of the field. The results from the FBPIC simulations are therefore expected to be more accurate in regards to this effect.

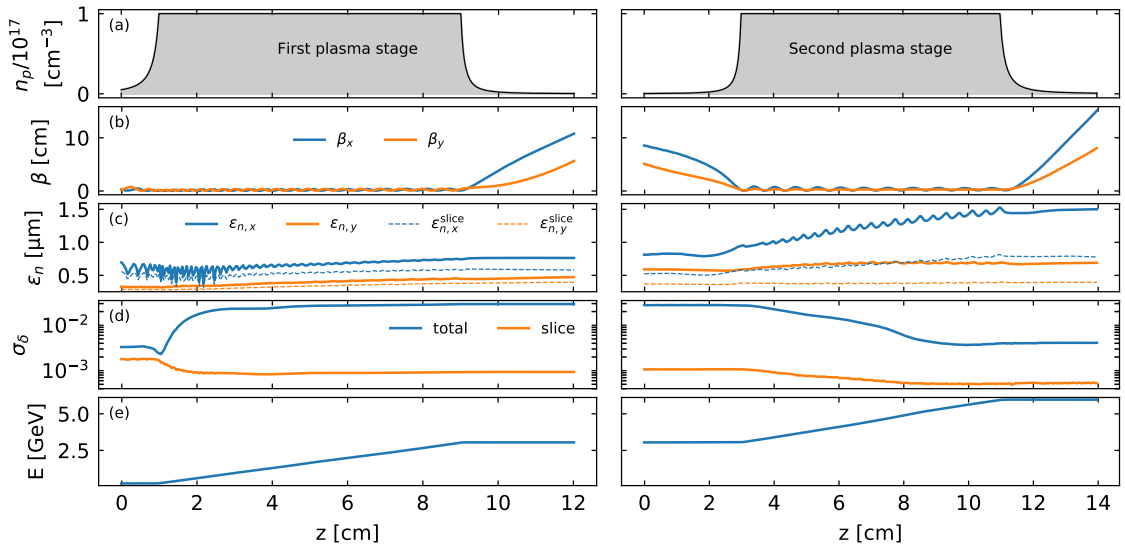

Figure 8.12.: Evolution of the parameters of the core part of the beam along both plasma stages: (a) overview of the on-axis plasma density profile in both stages, (b) beta function, (c) normalized emittance, (d) energy spread and (e) energy of the beam. The noisy behavior of the emittance at the beginning of the first plasma is due to the particle filtering applied for obtaining the bunch core.

which are located more than $\pm 5\sigma_{x|y}$ or $\pm 5\sigma_{p_x|p_y}$ away from the center. This filtering of beam particles was performed in order not to take into account a small fraction of the charge which is far away from the bunch core and which would otherwise greatly affect the value of the statistical RMS beam parameters.

A detailed view of the final longitudinal phase-space of this core as well as the value of the slice parameters along it can be seen in Figure 8.14. In addition, a complete overview of all relevant beam parameters at the end of the beamline is shown in Table 8.3 both for the original and the smoothed versions of the distribution. This table shows that the performance of both beams seems to be similar in terms of the emittance ($\epsilon_{n,x|y} \lesssim 1\,\mu$m), but

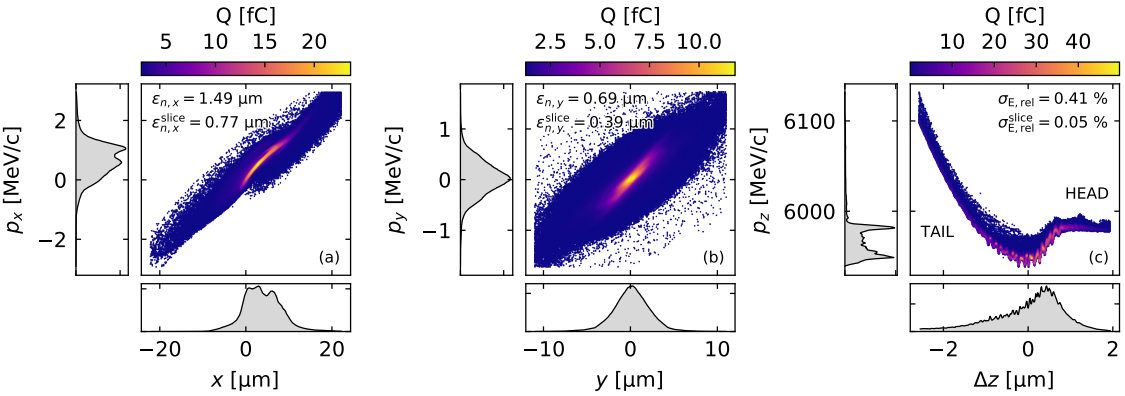

Figure 8.13.: (a) Horizontal, (b) vertical and (c) longitudinal phase-space of the initially-smoothed electron beam at the end of the second LWFA stage. Only the core of the beam is shown, as defined in the text.

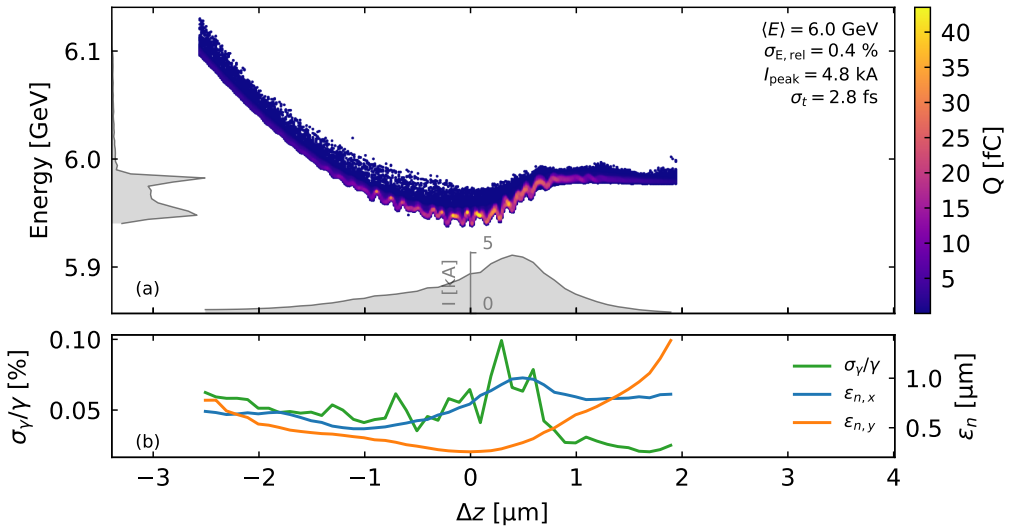

Figure 8.14.: Detailed view of the longitudinal properties of the initially-smoothed beam at the end of the second LWFA stage: (a) longitudinal phase-space including current profile and energy projection, (b) slice emittance and energy spread along the bunch for 0.1 µm-long slices. Only the core of the beam is shown, as defined in the text.

with strong differences regarding the peak current (and thus τ_{FWHM}) and energy spread, particularly at the slice level. In addition to these results, which come from FBPIC and ASTRA simulations, studies of the transport line performed with CSRtrack show that no detrimental effects from CSR are expected. These studies, which been carried out for the smoothed distribution, are included in Appendix B.2.

8.4.3. Discussion

In this section, a plasma-acceleration beamline for EuPRAXIA based on the multistage concept introduced in this chapter has been presented. This beamline, as the one in Section 8.3, was initially targeted at producing ∼5 GeV beams with a slice energy spread on the 10^{-4}-range. In this case, however, a more elaborate design addressing some of the issues of the original beamline has been used. The changes include considering the plasma ramps in both LWFAs, more space for the laser coupling, the introduction of quadrupoles in addition to the plasma lenses, and a higher flexibility for accommodating diagnostics. Furthermore, a realistic beam distribution from an RF linac featuring higher charge and peak current has now been used.

The results of the start-to-end simulations show that the externally-injected beams can be boosted to a final energy of ∼6 GeV with a slice energy spread of ∼0.05 %, satisfying the EuPRAXIA requirements. Achieving this beam quality requires, however, preventing the onset of micro-bunching in the magnetic chicane. For this, a smooth longitudinal current profile at the entrance of the first LWFA is needed, which might require an upgrade of the RF linac to include a laser heater. Further detailed studies of this issue as well as

Table 8.3.: Final parameters at the end of the second LWFA of the bunch core (as defined in the text) for both the original and the initially-smoothed distributions. A clear improvement on the slice energy spread can be observed in the smoothed case. The high peak current and short length when using the original beam are a direct consequence of the micro-bunching. The slice parameters correspond to the weighted average of the values computed for 0.1 µm-long slices.

Parameter	Units	Value (original beam)	Value (smoothed beam)
Q	pC	23.5	23.6
$\langle\gamma\rangle$	GeV	5.96	5.97
σ_δ	10^{-3}	6.18	4.11
I_{peak}	kA	9.93	4.77
τ_{FWHM}	fs	1.33	3.34
β_x | β_y	cm	15.2 | 8.2	15.3 | 8.2
α_x | α_y	-	-3.15 | -1.82	-3.25 | -1.90
$\epsilon_{\text{n,x}}$ | $\epsilon_{\text{n,y}}$	µm	1.49 | 0.67	1.49 | 0.69
$\epsilon_{\text{n,x,sl}}$ | $\epsilon_{\text{n,y,sl}}$	µm	0.76 | 0.38	0.77 | 0.39
$\sigma_{\delta,\text{sl}}$	10^{-3}	2.71	0.53

of the potential advantages of including a laser heater should therefore be carried out in the future.

Thanks to the good performance demonstrated, this multistage beamline was selected as a baseline option for the laser-driven plasma accelerator in the EuPRAXIA conceptual design report (CDR) [Ass+19]. In the CDR, in addition to the accelerator beamline presented here, a transfer line designed by A. Chancé to transport the beam from the second LWFA to the undulators without quality degradation is also included.

8.5. Conceptual design of a 1 GeV accelerator for ATHENA_e

In addition to the first proof-of-principle simulations and the more elaborate conceptual design for EuPRAXIA, an additional study for a 1 GeV beamline has been performed. The purpose of this design was to demonstrate that the presented multistage scheme can also be effectively applied to lower-energy beams which can be accelerated by more commonly available laser systems (instead of the petawatt-range lasers considered in the previous cases). In addition, this conceptual beamline was used to show that an implementation of the laser coupling based on conventional mirrors (instead of plasma mirrors) is also possible while leaving enough space (or having the tunability) to place the necessary diagnostics. The proposed design, being based on less demanding laser requirements and a more conservative approach for the laser coupling, could therefore be considered as a starting point for first proof-of-principle experimental tests which could be carried out within the ATHENA_e project at DESY.

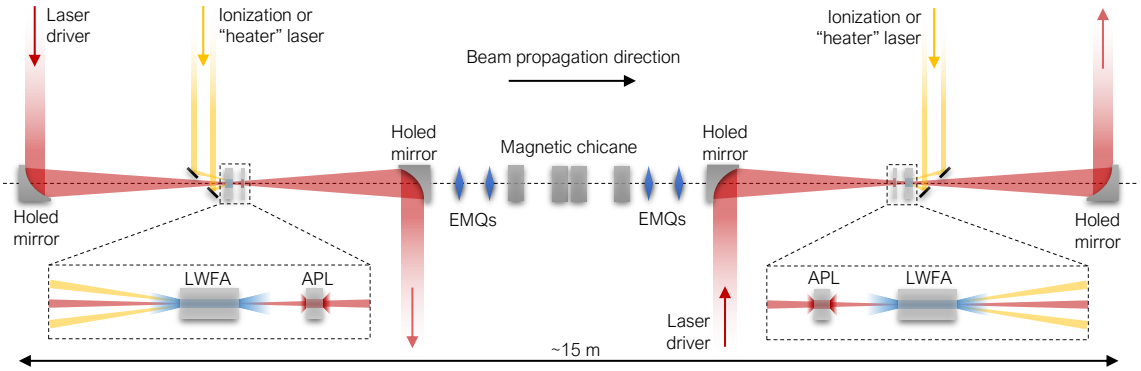

Figure 8.15.: Schematic view of the 1 GeV accelerator beamline. Due to the use of conventional (instead of plasma) mirrors, the total length is in this case dominated by the laser coupling. A more compact design could in principle be achieved by placing some (or all) quadrupoles and dipoles as well as the second mirror before the removal of the first laser pulse. However, this would require large apertures and thus potential problems with fringe fields.

8.5.1. Beamline design

A general overview of the conceptual design of this 1 GeV accelerator can be seen in Figure 8.15. As it can be observed, the size of the beamline is now dominated by the laser coupling with conventional mirrors, requiring a total length of ∼15 m. In the following, a detailed description of the different elements in this beamline is given.

Laser system and coupling

The biggest change of this design with respect to the previous ∼5 GeV cases is on the laser. Instead of using a 40 J pulse per plasma stage, the present study was performed for a 5 J system, i.e., with 2.5 J per plasma stage, which is in the range of currently available lasers (e.g. ANGUS [Del+18] at DESY or DRACO [Zei+10] at HZDR). Due to the lower peak power in this case, as seen in Table 8.4, a smaller spot size of $w_0 = 24\,\mu\text{m}$ is required to achieve an $a_0 = 2$ at the plasma-accelerating stages and excite a strong enough wakefield which is able to imprint a clear linear chirp to the witness beam. A consequence of this smaller spot size is that the laser pulse diverges faster (see Equation (3.63)). This allows the use of conventional mirrors for the in- and out-coupling of the laser while maintaining a relatively compact setup (few-metre scale). For the parameters shown in Table 8.4, if a laser-induced damage threshold (LIDT) in the mirrors of $\sim 0.1\,\text{J cm}^{-2}$ [LAY] is assumed, a distance of 3 m between the plasma cells and the mirrors is sufficient in order to prevent damage.

Active plasma lenses

The long drift between the end of the first LWFA and the mirror could, however, be an issue for the beam quality if its divergence is not controlled. This is because of the large

Table 8.4.: Parameters of the laser driver used in both LWFA stages of the 1 GeV beamline. A total of 5 J of laser energy is therefore required in this case.

Parameter	E_l	$P_{\mathrm{peak},l}$	$\tau_{\mathrm{FWHM},l}$	a_0	w_0	λ_l
Units	J	TW	fs	-	µm	nm
Value	2.5	85	30	2.0	24	800

energy spread expected at this point, which, combined with the divergence, can lead to large emittance growth (see Equation (3.108)). In order to avoid this, an active plasma lens is placed 10 cm after the accelerating plasma stage to reduce the beam divergence and achieve, ideally, $\alpha_{x|y} = 0$. This would effectively suppress the emittance growth after the APL and allow the beam to be safely transported past the mirror.

Such a setup implies, however, that the laser driver has to pass also through the APL. This is opposed to the previous conceptual designs, where it was assumed to be removed right after the LWFA stage. Therefore, it is important to make sure that no significant wakefields are generated by the laser in the lens and that its aperture is wide enough. An estimate of the laser spot size and a_0 at the entrance of the APL can be obtained by assuming that its properties have not changed during the first plasma stage (that is, perfect guiding and no depletion). This yields a transverse size $w \simeq 1\,\mathrm{mm}$ and $a_0 \simeq 0.04$, which, for a plasma density in the APL of $n_{p,\mathrm{APL}} = 10^{15}\,\mathrm{cm}^{-3}$, would lead to a linear wakefield with focusing strength $\ll 1\,\mathrm{T\,m}^{-1}$ according to Equation (3.96). This is much smaller than the typical focusing fields in APLs and can therefore be neglected. In order to safely let the laser go through, the aperture should however be of a few millimetres, which is larger than in typical APL designs used nowadays, where $\lesssim 1\,\mathrm{mm}$ capillaries are typically found. This is not a fundamental limit, though, since APL prototypes with centimetre-scale aperture with up to $600\,\mathrm{T\,m}^{-1}$ fields have been successfully demonstrated decades ago [Ste+92; Ste+96]. Therefore, for the 1 GeV beamline, it has been assumed that both plasma lenses have a gradient of $600\,\mathrm{T\,m}^{-1}$and length of 2.7 cm, as needed in order to bring the beam to a waist.

The same considerations apply for the second plasma lens, which focuses the beam into the second LWFA, since the beamline is symmetric with respect to the center of the chicane.

Plasma accelerating stages

Another significant change with respect to the EuPRAXIA beamline is on how the density ramps in the plasma targets have been treated. Previously, the ramps were assumed to be of finite extension and therefore to end sharply after a certain distance. This length, as well as the shape of the ramp, was then optimized to achieve certain beam parameters. However, in reality, the ramps do not end sharply but rather extend continuously into vacuum. Thus, a more realistic description has been adopted for the plasma stages in the

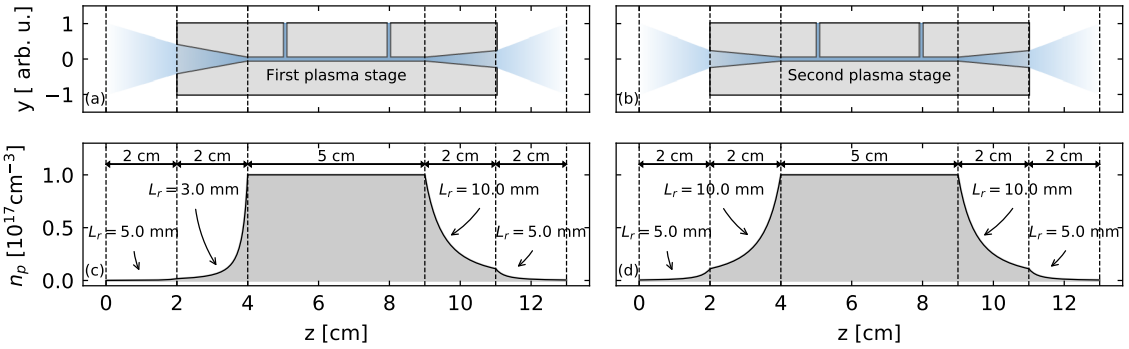

Figure 8.16.: Conceptual sketch ((a) and (b)) and density profile ((c) and (d)) of the plasma targets for the 1 GeV case. The density profile is based on the realistic fluid simulations included in Appendix C, which show that the ramp shape can be controlled by tailoring the transverse extent of the capillary. This is visualized here (only conceptually) by the opening angle of the capillary ends.

1 GeV beamline. Here, instead of ending the ramp after a certain optimized distance, the density of the gas flowing into vacuum has been taken into account until it no longer had a significant effect on the beam parameters.

A conceptual sketch of the two plasma cells and their corresponding density profiles is included in Figure 8.16. As it can be observed, each plasma ramp has two distinct sections: one with an optimized shape for beam matching or extraction and another which consists of the gas flowing freely into vacuum. The profile in both sections follows the expression $n_{p,r} = n_{p,0}/(1 + z/L_r)^2$, which shows good agreement with the fluid simulations included in Appendix C, and where $n_{p,0}$ and z are the density of and the distance to the top of the ramp. The density profile in the optimized part of the ramp, which has a length of 2 cm, is assumed to be controlled by the opening of the capillary radius, as observed in Appendix C. After this optimized section, the gas then flows freely into vacuum and the density decreases more sharply. For this part of the ramp in vacuum, the value $L_r = 5$ mm has been chosen to mimic the gas cell simulation in Figure C.1. A total extension of 2 cm into vacuum has been considered, which was sufficient to take into account the impact of these density tails on the beam parameters.

In the inner section of the ramps, the parameter L_r has been optimized to obtain a relaxed matching condition in the entrance of the first stage and to minimize the divergence at the exit. The downramp of the first stage and upramp of the second are identical to keep the symmetry of the transport line. On the other hand, the first upramp has a sharper density gradient due to the lower energy (and thus higher betatron frequency) of the beam at this point. The optimization of the plasma ramps was carried out by means of FBPIC simulation scans in which different values for L_r were tested. For the case of the upramp in the first LWFA, this optimization, as well as the calculation of the neces-

Table 8.5.: Parameters of the focusing elements transporting the beam between the two LWFA stages.

Element	APL 1	APL 2	EMQ 1	EMQ 2	EMQ 3	EMQ 4
Gradient [T/m]	600	600	19.58	-16.58	-16.60	19.42
Length [cm]	2.7	2.7	20	20	20	20

sary Twiss parameters at the plasma entrance were obtained by backtracking[2] a matched beam (at the plateau entrance) the beam through the ramp. Since all optimizations were constrained to a ramp length of 2 cm and a density profile given by the expression above, it is likely that further improvements can be achieved.

In addition to an optimized longitudinal density profile, both plasma stages require a parabolic transverse density gradient $n_p(r) = n_{p,0} + r^2/\pi r_e w_0^4$ for guiding the laser driver. Due to the small spot size ($w_0 = 24\,\mu m$) and relatively low plasma density ($n_p = 10^{17}\,cm^{-3}$), a pre-pulse or *heater* laser would be needed in addition to the discharge in order to achieve a deep enough density channel [Gon+19; Sha+19; Sha+18]. A conceptual implementation of this additional laser pulse is included in Figure 8.15 resembling the experimental layout in [Sha+19].

Chicane and transport line

The transport line between the two plasma stages, apart from the two APLs described above, is completed by two pairs of quadrupoles and the magnetic chicane, which are placed in the centre between the two holed parabolic mirrors. The purpose of the quadrupoles, whose parameters can be seen in Table 8.5, is to guide the beam through the chicane such that it has a waist in the middle. They also provide independent control of the focusing in the x and y planes, which might be useful for realistic beams where the properties are different in each transverse direction. They also allow for a higher degree of tunability in the beamline so that if additional space is needed, for example, to place diagnostic devices, the beam transport can be simply re-optimized by adjusting the quadrupole strengths without any change to the plasma lenses.

Apart from the focusing elements, the dipoles in the chicane have a length of 20 cm and a magnetic field of 0.5 T. They are separated by drifts of 37.5 cm, 5 cm and 37.5 cm.

Electron beam

For this 1 GeV beamline, an electron beam within the parameter range of ARES has been used. This means an energy of 100 MeV, a charge of ∼10 pC, a FWHM duration of ∼10 fs, a peak current of 1 kA, a normalized emittance of 0.3 µm and a relative energy spread of 0.3 %. For the combination of laser power, plasma density and peak current, the effects

[2] Backtracking means here that the beam was propagated through a downramp identical to the upramp.

of beam loading became significant in this case. Thus, to preserve a uniform linear chirp along the bunch, a flat-top current profile was considered. In the transverse phase-space, a cylindrically-symmetric Gaussian distribution was assumed. The initial longitudinal phase-space of this idealized bunch can be seen later in Figure 8.19(a). In addition, the complete list of parameters of this beam is included towards the end in Table 8.6, where they are compared to the final beam parameters at the exit of the second LWFA.

8.5.2. Start-to-end simulations

In this beamline, the plasma simulations of the accelerating stages and APLs have been again carried out with FBPIC, while the drifts and the transport line have been simulated with ASTRA to take into account 3D space-charge effects. No CSRtrack simulations were performed this time, since no meaningful CSR effects are expected based on the experience with the previous beamlines. Keeping the space-charge forces well described was however important given the lower beam energy in this case.

An overview of the evolution of the transverse beam parameters along the whole accelerator is shown in Figure 8.17. It can be observed that the emittance is preserved in the first LWFA, showing that the beam is well matched, and that it only grows after extraction until the divergence is controlled by the APL. After that, the beam propagates with virtually no emittance growth during the transport line until it is again strongly focused by the second APL for injection into the second plasma. A local reduction in the projected emittance can be observed in some parts of the beamline. This is likely caused by a partial realignment of the beam slices due to the phase advance at that point, which partially compensates the chromatic growth of the projected emittance described in Section 3.6.2. This is an effect that could be studied in more detail in the future to explore whether the transport line can be optimized to fully compensate for the chromatic emittance growth. Overall, the simulations show that, even in this long drift ($\sim$9 m) between the two accelerating stages, the beam can be successfully transported while maintaining a sub-micron projected emittance. Even at this lower energy ($\sim$650 MeV), no meaningful space-charge effects in the chicane are therefore observed.

In addition to the whole beamline, a detailed view of the evolution of the beam parameters in the two plasma stages is included in Figure 8.18. There, the effect of the plasma ramps on the beam divergence can be clearly observed by looking at the gamma function. The first upramp increases $\gamma_{x|y}$ by an order of magnitude from an initial value of $\sim$150 m^{-1} to $\sim$2500 m^{-1} at the beginning of the density plateau. This greatly reduces the requirements on the beam focusing elements before the plasma stage. The same considerations apply to the plasma downramps, which significantly reduce the beam divergence and facilitate its transport. It can also be seen that the impact of the ramps on $\gamma_{x|y}$ seems to be negligible after a distance of $\sim$1 cm from the capillary ends. This is both due to the reduced background density as well as the larger transverse size of the laser pulse, which quickly diverges and loses its driving strength.

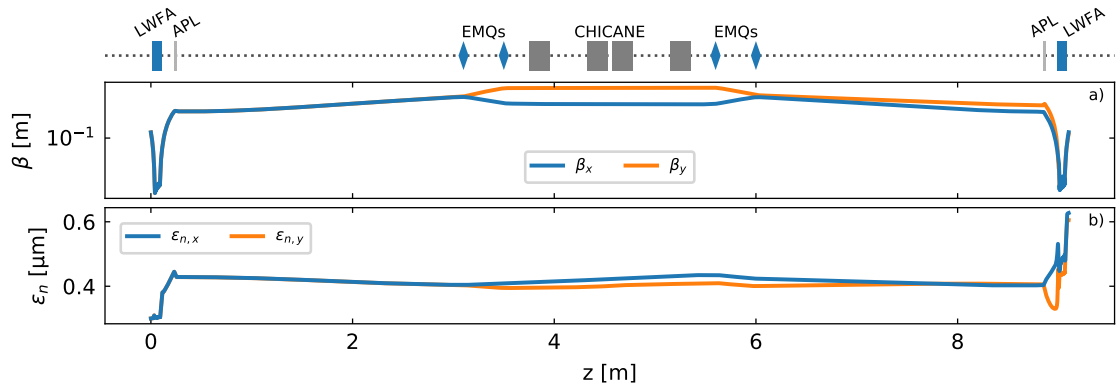

Figure 8.17.: Overview of the beamline and the evolution of the transverse beam parameters along it: (a) beta function and (b) normalized emittance. It should be noted that the horizontal beam parameters in the chicane are simply an interpolation between the initial and the final values. This parameters would otherwise appear distorted due to the horizontal dispersion.

In regards to the beam energy, each stage is able to give a ∼450 MeV boost for achieving the final target energy of ∼1 GeV. It is worth noting, however, that the laser pulse is still far from depletion at the end of each stage, so a potential upgrade of the beamline for a final energy of ∼2 GeV is likely feasible simply by increasing the length of the capillaries. The evolution of the energy spread in the second stage, which is reduced from ∼3 % to ∼0.5 %, also shows that the chirp is again successfully compensated for.

The evolution of the energy chirp along the beamline can be more clearly seen in Figure 8.19, where the longitudinal phase space of the beam is shown at different locations. It can be observed that, after the first LWFA, apart from a clear linear chirp, the beam has developed two spikes in the energy profile at the head and the tail. These peaks seem to arise due to longitudinal space-charge forces during the plasma stage as a consequence of the flat-top current profile of the bunch, which accelerate particles on the front and decelerate those at the end. Then, after passing through the chicane, the energy spikes are translated into the longitudinal current profile, leading to a peak current of ∼2.5 kA at the bunch head. In addition to the energy modulation due to these peaks, a clear second order contribution from the chicane can be seen in the final bunch after the linear chirp has been removed in the second plasma stage. This second order correlation, together with the spikes due to longitudinal space-charge, are the main sources of projected energy spread at the end of the accelerator.

A more detailed view of the final longitudinal phase-space of the beam in shown in Figure 8.20, where the slice parameters of the distribution are also included. Here it can be seen that, despite the two charge peaks at the head and the tail, most of the distribution remains with a current of ∼1 kA. The impact of these peaks on the slice parameters is also clearly observed in Figure 8.20(b). Thus, even though the central slices have an energy spread as low as ∼0.06 %, the substantial growth towards the peaks leads to an average slice energy spread slightly above 0.1 %. A complete list of the final beam parameters,

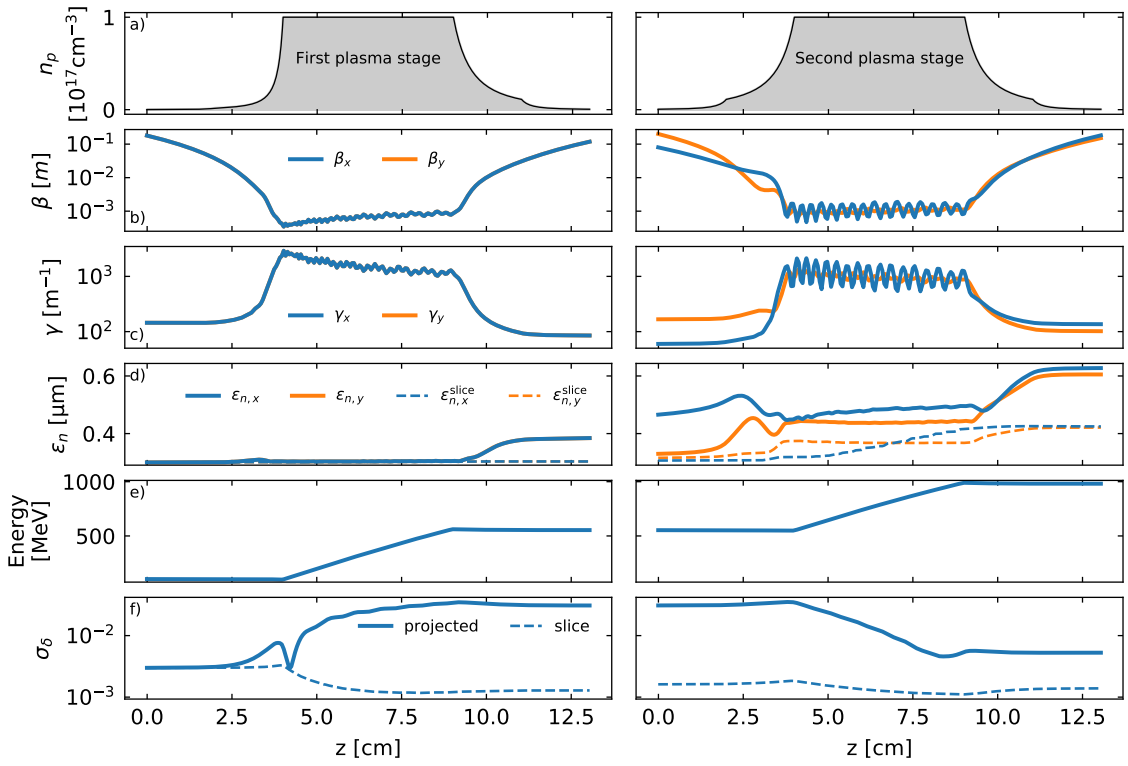

Figure 8.18.: Evolution of the beam parameters in both plasma stages: (a) overview of the plasma density profile, (b) beta function, (c) gamma function, (d) normalized emittance, (e) energy and (f) energy spread.

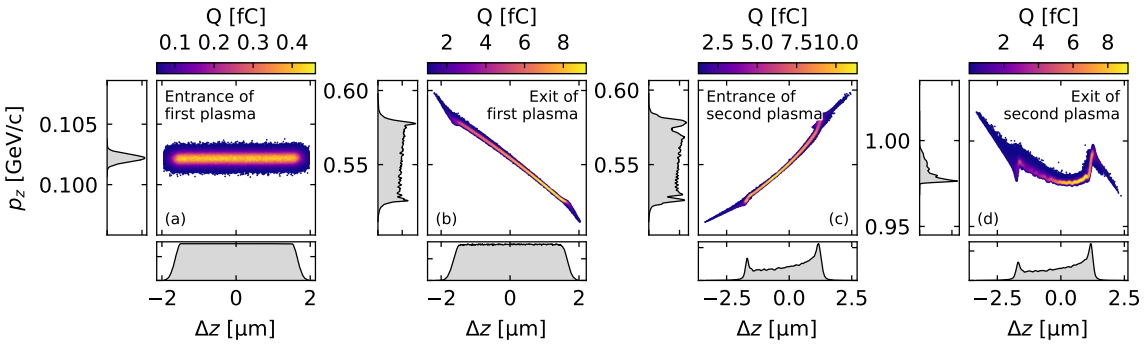

Figure 8.19.: Longitudinal phase-space of the beam at different locations along the accelerator: (a) at entrance and (b) exit of the first plasma stage, and (c) at entrance and (d) exit of the second plasma stage.

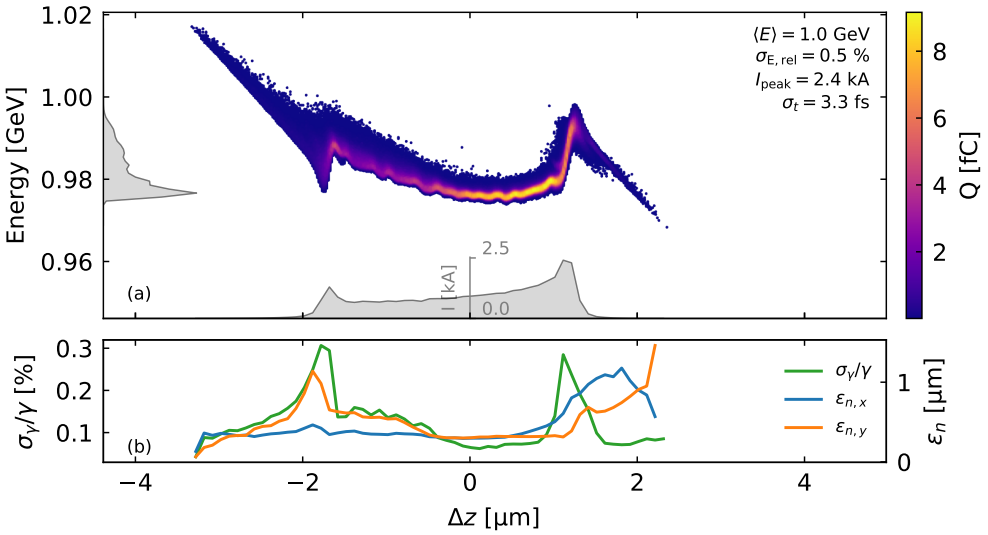

Figure 8.20.: Detailed view of the longitudinal properties of the initially-smoothed beam at the end of the second LWFA stage: (a) longitudinal phase-space including current profile and energy projection, (b) slice emittance and energy spread along the bunch for 0.1 µm-long slices.

compared to the initial ones, is shown in Table 8.6.

8.5.3. Discussion

The conceptual design and simulations presented in this section show that a lower-energy (1 GeV) version of the multistage acceleration scheme is possible. More importantly, they show that an implementation based on more conservative laser parameters (5 J system) and on conventional (instead of plasma) mirrors could be realized.

Thanks to an optimized plasma profile in the capillaries, which is based on realistic fluid simulations, a transfer line between the LWFAs could be designed which successfully maintains a sub-micron emittance over the ∼9 m drift between them. No meaningful space-charge effects are observed in the chicane, and the energy chirp can be effectively compensated for in the second LWFA. Thus, a beam with a final energy of ∼1 GeV, sub-percent (0.5 %) projected energy spread and up to sub-per-mille (0.06 % in the best slice) energy spread, is obtained.

Despite this good performance, some issues were found with the electron distribution used. In particular, sharp density peaks and energy modulations developed at the head and tail. This appears to be caused by longitudinal space-charge forces due to the flat-top current profile of the bunch. Thus, future work could focus on optimizing the bunch shape to prevent this issue and on simulating fully-realistic beam distributions, such as done before in Section 8.4.

Table 8.6.: Comparison of the beam parameters at the beginning and at the end of the 1 GeV beamline. The high peak current and short FWHM length in the final beam are a direct consequence of the density peaks developed due to longitudinal space-charge. The slice parameters correspond to the weighted average of the values computed for 0.1 µm-long slices.

Parameter	Units	Initial value	Final value
Q	pC	11.3	11.3
$\langle\gamma\rangle$	MeV	102	981
σ_δ	10^{-3}	3.01	5.27
I_{peak}	kA	1	2.41
τ_{FWHM}	fs	10.7	1.1
σ_t	fs	3.26	3.32
β_x | β_y	cm	18.0 | 18.0	18.3 | 15.1
α_x | α_y	-	5.00 | 5.00	-4.89 | -3.79
$\epsilon_{\text{n,x}}$ | $\epsilon_{\text{n,y}}$	µm	0.30 | 0.30	0.63 | 0.61
$\epsilon_{\text{n,x,sl}}$ | $\epsilon_{\text{n,y,sl}}$	µm	0.30 | 0.30	0.43 | 0.42
$\sigma_{\delta,\text{sl}}$	10^{-3}	3.00	1.39

8.6. Sensitivity and tolerance studies

The proof-of-principle simulations and conceptual beamlines studied so far have shown that this multistage scheme can perform well with a variety of implementations. However, all of the cases studied so far have been ideal setups without any kind of imperfections, something which can never be fully achieved in reality. Therefore, determining the sensitivity and tolerances of the scheme to any variations with respect to the ideal case is of key importance for assessing its experimental feasibility.

The need for performing tolerance studies for future plasma-based accelerator facilities is well known [CM19]. However, as pointed out in that reference, performing large and detailed tolerance studies with currently available PIC codes is unfeasible due to the high computational cost. Thus, there is also a need for faster numerical codes. As a consequence, tolerance studies performed so far are mostly limited to a single parameter, such as transverse beam offsets, and generally only by means of analytical models (e.g. [Lin+16; Thé+19; WR19]). More detailed studies have also been carried out for the undulator section of a plasma-based FEL [Seg15] but not for the plasma accelerator itself.

In this section, a comprehensive study of sensitivity and tolerances of the multistage concept is presented. This study, in which imperfections in the parameters of the electron beam, laser pulse, plasma profile and all beamline elements have been taken into account, is of unprecedented detail for a plasma-based accelerator. It has only been possible thanks to the Wake-T code presented in Chapter 4, which has allowed performing more than 10 000 simulations with different input parameters.

In addition to this simulation study, analytical expressions for the sensitivity of the scheme to the timing jitter between driver and witness have also been derived. These are useful to get a clear understanding of this possible source of energy jitter and to determine whether the multistage approach offers any improvement over single-stage acceleration.

8.6.1. Analytical estimates of sensitivity to timing jitter

In this section, analytical expressions for the final beam energy and energy spread with respect to initial injection phase in the first plasma stage are derived. In oder to simplify the problem, it will be assumed that both plasma stages are identical (same electric field slope E_z' and length L_p) and that the chicane has an $R_{56} = -2/\chi$, where χ is the chirp of the beam after the first stage. The fields are also assumed to be constant in time and E_z' to be uniform within the accelerating cavity. In this case, a particle injected in the reference (or ideal) longitudinal position ξ_{ref} would have an energy gain per stage of $\Delta\gamma_s = \mathcal{E}_{\text{ref}} L_p/c$, where $\mathcal{E}_{\text{ref}} = -eE_{z,\text{ref}}/mc$ and $E_{z,\text{ref}}$ is the longitudinal electric field experienced by the reference particle, i.e., $E_{z,\text{ref}} = E_z(\xi_{\text{ref}})$. Under these approximations, the final energy (after the second LWFA) of a particle which had an initial injection position $\xi_i = \xi - \xi_{\text{ref}}$ and an initial energy γ_0 can be expressed as

$$\gamma_f(\xi_i) = \gamma_0 + 2\Delta\gamma_s + \frac{3}{c^2}\frac{\mathcal{E}'^2 L_p^2}{\gamma_0 + \Delta\gamma_s}\xi_i^2 \,. \tag{8.3}$$

In order to obtain this expression, Equations (3.39) (up to second order) and (3.43) have been used and the equalities $\delta = \chi\xi_i$ and $\chi = (1/c)\mathcal{E}' L_p/(\gamma_0 + \Delta\gamma_s)$ have been applied. As expected, for $\xi_i = 0$, the final energy corresponds to that of the reference particle. However, when a certain injection offset exists, i.e., when $\xi_i \neq 0$, a second-order contribution appears due to the non-zero T_{566} in the chicane.

From Equation (8.3), which gives a clear correlation between the initial injection position and the final energy of a single particle, the final energy and energy spread of a particle bunch with arbitrary injection position can be obtained. Assuming a Gaussian bunch of length σ_z centered at $\xi_{i,c} = \langle\xi_i\rangle$, i.e., with a distribution function given by

$$f(\xi_i) = \frac{1}{\sqrt{2\pi}\sigma_z} e^{-\frac{(\xi_i - \xi_{i,c})^2}{2\sigma_z^2}} \,, \tag{8.4}$$

its final average energy can be calculated as

$$\langle\gamma_f\rangle = \int \gamma_f(\xi_i) f(\xi_i) d\xi_i = \gamma_0 + 2\Delta\gamma_s + \frac{3}{c^2}\frac{\mathcal{E}'^2 L_p^2}{\gamma_0 + \Delta\gamma_s}\left(\sigma_z^2 + \xi_{i,c}^2\right) \,, \tag{8.5}$$

where $\langle\gamma_0\rangle = \gamma_0$ is assumed. Again a second-order dependence with the injection position $\xi_{i,c}$ appears. The contribution from the bunch length arises due to the different energy of off-center particles, as predicted by Equation (8.3) and illustrated, for example,

in Figure 8.5. In the same way, the final energy spread of the bunch can also be obtained as

$$\sigma_\gamma = \left(\int \left[\gamma_f(\xi_i) - \langle \gamma_f \rangle \right]^2 f(\xi_i) d\xi_i \right)^{1/2} = \frac{3\sqrt{2}}{c^2} \frac{\mathcal{E}'^2 L_p^2}{\gamma_0 + \Delta\gamma_s} \sigma_z^2 \left(1 + 2\frac{\xi_{i,c}^2}{\sigma_z^2} \right)^{1/2} . \tag{8.6}$$

In a similar way, using Equation (8.5), the final RMS energy jitter $\sigma_{\langle\gamma\rangle}$ due to a normally-distributed initial timing jitter with an RMS value $\mathcal{T}_i$ can be found to be

$$\sigma_{\langle\gamma\rangle} = 3\sqrt{2} \frac{\mathcal{E}'^2 L_p^2}{\gamma_0 + \Delta\gamma_s} \mathcal{T}_i^2 . \tag{8.7}$$

In comparison, the RMS energy jitter for a single-stage accelerator with a length $L_p^{ss} = 2L_p$ would be given by $\sigma_{\langle\gamma\rangle}^{ss} = 2\mathcal{E}' L_p \mathcal{T}_i$. From this expression and Equation (8.7), it can then be obtained that the multistage scheme offers an improved energy stability with respect to single-stage acceleration, i.e., $\sigma_{\langle\gamma\rangle} < \sigma_{\langle\gamma\rangle}^{ss}$, if the timing jitter verifies the following condition:

$$\mathcal{T}_i < \frac{\sqrt{2}(\gamma_0 + \Delta\gamma_s)}{3\mathcal{E}' L_p} \simeq \frac{1}{\omega_p} , \tag{8.8}$$

where the second equality was obtained by assuming $\gamma_0 \ll \Delta\gamma_s = \mathcal{E}_{\text{ref}} L_p / c$ and typical blowout fields ($\mathcal{E}' = -\omega_p^2/2c$ and $\mathcal{E}_{\text{ref}} = \omega_p$). This equation therefore shows that the multistage concept is less sensitive to the incoming timing jitter as long as this jitter is below the plasma period. For example, for a typical density of $n_p = 10^{17}\,\text{cm}^{-3}$ and a timing jitter of $\mathcal{T}_i = 10\,\text{fs}$, the expressions obtained here indicate that the multistage concept effectively reduces the energy jitter by a factor of $\sim$5 with respect to a single-stage accelerator.

8.6.2. Detailed simulation study with Wake-T

In addition to the analytical studies for the energy and energy spread stability, a comprehensive study of the sensitivity of the scheme to variations of the beamline parameters (including the laser drivers, the witness beam and all the beamline elements) has been performed with the particle-tracking code Wake-T. This code, which was introduced in Chapter 4, was initially developed within the context of this thesis with the purpose of providing fast simulations for the initial design and sensitivity studies of plasma-based accelerators by using simplified wakefield models. In addition to plasma stages (including ramps) and plasma lenses, this code can also simulate other beamline elements such as drifts, dipoles, quadrupoles and sextupoles, therefore allowing for fast start-to-end simulations of complex accelerator beamlines such as in the multistage dechirping concept presented in this chapter.

This study of sensitivity and tolerances has been performed for a particular beamline configuration very similar to the original one presented in Section 8.3, but this time taking into account the presence of plasma up- and downramps. As a result, the requirements

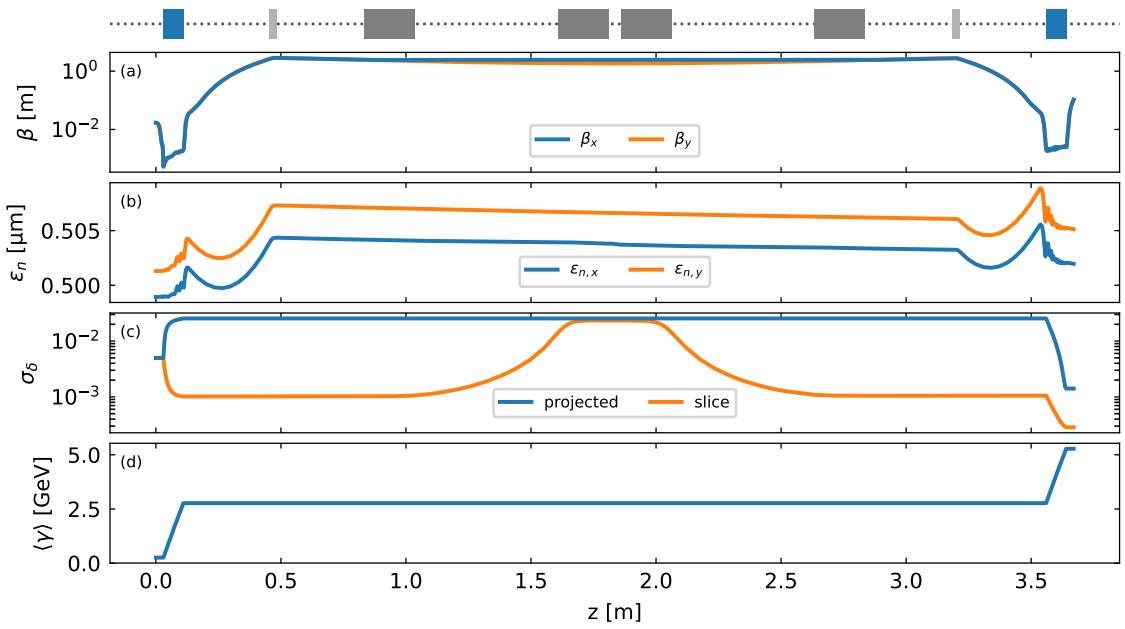

Figure 8.21.: Evolution of the beam parameters along the beamline used for the sensitivity and tolerances study. The parameters shown are (a) the beta function, (b) the normalized emittance, (c) the energy spread and (d) the energy. These parameters correspond to those of the reference case when no deviations from the ideal setup are present.

for matching the beam into the plasma stages are reduced, as well as its divergence after each stage. This allows the plasma lenses to be placed further away from the accelerating stages and reduces the required focusing strength. The resulting beamline has a total length of 3 m and is outlined in Figure 8.21 together with the evolution of the beam parameters for the reference case.

The plasma-accelerating stages have a length of 8 cm with up and down density ramps following the shape $n_{p,r} = n_{p,0}/(1 + z/L_r)^2$, where z represents the distance from the plateau and $n_{p,0} = 10^{17}\,\mathrm{cm}^{-3}$ is the plateau density. These ramps have a length of 3 cm and a L_r of 1 mm for the upramp of the first stage and of 2 mm for all others. The first and second APLs are placed 31.5 cm away from the end and beginning of the first and second plasma stage, respectively. They have a total length of 3 cm, a focusing gradient of $1000\,\mathrm{T\,m}^{-1}$ and are separated from each other by a distance of 2.7 m. This space is enough for placing the magnetic chicane, which is composed of 4 dipole magnets with a length of 20 cm and a magnetic field of 0.27 T, resulting in a bending angle $\theta = 5.9$ mrad. In this case, the separation between the first and second as well as the third and fourth dipoles is of 57.5 cm. These parameters are obtained from the required R_{56}, which is here of 49 µm as determined by the chirp $\chi = -4049\,\mathrm{m}^{-1}$ of the beam after the first stage. The witness electron beam is again externally injected and features the same initial parameters as in Section 8.3. That is, an energy of 250 MeV, a 0.5% energy spread with no chirp, a normalized transverse emittance $\epsilon_{n,x} = 0.5$ µm rad, 10 pC of charge, a FWHM

duration $\tau = 5$ fs and a peak current $I_{\text{peak}} \simeq 2$ kA. The only difference with respect to the initial proof-of-principle simulation study is on the Twiss parameters of the incoming beam. Due to the plasma upramp, the requirements on the beta function are relaxed to a value of $\beta_{x|y} = 1.7\,\text{cm}$, while a $\alpha_{x|y} = 0$ is maintained.

The simulation of the two plasma stages in Wake-T was performed using the "custom blowout" mode. This option allows one to manually specify the longitudinal (E_z and E_z') and transverse focusing ($K_{x|y}$) fields at the beam position and assumes that E_z' and $K_{x|y}$ are constant within the cavity. This is a good approximation for non-beamloaded cases and relatively short bunches ($\sigma_z \ll k_p^{-1}$), in which longitudinal variations in E_z' can be neglected, and for a guided laser far from depletion, so that the fields can be assumed constant in time. These conditions were well satisfied in the original proof-of-principle studies in Section 8.3. Therefore, the same wakefield excitation regime has been assumed here by using the values $E_z = -33\,\text{GV m}^{-1}$, $E_z' = 1.4 \times 10^{15}\,\text{V m}^{-2}$ and $K_{x|y} = 2.6\,\text{MT m}^{-1}$, which approximately correspond to the fields experienced by the beam in the PIC simulations performed for the proof-of-principle case in Section 8.3. In regards to the plasma ramps, they have been simulated assuming blowout focussing fields, i.e., $K_{x|y}(z) = (e/\epsilon_0 c) n_{p,r}(z)$, and neglecting the longitudinal fields. This is a good approximation for the high-power lasers under consideration, which are also able to generate strongly non-linear fields in the ramps. In addition, neglecting the longitudinal fields in the ramps is typically a good approximation due to their relatively short length and low density, which lead to a very small effect on the beam energy, as seen, for example, in Figures 8.12 and 8.18.

The study of sensitivities has been performed by varying independently and one by one the initial parameters of the beam and of the different beamline elements. In this way, the individual influence of each parameter on the properties of the final beam can be determined. The scanned input beam parameters include the initial Twiss functions ($\alpha_{x|y}$ and $\beta_{x|y}$), the initial transverse centroid offsets (x_c and y_c) and pointing angle (θ_x and θ_y) as well as longitudinal (or timing) offsets (ξ_0) with respect to the design injection phase. These are some of the most critical parameters to study for externally injected beams, because any pointing, position or timing jitter can have a potentially large impact on the final beam properties. Regarding the plasma cells, the list of tested variations includes the plasma density of both stages, the length of the plateau and the shape of the ramps, which has been studied by varying the parameter L_r for each ramp ($L_{\text{r,up,1}}$, $L_{\text{r,up,2}}$, $L_{\text{r,dn,1}}$ and $L_{\text{r,dn,2}}$). Fluctuations in the transport line have also been evaluated by testing variations in the focusing gradient of each plasma lens ($k_{\text{APL,1}}$ and $k_{\text{APL,2}}$) as well as in the bending angle of the magnets in the chicane (θ_m). In addition, the effect of fluctuations in the laser driver has also been studied, although limited only to the arrival time jitter in each stage ($\xi_{0,\text{laser,2}}$). This is because Wake-T does not currently have a model for realistic laser evolution nor for an accurate calculation of the wakefields in the blowout regime (fields must be instead specified externally), so fluctuations which would

affect the wakefield such as centroid offsets, pointing jitter, mismatched spot size to the plasma guiding channel or jitter in peak power or energy cannot be properly modelled. A systematic study of variations in these parameters would require instead a large number of expensive 3D PIC simulations which could not be carried out within the time frame of this thesis. The effect of plasma density fluctuations in wakefields could, however, be estimated because simple analytical scalings exist, i.e., $E_z \propto \sqrt{n_p}$, $E_z' \propto n_p$ and $K_{x|y} \propto n_p$.

The range of variations studied was different for each parameter. The transverse beam offsets were scanned between $\pm k_p^{-1} \simeq \pm 16.7\,\mu\text{m}$ while in the longitudinal plane the range was of $\pm 10\,\text{fs}$ and the pointing jitter at injection was between $\pm 1\,\text{mrad}$. On the Twiss parameters, a range of $\pm 50\,\%$ variations with respect to the design $\beta_{x|y}$ was studied, while the alpha parameter was varied between ± 1. The range for laser timing jitter in both stages was also related to the plasma skin depth as $\pm k_p^{-1}$. Regarding the plasma stages, the parameter L_r of each ramp was varied between $\pm 50\,\%$ of the design value, while the plasma density and length of the plateau were varied between $\pm 10\,\%$. Finally, the gradient of the plasma lenses and the bending angle of the magnets was also varied between $\pm 10\,\%$ of the design values. Each of these parameters was varied individually while keeping the rest with the ideal design values. A total of 30 simulations were performed for each parameter in addition to the reference case in which no variations were present. This accounts, therefore, for a total of 651 simulations which would have been unfeasible with a conventional PIC code. With Wake-T, however, the whole beamline can be simulated in less than a minute and multiple cases can be simultaneously computed in multi-core processors. Thus, this whole set of simulations was successfully performed in only $\sim$1 hour.

For each of the simulated cases, the final parameters of the electron beam at the end of the beamline (end of the last plasma downramp) were calculated. Therefore, the correlation between these final beam parameters, which can generally be denoted as b_i, and the input beamline parameters p_i can be studied. A widely used indicator for measuring the degree of correlation between two variables u and v is the Pearson correlation coefficient, which is defined as

$$\mathcal{P}(u,v) = \frac{\text{Cov}(u,v)}{\sigma_u \sigma_v}\,, \tag{8.9}$$

where $\text{Cov}(u,v)$ is the covariance between the two variables and σ_u and σ_v are the standard deviation of u and v, respectively. This parameter, which ranges between $-1 \leq \mathcal{P} \leq 1$, is a measure of the linear correlation between the two variables, where $\mathcal{P} = -1$ and $\mathcal{P} = 1$ indicate, respectively, a perfect negative or positive linear correlation. A value $\mathcal{P} = 0$ would instead imply that no linear correlation is present. However, in addition to linear relationships, for the range of parameter variations under consideration, some correlations are expected to be quadratic. In order to take into account these second-order contributions and determine whether a pair of variables features a linear or quadratic correlation, two values of the Pearson coefficient have been computed. That is, $\mathcal{P}_{\text{lin}} = \mathcal{P}(\Delta b_i, \Delta p_i)$ and $\mathcal{P}_{\text{quad}} = \mathcal{P}(\Delta b_i, \Delta p_i^2)$, where $\Delta b_i = b_i - b_{i,\text{ref}}$ and $\Delta p_i = p_i - p_{i,\text{ref}}$

are the variations of the final beam and input parameters with respect to their reference values.

The results of this analysis can be seen in Figure 8.22 for the linear correlations and in Figure 8.23 for the quadratic correlations. These matrices show that the correlations between variables are typically dominantly linear or quadratic, but not both at the same time. It can also be observed that the response of the final beam properties to changes in the input beamline parameters is symmetric in the x and y planes, while variations in the initial beam, such as transverse offsets or changes in the Twiss parameters, have an effect only on the transverse plane in which they occur. Regarding key parameters, such as the beam emittance, it can be seen that the contributions are predominantly of second order and arise mostly from transverse offsets and mismatched Twiss parameters. These mismatches can be caused by variations in the initial beam parameters, but also due to changes in the plasma ramps and the gradient of the plasma lenses, which change the evolution of the transverse phase-space of the beam, and due to fluctuations in the plasma density and length in the first stage, which would lead to beam energy fluctuations and thus affect the beam transport to the second stage. In terms of the beam energy, there are first order correlations with the plasma length and density, which obviously lead to changes in the total energy gain in the accelerator, as well as with the bending angle in the chicane and the timing of the second laser driver, since both have an impact on the the injection phase in the second stage. In addition, there are also second order correlations with the initial beam parameters, in particular with transverse (and pointing) offsets and timing jitter. This is because, as explained in Chapter 7, any betatron motion, enhanced by initial offsets and non-zero pointing angle will lead to a slippage towards the back of the wake, where the accelerating fields are stronger. The second-order correlation with the timing jitter is expected from the analytical derivations in Section 8.6.1 due to second-order contributions in the chicane for off-energy beams. The relative slice energy spread has the same linear correlations as the beam energy but with inverted sign. This is because changes which lead to increased energy naturally result in a smaller relative energy spread at the slice level. This is not visible for the projected energy spread because it is dominated by the energy chirp, whose correlations are predominantly of second order. These arise from any parameter fluctuations that might lead to an under- or overcompensation of the chirp, such as length or density changes in the two plasma stages or a different bending angle in the chicane. In addition, there is also a dependence on the timing jitter which is expected from second order effects in the chicane, as described in the previous section. The slice energy spread features also many quadratic correlations, all of them arising from parameters which might cause a mismatch of the beam and thus further enhance the betatron-induced energy spread as given by Equation 7.15. Finally, two other key beam parameters, the bunch length and peak current, exhibit correlations with the same input parameters but of opposite sign, since an increase in bunch length naturally leads to a smaller peak current, and vice-versa. The most im-

Table 8.7.: Set of requirements on the stability of certain key beam parameters used for the tolerance study. The gamma Twiss function is used as a measure of the beam divergence.

Parameter	**Symbol**	**Required stability [%]**
Normalized emittance	$\epsilon_{n,x\|y}$	50
Normalized emittance (slice)	$\epsilon_{n,x\|y,\mathrm{sl}}$	10
Mean energy	$\langle\gamma\rangle$	0.5
Relative energy spread	σ_δ	50
Relative energy spread (slice)	$\sigma_{\delta,\mathrm{sl}}$	10
Peak current	I_{peak}	10
Gamma Twiss function	$\gamma_{x\|y}$	50

portant correlations are linear, and arise from parameter fluctuations that might lead to a different bunch length after the chicane. That is, changes in the length and density in the first plasma stage, changes in the bending angle, or timing jitter at injection. Some second order correlations can also be seen with the initial transverse offsets and pointing angle, but they have a very small absolute effect on the bunch length ($\lesssim 0.03$ fs) and thus do not impact significantly the peak current.

The performed analysis shows that, for the range of variations considered, the main correlations in the system can be described by a linear or quadratic relationship and, therefore, by a second-order polynomial fit

$$\Delta b_i = a\,\Delta p_i^2 + b\,\Delta p_i\,, \tag{8.10}$$

where a and b are constant coefficients. Therefore, if a set of requirements on the final beam parameters is established, that is, on the maximum deviation from the reference value, the tolerances on the input parameters can then be determined. For the case presented here, the chosen requirements on the stability of the beam energy, energy spread, emittance, peak current and divergence are included in Table 8.7. From these specifications, the maximum tolerable variation in each input parameter has been calculated and is shown in Table 8.8. In order to obtain these values, two polynomial fits as in Equation (8.10) have been performed for each pair of variables: one for negative variations ($\Delta p_i \leq 0$) and another for positive deviations ($\Delta p_i \geq 0$). This allows for a more accurate modelling of the correlations, since the response of Δb_i is, in some cases, different for positive or negative variations in the input parameters.

The results of the tolerance study summarized in Table 8.8 show that, as expected, the maximum transverse and pointing offsets are limited by the projected emittance growth. With the specified requirements of a maximum 50 % emittance increase it is found that transverse offsets of up to $\sim$5 µm and pointing fluctuations of up to $\sim$0.3 mrad can be tolerated. These are values that should be achievable by current RF linacs, where the

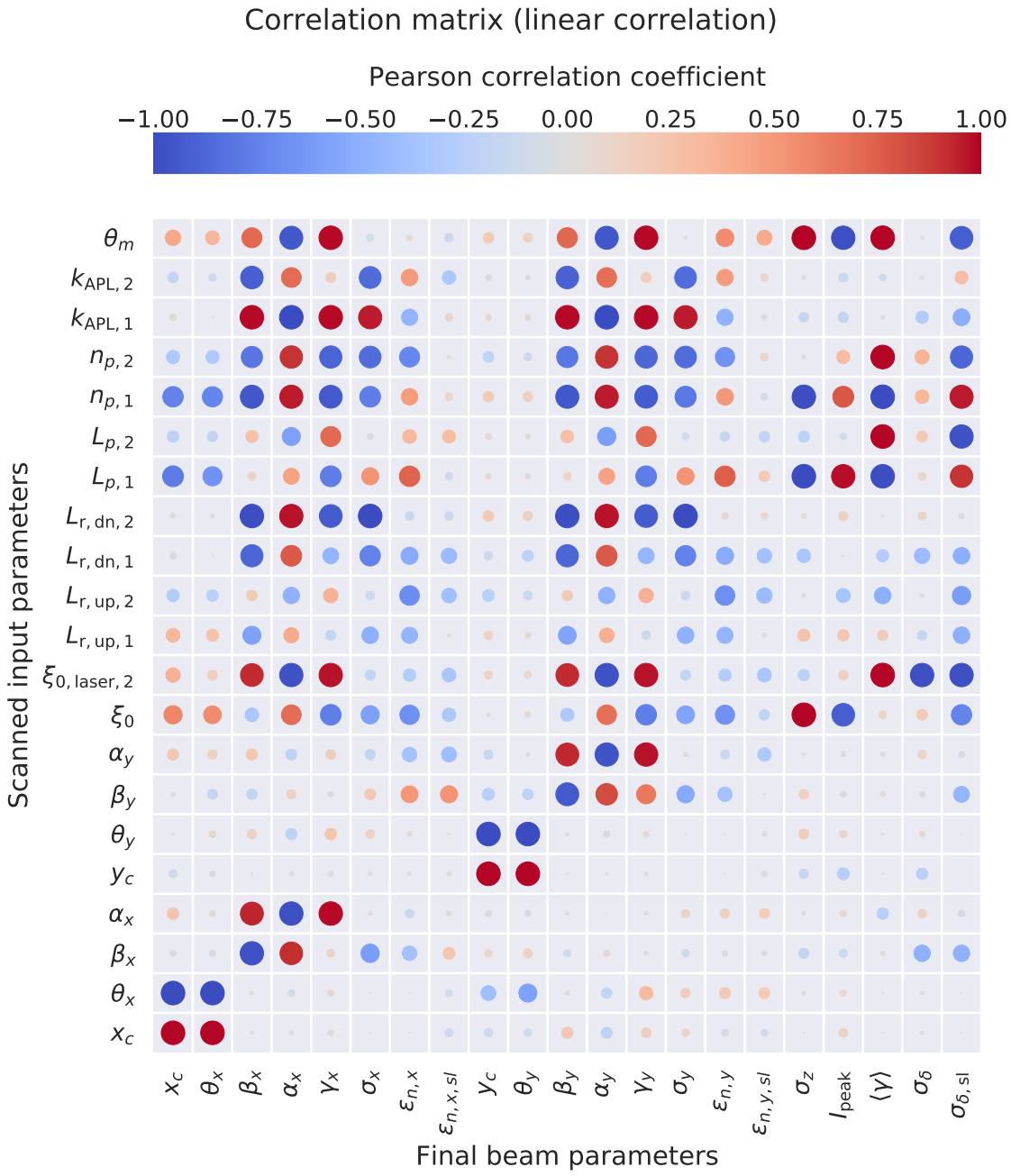

Figure 8.22.: Correlation matrix between the input parameters and the final beam properties showing whether a particular pair of parameters exhibits a linear correlation. The size of each dot is scaled with the absolute value of the Pearson coefficient. Thus, bigger dots are indicative of a more clear linear correlation.

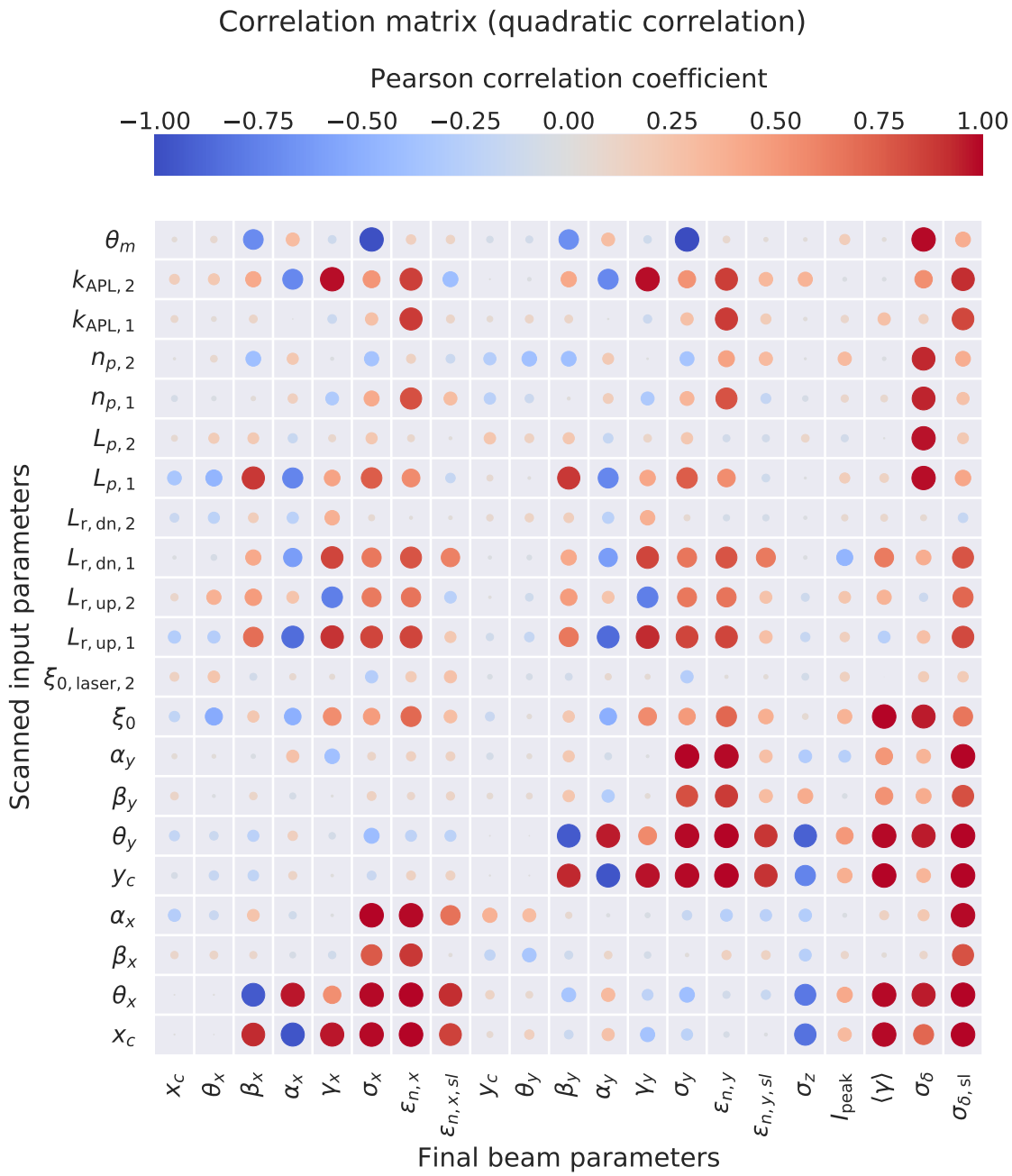

Figure 8.23.: Correlation matrix between the input parameters and the final beam properties showing whether a particular pair of parameters exhibits a quadratic correlation. The size of each dot is scaled with the absolute value of the Pearson coefficient. Thus, bigger dots are indicative of a more clear quadratic correlation.

Table 8.8.: Maximum tolerable variations in the input parameters so that the specified stability requirements are satisfied. The calculated range corresponds only to individual variations, i.e., to the maximum tolerable variation in a single parameter when all the other parameters have their ideal design value. For each input variable, the design value is shown in the third column and the maximum positive and negative variations with respect to this reference value are shown both in absolute and relative (in parenthesis) units. The requirement limiting each of these variations is shown in the two rightmost columns.

Input parameter			**Maximum variation**		**Limited by**	
Name	Units	Value	Negative	Positive	Negative	Positive
x_c	µm	0.0	−4.89 (-29.1%) *	4.85 (28.9%) *	$\epsilon_{n,x}$	$\epsilon_{n,x}$
θ_x	mrad	0.0	−0.28 **	0.28 **	$\epsilon_{n,x}$	$\epsilon_{n,x}$
β_x	mm	17.0	−11.27 (-66.3%)	20.86 (122.7%)	$\sigma_{\delta,\mathrm{sl}}$	$\epsilon_{n,x}$
α_x		0.0	−0.88 **	0.92 **	$\sigma_{\delta,\mathrm{sl}}$	$\sigma_{\delta,\mathrm{sl}}$
y_c	µm	0.0	−4.92 (-29.3%) *	4.90 (29.1%) *	$\epsilon_{n,y}$	$\epsilon_{n,y}$
θ_y	mrad	0.0	−0.28 **	0.28 **	$\epsilon_{n,y}$	$\epsilon_{n,y}$
β_y	mm	17.0	−11.18 (-65.8%)	22.63 (133.1%)	$\sigma_{\delta,\mathrm{sl}}$	$\epsilon_{n,y}$
α_y		0.0	−0.90 **	0.95 **	$\sigma_{\delta,\mathrm{sl}}$	$\sigma_{\delta,\mathrm{sl}}$
ξ_0	fs	0.0	−1.26 (-2.2%) *	1.10 (2.0%) *	σ_δ	σ_δ
$\xi_{0,\mathrm{laser},2}$	fs	0.0	−0.79 (-1.4%) *	0.79 (1.4%) *	$\langle\gamma\rangle$	$\langle\gamma\rangle$
$L_{\mathrm{r,up},1}$	mm	1.0	−0.19 (-19.1%)	0.40 (39.8%)	$\sigma_{\delta,\mathrm{sl}}$	$\sigma_{\delta,\mathrm{sl}}$
$L_{\mathrm{r,up},2}$	mm	2.0	−0.47 (-23.3%)	0.89 (44.4%)	γ_y	γ_y
$L_{\mathrm{r,dn},1}$	mm	2.0	−0.57 (-28.6%)	0.88 (43.8%)	$\epsilon_{n,y}$	$\sigma_{\delta,\mathrm{sl}}$
$L_{\mathrm{r,dn},2}$	mm	2.0	−0.24 (-11.8%)	0.48 (24.0%)	γ_x	γ_y
$L_{p,1}$	cm	8.0	−0.09 (-1.1%)	0.09 (1.1%)	$\langle\gamma\rangle$	$\langle\gamma\rangle$
$L_{p,2}$	cm	8.0	−0.09 (-1.1%)	0.09 (1.1%)	$\langle\gamma\rangle$	$\langle\gamma\rangle$
$n_{p,1}$	$10^{17}\mathrm{cm}^{-3}$	1.0	−0.02 (-2.4%)	0.03 (2.6%)	$\langle\gamma\rangle$	$\langle\gamma\rangle$
$n_{p,2}$	$10^{17}\mathrm{cm}^{-3}$	1.0	−0.02 (-2.4%)	0.03 (2.6%)	$\langle\gamma\rangle$	$\langle\gamma\rangle$
$k_{\mathrm{APL},1}$	$\mathrm{kT\,m}^{-1}$	1.0	−0.13 (-12.9%)	0.16 (15.9%)	$\epsilon_{n,x}$	$\epsilon_{n,y}$
$k_{\mathrm{APL},2}$	$\mathrm{kT\,m}^{-1}$	1.0	−0.10 (-9.9%)	0.09 (9.0%)	γ_y	γ_y
θ_m	mrad	5.9	−0.03 (-0.6%)	0.03 (0.6%)	$\langle\gamma\rangle$	$\langle\gamma\rangle$

* Relative variation calculated with respect to the plasma skin depth.
** Relative variation not calculated due to reference value being zero.

position jitter is typically a fraction of the beam size (on the micron level in this case) and the pointing jitter is typically on the few-µrad range. With respect to a mismatch in the initial Twiss parameters, the slice energy spread becomes also a limiting factor. This is again due to the slippage effects introduced in Chapter 7, whose impact on the slice energy spread is enhanced for mismatched beams as seen in Equation (7.15). The accepted variations are however relatively large, reaching even the $\sim$100 % range. These relatively relaxed tolerances both in the initial offsets and Twiss parameters can be attributed to the presence of plasma ramps, which greatly mitigate the impact of these imperfections. The most critical beam parameter appears to be the arrival time jitter, which should be on the $\sim$1 fs level to fulfill the stability requirements. This tight requirement, which is beyond current state-of-the-art, arises due to the second-order dispersion in the chicane and its impact on the energy, energy spread and current profile of off-energy beams. Ways of mitigating this issue, such as the insertion of sextupole magnets in the chicane, should therefore be explored in future work. Otherwise, this issue seems to indicate that a combination of this multistage scheme with the timing-jitter correction concept presented in Chapter 6 might be required. A future study on the feasibility of this combination would also be of high interest.

The timing jitter of the second laser with respect to the first could also be an issue if these two pulses cannot be synchronized down to the $\sim$1 fs level. For this, it is important that both drivers are intrinsically synchronized as could be achieved, for example, by splitting them from a single initial pulse. Otherwise, large energy fluctuations in the final beam energy could occur. The energy stability is also the limiting requirement for the main plasma parameters, i.e., the length and density of the plateau, which should be controlled down to the percent level. A stable shape of the plasma ramps is also important to have a stable beam divergence and avoid strong mismatches with the Twiss parameters of the beam in order prevent emittance and slice energy spread growth. The same reasoning applies to the beam transport elements, i.e., the plasma lenses in this case, although the tolerances on the focusing gradient allow for significant variations on the $\sim$10 % range. These relaxed conditions arise again, most likely, from the presence of plasma ramps. Finally, the analysis shows that the bending angle (and therefore the magnetic field) of the dipoles in the chicane should be controlled with sub-percent precision in order to avoid large fluctuations in the final beam energy, which is the main limiting factor for this parameter.

The performed tolerance analysis provides a useful overview about which parameters might be more critical for an experimental realization of the scheme, as well as the acceptable range of imperfections. It should be noted, however, that the tolerances shown in Table 8.8 were obtained for parameter variations performed independently and one-by-one. That is, they are the tolerances for the maximum variations in each parameter assuming that all the remaining input parameters retain their ideal design values. In a real setup, however, all parameters will have imperfections at the same time and might

also jitter on a shot-to-shot basis. Therefore, in order to evaluate the performance of the scheme when multiple errors are present, an additional simulation study with Wake-T has been performed. In this study, 10 000 different simulations have been carried out in which all the input parameters listed in Table 8.8 were simultaneously varied. For each of the simulated cases, the value of each input parameter was randomly selected from the tolerance range defined in the table. Owing to the large amount of simulations, which could only be carried out thanks the Wake-T code, the performance of the scheme can be statistically analyzed, including the expected beam parameters and their RMS fluctuations.

The results of this study are displayed in Figure 8.24, where the final parameters of the beam are shown for all simulated cases. As it can be seen, some variables such as the mean energy and peak current seem to be normally distributed, while others such as the emittance and energy spread (both projected and slice) or the divergence are negatively skewed. Although the average beam emittance and energy spread are larger than the design values in an ideal setup with no errors, a $\sim$1 µm emittance, sub-percent projected energy spread and sub-permille slice energy spread are still achieved, as required for FEL applications. The RMS jitter of the beam parameters is also not far from the original requirements listed in Table 8.7 and even below them for the case of the peak current and projected energy spread. This therefore indicates that the original tolerance requirements obtained for single parameter variations provide also an effective guideline when all parameters are allowed to fluctuate.

8.6.3. Discussion

In this section, a comprehensive simulation study of the sensitivity and tolerances of the multistage scheme has been performed. This study, in which possible errors in the parameters of the incoming beam, the laser, the plasma stages (including ramps), the plasma lenses and the chicane have been considered, is of unprecedented detail and scale for a plasma accelerator. It has only been possible here thanks to the fast Wake-T code developed within this thesis.

A first study was initially carried out to determine the effect of individual imperfections and clearly establish correlations to the final beam parameters. From this study, a set of tolerances could be defined by establishing a fixed set of stability requirements on the final beam parameters. After this initial analysis of correlations and tolerances, a second study was carried out in which the performance of the beamline was evaluated when all possible imperfections are allowed to occur simultaneously. For this, 10 000 different simulations with randomly selected input parameters (but within the tolerance range defined before) were performed.

The results from these studies suggest that this acceleration scheme seems to be most sensitive to the timing jitter between the laser and the electron beam, requiring a stability of $\sim$1 fs for the simulated beamline. This condition, which arises due to second order

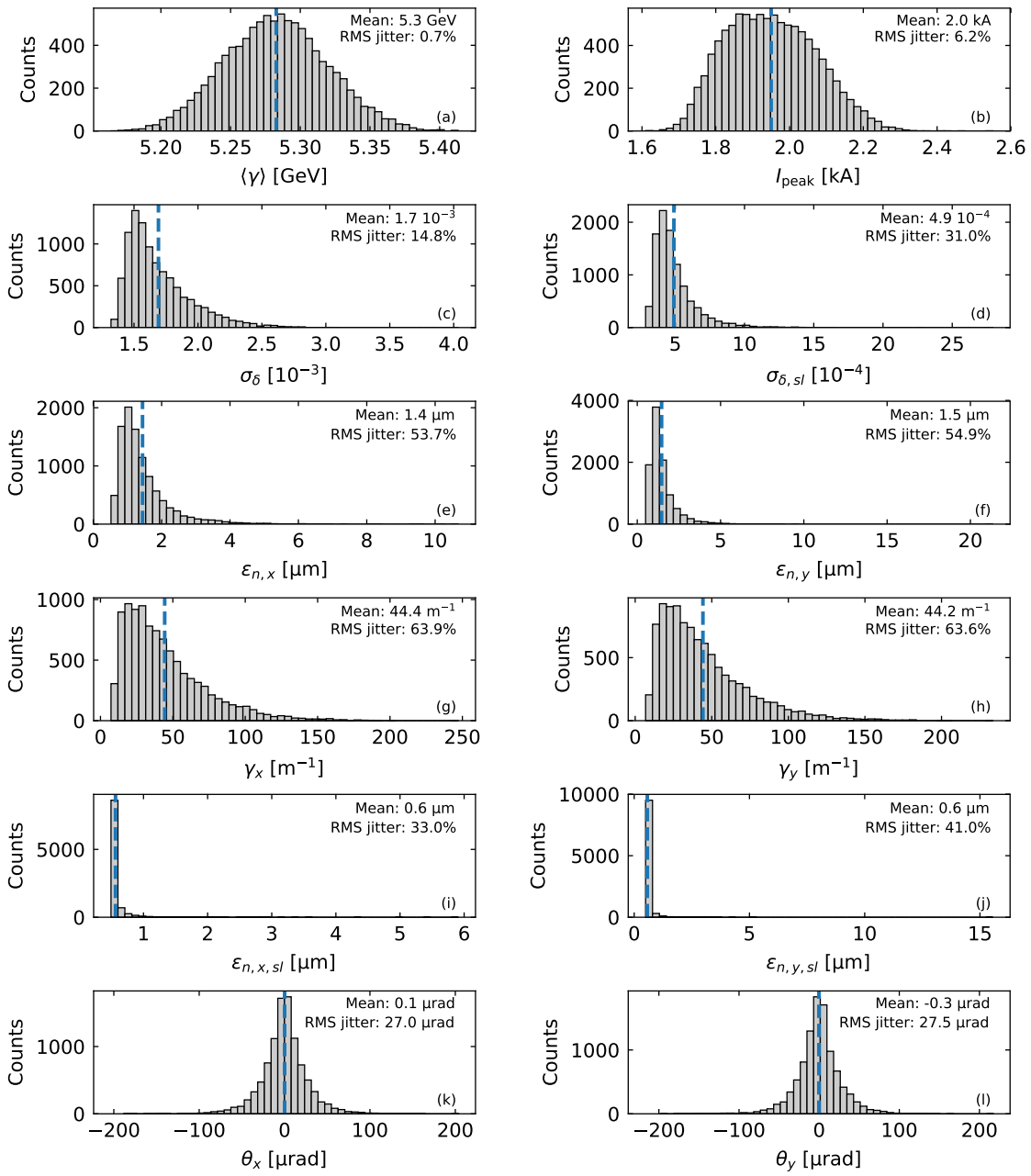

Figure 8.24.: Distribution of final beam parameters for all the 10 000 simulated cases: (a) mean energy, (b) peak current, (c) projected energy spread, (d) slice energy spread, (e) projected normalized emittance in x and (f) in y, (g) gamma function in x and (h) y, (i) slice normalized emittance in x and (j) in y, and (k) beam pointing in x and in (l) in y. The mean value of each distribution is indicated by a vertical dashed blue line.

dispersion in the chicane, is well beyond current state-of-the-art and should therefore be addressed in future work. Possible ways of mitigating it, such as including sextupole magnets in the chicane, should be explored. Of particular interest would be a combination of this multistage acceleration scheme with the timing-jitter correction concept presented in Chapter 6, which could potentially solve this issue.

Otherwise, when all tolerance requirements are satisfied, the study of random initial conditions has shown that beams suitable for FEL applications can be reliably produced. It should be noted, however, that not all possible sources of imperfections could be evaluated in this study due to current limitations of Wake-T. These include, for example, fluctuations in the laser power, shape, transverse position and jitter, or misalignments of the beamline elements. More detailed studies and even full PIC simulations might therefore be required for an accurate estimation of the impact of these imperfections.

To finalize, it should be noted that the numerical values for the tolerances and stability determined here apply only strictly to the particular beamline that was simulated. They should therefore not be taken as fundamental limits or requirements of this multistage scheme. They are however useful to determine and understand which parameters might or might not be critical for its performance and discern possible solutions.

8.7. Application to internal injection: towards stable beams with low energy spread

The multistage concept for plasma-based accelerators presented in this chapter has been shown to be an effective method for producing ultra-low energy spread beams in the GeV range fulfilling FEL requirements. Within this thesis, the performance of this concept has only been evaluated with externally-injected beams. However, since most of the current experiments with laser-driven accelerators rely on some kind of internal injection method, it is of general interest to discuss whether this multistage scheme can also be applied in this case, and whether it might offer any advantage. In this section, as a final remark for the chapter, a possible implementation of this scheme when the electron bunch is internally injected is proposed. Its potential and possible advantages in producing low energy spread beams with stable energy are briefly discussed, but no detailed studies or simulations are included. This should instead be the focus of future work.

In principle, if an LWFA stage with internal injection produces beams with a negative linear energy chirp, the same scheme as in Figure 8.1 could be directly applied making sure that no further injection is triggered in the second accelerating stage. However, as explained in the following, it might also be possible (and even more interesting) to apply this scheme when the beams from the first stage have no longitudinal energy correlation.

Such unchirped beams can be obtained when the charge is sufficiently high to beamload the wake and cancel the slope of the accelerating field. In this case, the higher charge maximizes the efficiency of the accelerator while minimizing the energy spread of the

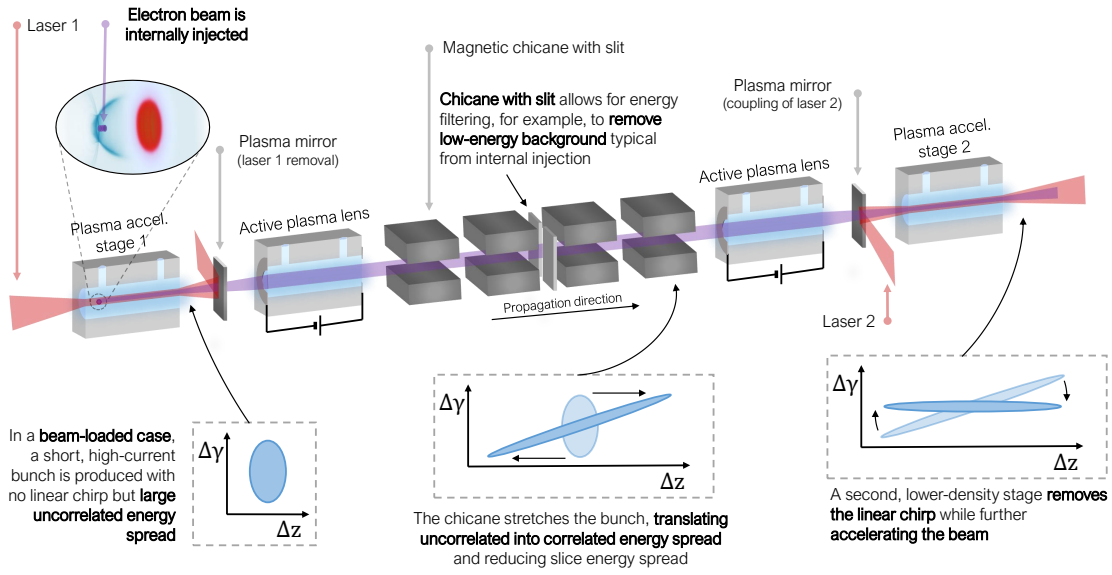

Figure 8.25.: Working principle of the multistage concept for the case of an internally-injected electron beam with optimal beam loading in the first stage. The large uncorrelated energy spread at the end of the first LWFA is converted into a positive chirp in the chicane which can then be effectively removed in the second stage.

beam. However, even with optimal beam-loading conditions, LWFAs with internal injection are known to produce a large energy spread even on the 10 % range [Cou+17]. The energy spread in these cases is therefore expected to be mostly uncorrelated, and could be arising due to effects such as the betatron slippage presented in Chapter 7.

Due to this high energy spread, a chicane can still be effectively used to modify the longitudinal phase space. In fact, if the energy spread is mostly uncorrelated, the beam can be interpreted to be at maximum compression, so the task of the chicane is only to shear forward the longitudinal phase space instead of performing a chirp inversion, or overcompression, as in the original concept. As seen in Figure 8.25, where this internal injection implementation is summarized, this shearing in the chicane translates the uncorrelated energy spread into a positive chirp by increasing the bunch length. In turn, this results also in a reduced slice energy spread and peak current [Mai+12]. Both the increase in bunch length and the reduction in slice energy spread are beneficial for FEL applications, and even a smaller peak current might be an advantage. This is because internally-injected beams in LWFAs can have a very large charge of up to $\gtrsim 100\,\mathrm{pC}$ with ultrashort durations down to $\lesssim 10\,\mathrm{fs}$, resulting in peak currents above 10 kA [Cou+17]. Therefore, for a typical energy of $\sim$100 MeV, this can lead to strong space-charge effects after the plasma stage and lead to emittance growth. Thus, increasing the bunch length by, for example, a factor of $\sim$10, would still allow to preserve a kA-range current, as needed for FELs, while mitigating these issues.

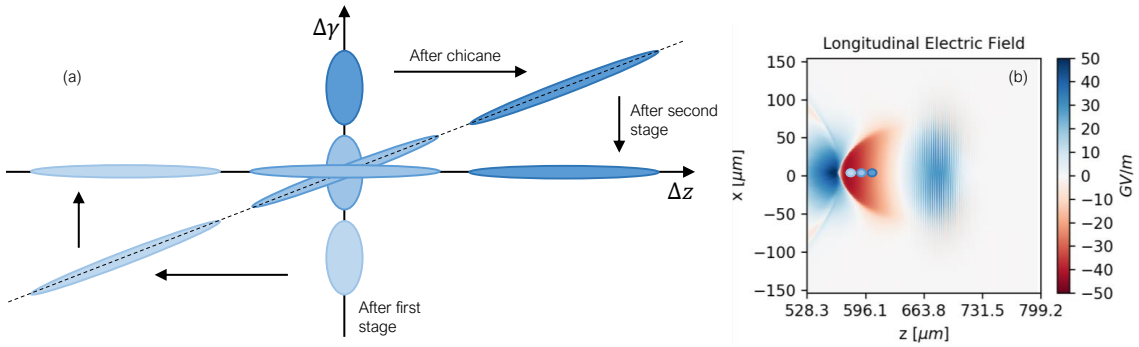

Figure 8.26.: Visualization of the correction of the beam energy spread and jitter in the multistage concept. (a) Longitudinal phase-space evolution of three beams with different energy after the first LWFA. The chicane correlates the beam energy to its arrival time at the second stage, which can then correct the initial energy differences and yield a stable energy output. (b) Schematic view of the longitudinal position of each beam in the wakefield of the second stage.

Apart from these benefits, the key point of this scheme is that the uncorrelated energy spread is translated into a positive energy correlation, which can therefore be corrected in a second stage and thus lead to a drastic reduction of the beam energy spread while, potentially, further boosting its energy. In contrast to the first stage, which would probably operate at a plasma density in the typical range of $10^{18}\,\mathrm{cm}^{-3}$ to $10^{19}\,\mathrm{cm}^{-3}$ used in internal injection, the second LWFA should have a lower density around $\lesssim 10^{17}\,\mathrm{cm}^{-3}$ to accommodate for the stretched bunch, and should operate in a regime where no further electron injection occurs.

Another potential advantage of this scheme is that, thanks to the combined action of the chicane and the second stage, it could allow for a significant improvement of the shot-to-shot stability of the final beam energy. The principle behind this, as outlined in Figure 8.26, is the same as in the case for external injection. Considering only the first-order dispersion in the chicane, any variation $\Delta\gamma = \gamma - \gamma_{\mathrm{ref}}$ with respect to the reference energy γ_{ref} after the first stage would result in a change in its longitudinal position $\Delta z = z - z_{\mathrm{ref}} = R_{56}\Delta\gamma$. Thus, beams with $\Delta\gamma < 0$ will move towards the back while those with $\Delta\gamma > 0$ will have an earlier arrival time at the second stage. Thanks to this, and assuming a constant $E_z' > 0$ around the reference injection phase in the second LWFA, the initial energy differences will be naturally compensated at the end of the accelerator.

This two-stage setup might therefore offer the possibility of strongly reducing the beam energy spread and energy jitter in comparison to a single-stage LWFA with internal injection. In addition, the chicane could also be used to filter the range of accepted energies by including a slit, as performed in [And+18], which would allow, for example, for the removal of the low-energy background typically observed in internal injection (see e.g. [Cou+17]). As such, this is an interesting option to consider in future studies which could be tested in existing LWFA accelerators and which would circumvent one of the biggest

challenges of an implementation with external injection: the timing jitter between driver and witness, as discussed in the previous section. In addition to FELs, a particularly interesting application of this scheme would its use as an injector for a storage ring, such as a synchrotron light source, where a sub-percent energy stability is required. This requirement arises due to the drop in dynamic aperture for any energy fluctuations, which should therefore be only a small fraction of the momentum acceptance, which typically is on the few-percent range [Sch+18; Bri19].

8.8. Summary and conclusion

In this chapter, a novel plasma-acceleration concept for producing beams with ultra-low energy spread has been presented. This scheme proposes performing the acceleration in two plasma stages which are joined by a magnetic chicane. In this way, the energy chirp naturally acquired in the first LWFA is inverted in the chicane and can be subsequently compensated for in the second. Detailed start-to-end simulations of this concept have shown that multi-GeV beams with sub-per-mille energy spread could be achieved, which is at least one order of magnitude beyond current state-of-the-art. The simulation studies have also shown that potential issues such as space-charge or CSR are not expected to be a problem. This scheme therefore offers a new solution to the major energy spread challenge of plasma-based accelerators, which currently limits their usability, and could pave the way towards groundbreaking applications such as compact free-electron lasers. A potential drawback of this scheme could be, however, its efficiency. This is because its energy spread performance relies on the linearity of the chirp after the first stage, which is more easily achieved in weakly beam-loaded (and thus less efficient) wakefields.

Thanks to the good performance demonstrated by the proof-of-principle simulations, a dedicated conceptual beamline for a 6 GeV EuPRAXIA accelerator based on this technique has been designed. Detailed start-to-end simulations of this setup also showed great promise and resulted in its selection as a baseline option for the EuPRAXIA CDR [Ass+19]. This study showed, however, that the microbunching instability in the chicane can be a severe issue. To avoid this, beams with a current profile that is initially smooth were found to be required, for which a laser heater in the RF linac might be necessary. Future detailed studies about this instability and about the potential benefits of laser heater should therefore be performed.

In addition to these studies, which relied on powerful lasers close to the petawatt range, a conceptual design for a lower-energy 1 GeV beamline which could be realized with more commonly available laser technology (5 J total energy and $<$100 TW per stage) has been presented. Detailed start-to-end simulations of this setup showed again that beams with sub-percent (total) and up to sub-per-mille (slice) energy spread could be achieved. This conceptual beamline has also shown that an implementation of the laser coupling based on conventional (instead of plasma) mirrors seems possible, and that the

beams can be successfully transported between LWFA stages separated by $\sim$9 m without meaningful impact on their quality.

Having shown that multiple implementations of this concept are possible with a variety of beamline designs, a comprehensive study of sensitivity and tolerances was carried out. From this analysis, which is of unprecedented detail for a plasma accelerator, it was determined that the most critical parameter appears to be the timing jitter between the driver and the witness. The required stability for the particular beamline tested was of $\sim$1 fs. Thus, a combination of this multistage scheme with the concept for timing jitter correction presented in Chapter 6 might be necessary. A future study on the feasibility of this combination would therefore be of high interest.

To finalize, a possible implementation of this scheme for an LWFA with internal injection has been discussed. Initial considerations seem to indicate that this scheme could significantly improve the energy stability and energy spread of these accelerators. At the same time, it would naturally overcome the timing jitter issue found with external injection. Therefore, it appears to be an option which presents multiple potential advantages and which would be worth exploring in future work.

Other studies which could not be performed within the thesis, but which would definitely be of interest are, for example, FEL simulations of the generated beams. This would be a relevant final test of the beam quality achieved, particularly because FELs are main target application of this scheme. In addition, since this multistage concept has been shown to heavily rely on active plasma lenses, further studies regarding these elements should be performed towards a realistic implementation. In particular, the possibility of realizing APLs operating at the low densities considered here should be explored, as well as designs with large apertures. The same could be said about the plasma mirrors. If an implementation of the laser coupling based on them is chosen, detailed simulations of their impact on the beam parameters should be performed. Also, further research in evaluating the use of liquid crystal films should be carried out.

9. Conclusion and outlook

In this thesis, two new concepts for producing stable and high-quality electron beams from plasma-based accelerators have been developed and studied in detail. Both solutions address important remaining challenges for these novel devices. Firstly, a scheme combining a short LWFA stage with a magnetic chicane has been shown to reduce the arrival time jitter between a laser pulse and an external electron beam down to the sub-femtosecond level. This unprecedented synchronization is an essential requirement for a reliable LWFA with external injection. Secondly, a novel multistage scheme for producing ultra-low energy spread beams with plasma-based accelerators has been devised. Detailed proof-of-principle simulations show that, even when including space-charge and CSR effects, electron beams with multi-GeV energy, kiloampere current, sub-micron emittance and sub-percent (total) and sub-permille (slice) energy spread could be produced, fulfilling FEL requirements. In addition to these studies, conceptual designs of a 6 GeV accelerator for EuPRAXIA as well as of a 1 GeV beamline for ATHENA which are based on this multistage scheme have been worked out.

Achieving beams with sub-permille energy spread in the simulated beamlines has only been possible thanks to a better understanding of the particle dynamics in plasma-based accelerators. Detailed studies of the single-particle evolution have shown that betatron motion, which is particularly relevant in this type of accelerators, can be a significant source of slice energy spread. In order to understand this previously neglected effect, a novel analytical theory which fully explains these dynamics and their impact on the beam has been developed. This has allowed certain guidelines to be defined on how to mitigate this issue such that the desired energy spread performance can be achieved.

In addition to the baseline multistage designs for ultra-low energy spread beams, a comprehensive study of sensitivity and tolerances of this scheme has been carried out. This has been possible thanks to a fast particle-tracking code based on simplified wakefield models which has been integrally developed within this thesis. The results of this study, for which more than 10 000 simulations have been performed, point particularly towards a high sensitivity of the multistage scheme to the arrival time jitter between the laser driver and the witness beam. Thus, for external injection, the two schemes for synchronization and low energy spread developed in this thesis could be combined in a single three-stage setup.

The new concepts for plasma-based acceleration presented in this work therefore offer a new path towards achieving electron beams of unprecedented quality and reliability. In fact, the energy spread performance of the produced beams approaches that of current

state-of-the-art RF accelerators. As such, LWFAs based on the principles presented here could offer a compact and cost-effective alternative to current FEL facilities, shrinking the accelerator length to the 10 m-scale, as shown in the presented studies. Thanks to these good prospects, the 6 GeV multistage LWFA beamline presented in this work was selected as a baseline design for the international EuPRAXIA project [Ass+19].

Further research in several fronts is however needed for a successful experimental demonstration of these promising schemes. One of the key items to be addressed is the need for further developments in the design of plasma capillaries, so that optimized plasma-to-vacuum transitions for beam matching and extraction can be produced. Another challenge is the development of thin plasma mirrors, such as those based on liquid crystal films, to allow for a compact setup of the laser in- and out-coupling while having no negative impact on the electron beam parameters. Of key importance is further progress in active plasma lenses, which are required for all the schemes presented here. In particular, plasma lenses which can operate at densities in the 10^{15} cm^{-3}-range should explored, as this might be required to minimize the impact of beam-induced wakefields. Also, depending on the laser coupling implementation, plasma lens designs with large, $\sim$1 cm apertures would be needed for good transmission of the laser driver.

In addition to the challenges posed by staging, further work is needed to evaluate the performance of the plasma-acceleration schemes when realistic laser profiles are considered. This is of particular importance with regards to guiding in the LWFA stages, for which the use of a laser pre-pulse should also be evaluated. It has also been shown that, for realistic electron beams produced in an RF linac, a micro-bunching instability can be triggered in the chicane. This is a well-known problem in FEL facilities which can be solved by the introduction of a laser heater. Thus, further studies should be carried out to determine whether such a device might also be required here. Finally, additional tolerance studies should be performed to determine the sensitivity to parameters such as laser imperfections (misalignments, energy jitter, etc.) which could not be evaluated here due to current limitations in the simulation tools used. In this regard, possible strategies for relaxing some tolerance requirements should be explored. For example, for the particular issue of the timing jitter, a combined version of the synchronization and energy spread compensation schemes should be developed. Alternatively, the addition of sextupoles to the chicane for minimizing the second order dispersion should be studied.

A possible way of overcoming the challenges posed by external injection, especially the timing jitter, would be to develop an implementation of the multistage concept based on internally-injected beams, as discussed at the end of this work. This could also lead to a more compact, simpler, and possibly more energy-efficient setup. It is therefore a promising alternative which could be implemented in existing LWFAs and lead to a significant improvement of the energy spread and energy stability performance of the accelerators. The potential of this new alternative concept for high-quality beams should therefore be explored in detail in future work.

Appendices

A. Detailed derivation of expressions in Chapter 7

A.1. Derivation of the longitudinal slippage

The longitudinal slippage of particles in the speed-of-light frame, as given by Equation (7.2), can be simplified, under the assumption that $v_z = (v^2 - v_x^2 - v_y^2)^{1/2} \simeq v - (v_x^2 + v_y^2)/2v$, to

$$\Delta\xi(t) = \int_0^t v_\xi(t)\, dt \simeq \int_0^t \left[(\beta(t) - 1)c - \frac{v_x^2(t) + v_y^2(t)}{2\beta(t)c} \right] dt \,, \tag{A.1}$$

where $\beta = \sqrt{1 - 1/\gamma^2}$. Finding an analytical solution of this expression requires solving the integral of the two terms on the right hand side.

The solution of the first integral is obtained by considering that

$$\beta = \sqrt{1 - \frac{1}{\gamma^2}} \simeq 1 - \frac{1}{2\gamma^2} \,, \tag{A.2}$$

and assuming that $\gamma(t) \simeq \gamma^{(0)}(t) = \gamma_0 + \mathcal{E}_0 t$ (and thus that $\dot{\gamma} = \mathcal{E}_0$), which leads to

$$\begin{aligned} \int_0^t (\beta(t) - 1)\, c\, dt &\simeq -\frac{c}{2} \int_0^t \frac{1}{\gamma^2(t)}\, dt = \frac{c}{2\dot{\gamma}} \int_0^t \frac{-\dot{\gamma}}{\gamma^2(t)}\, dt = \frac{c}{2\dot{\gamma}} \left(\frac{1}{\gamma(t)} - \frac{1}{\gamma_0} \right) \\ &= \frac{c}{2\mathcal{E}_0\gamma_0} \left(\Gamma(t)^{-1} - 1 \right) \,. \end{aligned} \tag{A.3}$$

For the second integral, the first step is to assume that, $\beta \simeq 1$, so that one can write

$$\int_0^t \frac{v_x^2(t) + v_y^2(t)}{2\beta(t)c}\, dt \simeq \frac{1}{2c} \int_0^t \left(v_x^2(t) + v_y^2(t) \right) dt \,. \tag{A.4}$$

Since the integrals of v_x^2 and v_y^2 are analogous, only the derivation of the first one is shown here. After substituting Equation (7.9) into v_x, the key point for finding an analytical solution of the integral is to consider that time interval over which the integral is performed is much longer that the betatron period of the oscillations. In this way, instead of considering the full oscillatory behavior of v_x^2, one can just retain its average value by substituting

$\sin^2(x)$ by $\langle \sin^2(x) \rangle = 1/2$, which allows the derivation below:

$$\begin{aligned}\int_0^t v_x^2(t)\,dt &\simeq A_{x,0}^2\omega_{x,0}^2 \int_0^t \Gamma(t)^{-3/2}\sin^2\left(\phi_x(t)+\phi_{x,0}\right)dt \simeq \frac{A_{x,0}^2\omega_{x,0}^2}{2}\int_0^t \Gamma(t)^{-3/2}\,dt \\ &= \frac{A_{x,0}^2\omega_{x,0}^2}{\dot{\Gamma}}\int_0^t \frac{\dot{\Gamma}}{2\Gamma(t)^{3/2}}\,dt = \frac{A_{x,0}^2\omega_{x,0}^2\gamma_0}{\mathcal{E}_0}\left(\Gamma^{1/2}(t)-1\right) \\ &= \frac{A_{x,0}^2\mathcal{K}_x}{\mathcal{E}_0}\left(\Gamma^{1/2}(t)-1\right)\,.\end{aligned} \tag{A.5}$$

Now that both integrals have been solved, they can be introduced in Equation (A.1) to finally find the expression for the slippage as given in Equation (7.11):

$$\begin{aligned}\Delta\xi(t) &= \frac{c}{2\mathcal{E}_0\gamma_0}\left(\Gamma(t)^{-1}-1\right) - \frac{1}{2c}\left(\frac{A_{x,0}^2\mathcal{K}_x}{\mathcal{E}_0}\left(\Gamma^{1/2}(t)-1\right)+\frac{A_{y,0}^2\mathcal{K}_y}{\mathcal{E}_0}\left(\Gamma^{1/2}(t)-1\right)\right) \\ &= \frac{c}{2\mathcal{E}_0\gamma_0}\left(\Gamma(t)^{-1}-1\right) - \frac{A_0^2\mathcal{K}}{2c\mathcal{E}_0}\left(\Gamma^{1/2}(t)-1\right)\,,\end{aligned} \tag{A.6}$$

where $\mathcal{K}_x = \mathcal{K}_y = \mathcal{K}$ has been assumed and $A_0^2 = A_{x,0}^2 + A_{y,0}^2$.

A.2. Derivation of the slice energy spread growth

The energy evolution of the particles p_1 and p_2, where the oscillation amplitude of the first is $A_{p_1} = 0$, can be written, according to Equation (7.13), as

$$\gamma_{p_1}(t) \simeq \gamma_{p_1} + \mathcal{E}_{p_1}t - \frac{c\mathcal{E}'_{p_1}}{2\mathcal{E}_{p_1}\gamma_{p_1}}t + \frac{\mathcal{E}'_{p_1}}{2}(c-v_w)\,t^2 + \frac{c\mathcal{E}'_{p_1}}{2\mathcal{E}_{p_1}^2}\ln\Gamma_{p_1}(t)\,, \tag{A.7}$$

$$\begin{aligned}\gamma_{p_2}(t) \simeq{}& \gamma_{p_2} + \mathcal{E}_{p_2}t - \frac{\mathcal{E}'_{p_2}}{2\mathcal{E}_{p_2}}\left(\frac{c}{\gamma_{p_2}}+\frac{A_{p_2}^2\mathcal{K}}{c}\right)t + \frac{\mathcal{E}'_{p_2}}{2}(c-v_w)\,t^2 \\ &+ \frac{c\mathcal{E}'_{p_2}}{2\mathcal{E}_{p_2}^2}\ln\Gamma_{p_2}(t) + \frac{\mathcal{E}'_{p_2}A_{p_2}^2\mathcal{K}\gamma_{p_2}}{c\mathcal{E}_{p_2}^2}\left(\Gamma_{p_2}(t)^{1/2}-1\right).\end{aligned} \tag{A.8}$$

In order to obtain a simple expression for the energy difference between them it will be assumed that the slope of the accelerating field is constant such that $\mathcal{E}'_{p_1} = \mathcal{E}'_{p_2} = \mathcal{E}'_s$. This allows writing the initial accelerating field experienced by the particles in terms of the field at the current slice $\mathcal{E}_s$ and the particle slippage, so that $\mathcal{E}_{p_1} = \mathcal{E}_s - \mathcal{E}'_s\Delta\xi_{p_1}$ and $\mathcal{E}_{p_2} = \mathcal{E}_s - \mathcal{E}'_s\Delta\xi_{p_2}$. These expressions for $\mathcal{E}_{p_1}$ and $\mathcal{E}_{p_2}$ will, however, only be used in the leading linear term in Equations (A.7) and (A.8), i.e., in the second term on the right hand side. In the rest of terms $\mathcal{E}_{p_1} \simeq \mathcal{E}_{p_2} \simeq \mathcal{E}_{0,s}$ will be assumed. After these assumptions, and considering that both particles have the same initial energy, $\gamma_{p_1} = \gamma_{p_2} = \gamma_0$, the energy

difference between them at any time t can finally be written as

$$\gamma_{p_2} - \gamma_{p_1} \simeq -\mathcal{E}_s' \left(\Delta\xi_{p_2} - \Delta\xi_{p_1}\right) t - \frac{\mathcal{E}_s' A_{p_2}^2 \mathcal{K}}{2c\mathcal{E}_{0,s}} t + \frac{\mathcal{E}_s' A_{p_2}^2 \mathcal{K}\gamma_0}{c\mathcal{E}_{0,s}^2} \left(\Gamma_s(t)^{1/2} - 1\right) , \tag{A.9}$$

where $\Gamma_s = \gamma_s/\gamma_0 = 1 + \mathcal{E}_{0,s}t$. In this expression, the difference in slippage between both particles can be directly obtained by using Equation (7.11) under the same assumptions as in Equation (A.9), which leads to

$$\Delta\xi_{p_2} - \Delta\xi_{p_1} \simeq \frac{A_{p_2}^2 \mathcal{K}}{2c\mathcal{E}_{0,s}} \left(\Gamma_s(t)^{-1/2} - 1\right) . \tag{A.10}$$

Now, by inserting Equation (A.10) into Equation (A.9), one finally finds the final expression for the energy difference as in Equation (7.14):

$$\gamma_{p_2} - \gamma_{p_1} \simeq \frac{\gamma_0 \mathcal{E}' \mathcal{K} A_{p_2}^2}{2c\mathcal{E}_{0,s}^2} \left(\Gamma_s(t)^{1/2} + \Gamma_s(t)^{-1/2} - 2\right) = \frac{\gamma_0 \mathcal{E}' \mathcal{K} A_{p_2}^2}{2c\mathcal{E}_{0,s}^2} \frac{\left(\Gamma_s(t)^{1/2} - 1\right)^2}{\Gamma_s(t)^{1/2}} . \tag{A.11}$$

From this equation, the absolute energy spread arising from particle slippage can be obtained by calculating the standard deviation of Equation (A.10) over all the particles within the slice. This yields

$$\sigma_{\gamma_s}^{\Delta\xi} = \sigma\left(\gamma_{p_2} - \gamma_{p_1}\right) \simeq \frac{\gamma_0 \mathcal{E}' \mathcal{K} \sigma(A_0^2)}{2c\mathcal{E}_{0,s}^2} \frac{\left(\bar{\Gamma}_s(t)^{1/2} - 1\right)^2}{\bar{\Gamma}_s(t)^{1/2}} , \tag{A.12}$$

where $\sigma(A_0^2)$ is the standard deviation of the oscillation amplitude of all slice particles and corresponds to the σ_{A^2} term defined in Equation (7.15). From here, the relative slice energy spread is directly obtained by dividing the expression above by the mean slice energy $\bar{\gamma}_s$:

$$\frac{\sigma_{\gamma_s}^{\Delta\xi}}{\bar{\gamma}_s} \simeq \frac{\mathcal{E}' \mathcal{K} \sigma(A_0^2)}{2c\mathcal{E}_{0,s}^2} \frac{\left(\bar{\Gamma}_s(t)^{1/2} - 1\right)^2}{\bar{\Gamma}_s(t)^{3/2}} , \tag{A.13}$$

where $\bar{\gamma}_s \simeq \bar{\gamma_0} + \mathcal{E}_{0,s}t$ and $\bar{\gamma_0} = \gamma_0$ has been used. This equation corresponds the first equality in Equation (7.15). To obtain the second one, an expression for $\sigma(A_0^2)$ has to be determined.

Remembering that $A_0^2 = A_{0,x}^2 + A_{0,y}^2$, if $A_{0,x}^2$ and $A_{0,y}^2$ are not correlated, the following equality applies:

$$\sigma(A_0^2) = \sigma\left(A_{0,x}^2 + A_{0,x}^2\right) = \sqrt{\sigma^2\left(A_{0,x}^2\right) + \sigma^2\left(A_{0,x}^2\right)} . \tag{A.14}$$

At the same time, since $A_{0,x}^2 = x_0^2 + v_{x,0}^2/\omega_{x,0}^2$, assuming the same condition for these two

terms yields again

$$\sigma\left(A_{0,x}^2\right) = \sigma\left(x_0^2 + \frac{v_{x,0}^2}{\omega_{x,0}^2}\right) = \sqrt{\sigma^2\left(x_0^2\right) + \sigma^2\left(\frac{v_{x,0}^2}{\omega_{x,0}^2}\right)}\,, \tag{A.15}$$

which also applies for the y-plane. This simplifies the problem, as the two terms on the right hand side of Equation (A.15) can be directly related to the geometric emittance, ϵ_x and Twiss parameters of the beam, α_x, β_x and γ_x. If the transverse particle distribution of the beam is assumed to be Gaussian, then $\sigma^2(x_0^2) = 2\sigma^4(x_0)$ and $\sigma^2(v_{x,0}^2/\omega_{x,0}^2) = 2\sigma^4(v_{x,0}/\omega_{x,0})$ and the following identities apply:

$$\sigma^2(x_0^2) = 2\sigma^4(x_0) = 2\epsilon_x^2\beta_x^2\,, \tag{A.16}$$

$$\sigma^2\left(\frac{v_{x,0}^2}{\omega_{x,0}^2}\right) = 2\sigma^4\left(\frac{v_{x,0}}{\omega_{x,0}}\right) = \frac{2c^4}{\omega_{x,0}^4}\sigma^4(x_0') = \frac{2c^4}{\omega_{x,0}^4}\frac{\epsilon_x^2}{\beta_x^2} = 2\beta_m^4\frac{\epsilon_x^2}{\beta_x^2}\,, \tag{A.17}$$

where it has been used that $\sigma_x = \sqrt{\epsilon_x\beta_x}$ and $\sigma_x' = \sqrt{\epsilon_x/\beta_x}$ for a beam which is at waist, i.e., with $\alpha_x = 0$ and thus with $\gamma_x = 1/\beta_x$. The second equation is obtained by assuming that the longitudinal velocity of the particle is relativistic, that is, $v_s \simeq c$, so that $x_0' \simeq v_{x,0}/c$, and by applying the definition of the matched beta function, $\beta_m = c/\omega_{x,0}$. Substituting Equations (A.16) and (A.17) into Equation (A.15) then yields

$$\sigma^2\left(A_{0,x}^2\right) = 2\epsilon_x^2\beta_x^2 + 2\beta_m^4\frac{\epsilon_x^2}{\beta_x^2} = 2\epsilon_x^2\frac{\beta_x^4 + \beta_m^4}{\beta_x^2}\,. \tag{A.18}$$

Since the expression for the y-plane is analogous to Equation (A.18), if the matched beta is the same in both planes, it is finally found that

$$\sigma(A_0^2) = \sqrt{2\epsilon_x^2\frac{\beta_x^4 + \beta_m^4}{\beta_x^2} + 2\epsilon_y^2\frac{\beta_y^4 + \beta_m^4}{\beta_y^2}}\,, \tag{A.19}$$

which can be written in a more convenient way and in terms of the normalized emittance, $\epsilon_n = \gamma_0\epsilon$, as

$$\begin{aligned}\sigma(A_0^2) &= \frac{\sqrt{2}}{\gamma_0}\sqrt{\epsilon_{n,x}^2\frac{\beta_x^4 + \beta_m^4}{\beta_x^2} + \epsilon_{n,y}^2\frac{\beta_y^4 + \beta_m^4}{\beta_y^2}} \\ &= \frac{\sqrt{2}\beta_m}{\gamma_0}\sqrt{\epsilon_{n,x}^2\frac{\beta_x^4 + \beta_m^4}{\beta_x^2\beta_m^2} + \epsilon_{n,y}^2\frac{\beta_y^4 + \beta_m^4}{\beta_y^2\beta_m^2}} = \sqrt{\frac{8c^2}{\gamma_0\mathcal{K}}\mathcal{A}^2}\,,\end{aligned} \tag{A.20}$$

where $\beta_m = c/\omega_0 = c\sqrt{\gamma_0/\mathcal{K}}$ has been used and $\mathcal{A}$ has been defined as

$$\mathcal{A}^2 = \frac{1}{4}\left(\epsilon_{n,x}^2\frac{\beta_x^4 + \beta_m^4}{\beta_x^2\beta_m^2} + \epsilon_{n,y}^2\frac{\beta_y^4 + \beta_m^4}{\beta_y^2\beta_m^2}\right)\,. \tag{A.21}$$

This corresponds to the definition given in the text after Equation (7.15). In addition, for the case of a cylindrically symmetric beam, where $\beta_x = \beta_y = \beta$ and $\epsilon_{n,x} = \epsilon_{n,y} = \epsilon_n$, Equation (A.21) can be further simplified to

$$\mathcal{A}^2 = \frac{1}{2}\epsilon_n^2 \frac{\beta^4 + \beta_m^4}{\beta^2 \beta_m^2} = \frac{1}{2}\epsilon_n^2 \frac{M^4 + 1}{M^2} = \epsilon_n^2 \mathcal{F}_m^2 \tag{A.22}$$

where a so-called "mismatch factor", defined as

$$\mathcal{F}_m = \sqrt{\frac{M^4 + 1}{2M^2}}\,, \tag{A.23}$$

with $M = \beta/\beta_m$, has been introduced. For the particular case of a matched beam, i.e., when $M = 1$, it is also found that $\mathcal{F}_m = 1$, which implies that $\mathcal{A} = \epsilon_n$.

As a last step, introducing Equations (A.20) and (A.21) into Equation (A.13) yields, finally:

$$\frac{\sigma_{\gamma_s}^{\Delta\xi}}{\bar{\gamma}} \simeq \sqrt{\frac{2\mathcal{K}}{\bar{\gamma}_{0,s}}} \frac{\mathcal{E}' \mathcal{F}_m \epsilon_n}{\mathcal{E}_0^2} \frac{\left(\bar{\Gamma}_s(t)^{1/2} - 1\right)^2}{\bar{\Gamma}_s(t)^{3/2}}\,, \tag{A.24}$$

which is the expression in the second equality of Equation (7.15).

A.3. Comparison between betatron slippage and betatron radiation

The impact of the emission of betatron radiation on the particle energy was studied in [Mic+06]. In this reference, Equation (53) shows the energy evolution of a single particle under the influence of a constant accelerating field and taking into account the energy loss due to radiation. This equation, written with the variable notation used in Chapter 7, reads

$$\gamma^{\mathrm{BR},x} = \gamma_0 + \mathcal{E}_0 t + \frac{2\nu_{\gamma,x}\gamma_0^2}{5\mathcal{E}_0}\left(1 - \Gamma(t)^{5/2}\right)\,, \tag{A.25}$$

where the last term represents the energy loss due to betatron oscillations in the x-plane, and where $\nu_{\gamma,x}$, defined as

$$\nu_{\gamma,x} = \frac{r_e}{3c^2}\mathcal{K}_x^2 A_{x,0}^2 \gamma_0\,, \tag{A.26}$$

is known as the radiative damping rate. Since the effect of oscillations on the y-plane would be analogous, extending Equation (A.25) to include the motion in both transverse planes can be done simply by adding an extra term:

$$\begin{aligned}\gamma^{\mathrm{BR}} &= \gamma_0 + \mathcal{E}_0 t + \frac{2\nu_{\gamma,x}\gamma_0^2}{5\mathcal{E}_0}\left(1 - \Gamma(t)^{5/2}\right) + \frac{2\nu_{\gamma,y}\gamma_0^2}{5\mathcal{E}_0}\left(1 - \Gamma(t)^{5/2}\right) \\ &= \gamma_0 + \mathcal{E}_0 t + \frac{2r_e}{15c^3}\frac{\mathcal{K}^2 A_0^2 \gamma_0^3}{\mathcal{E}_0}\left(1 - \Gamma(t)^{5/2}\right)\,,\end{aligned} \tag{A.27}$$

where it has been used that $A_0^2 = A_{x,0}^2 + A_{y,0}^2$. The slice energy spread induced by the emission of betatron radiation can then be directly obtained from the standard deviation of Equation (A.27), which results in

$$\frac{\sigma_{\gamma_s}^{\mathrm{BR}}}{\bar{\gamma}_s} \simeq \frac{2r_e}{15c^3}\frac{\mathcal{K}^2\sigma_{A^2}\bar{\gamma}_{0,s}^2}{\mathcal{E}_0}\frac{(\bar{\Gamma}_s^{5/2}-1)}{\bar{\Gamma}_s}\,, \tag{A.28}$$

where $\bar{\Gamma}_s = 1 + \mathcal{E}_{0,s}t/\bar{\gamma}_0$ and $\bar{\gamma}_0 = \gamma_0$ has been used. In this equation, the term σ_{A^2} represents, in the same way as in Equation 7.15, the standard deviation of A_0^2 for all the particles within the slice, i.e., $\sigma(A_0^2)$. Equation (A.28) is equivalent to that in Equation (55) in [Mic+06], with the addition that it takes into account also the oscillations in the y-plane.

In order to compare the relative relevance of the contributions to the slice energy spread from betatron slippage, given by Equation (7.15), and betatron radiation, as given by Equation (A.28), the following coefficients will be defined, which correspond to the constant terms in both equations:

$$C^{\Delta\xi} = \frac{\mathcal{E}'\mathcal{K}\sigma(A_0^2)}{2c\mathcal{E}_{0,s}^2}\,, \tag{A.29}$$

$$C^{\mathrm{BR}} = \frac{2r_e}{15c^3}\frac{\mathcal{K}^2\sigma_{A^2}\bar{\gamma}_{0,s}^2}{\mathcal{E}_0}\,, \tag{A.30}$$

as well as the ratio between them:

$$\mathcal{R} = \frac{C^{\mathrm{BR}}}{C^{\Delta\xi}} = \frac{e^2}{15\pi\epsilon_0 mc^4}\frac{\mathcal{K}\mathcal{E}_0\gamma_0}{\mathcal{E}'}\,. \tag{A.31}$$

This ratio will be a useful parameter to consider, as it can generally be considered to be $\mathcal{R} \ll 1$. This can be seen by assuming a blowout with $\mathcal{E}' = c\mathcal{K} = \omega_p^2/2$ and $\mathcal{E}_0 = \omega_p$, which allows this parameter to be expressed as $\mathcal{R} = (1/15\pi)(e^6/\epsilon_0^3 m^3 c^6)^{1/2}\gamma_0^2\sqrt{n_p} \simeq 1.41\times10^{-22}\gamma_0^2\sqrt{n_p}$, which depends only on the initial beam energy and plasma density. As an example, for a typical plasma density of $n_p = 1\times10^{17}\,\mathrm{cm}^{-3}$, it is found that $\mathcal{R} \leq 1$ for $\gamma_0 \lesssim 1.5\times10^5$, i.e., until an initial energy of $\sim 75\,\mathrm{GeV}$. Thus, for typical cases where γ_0 is much smaller, it can generally be assumed that $\mathcal{R} \ll 1$, which in principle also indicates that betatron radiation effects are expected to be small compared to those from slippage.

To determine energy ranges in which the slice energy spread is dominated by each of these effects, the intersections between Equations (7.15) and (A.28) have to be found. This will be done by equating both expressions and finding the roots of the resulting polynomial:

$$\frac{\sigma_{\gamma_s}^{\mathrm{BR}}}{\bar{\gamma}_s} = \frac{\sigma_{\gamma_s}^{\Delta\xi}}{\bar{\gamma}_s} \Leftrightarrow \mathcal{R}\Gamma^3 - \Gamma + (2-\mathcal{R})\Gamma^{1/2} - 1 = 0\,. \tag{A.32}$$

In to achieve this, one can take advantage of $\mathcal{R}$ being a small parameter and using per-

turbation methods to find approximate solutions. A first clue of the location of two roots can be obtained by checking the initial slope of both curves, i.e., at $\Gamma = 1$, which is found to be

$$\frac{\partial}{\partial\Gamma}\left(\frac{\sigma_{\gamma_s}^{\Delta\xi}}{\bar{\gamma}_s}\right)_{\Gamma=1} = 0\,, \quad \frac{\partial}{\partial\Gamma}\left(\frac{\sigma_{\gamma_s}^{\mathrm{BR}}}{\bar{\gamma}_s}\right)_{\Gamma=1} > 0\,. \tag{A.33}$$

Since both Equation (7.15) and (A.28) are 0 at $\Gamma = 1$, the derivatives above indicate that betatron radiation must start as the dominating effect, since it's derivative is positive from the beginning, while Equation (7.15) starts flat. This, however, contradicts the initial guess that radiation effects are smaller than those from slippage. A possible explanation for this is that although Equation (A.28) grows faster at the very beginning, it quickly gets surpassed by Equation (7.15). If this was the case, another root of the polynomial would be expected shortly after the one at $\Gamma = 1$. To study this, the following change of variable $p = \Gamma^{1/2}$ will be performed, which turns Equation (A.32) into

$$\mathcal{R}p^6 - p^2 + (2 - \mathcal{R})p - 1 = 0\,, \tag{A.34}$$

and it will be assumed that the roots can be expressed as a power series of $\mathcal{R}$:

$$p = p_{(0)} + \mathcal{R}p_{(1)} + \mathcal{R}^2 p_{(2)} + \mathcal{O}(\mathcal{R}^3)\,. \tag{A.35}$$

Substituting this into Equation (A.34) results in

$$\begin{aligned}\mathcal{R}p_{(0)}^6 + 6\mathcal{R}^2 p_{(0)}p_{(1)} - p_{(0)}^2 - 2\mathcal{R}p_{(0)}p_{(1)} - 2\mathcal{R}^2 p_{(0)}p_{(2)} - \mathcal{R}^2 p_{(1)}^2 \\ +2p_{(0)} + 2\mathcal{R}p_{(1)} + 2\mathcal{R}^2 p_{(2)} - \mathcal{R}p_{(0)} - \mathcal{R}^2 p_{(1)} - 1 + \mathcal{O}(\mathcal{R}^3) = 0\,,\end{aligned} \tag{A.36}$$

where only the terms up to second order in $\mathcal{R}$ have been kept. By grouping the terms in Equation (A.36) according to their order, the following three equations are found:

$$\mathcal{O}(\mathcal{R}^0) \longrightarrow p_{(0)}^2 - 2p_{(0)} + 1 = 0 \tag{A.37}$$

$$\mathcal{O}(\mathcal{R}^1) \longrightarrow p_{(0)}^6 - 2p_{(0)}p_{(1)} + 2p_{(1)} - p_{(0)} = 0 \tag{A.38}$$

$$\mathcal{O}(\mathcal{R}^2) \longrightarrow 6p_{(0)}p_{(1)} - 2p_{(0)}p_{(2)} - p_{(1)}^2 + 2p_{(2)} - p_{(1)} = 0 \tag{A.39}$$

from which the zero and first order terms of the roots can be calculated. Equation (A.37) yields a double root $p_{(0)}^a = p_{(0)}^b = 1$, Equation (A.38) gives no useful information, as it results in $0 = 0$, and Equation (A.39) returns $p_{(1)}^a = 0$, $p_{(1)}^b = 5$. Thus, to first order in $\mathcal{R}$, two distinct roots of Equation (A.34) have been found:

$$p^a \simeq 1\,, \tag{A.40}$$

$$p^b \simeq 1 + 5\mathcal{R}\,, \tag{A.41}$$

which, returning to the original variable, $\Gamma = p^2$, result in

$$\Gamma^a \simeq 1 \,, \tag{A.42}$$

$$\Gamma^b \simeq 1 + 10\mathcal{R} + 25\mathcal{R}^2 \,. \tag{A.43}$$

The first root, Γ^a, was expected since in the beginning both Equation (7.15) and (A.28) are 0. The existence of a second root, Γ^b, confirms that the slippage effects quickly start to dominate over betatron radiation when $\mathcal{R}$ is small. In fact, it can be assumed that slippage is the dominating contribution from the beginning if $\Gamma^b \simeq \Gamma^a$, which, by keeping only the zero- and first-order terms in Equation (A.43), is true if

$$\mathcal{R} \ll 0.1 \,. \tag{A.44}$$

Equation (A.44) is therefore the rigorous condition for slippage effects to be initially dominating over betatron radiation. However, a transition into a betatron-radiation-dominated regime is expected at some point. This is because while Equation (A.28) is monotonically increasing, Equation (7.15) becomes monotonically decreasing after $\Gamma = 9$. In order to obtain the transition point, Γ_t, the method of the dominant balance will be used. For this, it will be assumed that the two first terms in Equation (A.34) are dominant, i.e., much larger than the other two. This implies that

$$\mathcal{R}p^6 - p^2 = 0 \Rightarrow p^2(\mathcal{R}p^4 - 1) = 0 \,, \tag{A.45}$$

whose only non-zero root is $p = \pm\mathcal{R}^{-1/4}$. This is indeed a consistent choice of dominant balance, because if $\mathcal{R} \ll 1$, then $\mathcal{R}^{-1/4} \gg \mathcal{R}^{-1/2} \gg 1 \gg \mathcal{R}^{3/4}$, confirming that the two terms selected as dominant are much larger than the other.

This dominant balance therefore suggests performing the scaling $p = \mathcal{R}^{-1/4}P$, which turns Equation (A.34) into

$$P^6 - P^2 + (2 - \mathcal{R})\mathcal{R}^{1/4}P - \mathcal{R}^{-1/2} = 0 \,, \tag{A.46}$$

whose roots will be now be expressed in powers of $\mathcal{R}^{1/4}$:

$$P = P_{(0)} + \mathcal{R}^{1/4}P_{(1)} + \mathcal{O}(\mathcal{R}^{1/2}) \,. \tag{A.47}$$

Substituting this into Equation (A.46) yields

$$P_{(0)}^6 + 6\mathcal{R}^{1/4}P_{(0)}^5P_{(1)} - P_{(0)}^2 - 2\mathcal{R}^{1/4}P_{(0)}P_{(1)} + 2\mathcal{R}^{1/4}P_{(0)} + \mathcal{O}(\mathcal{R}^{1/2}) = 0 \,, \tag{A.48}$$

where only the terms up to first order in $\mathcal{R}^{1/4}$ have been kept and from which the two

following equations are obtained:

$$\mathcal{O}(\mathcal{R}^0) \longrightarrow P_{(0)}^6 - P_{(0)}^2 = 0\,, \tag{A.49}$$

$$\mathcal{O}(\mathcal{R}^{1/4}) \longrightarrow 6P_{(0)}^5 P_{(1)} - 2P_{(0)}P_{(1)} + 2P_{(0)} = 0\,. \tag{A.50}$$

From Equation (A.49), the zero-order roots $P_{(0)}^a = 0$ with multiplicity 2 and $P_{(0)}^b = 1$ with multiplicity 4 are found. Substituting this values in Equation (A.50) results in $0 = 0$ when using $P_{(0)}^a$, but yields $P_{(1)}^b = -1/2$ when using $P_{(0)}^b$. Thus, in the end, these two roots have been found to first order in $\mathcal{R}^{1/4}$:

$$P^a = 0\,, \tag{A.51}$$

$$P^b \simeq 1 - \frac{1}{2}\mathcal{R}^{1/4}\,. \tag{A.52}$$

Reverting now the change of variables $p = \mathcal{R}^{-1/4}P$ results in

$$p^a \simeq 0\,, \tag{A.53}$$

$$p^b \simeq \mathcal{R}^{1/4} - \frac{1}{2}\,, \tag{A.54}$$

which, in the original variable $\Gamma = p^2$ are expressed as

$$\Gamma^a \simeq 0\,, \tag{A.55}$$

$$\Gamma^b \simeq \mathcal{R}^{-1/2} - \mathcal{R}^{-1/4} + \frac{1}{4}\,. \tag{A.56}$$

The first root is not of interest, since $\Gamma = \gamma/\gamma_0$ will generally grow in the accelerator and can never be strictly zero, since $\gamma \geq 1$ always. Thus, it is the second root that gives the point at which transition to a regime dominated by betatron radiation. Since $\mathcal{R} \ll 1$, the first term in Equation (A.56) is dominating and the transition energy can be simplified to

$$\bar{\Gamma}_t \simeq \mathcal{R}^{-1/2}\,, \tag{A.57}$$

as written in Section 7.3.2.

B. Detailed study of space-charge and CSR effects in Chapter 8

A potentially critical point of the multistage acceleration scheme presented in Chapter 8 is the negative impact on the beam quality of space-charge and CSR effects in the magnetic chicane. One of the reasons why this could be suspected to be an issue is that the beam undergoes full compression at the center of the chicane and can therefore reach a high charge density. This could lead to strong longitudinal and transverse space-charge fields which, in turn, could result in increased longitudinal and transverse emittance. Another reason is the emission of CSR due to the bending in the dipoles. As reviewed in Section 3.2.3, this could lead not only to transverse emittance growth, but also to energy changes in the longitudinal phase-space (resulting in higher energy spread) as well as transverse kicks along the bunch. These kicks would therefore result in transverse offsets at the entrance of the second LWFA which would induce betatron oscillations and, if significant, result in increased emittance and slice energy spread, as described in Chapter 7.

To carefully evaluate the impact of these potential issues, detailed simulations of the magnetic chicane with ASTRA and CSRtrack have been carried out and are presented in this appendix. In first place, the studies performed for the 5 GeV proof-of-principle beamline are included. These consist on a series of resolution scans to determine the convergence of both codes and accurately simulate the impact of both effects. Afterwards, a dedicated study of CSR effects in the beamline designed for EuPRAXIA is also shown. No dedicated simulation scans for the 1 GeV beamline have been carried out since, based on the results obtained from the other two cases presented here, no significant impact from these issues is expected.

B.1. Studies for the 5 GeV proof-of-principle beamline

The most detailed study of space-charge and CSR effects was performed for the proof-of-principle beamline presented in Section 8.3, whose results were published in [Fer+19]. In this case, simulation scans with ASTRA and CSRtrack were carried out to determine the necessary resolution for obtaining accurate results and finding out the impact of space-charge fields and the emission of CSR on the beam quality.

Table B.1.: Longitudinal and transverse resolution of the numerical grid used for computing the space-charge forces in the different ASTRA simulations. A reference case with no space-charge was also simulated.

Simulation	Case 0	Case 1	Case 2	Case 3	Case 4
Space-charge forces	off	3D	3D	3D	3D
Longitudinal resolution [# of cells]	-	16	32	64	256
Transverse resolution [# of cells]	-	16	32	64	64

B.1.1. Space-charge studies with ASTRA

Using the particle distribution of the beam after the first plasma lens, a series of ASTRA simulations of the chicane were performed using the 3D space-charge solver. In addition to the different grid resolutions tested, which are summarized in Table B.1, a reference case with no space-charge forces was also simulated. For each simulation, the normalized emittance (transverse and longitudinal) of the beam at the end of the chicane was calculated and compared to this reference case.

The results of this resolution scan are shown in Figure B.1, where the emittance variation with respect to the reference case can be seen for all tested resolutions. This figure shows that the impact of space-charge can be considered negligible, since the most affected parameter, $\epsilon_{n,x}$, presents an increase of only $<1\,\%$ with respect to the reference case. It can also be seen that convergence is quickly reached for a resolution of 64×64 grid elements. Increasing the longitudinal resolution to 256 elements only marginally changes the already small variation in longitudinal emittance.

B.1.2. CSR studies with CSRtrack

A similar resolution scan was also performed with CSRtrack. In this case, however, due to the computational cost of 3D CSR simulations with a particle distribution of one million particles, 1D and 3D resolution scans with a reduced beam (of only 50 000 randomly selected particles) have been performed. After these scans, two more 3D simulations with the complete beam were also carried out to validate the results and obtain the full particle distribution at the end of the chicane. As in the previous case, a reference simulation without CSR was also performed for each scan. The information about the resolution used in each simulation can be seen in Table B.2.

The results of the resolution scans are shown in Figure B.2. Since in CSRtrack the detail of the simulation is established by specifying the dimensions of the sub-bunches (smaller sub-bunches imply higher accuracy), the resolution has been here defined as the inverse of the sub-bunch dimensions so that a higher value corresponds also to a higher accuracy. In this case, the displayed parameters are the position of the transverse centroid $\langle x \rangle$ and the pointing angle $\langle x' \rangle$, which could both be affected by CSR kicks, as well as the transverse and longitudinal emittance. It can be seen that all scans, both with 1D and 3D

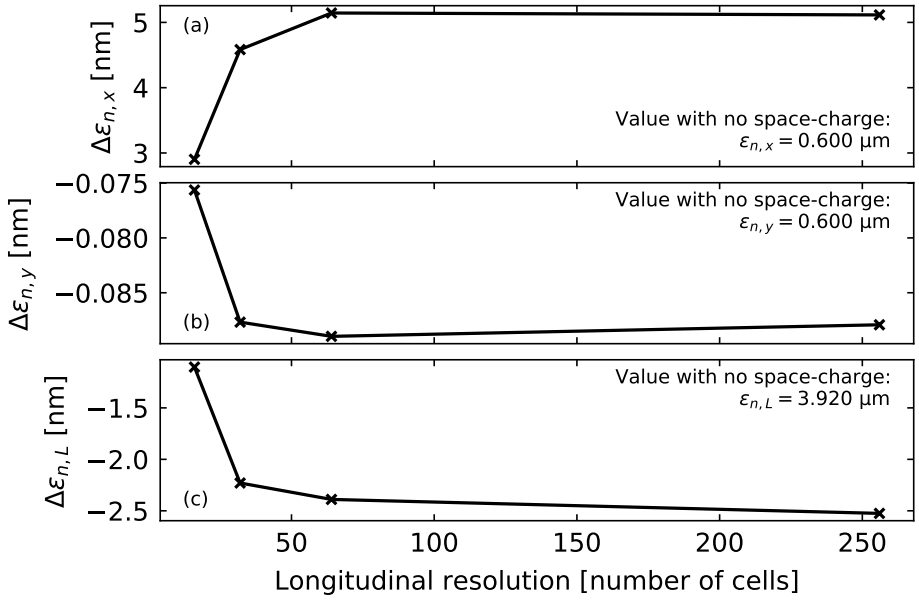

Figure B.1.: Resolution scan performed with ASTRA to study the impact of space-charge effects in the chicane of the 5 GeV proof-of-principle beamline. For each tested resolution, the variation of the emittance with respect to a case with no space-charge forces is shown for (a) the x-plane, (b) the y-plane and (c) the longitudinal plane. As noted in the text, the impact of space-charge is not significant, inducing only a <1 % growth in $\epsilon_{n,x}$, the most affected parameter.

Table B.2.: Longitudinal and transverse size of the sub-bunches in the different CSRtrack simulations performed for the 5 GeV proof-of-principle beamline. A reference case with no CSR effects was also simulated for each resolution scan (simulation 0). The 3D simulations were performed with the `g_to_m` method.

Simulation	0	1	2	3	4	5	6	7
1D scan with reduced beam								
Sub-bunch length ($\sigma_{s,l}$) [µm]	-	1	0.5	0.2	0.1	0.05	0.01	0.005
3D scan with reduced beam								
Sub-bunch length ($\sigma_{s,l}$) [µm]	-	1	0.5	0.2	0.1			
Sub-bunch size ($\sigma_{s,x\|y}$) [µm]	-	1	0.5	0.5	0.5			
3D scan with whole beam								
Sub-bunch length ($\sigma_{s,l}$) [µm]	-	0.2	0.1					
Sub-bunch size ($\sigma_{s,x\|y}$) [µm]	-	0.5	0.5					

models, agree to predict a $\sim$2 µm centroid deviation due to CSR. This is, however, only a small fraction of the overall beam size, as seen in Figure B.3. A small change in pointing angle of $\lesssim$0.1 µrad can also be observed, which the 1D model seems to overestimate. Regarding the beam emittance, the biggest impact seems to be now on the longitudinal plane, where a $\sim$7 % increase can be observed. This seems to be arising from an increase of the uncorrelated component of the energy spread due to the radiated power. On the horizontal plane, the induced emittance growth is still limited to $\sim$1 %.

Figure B.2 also shows, looking at the 1D scan, that convergence in all beam parameters seems to be reached for a longitudinal sub-bunch size of 0.01 µm. This resolution, however, is too high for a 3D simulation with the whole beam to be completed in a reasonable time (below 1 week in a high-performed computing cluster). Therefore, the sub-bunch length used for the most detailed 3D simulation was of 0.1 µm, which corresponds to a resolution where the two most relevant effects (transverse kicks and longitudinal emittance growth) are already well modelled.

The impact of CSR effects on the beam parameters, although more significant than that due to space-charge forces, is still small. To further illustrate this, a series of longitudinal phase-space plots of the particle distribution after the chicane, with and without CSR effects, are shown in Figure B.4. In this comparison, no evident differences can be seen between the two cases, and a statistical analysis is needed to discern the percent to sub-percent variations. Thanks to this small impact, the performance of this multistage scheme is not significantly affected by CSR effects. This can be seen in Section 8.3, where the beam obtained from CSRtrack was used for the start-to-end simulations so that the effect of CSR kicks and longitudinal emittance growth could be fully taken into account.

B.2. Study of CSR effects in the EuPRAXIA beamline

As explained in Section 8.4, the start-to-end simulations of the EuPRAXIA beamline were performed taking into account space-charge effects, but no CSR. Therefore, to confirm the validity of these results and check that CSR effects do not play an important role, another set of simulations with CSRtrack was performed and is presented in this section. This study of CSR effects was performed for the case in which the smoothed beam is used, as described in Section 8.4.

Since the 1D model proved to be sufficiently accurate in the previous case, only 1D CSR simulations were carried out for the EuPRAXIA beamline. A resolution scan was again performed and is shown in Figure B.5. From this scan it can be seen that, as expected from the higher peak current in this case, the impact on the beam centroid is higher, inducing a $\sim$4 µm displacement with respect to a case with no CSR effects. In this beamline simulation, which was performed with a realistic beam, the CSR kicks are however not the dominant contribution to the transverse offset in the chicane, which is instead mostly caused by the pointing angle of the beam after the first plasma stage. More surprising

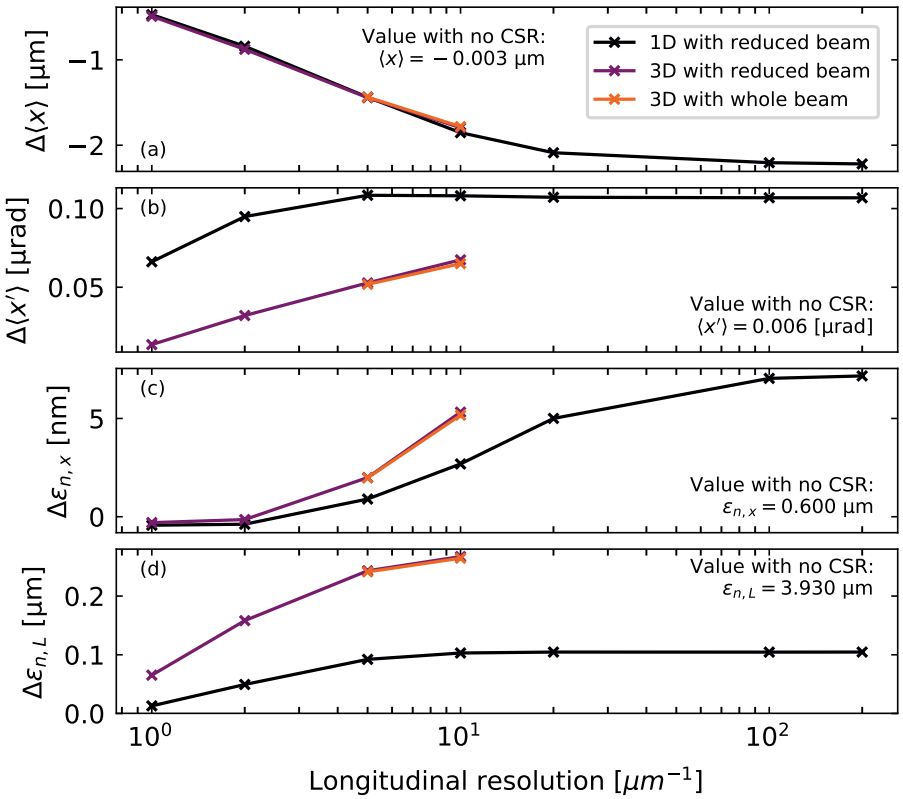

Figure B.2.: Resolution scans performed with CSRtrack for the 5 GeV proof-of-principle beamline using different CSR solvers (1D and 3D). As explained in the text, the resolution is here simply defined as the inverse of the sub-bunch dimensions. Due to the large amount of particles in the original beam distribution, scans were also performed with a reduced distribution of 50 000 randomly selected particles for faster simulations. The displayed parameters are the variations, with respect to the reference case with no CSR effects, of (a) the average transverse position, (b) the average pointing angle, (c) the normalized horizontal emittance and (d) the normalized longitudinal emittance. In addition to the curves corresponding to each scan, the value of each parameter for the reference simulation is included.

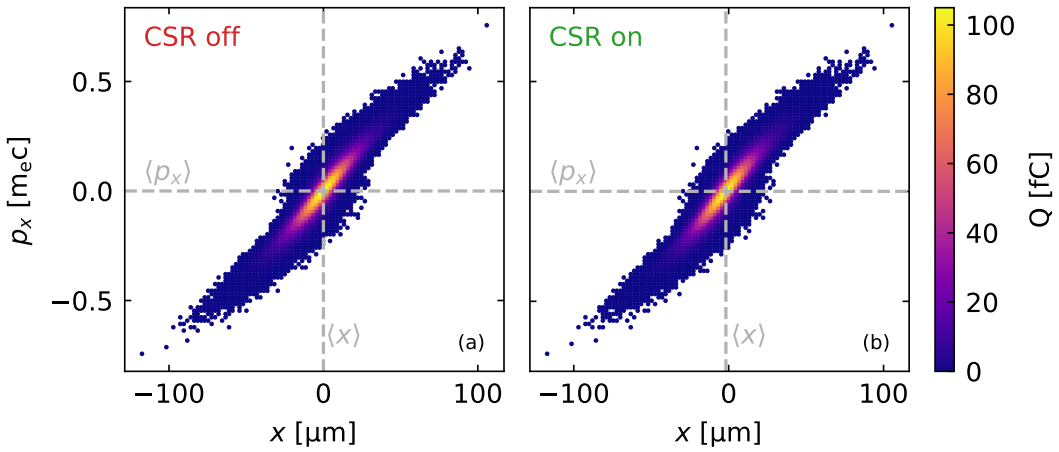

Figure B.3.: Transverse phase-space of the beam after the chicane in the 5 GeV proof-of-principle beamline. The distribution is shown for a case without (a) and with (b) CSR effects included. The case with CSR corresponds to a simulation with a 3D CSR model using the whole particle distribution and a longitudinal sub-bunch size of 0.1 µm. The horizontal and vertical dashed lines indicate the location of the average transverse position and momentum. A very small offset due to CSR effects can be seen in case (b).

is the fact that, as seen for the transverse and longitudinal emittance, the effect of CSR seems to be beneficial for this particular beam distribution, since it leads to a reduction of both parameters by ∼10 % and ∼2 %, respectively. It should be noted here that the parameters shown in Figure B.5 are not those of the whole distribution. Instead, they correspond to the statistical parameters of a region between $\pm 4\sigma_x$ and $\pm 4\sigma_{p_x}$ and with a longitudinal range between −7.5 µm and 5 µm around the bunch center $\langle z \rangle$. This region, which is the same displayed later in Figure B.7, contains ∼91 % of the charge. This particle filtering was performed in order to not take into account a small fraction of the charge which is far away from the bunch core and which would otherwise greatly affect the value of the statistical beam parameters. The less clear convergence in this case for higher resolution could be partly due to this filtering, since a different subset of particles might fulfill the filter conditions in each case.

The reason for the emittance improvement due to CSR, which is more noticeable in the transverse plane, can be seen in Figure B.6. There, it can be observed that, for this particular beam distribution, the emission of CSR seems to bring closer to each other different regions of high charge density in the horizontal phase-space, thus minimizing the RMS emittance. More details about the impact of CSR effects on this beam distribution can be seen Figure B.7, where phase-space plots of x, p_x and p_z along the longitudinal direction are shown with and without CSR effects. As expected, the biggest differences arise again in the regions of higher charge density, where more radiation is emitted.

To test whether these variations have a significant effect on the beam evolution and final parameters at the end of the accelerator, i.e., at the end of the second plasma stage, the particle distribution from CSRtrack was also used for the beamline simulations down-

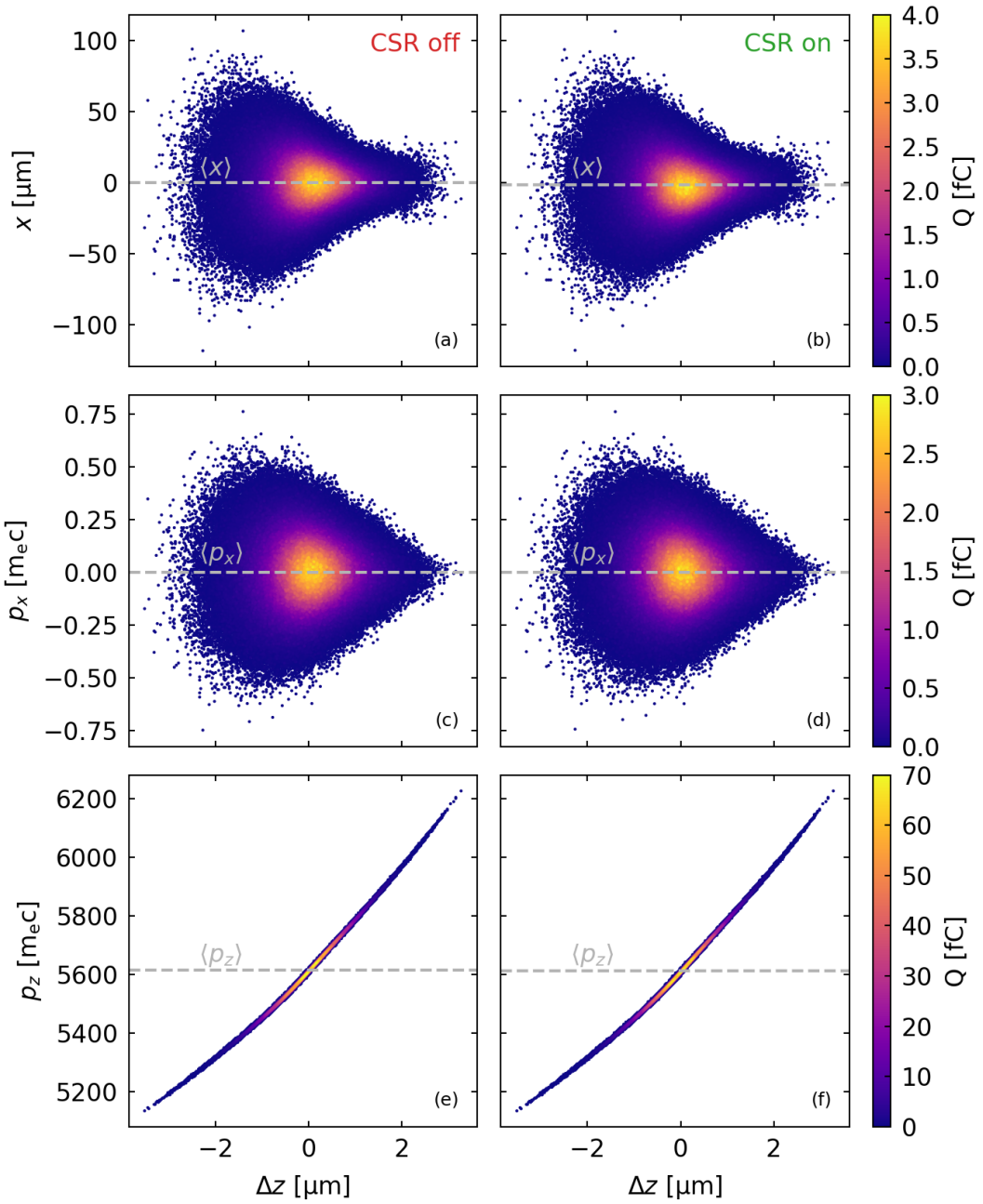

Figure B.4.: Phase-space plots along the longitudinal coordinate ($\Delta z = z - \langle z \rangle$) for the beam distribution after the chicane in the 5 GeV proof-of-principle beamline. Again, two cases with and without CSR effects are compared (same cases as in Figure B.3). The displayed variables are the transverse position ((a) and (b)), transverse momentum ((c) and (d)) and the longitudinal momentum ((e) and (f)). The horizontal lines indicate the average of the displayed variable. Only subtle differences between the average values can be observed.

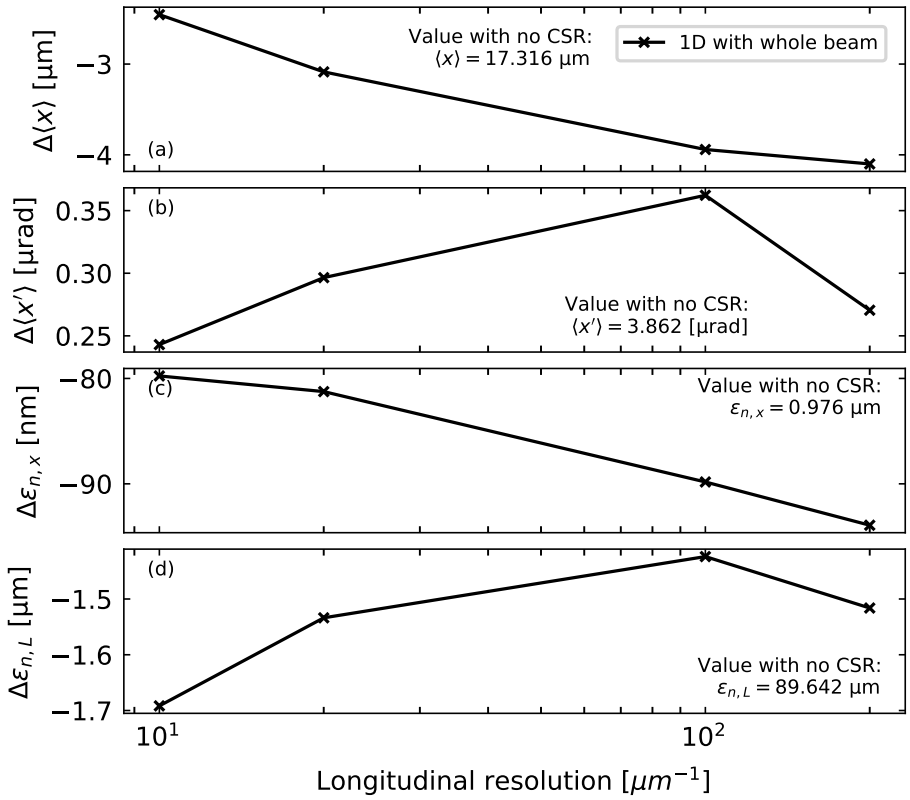

Figure B.5.: Resolution scan performed with CSRtrack (using the 1D CSR model) for the EuPRAXIA beamline. As explained in the text, the resolution is here simply defined as the inverse of the sub-bunch dimensions. The displayed parameters are the variations, with respect to the reference case with no CSR effects, of (a) the average transverse position, (b) the average pointing angle, (c) the normalized horizontal emittance and (d) the normalized longitudinal emittance. In addition to the curves corresponding to each scan, the value of each parameter for the reference simulation is displayed. As explained in the text, the parameters in this figure correspond to those of a region containing $\sim$91 % of the charge which extends between $\pm 4\sigma_x$ and $\pm 4\sigma_{p_x}$ and with a longitudinal range between -7.5 µm and 5 µm around the bunch center $\langle z \rangle$.

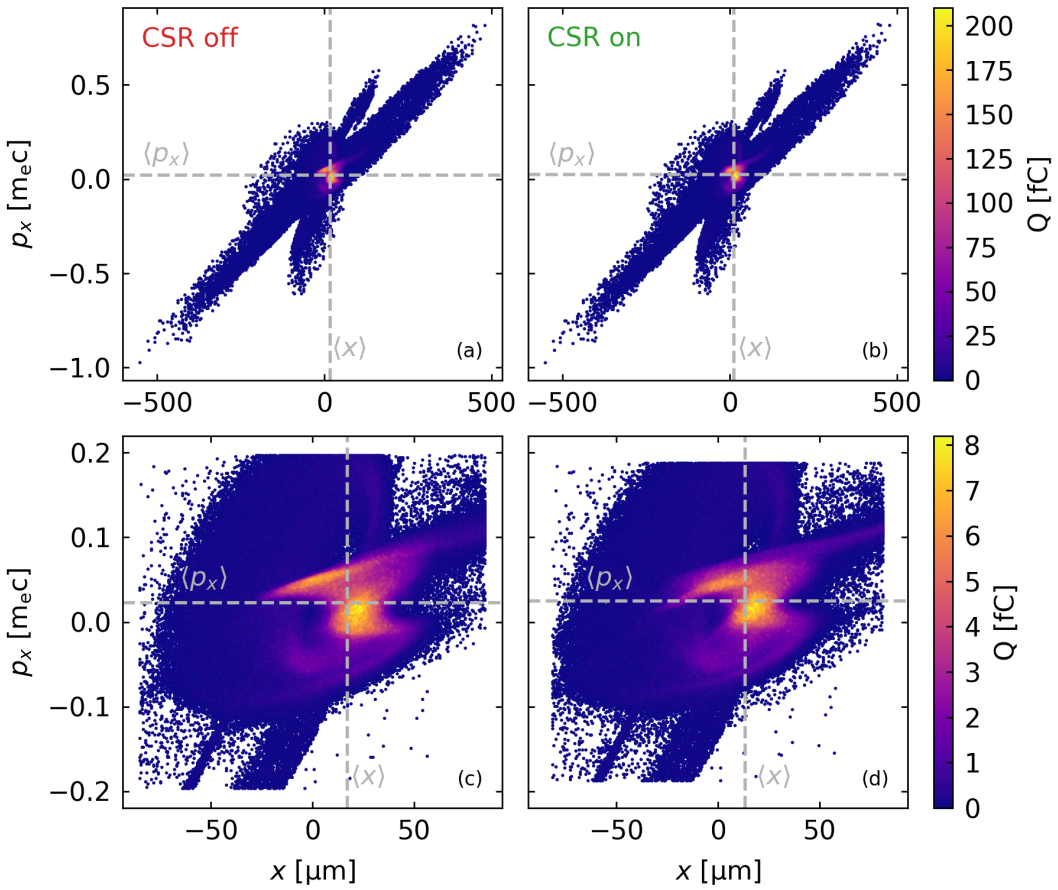

Figure B.6.: Transverse phase-space of the beam after the chicane in the EuPRAXIA beamline. The distribution is shown for a case without (a) and with (b) CSR effects included. The case with CSR corresponds to a simulation with a longitudinal sub-bunch size of 0.01 μm. The horizontal and vertical dashed lines indicate the location of the average transverse position and momentum. Since this beam has some particles far away from the center, a detailed view of the core is included in (c) and (d). This core, which contains ∼93 % of the charge, has been obtained by retaining only the particles within $\pm 4\sigma_x$ and $\pm 4\sigma_{p_x}$. Some differences in the position of regions of high charge density can be observed which, as explained in the text, lead to a small (∼10 %) emittance reduction when CSR effects are enabled.

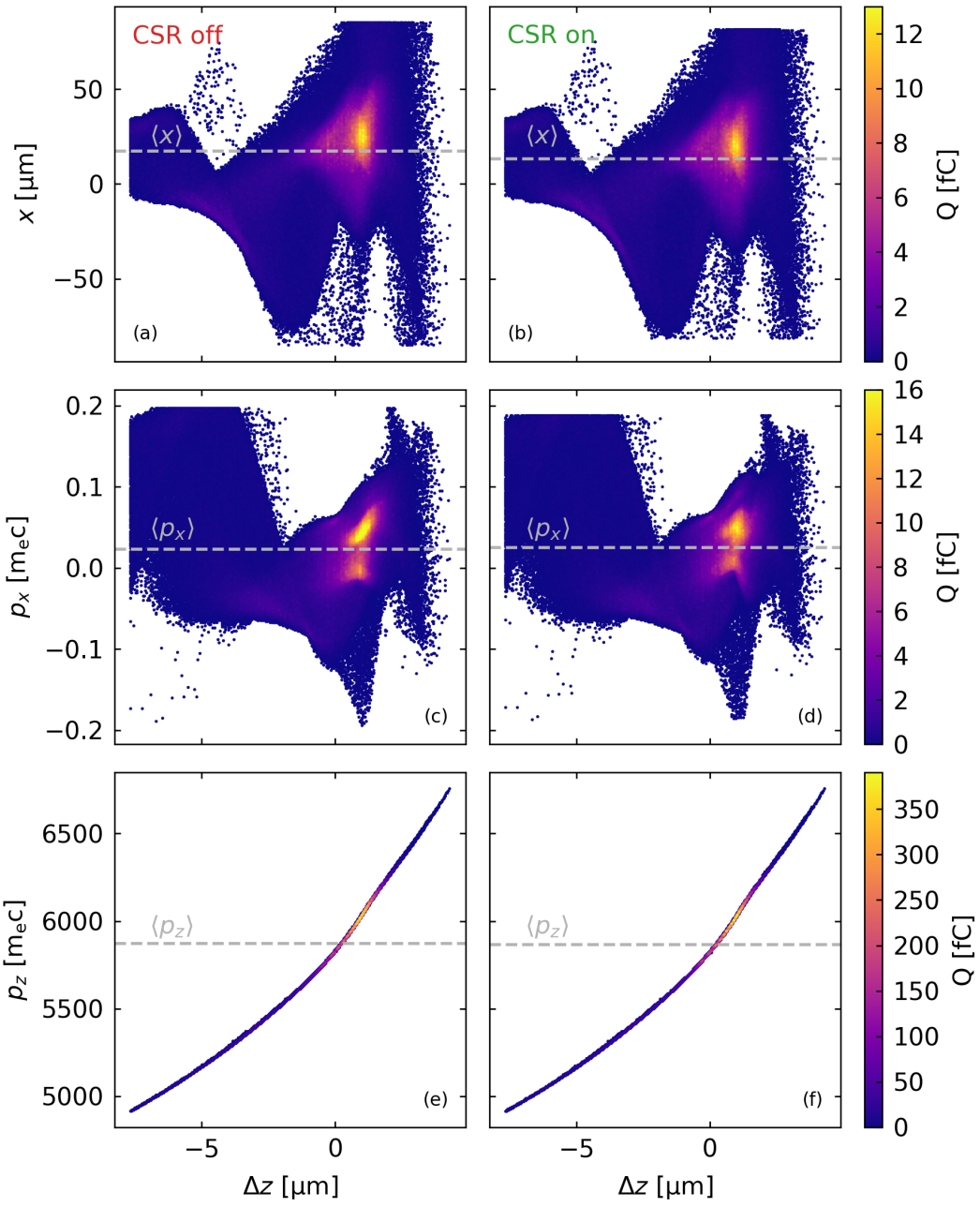

Figure B.7.: Phase-space plots along the longitudinal coordinate ($\Delta z = z - \langle z \rangle$) for the beam distribution after the chicane in the EuPRAXIA beamline. Again, two cases with and without CSR effects are compared (same cases as in Figure B.6). Here, however, in addition to filtering particles beyond $\pm 4\sigma_x$ and $\pm 4\sigma_{p_x}$, only a longitudinal region between $-7.5\,\mu$m and $5\,\mu$m around $\langle \Delta z \rangle$, containing $\sim$91 % of the charge, is shown. The displayed variables are the transverse position ((a) and (b)), transverse momentum ((c) and (d)) and the longitudinal momentum ((e) and (f)). The horizontal lines indicate the average of the displayed variable. Some differences can be observed in the regions of higher charge density and, more notably, on the average transverse position $\langle x \rangle$.

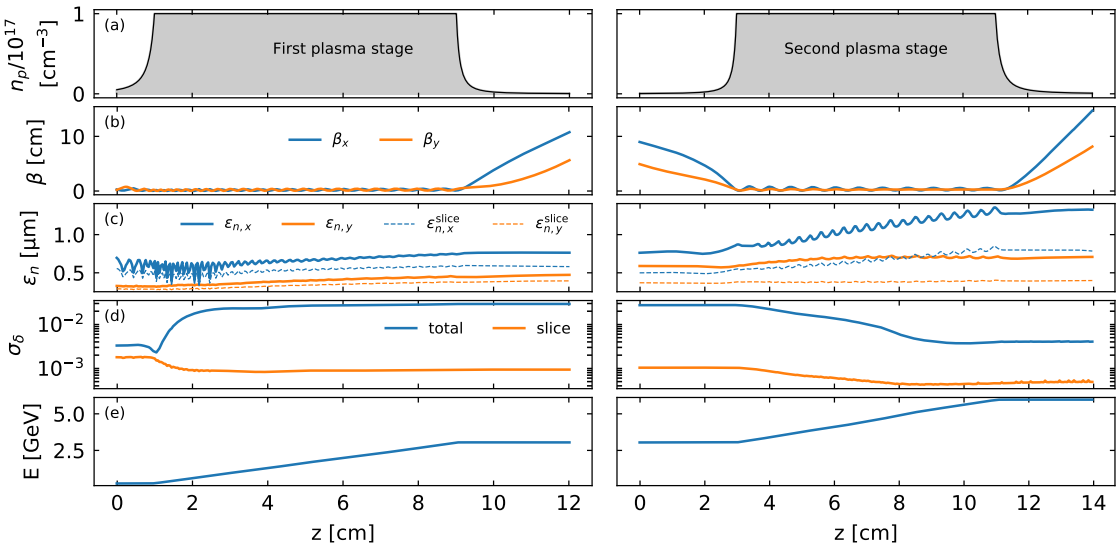

Figure B.8.: Evolution of the beam parameters in the two plasma stages of the EuPRAXIA beamline. This figure is analogous to Figure 8.12 but using the beam from CSRtrack simulations of the chicane (instead of that from ASTRA). It is shown: (a) an overview of the plasma density profile, (b) the beta function, (c) the normalized emittance, (d) the energy spread and (e) the energy of the beam. Only very small differences with respect to the case in Figure 8.12 can be appreciated. Most noticeable is a slightly smaller emittance.

stream of the chicane. The results of this start-to-end simulation can be seen in Figure B.8, which is analogous to Figure 8.12 but where the beam from CSRtrack instead of ASTRA has been used after the chicane. The differences are thus only in the beam evolution in the second plasma stage. The most visible one is a slightly smaller horizontal emittance due to the effect described above. A comparison between the final beam parameters obtained in Section 8.4 (chicane simulated with ASTRA) and the final parameters obtained here when the chicane is simulated with CSRtrack (using 1D CSR model) can be seen in Table B.3. The parameter values displayed there confirm that the differences between both cases are small and that neither space-charge nor CSR in the chicane critically affect the final beam quality. It could be tested in future work whether some of the observed differences, such as a slightly higher peak current and smaller bunch length and slice energy spread, arise due to presence of CSR or rather due to the lack of space-charge forces in the 1D CSRtrack simulations.

B.3. Conclusion

In this appendix, the results from detailed space-charge and CSR simulations of the 5 GeV and EuPRAXIA beamlines presented in Chapter 8 have been reported. These simulations have shown that none of these two potential issues play a dominant role in the overall performance of the multistage scheme. Space-charge forces seem to have an almost negligible influence on the beam parameters at the multi-GeV energies considered, leading

Table B.3.: Comparison of the beam parameters at the end of the EuPRAXIA beamline (end of the second plasma stage) when the chicane is simulated including 3D space-charge effects (as obtained in Section 8.4) and when the chicane is simulated with CSRtrack using a 1D CSR model. To be consistent with Section 8.4, the parameters in both cases correspond to the bunch core, defined as the region within $\pm 5\sigma_{x|y}$ and $\pm 5\sigma_{p_x|p_y}$ and a longitudinal extension of $\sim$12 fs around the peak in the current profile.

Parameter	Units	Value (with 3D space-charge)	Value (with 1D CSR)
Q	pC	23.7	23.5
$\epsilon_{\mathrm{n,x}}$	µm	1.50	1.32
$\epsilon_{\mathrm{n,y}}$	µm	0.69	0.71
$\langle\gamma\rangle$	GeV	6.0	6.0
σ_δ	10^{-3}	4.1	4.0
I_{peak}	kA	4.8	4.9
τ_{FWHM}	fs	3.3	3.0
$\epsilon_{\mathrm{n,x,sl}}$	µm	0.77	0.78
$\epsilon_{\mathrm{n,y,sl}}$	µm	0.40	0.40
$\sigma_{\delta,\mathrm{sl}}$	10^{-3}	0.54	0.50

to changes only on the $\sim$1 % level and below. CSR effects appear to be more significant, leading to transverse centroid deviations on the few-µm-level. These offsets are however small compared to the beam size and do not appear to play a significant role on the final beam quality either.

C. Realistic density profiles in plasma capillaries

As seen in multiple simulation studies along this thesis, the plasma density ramps at the entrance and exit of the LWFA stages have a great influence on the beam properties. In particular, well-tailored ramps can help to relax the matching requirements at injection and greatly reduce the divergence when the beam leaves the plasma. The beam dynamics in these ramps is by now well understood, and several analytical and numerical models for determining optimized ramp shapes exist [Meh+12; Flo14b; DFM15; Xu+16; LCN19]. However, little work has been performed towards determining whether such optimized profiles can be realistically obtained in an experiment.

In order to have at least a realistic estimate of the ramp shapes that could be experimentally expected in plasma capillaries, data from the little existing literature on this topic [Bag+17] has been analyzed. This data, which consists of a plasma density profile inside a capillary, was kindly provided by the author of the study, Dr. G. Bagdasarov. A 2D and 1D view of this data, which was obtained from fluid simulations of the gas (hydrogen) flow, is shown in Figure C.1. This is an advantage here, because experimental measurements of plasma ramps cannot generally resolve densities below $\sim 10^{17}\,\mathrm{cm}^{-3}$. On the contrary, numerical simulations can accurately resolve much lower densities, which can still have a significant impact on the beam parameters depending on the strength of the driver (even for densities as low as $\sim 10^{14}\,\mathrm{cm}^{-3}$ or $\sim 10^{15}\,\mathrm{cm}^{-3}$).

As it can be observed in Figure C.1, the shape of the ramps is strongly correlated to the transverse shape of the capillary. Regions where the radius is increased correspond to a strong reduction of the plasma density. In fact, it has been found that the profile of these ramps agrees very well with the expression

$$n_{p,\mathrm{ramp}} = \frac{n_{p,0}}{1 + (z/L_r)^2}\,, \tag{C.1}$$

where $n_{p,0}$ is the density at the start of the ramp, z is the distance to this start, and L_r is a characteristic length determining how fast the density decreases along the ramp. This inverse-square expression agrees intuitively well with what would be expected from a gas expanding uniformly in both the x and y directions.

To characterize each of the ramp sections seen in Figure C.1(b), a fit to Equation (C.1) with L_r as free parameter has been performed. The obtained profiles, which are shown in the figure itself including the value of L_r, show good agreement with the numerical

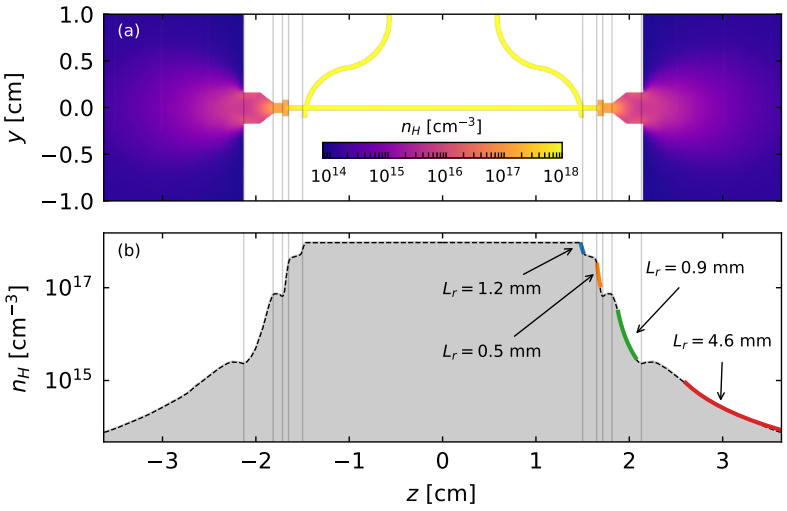

Figure C.1.: (a) View of the hydrogen density within a capillary before ionization. Image adapted from [Bag+17]. (b) On-axis value of the hydrogen density along the same capillary. The fits to Equation (C.1) of different sections along the ramp are included. The on-axis data has been provided by Dr. G. Bagdasarov.

data. From these fits, it can be observed that the steeper ramps (lower L_r) seem to occur within the cell, while in vacuum this value grows up to $\sim$5 mm. This is likely caused by the higher pressure within the cell and seems to indicate that a slower increase of the capillary radius could allow for lower values of L_r, which could potentially be optimized for beam matching and extraction. This considerations were particularly taken into account when designing the plasma profiles for the 1 GeV beamline in Section 8.5. There, a higher value of $L_r = 10$ mm within the cell was used, while for the ramps in vacuum a value of $L_r = 5$ mm was considered, as observed in this case.

It should be noted, however, that the fluid simulations in [Bag+17] (and, thus, in Figure C.1), were performed without taking into account the viscosity of the gas. This was pointed out by the author of these capillary studies, which also kindly offered to provide and additional simulation of the same capillary but including this property. The results from this simulation are shown in Figure C.2. Some apparent differences can be observed within the capillary, where the density profile shows more pronounced peaks and a more complex shape. After the capillary exit, however, the ramp shape seems to follow the same inverse-square law, although with a lower L_r than before. This could be due to the higher density (and thus pressure) at the end of the capillary, which has a value of 9.7×10^{15} cm^{-3} in this case, compared with 2.3×10^{15} cm^{-3} before.

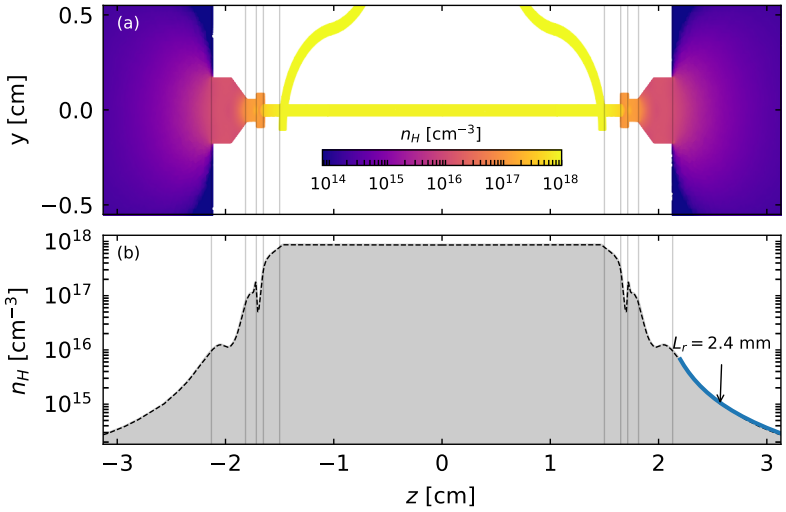

Figure C.2.: (a) View of the gas density in the same capillary as in Figure C.1 but from a simulation in which the viscosity of hydrogen was taken into account. (b) On-axis value of the density along the capillary. A fit to Equation (C.1) of the plasma ramp in vacuum is included. All data was provided by Dr. G. Bagdasarov.

Bibliography

[] *Wake-T repository*. URL: https://github.com/AngelFP/Wake-T.

[Adl+19] E. Adli et al. "Towards an Advanced Linear International Collider". In: (Jan. 2019). arXiv: 1901.10370 [physics.acc-ph]. URL: https://arxiv.org/pdf/1901.10370.

[Aga+14] I. Agapov et al. "OCELOT: A software framework for synchrotron light source and FEL studies". In: *Nucl. Instrum. Methods Phys. Res. A* 768 (2014), pp. 151–156. DOI: 10.1016/j.nima.2014.09.057.

[Ami+98] F. Amiranoff et al. "Observation of Laser Wakefield Acceleration of Electrons". In: *Phys. Rev. Lett.* 81 (5 Aug. 1998), pp. 995–998. DOI: 10.1103/PhysRevLett.81.995.

[And+18] T. André et al. "Control of laser plasma accelerated electrons for light sources". In: *Nat. Commun.* 9.1 (2018), p. 1334. DOI: 10.1038/s41467-018-03776-x.

[Ant+14] S. Antipov et al. "Experimental Demonstration of Energy-Chirp Compensation by a Tunable Dielectric-Based Structure". In: *Phys. Rev. Lett.* 112 (11 Mar. 2014), p. 114801. DOI: 10.1103/PhysRevLett.112.114801.

[AP56] A. Akhiezer and R. Polovin. "Theory of wave motion of an electron plasma". In: *Soviet Phys. JETP* 3.5 (Dec. 1956), pp. 696–705. URL: http://www.jetp.ac.ru/cgi-bin/dn/e_003_05_0696.pdf.

[Art+02] J. Arthur et al. "Linac coherent light source (LCLS) conceptual design report". In: (Apr. 2002). DOI: 10.2172/808719.

[AS+18] R. W. Assmann, U. Schramm et al. "Proposal for a large investment Accelerator Technology HElmholtz iNfrAstructure (ATHENA)". (not published). 2018. URL: %5Curl%7Bhttps://www.athena-helmholtz.de/%7D.

[Asc+16] A. Aschikhin et al. "The FLASHForward facility at DESY". In: *Nucl. Instrum. Methods Phys. Res. A* 806 (2016), pp. 175–183. DOI: 10.1016/j.nima.2015.10.005.

[Ass+14] R. Assmann et al. "SINBAD - A Proposal for a Dedicated Accelerator Research Facility at DESY". In: *Proc. 5th International Particle Accelerator Conference (IPAC'14)* (Dresden, Germany). June 2014, pp. 1466–1469. DOI: 10.18429/JACoW-IPAC2014-TUPME047.

[Ass+19] R. Assmann et al. *EuPRAXIA Conceptual Design Report*. Ed. by R. Assmann and M. Weikum. Oct. 2019. URL: http://www.eupraxia-project.eu/eupraxia-conceptual-design-report.html.

[AY98] R. Assmann and K. Yokoya. "Transverse beam dynamics in plasma-based linacs". In: *Nucl. Instrum. Methods Phys. Res. A* 410.3 (1998), pp. 544–548. DOI: 10.1016/S0168-9002(98)00187-9.

[Bag+17] G. A. Bagdasarov et al. "Laser beam coupling with capillary discharge plasma for laser wakefield acceleration applications". In: *Phys. Plasmas* 24.8 (2017), p. 083109. DOI: 10.1063/1.4997606.

[Bar+17] S. K. Barber et al. "Measured Emittance Dependence on the Injection Method in Laser Plasma Accelerators". In: *Phys. Rev. Lett.* 119 (10 Sept. 2017), p. 104801. DOI: 10.1103/PhysRevLett.119.104801.

[Beh+13] T. Behnke et al. "The International Linear Collider Technical Design Report - Volume 1: Executive Summary". In: (2013). arXiv: 1306.6327.

[BEW05] D. H. Bilderback, P. Elleaume and E. Weckert. "Review of third and next generation synchrotron light sources". In: *J. Phys. B* 38.9 (Apr. 2005), S773–S797. DOI: 10.1088/0953-4075/38/9/022.

[BKS89] S. Bulanov, V. Kirsanov and A. Sakharov. "Excitation of ultrarelativistic plasma waves by pulse of electromagnetic radiation". In: *JETP Lett* 50 (4 1989), pp. 4–25. URL: http://www.jetpletters.ac.ru/ps/1127/article_17078.pdf.

[Blu+07] I. Blumenfeld et al. "Energy doubling of 42 GeV electrons in a metre-scale plasma wakefield accelerator". In: *Nature* 445.7129 (2007), p. 741. DOI: 10.1038/nature05538.

[BM90] V. Berezhiani and I. Murusidze. "Relativistic wake-field generation by an intense laser pulse in a plasma". In: *Phys. Lett. A* 148.6 (1990), pp. 338–340. DOI: 10.1016/0375-9601(90)90813-4.

[BM92] V. I. Berezhiani and I. G. Murusidze. "Interaction of highly relativistic short laser pulses with plasmas and nonlinear wake-field generation". In: *Physica Scripta* 45.2 (Feb. 1992), pp. 87–90. DOI: 10.1088/0031-8949/45/2/007.

[Bor00] M. Borland. "ELEGANT: A flexible SDDS-compliant code for accelerator simulation". In: (Aug. 2000). DOI: 10.2172/761286.

[Bor14] M. Borland. "Ultra-Low-Emittance Light Sources". In: *Synchrotron Radiation News* 27.6 (2014), pp. 2–2. DOI: 10.1080/08940886.2014.970927.

[BPN84] R. Bonifacio, C. Pellegrini and L. M. Narducci. "Collective instabilities and high-gain regime free electron laser". In: *AIP Conference Proceedings* 118.1 (1984), pp. 236–259. DOI: 10.1063/1.34640.

[Bri+17] R. Brinkmann et al. "Chirp Mitigation of Plasma-Accelerated Beams by a Modulated Plasma Density". In: *Phys. Rev. Lett.* 118 (21 May 2017), p. 214801. DOI: 10.1103/PhysRevLett.118.214801.

[Bri19] R. Brinkmann. Private communication. 2019.

[Bru+10] E. Brunetti et al. "Low Emittance, High Brilliance Relativistic Electron Beams from a Laser-Plasma Accelerator". In: *Phys. Rev. Lett.* 105 (21 Nov. 2010), p. 215007. DOI: 10.1103/PhysRevLett.105.215007.

[Bry00] P. J. Bryant. "AGILE, a tool for interactive lattice design". In: CERN-PS-2000-036-DR (July 2000), 4 p. URL: http://cds.cern.ch/record/447856.

[BS12] K. Bane and G. Stupakov. "Corrugated pipe as a beam dechirper". In: *Nucl. Instr. Meth. Phys. Res., Sect. A* 690 (2012), pp. 106–110. DOI: 10.1016/j.nima.2012.07.001.

[BS85] K. L. Brown and R. V. Servranckx. "First- and second-order charged particle optics". In: *AIP Conference Proceedings* 127.1 (1985), pp. 62–138. DOI: 10.1063/1.35177.

[Buc+11] A. Buck et al. "Real-time observation of laser-driven electron acceleration". In: *Nat. Phys.* 7.7 (2011), p. 543. DOI: 10.1038/nphys1942.

[Buc+13] A. Buck et al. "Shock-Front Injector for High-Quality Laser-Plasma Acceleration". In: *Phys. Rev. Lett.* 110 (18 May 2013), p. 185006. DOI: 10.1103/PhysRevLett.110.185006.

[Bul+97] S. V. Bulanov et al. "Transverse-Wake Wave Breaking". In: *Phys. Rev. Lett.* 78 (22 June 1997), pp. 4205–4208. DOI: 10.1103/PhysRevLett.78.4205.

[Bul+98] S. Bulanov et al. "Particle injection into the wave acceleration phase due to nonlinear wake wave breaking". In: *Phys. Rev. E* 58 (5 Nov. 1998), R5257–R5260. DOI: 10.1103/PhysRevE.58.R5257.

[Bur+18] P. Burrows et al. *The Compact Linear Collider (CLIC) - 2018 Summary Report*. Ed. by P. Burrows. CERN Yellow Reports: Monographs. Published as CERN Yellow Report Monograph Vol. 2/2018. Dec. 2018. DOI: 10.23731/CYRM-2018-002.

[Cha+13] A. W. Chao et al. *Handbook of Accelerator Physics and Engineering*. 2nd. WORLD SCIENTIFIC, 2013. DOI: 10.1142/8543.

[Che+06] M. Chen et al. "Electron injection and trapping in a laser wakefield by field ionization to high-charge states of gases". In: *J. Appl. Phys.* 99.5 (2006), p. 056109. DOI: 10.1063/1.2179194.

[Che+85] P. Chen et al. "Acceleration of Electrons by the Interaction of a Bunched Electron Beam with a Plasma". In: *Phys. Rev. Lett.* 54 (7 Feb. 1985), pp. 693–696. DOI: 10.1103/PhysRevLett.54.693.

[Che84] F. F. Chen. *Introduction to Plasma Phys. Control. Fusion*. Vol. 1. Springer, 1984.

[Che87] P. Chen. "A Possible Final Focusing Mechanism for Linear Colliders". In: *Part. Accel.* 20 (1987), pp. 171–182. URL: https://inspirehep.net/files/5c5423497fca5f44fe974e88b7ebca74.

[Chi+95] T. C. Chiou et al. "Laser wake-field acceleration and optical guiding in a hollow plasma channel". In: *Phys. Plasmas* 2.1 (1995), pp. 310–318. DOI: 10.1063/1.871107.

[Cla+85] C. E. Clayton et al. "Relativistic Plasma-Wave Excitation by Collinear Optical Mixing". In: *Phys. Rev. Lett.* 54 (21 May 1985), pp. 2343–2346. DOI: 10.1103/PhysRevLett.54.2343.

[Cla+93] C. E. Clayton et al. "Ultrahigh-gradient acceleration of injected electrons by laser-excited relativistic electron plasma waves". In: *Phys. Rev. Lett.* 70 (1 Jan. 1993), pp. 37–40. DOI: 10.1103/PhysRevLett.70.37.

[CM08] M. Conte and W. W. MacKay. *An introduction to the physics of particle accelerators*. World Scientific Publishing Company, 2008. URL: https://books.google.mg/books?id=H21IDQAAQBAJ.

[CM19] B. Cros and P. Muggli. "ALEGRO input for the 2020 update of the European Strategy". In: (Jan. 2019). arXiv: 1901.08436 [physics.acc-ph].

[Cor+13] S. Corde et al. "Femtosecond x rays from laser-plasma accelerators". In: *Rev. Mod. Phys.* 85 (1 Jan. 2013), pp. 1–48. DOI: 10.1103/RevModPhys.85.1.

[Cor+15] S. Corde et al. "Multi-gigaelectronvolt acceleration of positrons in a self-loaded plasma wakefield". In: *Nature* 524.7566 (2015), pp. 442–445. DOI: 10.1038/nature14890.

[Cou+17] J. Couperus et al. "Demonstration of a beam loaded nanocoulomb-class laser wakefield accelerator". In: *Nat. Commun.* 8.1 (2017), p. 487. DOI: 10.1038/s41467-017-00592-7.

[Cra+18] P. Craievich et al. "Status of the Polarix-TDS Project". In: *Proc. 9th Int. Particle Accelerator Conf.(IPAC'18)* (Vancouver, BC, Canada). Geneva, Switzerland: JACoW Publishing, June 2018, pp. 3808–3811. DOI: doi:10.18429/JACoW-IPAC2018-THPAL068.

[CS00] E. Courant and H. Snyder. "Theory of the Alternating-Gradient Synchrotron". In: *Ann. Phys. (N. Y.)* 281.1 (2000), pp. 360–408. DOI: 10.1006/aphy.2000.6012.

[CS93] X. L. Chen and R. N. Sudan. "Two-dimensional self-focusing of short intense laser pulse in underdense plasma". In: *Phys. Fluids* 5.4 (1993), pp. 1336–1348. DOI: 10.1063/1.860923.

[CS96] C. E. Clayton and L. Serafini. "Generation and transport of ultrashort phase-locked electron bunches to a plasma beatwave accelerator". In: *IEEE Trans. Plasma Sci.* 24.2 (Apr. 1996), pp. 400–408. DOI: 10.1109/27.510004.

[Cur+17] A. Curcio et al. "Trace-space reconstruction of low-emittance electron beams through betatron radiation in laser-plasma accelerators". In: *Phys. Rev. Accel. Beams* 20 (1 Jan. 2017), p. 012801. DOI: 10.1103/PhysRevAccelBeams.20.012801.

[DAr+19] R. D'Arcy et al. "Tunable Plasma-Based Energy Dechirper". In: *Phys. Rev. Lett.* 122 (3 Jan. 2019), p. 034801. DOI: 10.1103/PhysRevLett.122.034801.

[Dav+15] A. Davidson et al. "Implementation of a hybrid particle code with a PIC description in r–z and a gridless description in phi into OSIRIS". In: *J. Comput. Phys.* 281 (2015), pp. 1063–1077. DOI: 10.1016/j.jcp.2014.10.064.

[Daw59] J. M. Dawson. "Nonlinear Electron Oscillations in a Cold Plasma". In: *Phys. Rev.* 113 (2 Jan. 1959), pp. 383–387. DOI: 10.1103/PhysRev.113.383.

[Daw83] J. M. Dawson. "Particle simulation of plasmas". In: *Rev. Mod. Phys.* 55 (2 Apr. 1983), pp. 403–447. DOI: 10.1103/RevModPhys.55.403.

[Deb+19] A. Debus et al. "Circumventing the Dephasing and Depletion Limits of Laser-Wakefield Acceleration". In: *Phys. Rev. X* 9 (3 Sept. 2019), p. 031044. DOI: 10.1103/PhysRevX.9.031044.

[Del+18] N. Delbos et al. "Lux – A laser–plasma driven undulator beamline". In: *Nucl. Instrum. Methods Phys. Res. A* 909 (2018), pp. 318–322. DOI: 10.1016/j.nima.2018.01.082.

[Der+95] Y. S. Derbenev et al. *Microbunch radiative tail - head interaction*. Tech. rep. TESLA-FEL 1995-05. 1995, p. 12. DOI: 10.3204/PUBDB-2018-04128.

[DFM15] I. Dornmair, K. Floettmann and A. R. Maier. "Emittance conservation by tailored focusing profiles in a plasma accelerator". In: *Phys. Rev. ST Accel. Beams* 18 (4 Apr. 2015), p. 041302. DOI: 10.1103/PhysRevSTAB.18.041302.

[DKL00] M. Dohlus, A. Kabel and T. Limberg. "Efficient field calculation of 3D bunches on general trajectories". In: *Nucl. Instr. Meth. Phys. Res., Sect. A* 445.1 (2000), pp. 338–342. DOI: 10.1016/S0168-9002(00)00139-X.

[DL04] M. Dohlus and T. Limberg. "CSRtrack: Faster calculation of 3-D CSR effects". In: *Free electron lasers. Proceedings, 26th International Conference, FEL 2004, and 11th FEL Users Workshop, Trieste, Italy, August 29-September 3, 2004*. 2004, pp. 18–21. URL: http://accelconf.web.cern.ch/AccelConf/f04/papers/MOCOS05/MOCOS05.PDF.

[DL97] M. Dohlus and T. Limberg. “Emittance growth due to wake fields on curved bunch trajectories”. In: *Nucl. Instr. Meth. Phys. Res., Sect. A* 393.1 (1997), pp. 494–499. DOI: 10.1016/S0168-9002(97)00552-4.

[DLE05] M. Dohlus, T. Limberg and P. Emma. “Bunch compression for linac-based FEL’s. Electron bunch length compression”. In: *ICFA Beam Dyn. Newslett.* 38 (2005), pp. 15–37. URL: http://icfa-usa.jlab.org/archive/newsletter/icfa_bd_nl_38.pdf.

[DM93] C. G. Durfee and H. M. Milchberg. “Light pipe for high intensity laser pulses”. In: *Phys. Rev. Lett.* 71 (15 Oct. 1993), pp. 2409–2412. DOI: 10.1103/PhysRevLett.71.2409.

[DO62] J. Dawson and C. Oberman. “High-Frequency Conductivity and the Emission and Absorption Coefficients of a Fully Ionized Plasma”. In: *The Physics of Fluids* 5.5 (1962), pp. 517–524. DOI: 10.1063/1.1706652.

[Dob04] S. Dobert. “Gradient limitations for high-frequency accelerators”. In: *Proc. 22nd International Linear Accelerator Conference (LINAC’04)* (Luebeck, Germany). Aug. 2004. URL: https://slac.stanford.edu/pubs/slacpubs/10500/slac-pub-10690.pdf.

[Döp+18] A. Döpp et al. “Energy-Chirp Compensation in a Laser Wakefield Accelerator”. In: *Phys. Rev. Lett.* 121 (7 Aug. 2018), p. 074802. DOI: 10.1103/PhysRevLett.121.074802.

[Dor+18] U. Dorda et al. “Status and objectives of the dedicated accelerator R&D facility “SINBAD” at DESY”. In: *Nucl. Instrum. Methods Phys. Res. A* 909 (2018), pp. 239–242. DOI: 10.1016/j.nima.2018.01.036.

[Emm+10] P. Emma et al. “First lasing and operation of an ångstrom-wavelength free-electron laser”. In: *Nature Photon.* 4.9 (2010), pp. 641–647. DOI: 10.1038/nphoton.2010.176.

[Eng+05] R. J. England et al. “Sextupole correction of the longitudinal transport of relativistic beams in dispersionless translating sections”. In: *Phys. Rev. ST Accel. Beams* 8 (1 Jan. 2005), p. 012801. DOI: 10.1103/PhysRevSTAB.8.012801.

[Eng+14] R. J. England et al. “Dielectric laser accelerators”. In: *Rev. Mod. Phys.* 86 (4 Dec. 2014), pp. 1337–1389. DOI: 10.1103/RevModPhys.86.1337.

[EP95] E. Esarey and M. Pilloff. “Trapping and acceleration in nonlinear plasma waves”. In: *Phys. Plasmas* 2.5 (1995), pp. 1432–1436. DOI: 10.1063/1.871358.

[Esa+02] E. Esarey et al. “Synchrotron radiation from electron beams in plasma-focusing channels”. In: *Phys. Rev. E* 65 (5 May 2002), p. 056505. DOI: 10.1103/PhysRevE.65.056505.

[Esa+93] E. Esarey et al. "Optically guided laser wake-field acceleration*". In: *Phys. Fluids* 5.7 (1993), pp. 2690–2697. DOI: 10.1063/1.860707.

[Esa+96] E. Esarey et al. "Overview of plasma-based accelerator concepts". In: *IEEE Trans. Plasma Sci.* 24.2 (Apr. 1996), pp. 252–288. DOI: 10.1109/27.509991.

[Esa+97a] E. Esarey et al. "Electron Injection into Plasma Wakefields by Colliding Laser Pulses". In: *Phys. Rev. Lett.* 79 (14 Oct. 1997), pp. 2682–2685. DOI: 10.1103/PhysRevLett.79.2682.

[Esa+97b] E. Esarey et al. "Self-focusing and guiding of short laser pulses in ionizing gases and plasmas". In: *IEEE J. Quantum Electron.* 33.11 (Nov. 1997), pp. 1879–1914. DOI: 10.1109/3.641305.

[ESL09] E. Esarey, C. B. Schroeder and W. P. Leemans. "Physics of laser-driven plasma-based electron accelerators". In: *Rev. Mod. Phys.* 81 (3 Aug. 2009), pp. 1229–1285. DOI: 10.1103/RevModPhys.81.1229.

[Eve+94] M. Everett et al. "Trapped electron acceleration by a laser-driven relativistic plasma wave". In: *Nature* 368.6471 (1994), p. 527. DOI: doi.org/10.1038/368527a0.

[FAM17] A. Ferran Pousa, R. W. Assmann and A. Martinez de la Ossa. "VisualPIC: A New Data Visualizer and Post-Processor for Particle-in-Cell Codes". In: *Proc. of 8th International Particle Accelerator Conference (IPAC'17)* (Copenhagen, Denmark). May 2017, pp. 1696–1698. DOI: 10.18429/JACoW-IPAC2017-TUPIK007.

[FAM18] A. Ferran Pousa, R. Assmann and A. Martinez de la Ossa. "Beam Quality Limitations of Plasma-Based Accelerators". In: *Proc. 9th Int. Particle Accelerator Conf. (IPAC'18)* (Vancouver, BC, Canada). May 2018, pp. 607–611. DOI: 10.18429/JACoW-IPAC2018-TUXGBE4.

[FAM19] A. Ferran Pousa, R. Assmann and A. Martinez de la Ossa. "Wake-T: a fast particle tracking code for plasma-based accelerators". In: *J. Phys. Conf. Ser.* 1350 (Nov. 2019), p. 012056. DOI: 10.1088/1742-6596/1350/1/012056.

[Fau+04] J. Faure et al. "A laser–plasma accelerator producing monoenergetic electron beams". In: *Nature* 431.7008 (2004), p. 541. DOI: 10.1038/nature02963.

[Fau+06] J. Faure et al. "Controlled injection and acceleration of electrons in plasma wakefields by colliding laser pulses". In: *Nature* 444.7120 (2006), p. 737. DOI: 10.1038/nature05393.

[Fau+10] J. Faure et al. "Injection and acceleration of quasimonoenergetic relativistic electron beams using density gradients at the edges of a plasma channel". In: *Phys. Plasmas* 17.8 (2010), p. 083107. DOI: 10.1063/1.3469581.

[Fed10] T. Feder. "Accelerator school travels university circuit". In: *Phys. Today* 63.2 (2010), p. 20. DOI: 10.1063/1.3326981.

[Fer+00] M. Ferrario et al. "Adiabatic plasma buncher". In: *IEEE Trans. Plasma Sci.* 28.4 (Aug. 2000), pp. 1152–1158. DOI: 10.1109/27.893295.

[Fer+13] M. Ferrario et al. "SPARC_LAB present and future". In: *Nuclear Instruments and Methods in Physics Research Section B: Beam Interactions with Materials and Atoms* 309 (2013), pp. 183–188. DOI: 10.1016/j.nimb.2013.03.049.

[Fer+17] A. Ferran Pousa et al. "External injection into a laser-driven plasma accelerator with sub-femtosecond timing jitter". In: *J. Phys.: Conf. Ser.* 874.1 (2017), p. 012032. DOI: 10.1088/1742-6596/874/1/012032.

[Fer+19] A. Ferran Pousa et al. "Compact Multistage Plasma-Based Accelerator Design for Correlated Energy Spread Compensation". In: *Phys. Rev. Lett.* 123 (5 July 2019), p. 054801. DOI: 10.1103/PhysRevLett.123.054801.

[Fer16] M. Ferrario. "Injection, Extraction and Matching". In: *CAS - CERN Accelerator School: Plasma Wake Acceleration*. Geneva: CERN, 2016, pp. 159–179. DOI: 10.5170/CERN-2016-001.159.

[Fer18] M. Ferrario. "Space Charge Mitigation". In: *CERN Yellow Reports: School Proceedings* 5.0 (2018), p. 89. URL: https://publishing.cern.ch/index.php/CYRSP/article/view/816.

[Flo03] K. Floettmann. "Some basic features of the beam emittance". In: *Phys. Rev. ST Accel. Beams* 6 (3 Mar. 2003), p. 034202. DOI: 10.1103/PhysRevSTAB.6.034202.

[Flo14a] K. Floettmann. "Generation of sub-fs electron beams at few-MeV energies". In: *Nucl. Instrum. Methods Phys. Res. A* 740 (2014), pp. 34–38. DOI: 10.1016/j.nima.2013.12.031.

[Flo14b] K. Floettmann. "Adiabatic matching section for plasma accelerated beams". In: *Phys. Rev. ST Accel. Beams* 17 (5 May 2014), p. 054402. DOI: 10.1103/PhysRevSTAB.17.054402.

[Flo17] K. Floettmann. "Astra: A space charge tracking algorithm". In: *Manual, Version* (2017). URL: http://www.desy.de/~mpyflo/Astra_manual/Astra-Manual_V3.2.pdf.

[FLS11] R. P. Feynman, R. B. Leighton and M. Sands. *The Feynman lectures on physics, Vol. II: The new millennium edition: mainly electromagnetism and matter*. Basic books, 2011. URL: https://www.feynmanlectures.caltech.edu/II_toc.html.

[FMA19] A. Ferran Pousa, A. Martinez de la Ossa and R. W. Assmann. "Intrinsic energy spread and bunch length growth in plasma-based accelerators due to betatron motion". In: *Scientific Reports* 9.1 (2019), pp. 1–11. DOI: doi:10.1038/s41598-019-53887-8.

[FMP14] M. Ferrario, M. Migliorati and L. Palumbo. "Space Charge Effects". In: *CERN Accelerator School: Advanced Accelerator Physics Course*. 2014, pp. 331–356. DOI: 10.5170/CERN-2014-009.331.

[Fon+02] R. A. Fonseca et al. "OSIRIS: A Three-Dimensional, Fully Relativistic Particle in Cell Code for Modeling Plasma Based Accelerators". In: *The 2002 International Conference on Computational Science*. Amsterdam: Springer, 2002. URL: https://link.springer.com/chapter/10.1007%2F3-540-47789-6_36.

[Fri+04] S. Fritzler et al. "Emittance Measurements of a Laser-Wakefield-Accelerated Electron Beam". In: *Phys. Rev. Lett.* 92 (16 Apr. 2004), p. 165006. DOI: 10.1103/PhysRevLett.92.165006.

[Fro+19] D. H. Froula et al. "Flying focus: Spatial and temporal control of intensity for laser-based applications". In: *Phys. Plasmas* 26.3 (2019), p. 032109. DOI: 10.1063/1.5086308.

[Fuc+09] M. Fuchs et al. "Laser-driven soft-X-ray undulator source". In: *Nat. Phys.* 5.11 (2009), p. 826. DOI: 10.1038/nphys1404.

[Gan10] R. Ganter. *SwissFEL-Conceptual design report*. Tech. rep. Paul Scherrer Institute (PSI), 2010. URL: https://inis.iaea.org/collection/NCLCollectionStore/_Public/42/006/42006326.pdf.

[Ged+04] C. Geddes et al. "High-quality electron beams from a laser wakefield accelerator using plasma-channel guiding". In: *Nature* 431.7008 (2004), p. 538. DOI: 10.1038/nature02900.

[Ged+08] C. G. R. Geddes et al. "Plasma-Density-Gradient Injection of Low Absolute-Momentum-Spread Electron Bunches". In: *Phys. Rev. Lett.* 100 (21 May 2008), p. 215004. DOI: 10.1103/PhysRevLett.100.215004.

[Gib16] P. Gibbon. "Introduction to Plasma Physics". In: *CAS - CERN Accelerator School: Plasma Wake Acceleration*. Geneva: CERN, 2016, pp. 51–65. DOI: 10.5170/CERN-2016-001.51.

[GK87] L. Gorbunov and V. Kirsanov. "Excitation of plasma waves by an electromagnetic wave packet". In: *Sov. Phys. JETP* 66.2 (1987), pp. 290–294. URL: http://www.jetp.ac.ru/cgi-bin/dn/e_066_02_0290.pdf.

[GMA00] D. F. Gordon, W. B. Mori and T. M. Antonsen. "A ponderomotive guiding center particle-in-cell code for efficient modeling of laser-plasma interactions". In: *IEEE Trans. Plasma Sci.* 28.4 (Aug. 2000), pp. 1135–1143. DOI: 10.1109/27.893300.

[God74] B. B. Godfrey. "Numerical Cherenkov instabilities in electromagnetic particle codes". In: *J. Comput. Phys.* 15.4 (1974), pp. 504–521. DOI: 10.1016/0021-9991(74)90076-X.

[Gol+15] G. Golovin et al. “Tunable monoenergetic electron beams from independently controllable laser-wakefield acceleration and injection”. In: *Phys. Rev. ST Accel. Beams* 18 (1 Jan. 2015), p. 011301. DOI: 10.1103/PhysRevSTAB.18.011301.

[Gol+16] G. Golovin et al. “Intrinsic beam emittance of laser-accelerated electrons measured by x-ray spectroscopic imaging”. In: *Sci. Rep.* 6 (2016), p. 24622. DOI: 10.1038/srep24622.

[Gon+11] A. Gonsalves et al. “Tunable laser plasma accelerator based on longitudinal density tailoring”. In: *Nat. Phys.* 7.11 (2011), p. 862. DOI: 10.1038/nphys2071.

[Gon+19] A. J. Gonsalves et al. “Petawatt Laser Guiding and Electron Beam Acceleration to 8 GeV in a Laser-Heated Capillary Discharge Waveguide”. In: *Phys. Rev. Lett.* 122 (8 Feb. 2019), p. 084801. DOI: 10.1103/PhysRevLett.122.084801.

[GP05] S. Gordienko and A. Pukhov. “Scalings for ultrarelativistic laser plasmas and quasimonoenergetic electrons”. In: *Phys. Plasmas* 12.4 (2005), p. 043109. DOI: 10.1063/1.1884126.

[Gre+14] J. Grebenyuk et al. “Laser-driven Acceleration with External Injection at SINBAD”. In: *5th International Particle Accelerator Conference (IPAC'14)*. Dresden, Germany, June 2014. DOI: 10.18429/JACoW-IPAC2014-TUPME064.

[Grü+07] F. Grüner et al. “Design considerations for table-top, laser-based VUV and X-ray free electron lasers”. In: *Appl. Phys. B* 86.3 (Feb. 2007), pp. 431–435. DOI: 10.1007/s00340-006-2565-7.

[GS03] H. Grote and F. Schmidt. “Mad-X - an upgrade from mad8”. In: *Proceedings of the 2003 Particle Accelerator Conference*. Vol. 5. May 2003, pp. 3497–3499. DOI: 10.1109/PAC.2003.1289960.

[Gsc+16] E. Gschwendtner et al. “AWAKE, The Advanced Proton Driven Plasma Wakefield Acceleration Experiment at CERN”. In: *Nucl. Instrum. Methods Phys. Res. A* 829 (2016), pp. 76–82. DOI: 10.1016/j.nima.2016.02.026.

[Haf+08] N. A. Hafz et al. “Stable generation of GeV-class electron beams from self-guided laser–plasma channels”. In: *Nat. Photonics* 2.9 (2008), p. 571. DOI: 10.1038/nphoton.2008.155.

[HDS12] Z. Huang, Y. Ding and C. B. Schroeder. “Compact X-ray Free-Electron Laser from a Laser-Plasma Accelerator Using a Transverse-Gradient Undulator”. In: *Phys. Rev. Lett.* 109 (20 Nov. 2012), p. 204801. DOI: 10.1103/PhysRevLett.109.204801.

[Hel+16] A. Helm et al. "Implementation of a 3D version of ponderomotive guiding center solver in particle-in-cell code OSIRIS". In: *APS Division of Plasma Physics Meeting Abstracts*. Vol. 2016. APS Meeting Abstracts. Oct. 2016, GP10.011, GP10.011.

[HH12] R. W. Hamm and M. E. Hamm. *Industrial accelerators and their applications*. World Scientific, 2012.

[Hid+10] B. Hidding et al. "Monoenergetic Energy Doubling in a Hybrid Laser-Plasma Wakefield Accelerator". In: *Phys. Rev. Lett.* 104 (19 May 2010), p. 195002. DOI: 10.1103/PhysRevLett.104.195002.

[Hid+12] B. Hidding et al. "Ultracold Electron Bunch Generation via Plasma Photocathode Emission and Acceleration in a Beam-Driven Plasma Blowout". In: *Phys. Rev. Lett.* 108 (3 Jan. 2012), p. 035001. DOI: 10.1103/PhysRevLett.108.035001.

[HK07] Z. Huang and K.-J. Kim. "Review of x-ray free-electron laser theory". In: *Phys. Rev. ST Accel. Beams* 10 (3 Mar. 2007), p. 034801. DOI: 10.1103/PhysRevSTAB.10.034801.

[Hua+04] Z. Huang et al. "Suppression of microbunching instability in the linac coherent light source". In: *Phys. Rev. ST Accel. Beams* 7 (7 July 2004), p. 074401. DOI: 10.1103/PhysRevSTAB.7.074401.

[Hue+18] A. Huebl et al. *openPMD 1.1.0: Base paths for mesh- and particle- only files and updated attributes*. Version 1.1.0. Feb. 2018. DOI: 10.5281/zenodo.1167843.

[HWL19] J. Hua, Y. Wu and W. Lu. "External injection from a Linac into a LWFA with ~100% capture efficiency (Conference Presentation)". In: *Laser Acceleration of Electrons, Protons, and Ions V*. Vol. 11037. International Society for Optics and Photonics. 2019. DOI: 10.1117/12.2520697.

[Irm+07] A. Irman et al. "Design and simulation of laser wakefield acceleration with external electron bunch injection in front of the laser pulse". In: *J. Appl. Phys.* 102.2 (2007), p. 024513. DOI: 10.1063/1.2759878.

[Ish+12] T. Ishikawa et al. "A compact X-ray free-electron laser emitting in the sub-ångström region". In: *Nat. Photonics* 6.8 (2012), p. 540. DOI: 10.1038/nphoton.2012.141.

[Jac98] J. D. Jackson. *Classical Electrodynamics*. Wiley, 1998.

[Jos+18] C. Joshi et al. "Plasma wakefield acceleration experiments at FACET II". In: *Plasma Phys. Control. Fusion* 60.3 (Jan. 2018), p. 034001. DOI: 10.1088/1361-6587/aaa2e3.

[Kal+09] S. Kalmykov et al. “Electron Self-Injection and Trapping into an Evolving Plasma Bubble”. In: *Phys. Rev. Lett.* 103 (13 Sept. 2009), p. 135004. DOI: 10.1103/PhysRevLett.103.135004.

[Kal+11] S. Y. Kalmykov et al. “Electron self-injection into an evolving plasma bubble: Quasi-monoenergetic laser-plasma acceleration in the blowout regime”. In: *Phys. Plasmas* 18.5 (2011), p. 056704. DOI: 10.1063/1.3566062.

[Kam+08] T. Kameshima et al. “0.56 GeV laser electron acceleration in ablative-capillary-discharge plasma channel”. In: *Appl. Phys. Express* 1.6 (May 2008), p. 066001. URL: https://doi.org/10.1143%2Fapex.1.066001.

[Kan66] Kane Yee. “Numerical solution of initial boundary value problems involving maxwell’s equations in isotropic media”. In: *IEEE Trans. Antennas Propag.* 14.3 (May 1966), pp. 302–307. DOI: 10.1109/TAP.1966.1138693.

[Kar+07] S. Karsch et al. “GeV-scale electron acceleration in a gas-filled capillary discharge waveguide”. In: *New J. Phys.* 9.11 (Nov. 2007), p. 415. DOI: 10.1088/1367-2630/9/11/415.

[Kat+87] T. C. Katsouleas et al. “Beam Loading in Plasma Accelerators”. In: *Part. Accel.* 22 (1987), pp. 81–99. URL: https://inspirehep.net/files/30e3b8e467eb7298ce19d6bbc95b457f.

[Kat+96] T. C. Katsouleas et al. “A plasma klystron for generating ultra-short electron bunches”. In: *IEEE Trans. Plasma Sci.* 24.2 (Apr. 1996), pp. 443–447. DOI: 10.1109/27.510009.

[Kat86] T. Katsouleas. “Physical mechanisms in the plasma wake-field accelerator”. In: *Phys. Rev. A* 33 (3 Mar. 1986), pp. 2056–2064. DOI: 10.1103/PhysRevA.33.2056.

[KD83] T. Katsouleas and J. M. Dawson. “Unlimited Electron Acceleration in Laser-Driven Plasma Waves”. In: *Phys. Rev. Lett.* 51 (5 Aug. 1983), pp. 392–395. DOI: 10.1103/PhysRevLett.51.392.

[Kit+92] Y. Kitagawa et al. “Beat-wave excitation of plasma wave and observation of accelerated electrons”. In: *Phys. Rev. Lett.* 68 (1 Jan. 1992), pp. 48–51. DOI: 10.1103/PhysRevLett.68.48.

[Kne+12] S. Kneip et al. “Characterization of transverse beam emittance of electrons from a laser-plasma wakefield accelerator in the bubble regime using betatron x-ray radiation”. In: *Phys. Rev. ST Accel. Beams* 15 (2 Feb. 2012), p. 021302. DOI: 10.1103/PhysRevSTAB.15.021302.

[Kot+08] H. Kotaki et al. “Improvement of the Quality and Stability of Electron Bunch Using Countercrossing Laser Beam”. In: *IEEE Trans. Plasma Sci.* 36.4 (Aug. 2008), pp. 1760–1764. DOI: 10.1109/TPS.2008.927944.

[Kot+09] H. Kotaki et al. "Electron Optical Injection with Head-On and Countercrossing Colliding Laser Pulses". In: *Phys. Rev. Lett.* 103 (19 Nov. 2009), p. 194803. DOI: 10.1103/PhysRevLett.103.194803.

[KPK04] I. Kostyukov, A. Pukhov and S. Kiselev. "Phenomenological theory of laser-plasma interaction in "bubble" regime". In: *Phys. Plasmas* 11.11 (2004), pp. 5256–5264. DOI: 10.1063/1.1799371.

[KS80] A. M. Kondratenko and E. L. Saldin. "Generating of coherent radiation by a relativistic electron beam in an ondulator". In: *Part. Accel.* 10 (1980), pp. 207–216. URL: https://inspirehep.net/files/872da099a0e9c171a4dca19256f7ca0e.

[Kur+19] T. Kurz et al. "Demonstration of a compact plasma accelerator powered by laser-accelerated electron beams". In: (Sept. 2019). arXiv: 1909.06676 [physics.acc-ph].

[LA18] C. A. Lindstrøm and E. Adli. "Analytic plasma wakefield limits for active plasma lenses". In: (Feb. 2018). arXiv: 1802.02750 [physics.acc-ph].

[LAY] LAYERTEC. *LAYERTEC - High Power Femtosecond Laser Optics*. https://www.layertec.de/en/capabilities/femtosecond-lasers/high-power/. Accessed: 21/10/2019.

[LCN19] X. Li, A. Chancé and P. A. P. Nghiem. "Preserving emittance by matching out and matching in plasma wakefield acceleration stage". In: *Phys. Rev. Accel. Beams* 22 (2 Feb. 2019), p. 021304. DOI: 10.1103/PhysRevAccelBeams.22.021304.

[LE09] W. Leemans and E. Esarey. "Laser-driven plasma-wave electron accelerators". In: *Phys. Today* 62.3 (2009), pp. 44–49. DOI: 10.1063/1.3099645.

[Lee+06] W. P. Leemans et al. "GeV electron beams from a centimetre-scale accelerator". In: *Nat. Phys.* 2.10 (2006), p. 696. DOI: 10.1038/nphys418.

[Lee+14] W. P. Leemans et al. "Multi-GeV Electron Beams from Capillary-Discharge-Guided Subpetawatt Laser Pulses in the Self-Trapping Regime". In: *Phys. Rev. Lett.* 113 (24 Dec. 2014), p. 245002. DOI: 10.1103/PhysRevLett.113.245002.

[Lee+19] W. Leemans et al. "KALDERA – High average power laser plasma accelerator project at DESY". EAAC19. 2019. URL: https://agenda.infn.it/event/17304/contributions/97644/.

[Leh+14] R. Lehe et al. "Laser-plasma lens for laser-wakefield accelerators". In: *Phys. Rev. ST Accel. Beams* 17 (12 Dec. 2014), p. 121301. DOI: 10.1103/PhysRevSTAB.17.121301.

[Leh+16] R. Lehe et al. "A spectral, quasi-cylindrical and dispersion-free Particle-In-Cell algorithm". In: *Comput. Phys. Commun.* 203 (2016), pp. 66–82. DOI: 10.1016/j.cpc.2016.02.007.

[Leh+17] R. Lehe et al. "Saturation of the Hosing Instability in Quasilinear Plasma Accelerators". In: *Phys. Rev. Lett.* 119 (24 Dec. 2017), p. 244801. DOI: 10.1103/PhysRevLett.119.244801.

[Li+13] F. Y. Li et al. "Dense Attosecond Electron Sheets from Laser Wakefields Using an Up-Ramp Density Transition". In: *Phys. Rev. Lett.* 110 (13 Mar. 2013), p. 135002. DOI: 10.1103/PhysRevLett.110.135002.

[Li+18] S. Li et al. "Correlation between macroscopic plasma dynamics and electron beam parameters in a laser-plasma accelerator". In: *Plasma Phys. Control. Fusion* 60.8 (July 2018), p. 085020. DOI: 10.1088/1361-6587/aacd59.

[Lim+96] T. Limberg et al. "The bunch compression system at the TESLA test facility FEL". In: *Nucl. Instrum. Methods Phys. Res. A* 375.1 (1996), pp. 322–324. DOI: 10.1016/0168-9002(95)01470-5.

[Lin+16] C. Lindstrøm et al. "Transverse Tolerances of a Multi-Stage Plasma Wakefield Accelerator". In: *Proc. 7th International Particle Accelerator Conference (IPAC'16)* (Busan, Korea). May 2016, WEPMY009. DOI: 10.18429/JACoW-IPAC2016-WEPMY009.

[Lin+18] C. A. Lindstrøm et al. "Emittance Preservation in an Aberration-Free Active Plasma Lens". In: *Phys. Rev. Lett.* 121 (19 Nov. 2018), p. 194801. DOI: 10.1103/PhysRevLett.121.194801.

[Liu+11] J. S. Liu et al. "All-Optical Cascaded Laser Wakefield Accelerator Using Ionization-Induced Injection". In: *Phys. Rev. Lett.* 107 (3 July 2011), p. 035001. DOI: 10.1103/PhysRevLett.107.035001.

[LM79] K. R. Lea and I. H. Munro. "THE SYNCHROTRON RADIATION SOURCE AT DARESBURY LABORATORY." In: *In *Daresbury 1979, Proceedings, Application Of Synchrotron Radiation*, 119-124*. 1979.

[LNM18] X. Li, P. A. P. Nghiem and A. Mosnier. "Toward low energy spread in plasma accelerators in quasilinear regime". In: *Phys. Rev. Accel. Beams* 21 (11 Nov. 2018), p. 111301. DOI: 10.1103/PhysRevAccelBeams.21.111301.

[Lot04] K. V. Lotov. "Blowout regimes of plasma wakefield acceleration". In: *Phys. Rev. E* 69 (4 Apr. 2004), p. 046405. DOI: 10.1103/PhysRevE.69.046405.

[Lot05] K. V. Lotov. "Efficient operating mode of the plasma wakefield accelerator". In: *Phys. Plasmas* 12.5 (2005), p. 053105. DOI: 10.1063/1.1889444.

[Lou+15] A. Loulergue et al. "Beam manipulation for compact laser wakefield accelerator based free-electron lasers". In: *New J. Phys.* 17.2 (Feb. 2015), p. 023028. DOI: 10.1088/1367-2630/17/2/023028.

[Lu+06a] W. Lu et al. "A nonlinear theory for multidimensional relativistic plasma wave wakefields". In: *Phys. Plasmas* 13.5 (2006), p. 056709. DOI: 10.1063/1.2203364.

[Lu+06b] W. Lu et al. "Nonlinear Theory for Relativistic Plasma Wakefields in the Blowout Regime". In: *Phys. Rev. Lett.* 96 (16 Apr. 2006), p. 165002. DOI: 10.1103/PhysRevLett.96.165002.

[Lu+07] W. Lu et al. "Generating multi-GeV electron bunches using single stage laser wakefield acceleration in a 3D nonlinear regime". In: *Phys. Rev. ST Accel. Beams* 10 (6 June 2007), p. 061301. DOI: 10.1103/PhysRevSTAB.10.061301.

[Lun+11] O. Lundh et al. "Few femtosecond, few kiloampere electron bunch produced by a laser–plasma accelerator". In: *Nat. Phys.* 7.3 (2011), p. 219. DOI: 10.1038/nphys1872.

[Luo+18] J. Luo et al. "Multistage Coupling of Laser-Wakefield Accelerators with Curved Plasma Channels". In: *Phys. Rev. Lett.* 120 (15 Apr. 2018), p. 154801. DOI: 10.1103/PhysRevLett.120.154801.

[MA97] P. Mora and T. M. Antonsen Jr. "Kinetic modeling of intense, short laser pulses propagating in tenuous plasmas". In: *Phys. Plasmas* 4.1 (1997), pp. 217–229. DOI: 10.1063/1.872134.

[Mad71] J. M. J. Madey. "Stimulated Emission of Bremsstrahlung in a Periodic Magnetic Field". In: *J. Appl. Phys.* 42.5 (1971), pp. 1906–1913. DOI: 10.1063/1.1660466.

[Mai+12] A. R. Maier et al. "Demonstration Scheme for a Laser-Plasma-Driven Free-Electron Laser". In: *Phys. Rev. X* 2 (3 Sept. 2012), p. 031019. DOI: 10.1103/PhysRevX.2.031019.

[Mal+01] V. Malka et al. "Characterization of electron beams produced by ultrashort (30 fs) laser pulses". In: *Phys. Plasmas* 8.6 (2001), pp. 2605–2608. DOI: 10.1063/1.1374584.

[Mal+02] V. Malka et al. "Electron Acceleration by a Wake Field Forced by an Intense Ultrashort Laser Pulse". In: *Science* 298.5598 (2002), pp. 1596–1600. DOI: 10.1126/science.1076782.

[Mal+08] V. Malka et al. "Principles and applications of compact laser–plasma accelerators". In: *Nat. Phys.* 4.6 (2008), p. 447. DOI: 10.1038/nphys966.

[Man+04] S. P. Mangles et al. "Monoenergetic beams of relativistic electrons from intense laser–plasma interactions". In: *Nature* 431.7008 (2004), p. 535. DOI: 10.1038/nature02939.

[Man+17] G. Manahan et al. “Single-stage plasma-based correlated energy spread compensation for ultrahigh 6D brightness electron beams”. In: *Nat. Commun.* 8.15705 (2017). DOI: 10.1038/ncomms15705.

[Mar+13] A. Martinez de la Ossa et al. “High-Quality Electron Beams from Beam-Driven Plasma Accelerators by Wakefield-Induced Ionization Injection”. In: *Phys. Rev. Lett.* 111 (24 Dec. 2013), p. 245003. DOI: 10.1103/PhysRevLett.111.245003.

[Mar+15] A. Martinez de la Ossa et al. “Wakefield-induced ionization injection in beam-driven plasma accelerators”. In: *Phys. Plasmas* 22.9 (2015), p. 093107. DOI: 10.1063/1.4929921.

[Mar+16] B. Marchetti et al. “Electron-beam manipulation techniques in the SINBAD Linac for external injection in plasma wake-field acceleration”. In: *Nucl. Instrum. Methods Phys. Res. A* 829 (2016), pp. 278–283. DOI: 10.1016/j.nima.2016.03.041.

[Mar+17] B. Marchetti et al. “Status Update of the SINBAD-ARES Linac Under Construction at DESY”. In: *Proceedings, 8th International Particle Accelerator Conference (IPAC 2017): Copenhagen, Denmark, May 14-19, 2017*. 2017, TUPAB040. DOI: 10.18429/JACoW-IPAC2017-TUPAB040.

[Mar+18] B. Marchetti et al. “Conceptual and Technical Design Aspects of Accelerators for External Injection in LWFA”. In: *Appl. Sci.* 8.5 (2018). URL: http://www.mdpi.com/2076-3417/8/5/757.

[Mar+19a] A. Martinez de la Ossa et al. “Hybrid LWFA-PWFA staging as a beam energy and brightness transformer: conceptual design and simulations”. In: *Philos. Trans. R. Soc. A* 377.2151 (2019). DOI: 10.1098/rsta.2018.0175.

[Mar+19b] D. Marx et al. “Simulation studies for characterizing ultrashort bunches using novel polarizable X-band transverse deflection structures”. In: *Scientific Reports* 9 (2019). DOI: 10.1038/s41598-019-56433-8.

[Mar18] A. Martinez de la Ossa. “PIC-VTK”. A 3D visualization toolkit for PIC codes. 2018.

[Mar19] D. Marx. “Characterization of Ultrashort Electron Bunches at the SINBAD-ARES Linac”. Dissertation, Universität Hamburg, 2019. PhD thesis. 2019. DOI: 10.3204/PUBDB-2019-04190.

[Mee85] S. van der Meer. *Improving the power efficiency of the plasma wakefield accelerator*. Tech. rep. CERN-PS-85-65-AA. CLIC-Note-3. Geneva: CERN, 1985. URL: https://cds.cern.ch/record/163918.

[Meh+12] T. Mehrling et al. “Transverse emittance growth in staged laser-wakefield acceleration”. In: *Phys. Rev. ST Accel. Beams* 15 (11 Nov. 2012), p. 111303. DOI: 10.1103/PhysRevSTAB.15.111303.

[Meh+14] T. Mehrling et al. "HiPACE: a quasi-static particle-in-cell code". In: *Plasma Phys. Control. Fusion* 56.8 (July 2014), p. 084012. DOI: 10.1088/0741-3335/56/8/084012.

[Meh+17] T. J. Mehrling et al. "Mitigation of the Hose Instability in Plasma-Wakefield Accelerators". In: *Phys. Rev. Lett.* 118 (17 Apr. 2017), p. 174801. DOI: 10.1103/PhysRevLett.118.174801.

[Meh14] T. J. Mehrling. "Theoretical and numerical studies on the transport of transverse beam quality in plasma-based accelerators". PhD thesis. U. Hamburg, Dept. Phys., 2014. DOI: 10.3204/DESY-THESIS-2014-040.

[Mic+06] P. Michel et al. "Radiative damping and electron beam dynamics in plasma-based accelerators". In: *Phys. Rev. E* 74 (2 Aug. 2006), p. 026501. DOI: 10.1103/PhysRevE.74.026501.

[Mig+13] M. Migliorati et al. "Intrinsic normalized emittance growth in laser-driven electron accelerators". In: *Phys. Rev. ST Accel. Beams* 16 (1 Jan. 2013), p. 011302. DOI: 10.1103/PhysRevSTAB.16.011302.

[Mir+15] M. Mirzaie et al. "Demonstration of self-truncated ionization injection for GeV electron beams". In: *Sci. Rep.* 5 (2015), p. 14659. DOI: 10.1038/srep14659.

[Mod+95] A. Modena et al. "Electron acceleration from the breaking of relativistic plasma waves". In: *Nature* 377.6550 (1995), p. 606. DOI: 10.1038/377606a0.

[Moo+97] C. I. Moore et al. "Electron Trapping in Self-Modulated Laser Wakefields by Raman Backscatter". In: *Phys. Rev. Lett.* 79 (20 Nov. 1997), pp. 3909–3912. DOI: 10.1103/PhysRevLett.79.3909.

[Moo+99] C. I. Moore et al. "A Laser-Accelerator Injector Based on Laser Ionization and Ponderomotive Acceleration of Electrons". In: *Phys. Rev. Lett.* 82 (8 Feb. 1999), pp. 1688–1691. DOI: 10.1103/PhysRevLett.82.1688.

[Nan+15] E. A. Nanni et al. "Terahertz-driven linear electron acceleration". In: *Nat. Commun.* 6 (2015), p. 8486. DOI: 10.1038/ncomms9486.

[Ngh+19] P. A. P. Nghiem et al. "EuPRAXIA, A Step Toward A Plasma-Wakefield Based Accelerator With High Beam Quality". In: *J. Phys. Conf. Ser.* 1350 (Nov. 2019), p. 012068. DOI: 10.1088/1742-6596/1350/1/012068.

[Nic83] D. R. Nicholson. *Introduction to plasma theory*. Wiley New York, 1983.

[OO07] T. Okada and K. Ogawa. "Saturated magnetic fields of Weibel instabilities in ultraintense laser-plasma interactions". In: *Phys. Plasmas* 14.7 (2007), p. 072702. DOI: 10.1063/1.2746023.

[Orl+04] D. Orlov et al. "Ultra-cold electron source with a GaAs-photocathode". In: *Nucl. Instrum. Methods Phys. Res. A* 532.1 (2004), pp. 418–421. DOI: 10.1016/j.nima.2004.06.048.

[Ost09] J. Osterhoff. "Stable, ultra-relativistic electron beams by laser-wakefield acceleration". Jan. 2009. URL: http://nbn-resolving.de/urn:nbn:de:bvb:19-96539.

[Oz+07] E. Oz et al. "Ionization-Induced Electron Trapping in Ultrarelativistic Plasma Wakes". In: *Phys. Rev. Lett.* 98 (8 Feb. 2007), p. 084801. DOI: 10.1103/PhysRevLett.98.084801.

[Pak+10] A. Pak et al. "Injection and Trapping of Tunnel-Ionized Electrons into Laser-Produced Wakes". In: *Phys. Rev. Lett.* 104 (2 Jan. 2010), p. 025003. DOI: 10.1103/PhysRevLett.104.025003.

[Pal+20] J. P. Palastro et al. "Dephasingless Laser Wakefield Acceleration". In: *Phys. Rev. Lett.* 124 (13 Mar. 2020), p. 134802. DOI: 10.1103/PhysRevLett.124.134802.

[Pen+12] G. Penco et al. "Time-sliced emittance and energy spread measurements at FERMI@Elettra". In: *Proc. 34th International Free-Electron Laser Conference (FEL2012)* (Nara, Japan). Aug. 2012, pp. 26–31. URL: http://accelconf.web.cern.ch/FEL2012/papers/wepd20.pdf.

[Pla+12] G. R. Plateau et al. "Low-Emittance Electron Bunches from a Laser-Plasma Accelerator Measured using Single-Shot X-Ray Spectroscopy". In: *Phys. Rev. Lett.* 109 (6 Aug. 2012), p. 064802. DOI: 10.1103/PhysRevLett.109.064802.

[PMR16] C. Pellegrini, A. Marinelli and S. Reiche. "The physics of x-ray free-electron lasers". In: *Rev. Mod. Phys.* 88 (1 Mar. 2016), p. 015006. DOI: 10.1103/RevModPhys.88.015006.

[Pol+11] B. B. Pollock et al. "Demonstration of a Narrow Energy Spread, ~ 0.5 GeV Electron Beam from a Two-Stage Laser Wakefield Accelerator". In: *Phys. Rev. Lett.* 107 (4 July 2011), p. 045001. DOI: 10.1103/PhysRevLett.107.045001.

[Pom+17] R. Pompili et al. "Experimental characterization of active plasma lensing for electron beams". In: *Appl. Phys. Lett.* 110.10 (2017), p. 104101. DOI: 10.1063/1.4977894.

[Poo+16] P. Poole et al. "Experiment and simulation of novel liquid crystal plasma mirrors for high contrast, intense laser pulses". In: *Sci. Rep.* 6 (2016), p. 32041. DOI: 10.1038/srep32041.

[PSW07] G. Pennt, A. M. Sessler and J. Wurtelel. "A plasma channel beam conditioner for a free electron laser". In: *Proc. 22nd Particle Accelerator Conference (PAC'07)* (Albuquerque, New Mexico, USA). IEEE. June 2007. URL: https://doi.org/10.1109/PAC.2007.4441021.

[PW56] W. K. H. Panofsky and W. A. Wenzel. "Some Considerations Concerning the Transverse Deflection of Charged Particles in Radio-Frequency Fields". In: *Review of Scientific Instruments* 27.11 (1956), pp. 967–967. DOI: 10.1063/1.1715427.

[Raj+20] G. Raj et al. "Probing ultrafast magnetic-field generation by current filamentation instability in femtosecond relativistic laser-matter interactions". In: *Phys. Rev. Research* 2 (2 May 2020), p. 023123. DOI: 10.1103/PhysRevResearch.2.023123.

[Rec+09] C. Rechatin et al. "Controlling the Phase-Space Volume of Injected Electrons in a Laser-Plasma Accelerator". In: *Phys. Rev. Lett.* 102 (16 Apr. 2009), p. 164801. DOI: 10.1103/PhysRevLett.102.164801.

[Rec+10] C. Rechatin et al. "Characterization of the beam loading effects in a laser plasma accelerator". In: *New J. Phys.* 12.4 (Apr. 2010), p. 045023. DOI: 10.1088/1367-2630/12/4/045023.

[Rei91] M. B. Reid. "Electron beam emittance growth in thin foils: A betatron function analysis". In: *J. Appl. Phys.* 70.11 (1991), pp. 7185–7187. DOI: 10.1063/1.349761.

[RGM10] I. Robinson, G. Gruebel and S. Mochrie. "Focus on X-ray beams with high coherence". In: *New J. Phys.* 12.3 (Mar. 2010), p. 035002. DOI: 10.1088/1367-2630/12/3/035002.

[RJ04] A. Reitsma and D. Jaroszynski. "Coupling of longitudinal and transverse motion of accelerated electrons in laser wakefield acceleration". In: *Laser Part. Beams* 22.4 (2004), pp. 407–413. URL: https://doi.org/10.1017/S0263034604040054.

[RL72] M. N. Rosenbluth and C. S. Liu. "Excitation of Plasma Waves by Two Laser Beams". In: *Phys. Rev. Lett.* 29 (11 Sept. 1972), pp. 701–705. DOI: 10.1103/PhysRevLett.29.701.

[RM73] E. M. Rowe and F. E. Mills. "Tantalus I: a dedicated storage ring synchrotron radiation source". In: *Part. Accel.* 4 (1973), pp. 211–227. URL: https://inspirehep.net/files/dde09a9a460372a3a43ff568509ad1f4.

[Ros+14] A. R. Rossi et al. "The External-Injection experiment at the SPARC_LAB facility". In: *Nucl. Instrum. Methods Phys. Res. A* 740 (2014), pp. 60–66. DOI: 10.1016/j.nima.2013.10.063.

[Ros+18] A. Rossi et al. "Plasma boosted electron beams for driving Free Electron Lasers". In: *Nucl. Instrum. Methods Phys. Res. A* 909 (2018), pp. 54–57. DOI: 10.1016/j.nima.2018.02.092.

[Ros+91] J. B. Rosenzweig et al. “Acceleration and focusing of electrons in two-dimensional nonlinear plasma wake fields”. In: *Phys. Rev. A* 44 (10 Nov. 1991), R6189–R6192. DOI: 10.1103/PhysRevA.44.R6189.

[Row+08] T. P. Rowlands-Rees et al. “Laser-Driven Acceleration of Electrons in a Partially Ionized Plasma Channel”. In: *Phys. Rev. Lett.* 100 (10 Mar. 2008), p. 105005. DOI: 10.1103/PhysRevLett.100.105005.

[SAH00] W. J. Schroeder, L. S. Avila and W. Hoffman. “Visualizing with VTK: a tutorial”. In: *IEEE Computer Graphics and Applications* 20.5 (Sept. 2000), pp. 20–27. DOI: 10.1109/38.865875.

[Sch+10a] K. Schmid et al. “Density-transition based electron injector for laser driven wakefield accelerators”. In: *Phys. Rev. ST Accel. Beams* 13 (9 Sept. 2010), p. 091301. DOI: 10.1103/PhysRevSTAB.13.091301.

[Sch+10b] C. B. Schroeder et al. “Physics considerations for laser-plasma linear colliders”. In: *Phys. Rev. ST Accel. Beams* 13 (10 Oct. 2010), p. 101301. DOI: 10.1103/PhysRevSTAB.13.101301.

[Sch+11] C. B. Schroeder et al. “Nonlinear Pulse Propagation and Phase Velocity of Laser-Driven Plasma Waves”. In: *Phys. Rev. Lett.* 106 (13 Mar. 2011), p. 135002. DOI: 10.1103/PhysRevLett.106.135002.

[Sch+18] C. G. Schroer et al. “PETRA IV: the ultralow-emittance source project at DESY”. In: *J. Synchrotron Radiat.* 25.5 (Sept. 2018), pp. 1277–1290. DOI: 10.1107/S1600577518008858.

[Sch+99] C. B. Schroeder et al. “Generation of ultrashort electron bunches by colliding laser pulses”. In: *Phys. Rev. E* 59 (5 May 1999), pp. 6037–6047. DOI: 10.1103/PhysRevE.59.6037.

[SE92] P. Sprangle and E. Esarey. “Interaction of ultrahigh laser fields with beams and plasmas”. In: *Phys. Fluids* 4.7 (1992), pp. 2241–2248. DOI: 10.1063/1.860192.

[Sea+10] C. M. S. Sears et al. “Emittance and divergence of laser wakefield accelerated electrons”. In: *Phys. Rev. ST Accel. Beams* 13 (9 Sept. 2010), p. 092803. DOI: 10.1103/PhysRevSTAB.13.092803.

[Seg15] T. Seggebrock. “Conceptual design of a laser-plasma accelerator driven free-electron laser demonstration experiment”. July 2015. URL: http://nbn-resolving.de/urn:nbn:de:bvb:19-184314.

[SET90a] P. Sprangle, E. Esarey and A. Ting. “Nonlinear interaction of intense laser pulses in plasmas”. In: *Phys. Rev. A* 41 (8 Apr. 1990), pp. 4463–4469. DOI: 10.1103/PhysRevA.41.4463.

[SET90b] P. Sprangle, E. Esarey and A. Ting. "Nonlinear theory of intense laser-plasma interactions". In: *Phys. Rev. Lett.* 64 (17 Apr. 1990), pp. 2011–2014. DOI: 10.1103/PhysRevLett.64.2011.

[SF15] S. Schreiber and B. Faatz. "The free-electron laser FLASH". In: *High Power Laser Sci. Eng.* 3 (2015). DOI: 10.1017/hpl.2015.16.

[Sha+18] R. J. Shalloo et al. "Hydrodynamic optical-field-ionized plasma channels". In: *Phys. Rev. E* 97 (5 May 2018), p. 053203. DOI: 10.1103/PhysRevE.97.053203.

[Sha+19] R. J. Shalloo et al. "Low-density hydrodynamic optical-field-ionized plasma channels generated with an axicon lens". In: *Phys. Rev. Accel. Beams* 22 (4 Apr. 2019), p. 041302. DOI: 10.1103/PhysRevAccelBeams.22.041302.

[Shi12] V. D. Shiltsev. "High-energy particle colliders: past 20 years, next 20 years, and beyond". In: *Physics-Uspekhi* 55.10 (Oct. 2012), pp. 965–976. DOI: 10.3367/ufne.0182.201210d.1033.

[Shi14] V. Shiltsev. "A phenomenological cost model for high energy particle accelerators". In: *J. Instrum.* 9.07 (July 2014), T07002–T07002. DOI: 10.1088/1748-0221/9/07/t07002.

[Shp+19] V. Shpakov et al. "Longitudinal Phase-Space Manipulation with Beam-Driven Plasma Wakefields". In: *Phys. Rev. Lett.* 122 (11 Mar. 2019), p. 114801. URL: https://link.aps.org/doi/10.1103/PhysRevLett.122.114801.

[Sie86] A. Siegman. *Lasers*. University Science Books, 1986. URL: https://books.google.de/books?id=1BZVwUZLTkAC.

[Sis+19] E. Sistrunk et al. "Laser Technology Development for High Peak Power Lasers Achieving Kilowatt Average Power and Beyond". In: *Short-pulse High-energy Lasers and Ultrafast Optical Technologies*. Vol. 11034. International Society for Optics and Photonics. SPIE, 2019, pp. 1–8. DOI: 10.1117/12.2525380.

[SM85] D. Strickland and G. Mourou. "Compression of amplified chirped optical pulses". In: *Optics Communications* 55.6 (1985), pp. 447–449. DOI: 10.1016/0030-4018(85)90151-8.

[Spa+14] S. Spampinati et al. "Laser heater commissioning at an externally seeded free-electron laser". In: *Phys. Rev. ST Accel. Beams* 17 (12 Dec. 2014), p. 120705. DOI: 10.1103/PhysRevSTAB.17.120705.

[Spr+01] P. Sprangle et al. "Wakefield generation and GeV acceleration in tapered plasma channels". In: *Phys. Rev. E* 63 (5 Apr. 2001), p. 056405. DOI: 10.1103/PhysRevE.63.056405.

[Spr+88] P. Sprangle et al. “Laser wakefield acceleration and relativistic optical guiding”. In: *AIP Conference Proceedings* 175.1 (1988), pp. 231–239. DOI: 10.1063/1.37621.

[Spr+92] P. Sprangle et al. “Propagation and guiding of intense laser pulses in plasmas”. In: *Phys. Rev. Lett.* 69 (15 Oct. 1992), pp. 2200–2203. DOI: 10.1103/PhysRevLett.69.2200.

[SSE09] B. A. Shadwick, C. B. Schroeder and E. Esarey. “Nonlinear laser energy depletion in laser-plasma accelerators”. In: *Phys. Plasmas* 16.5 (2009), p. 056704. DOI: 10.1063/1.3124185.

[SSY04] E. Saldin, E. Schneidmiller and M. Yurkov. “Longitudinal space charge-driven microbunching instability in the TESLA Test Facility linac”. In: *Nucl. Instrum. Methods Phys. Res. A* 528.1 (2004), pp. 355–359. DOI: 10.1016/j.nima.2004.04.067.

[Ste+16] S. Steinke et al. “Multistage coupling of independent laser-plasma accelerators”. In: *Nature* 530.7589 (2016), p. 190. DOI: 10.1038/nature16525.

[Ste+17] E. V. Stenson et al. “Debye length and plasma skin depth: two length scales of interest in the creation and diagnosis of laboratory pair plasmas”. In: *J. Plasma Phys.* 83.1 (2017), p. 595830106. DOI: 10.1017/S0022377817000022.

[Ste+92] M. Stetter et al. “Plasma lens studies at Erlangen University”. In: *Proc. of 3rd European Particle Accelerator Conference (EPAC'92)* (Berlin, Germany). Mar. 1992. URL: https://accelconf.web.cern.ch/e92/PDF/EPAC1992_1542.PDF.

[Ste+96] M. Stetter et al. “The high current plasma lens: investigations of fine focusing of high energy heavy ion beams”. In: *Fusion Eng. Des.* 32-33 (1996), pp. 503–509. DOI: 10.1016/S0920-3796(96)00506-6.

[STE87] P. Sprangle, C. Tang and E. Esarey. “Relativistic Self-Focusing of Short-Pulse Radiation Beams in Plasmas”. In: *IEEE Trans. Plasma Sci.* 15.2 (Apr. 1987), pp. 145–153. DOI: 10.1109/TPS.1987.4316677.

[Str+18] M. J. V. Streeter et al. “Temporal feedback control of high-intensity laser pulses to optimize ultrafast heating of atomic clusters”. In: *Appl. Phys. Lett.* 112.24 (2018), p. 244101. DOI: 10.1063/1.5027297.

[Stu18] G. Stupakov. “Short-range wakefields generated in the blowout regime of plasma-wakefield acceleration”. In: *Phys. Rev. Accel. Beams* 21 (4 Apr. 2018), p. 041301. DOI: 10.1103/PhysRevAccelBeams.21.041301.

[Sun+87] G.-Z. Sun et al. “Self-focusing of short intense pulses in plasmas”. In: *The Physics of Fluids* 30.2 (1987), pp. 526–532. DOI: 10.1063/1.866349.

[Svy+18] E. Svystun et al. "Beam quality preservation studies in a laser-plasma accelerator with external injection for EuPRAXIA". In: *Nucl. Instrum. Methods Phys. Res. A* 909 (2018), pp. 90–94. DOI: 10.1016/j.nima.2018.02.060.

[SWY92] A. M. Sessler, D. H. Whittum and L.-H. Yu. "Radio-frequency beam conditioner for fast-wave free-electron generators of coherent radiation". In: *Phys. Rev. Lett.* 68 (3 Jan. 1992), pp. 309–312. DOI: 10.1103/PhysRevLett.68.309.

[SY11] E. Schneidmiller and M. Yurkov. *Photon beam properties at the European XFEL*. DESY, 2011. URL: https://bib-pubdb1.desy.de/record/95609/files/desy11-152%5B1%5D.pdf.

[TD79] T. Tajima and J. M. Dawson. "Laser Electron Accelerator". In: *Phys. Rev. Lett.* 43 (4 July 1979), pp. 267–270. DOI: 10.1103/PhysRevLett.43.267.

[TES90] A. Ting, E. Esarey and P. Sprangle. "Nonlinear wake-field generation and relativistic focusing of intense laser pulses in plasmas". In: *Phys. Fluids* 2.6 (1990), pp. 1390–1394. DOI: 10.1063/1.859561.

[Tha+07] C. Thaury et al. "Plasma mirrors for ultrahigh-intensity optics". In: *Nat. Phys.* 3.6 (2007), p. 424. DOI: 10.1038/nphys595.

[Tha+15] C. Thaury et al. "Demonstration of relativistic electron beam focusing by a laser-plasma lens". In: *Nat. Commun.* 6 (2015), p. 6860. DOI: 10.1038/ncomms7860.

[Thé+19] M. Thévenet et al. "Emittance growth due to misalignment in multistage laser-plasma accelerators". In: *Phys. Rev. Accel. Beams* 22 (5 May 2019), p. 051302. DOI: 10.1103/PhysRevAccelBeams.22.051302.

[Tho+16] J. Thomas et al. "Non-linear theory of a cavitated plasma wake in a plasma channel for special applications and control". In: *Phys. Plasmas* 23.5 (2016), p. 053108. DOI: 10.1063/1.4948712.

[Tie+09] K. Tiedtke et al. "The soft x-ray free-electron laser FLASH at DESY: beamlines, diagnostics and end-stations". In: *New J. Phys.* 11.2 (Feb. 2009), p. 023029. DOI: 10.1088/1367-2630/11/2/023029.

[Til+15] J. van Tilborg et al. "Active Plasma Lensing for Relativistic Laser-Plasma-Accelerated Electron Beams". In: *Phys. Rev. Lett.* 115 (18 Oct. 2015), p. 184802. DOI: 10.1103/PhysRevLett.115.184802.

[Til+18] J. van Tilborg et al. "Comparative study of active plasma lenses in high-quality electron accelerator transport lines". In: *Phys. Plasmas* 25.5 (2018), p. 056702. DOI: 10.1063/1.5018001.

[Tit] M. Titberidze. "Pilot Study of Synchronization on a Femtosecond Scale between the Electron Gun REGAE and a Laser-Plasma Accelerator". Dissertation, Universität Hamburg, 2016. PhD thesis. DOI: 10.3204/PUBDB-2017-11374.

[Tit+17] M. Titberidze et al. "Fs level laser-to-RF synchronization at REGAE". In: *J. Phys. Conf. Ser.* 874 (July 2017), p. 012085. DOI: 10.1088/1742-6596/874/1/012085.

[Too+17] M. P. Tooley et al. "Towards Attosecond High-Energy Electron Bunches: Controlling Self-Injection in Laser-Wakefield Accelerators Through Plasma-Density Modulation". In: *Phys. Rev. Lett.* 119 (4 July 2017), p. 044801. DOI: 10.1103/PhysRevLett.119.044801.

[Tzo+08] M. Tzoufras et al. "Beam Loading in the Nonlinear Regime of Plasma-Based Acceleration". In: *Phys. Rev. Lett.* 101 (14 Sept. 2008), p. 145002. DOI: 10.1103/PhysRevLett.101.145002.

[Tzo+09] M. Tzoufras et al. "Beam loading by electrons in nonlinear plasma wakes". In: *Phys. Plasmas* 16.5 (2009), p. 056705. DOI: 10.1063/1.3118628.

[UKD96] D. Umstadter, J. K. Kim and E. Dodd. "Laser Injection of Ultrashort Electron Pulses into Wakefield Plasma Waves". In: *Phys. Rev. Lett.* 76 (12 Mar. 1996), pp. 2073–2076. DOI: 10.1103/PhysRevLett.76.2073.

[Ums+96] D. Umstadter et al. "Nonlinear Optics in Relativistic Plasmas and Laser Wake Field Acceleration of Electrons". In: *Science* 273.5274 (1996), pp. 472–475. DOI: 10.1126/science.273.5274.472.

[Vay07] J.-L. Vay. "Noninvariance of Space- and Time-Scale Ranges under a Lorentz Transformation and the Implications for the Study of Relativistic Interactions". In: *Phys. Rev. Lett.* 98 (13 Mar. 2007), p. 130405. DOI: 10.1103/PhysRevLett.98.130405.

[Vie+11] J. Vieira et al. "Magnetic Control of Particle Injection in Plasma Based Accelerators". In: *Phys. Rev. Lett.* 106 (22 May 2011), p. 225001. DOI: 10.1103/PhysRevLett.106.225001.

[Wal+17] P. A. Walker et al. "Horizon 2020 EuPRAXIA design study". In: *J. Phys.: Conf. Ser.* 874.1 (2017), p. 012029. URL: http://stacks.iop.org/1742-6596/874/i=1/a=012029.

[Wan+02] S. Wang et al. "X-Ray Emission from Betatron Motion in a Plasma Wiggler". In: *Phys. Rev. Lett.* 88 (13 Mar. 2002), p. 135004. DOI: 10.1103/PhysRevLett.88.135004.

[Wan+13] X. Wang et al. "Quasi-monoenergetic laser-plasma acceleration of electrons to 2 GeV". In: *Nat. Commun.* 4 (2013), p. 1988. DOI: 10.1038/ncomms2988.

[Wan+16] W. T. Wang et al. "High-Brightness High-Energy Electron Beams from a Laser Wakefield Accelerator via Energy Chirp Control". In: *Phys. Rev. Lett.* 117 (12 Sept. 2016), p. 124801. DOI: 10.1103/PhysRevLett.117.124801.

[Wan08] T. P. Wangler. *RF linear accelerators*. 2008.

[WD12] H. Winick and S. Doniach. *Synchrotron radiation research*. Springer Science & Business Media, 2012.

[Wei+12] R. Weingartner et al. "Ultralow emittance electron beams from a laser-wakefield accelerator". In: *Phys. Rev. ST Accel. Beams* 15 (11 Nov. 2012), p. 111302. DOI: 10.1103/PhysRevSTAB.15.111302.

[Wei+16] M. Weikum et al. "Generation of attosecond electron bunches in a laser-plasma accelerator using a plasma density upramp". In: *Nucl. Instr. Meth. Phys. Res., Sect. A* 829 (2016), pp. 33–36. DOI: 10.1016/j.nima.2016.01.003.

[Wei+17] M. Weikum et al. "Improved Electron Beam Quality from External Injection in Laser-Driven Plasma Acceleration at SINBAD". In: *Proc. 8th International Particle Accelerator Conference (IPAC'17)* (Copenhagen, Denmark). May 2017, pp. 1707–1710. DOI: 10.18429/JACoW-IPAC2017-TUPIK013.

[Wei+19a] M. K. Weikum et al. "Status of the Horizon 2020 EuPRAXIA conceptual design study". In: *J. Phys. Conf. Ser.* 1350 (Nov. 2019), p. 012059. DOI: 10.1088/1742-6596/1350/1/012059.

[Wei+19b] M. K. Weikum et al. "EuPRAXIA – a compact, cost-efficient particle and radiation source". In: *AIP Conference Proceedings* 2160.1 (2019), p. 040012. DOI: 10.1063/1.5127692.

[Whi+91] D. H. Whittum et al. "Electron-hose instability in the ion-focused regime". In: *Phys. Rev. Lett.* 67 (8 Aug. 1991), pp. 991–994. DOI: 10.1103/PhysRevLett.67.991.

[Wie14] K. Wiesemann. "A short introduction to plasma physics". In: (2014). arXiv: 1404.0509 [physics.plasm-ph].

[Wie15] H. Wiedemann. *Particle Accelerator Physics*. Graduate Texts in Physics. Berlin, Germany: Springer, 2015. DOI: 10.1007/978-3-319-18317-6.

[Win97] H. Winick. "Fourth generation light sources". In: *Proc. 17th IEEE Particle Accelerator Conference (PAC'97)* (Vancouver, BC, Canada). Vol. 1. May 1997. DOI: 10.1109/PAC.1997.749539.

[WL96] J. W. Wang and G. A. Loew. "Field emission and RF breakdown in high gradient room temperature linac structures". In: *Proc. Joint CERN-US-Japan Accelerator School: Frontiers of Accelerator Technology* (Hayama and Tsukuba, Japan). Sept. 1996, pp. 768–794. URL: https://slac.stanford.edu/pubs/slacpubs/7500/slac-pub-7684.pdf.

[WR19] G. White and T. Raubenheimer. "Transverse Jitter Tolerance Issues for Beam-Driven Plasma Accelerators". In: *Proc. 10th International Particle Accelerator Conference (IPAC'19)* (Melbourne, Australia). 10. May 2019, pp. 3774–3777. DOI: 10.18429/JACoW-IPAC2019-THPGW087.

[Wu+19a] Y. P. Wu et al. "Phase Space Dynamics of a Plasma Wakefield Dechirper for Energy Spread Reduction". In: *Phys. Rev. Lett.* 122 (20 May 2019), p. 204804. DOI: 10.1103/PhysRevLett.122.204804.

[Wu+19b] Y. Wu et al. "Near-Ideal Dechirper for Plasma-Based Electron and Positron Acceleration Using a Hollow Channel Plasma". In: *Phys. Rev. Applied* 12 (6 Dec. 2019), p. 064011. DOI: 10.1103/PhysRevApplied.12.064011.

[Xie95] M. Xie. "Design optimization for an X-ray free electron laser driven by SLAC linac". In: *Proc. 16th Particle Accelerator Conference (PAC'95)*. Vol. 1. May 1995, 183–185 vol.1. DOI: 10.1109/PAC.1995.504603.

[Xu+14] X. L. Xu et al. "Phase-Space Dynamics of Ionization Injection in Plasma-Based Accelerators". In: *Phys. Rev. Lett.* 112 (3 Jan. 2014), p. 035003. DOI: 10.1103/PhysRevLett.112.035003.

[Xu+16] X. L. Xu et al. "Physics of Phase Space Matching for Staging Plasma and Traditional Accelerator Components Using Longitudinally Tailored Plasma Profiles". In: *Phys. Rev. Lett.* 116 (12 Mar. 2016), p. 124801. DOI: 10.1103/PhysRevLett.116.124801.

[Yi+13] S. A. Yi et al. "Analytic model of electromagnetic fields around a plasma bubble in the blow-out regime". In: *Phys. Plasmas* 20.1 (2013), p. 013108. DOI: 10.1063/1.4775774.

[Yu+14] L.-L. Yu et al. "Two-Color Laser-Ionization Injection". In: *Phys. Rev. Lett.* 112 (12 Mar. 2014), p. 125001. DOI: 10.1103/PhysRevLett.112.125001.

[Zei] B. Zeitler. "Phase Space Linearization and External Injection of Electron Bunches into Laser-Driven Plasma Wakefields at REGAE". Dissertation, Universität Hamburg, 2016. PhD thesis. DOI: 10.3204/PUBDB-2017-00801.

[Zei+10] K. Zeil et al. "The scaling of proton energies in ultrashort pulse laser plasma acceleration". In: *New J. Phys.* 12.4 (Apr. 2010), p. 045015. DOI: 10.1088/1367-2630/12/4/045015.

[Zen+14] M. Zeng et al. "Self-truncated ionization injection and consequent monoenergetic electron bunches in laser wakefield acceleration". In: *Phys. Plasmas* 21.3 (2014), p. 030701. DOI: 10.1063/1.4868404.

[Zew00] A. H. Zewail. "Femtochemistry: Atomic-scale dynamics of the chemical bond". In: *J. Phys. Chem. A* 104.24 (2000), pp. 5660–5694. DOI: 10.1021/jp001460h
.

[Zhu+16] J. Zhu et al. “Sub-fs electron bunch generation with sub-10-fs bunch arrival-time jitter via bunch slicing in a magnetic chicane”. In: *Phys. Rev. Accel. Beams* 19 (5 May 2016), p. 054401. DOI: 10.1103/PhysRevAccelBeams.19.054401.

[Zhu+18] J. Zhu et al. “Simulation Study of an RF Injector for the LWFA Configuration at EuPRAXIA”. In: *Proc. 9th International Particle Accelerator Conference (IPAC'18)* (Vancouver, BC, Canada). 2018, pp. 3025–3028. DOI: 10.18429/JACoW-IPAC2018-THPAF032.

[Zhu16] K. Zhukovsky. “Undulators for Short Pulse X-Ray Self-Amplified Spontaneous Emission-Free Electron Lasers”. In: *High Energy and Short Pulse Lasers*. Ed. by R. Viskup. IntechOpen, 2016. DOI: 10.5772/64439.

[Zhu17] J. Zhu. “Design Study for Generating Sub-femtosecond to Femtosecond Electron Bunches for Advanced Accelerator Development at SINBAD”. Dissertation, University of Hamburg, 2017. PhD thesis. 2017. DOI: 10.3204/PUBDB-2018-01379.

[Zhu18] J. Zhu. Private communication. 2018.

[Zig+96] A. Zigler et al. “Optical guiding of high-intensity laser pulses in a long plasma channel formed by a slow capillary discharge”. In: *J. Opt. Soc. Am. B* 13.1 (Jan. 1996), pp. 68–71. DOI: 10.1364/JOSAB.13.000068.

[Zim18] F. Zimmermann. “Future colliders for particle physics—“Big and small””. In: *Nucl. Instrum. Methods Phys. Res. A* 909 (2018), pp. 33–37. DOI: 10.1016/j.nima.2018.01.034.

[Zou+15] J. Zou et al. “Design and current progress of the Apollon 10 PW project”. In: *High Power Laser Sci. Eng.* 3 (2015), e2. DOI: 10.1017/hpl.2014.41.

Acknowledgements

I would like to start by thanking my first supervisor, Dr. Ralph Aßmann, for having believed in me from the beginning, even when I barely knew what laser, a plasma, or an accelerator were, and for always strongly supporting me and my work throughout my PhD. My gratitude also goes to Prof. Dr. Florian Grüner for taking the role as second supervisor. A big special thanks goes to Dr. Alberto Martinez de la Ossa, my third and last, but in no way the least, supervisor for the unmeasurable amount of time and effort he has put into my work and always being there when needed.

Although not officially a supervisor, I would like to express my sincere gratitude for having had the chance to work with Dr. Reinhard Brinkmann. His ideas, of which he never seems to be short of, gave an initial purpose to my PhD and eventually led to the development of the acceleration concepts presented in this thesis. I cannot claim any of them solely as my own, since either in parallel or already in previous times these ideas had also surfaced in his mind.

There is a number of people from which I have greatly profited during my PhD, both for my research and personal life. Among these, I would like to highlight Dr. Daniel Marx and Dr. Thorsten Hellert for making my time at DESY a more enjoyable experience. My special thanks go also to the whole MPY-1 group (old and current), particularly to those with which I have worked closer, namely Thomas Heinemann, Dr. Elena Svystun, Dr. Maria Weikum, Dr. Christoph Lechner, Dr. Jun Zhu, Dr. Frank Mayet, Willi Kuropka, Farzad Jafarinia, Sumera Yamin, Dr. Francois Lemery and of course to Dr. Ulrich Dorda, Dr. Barbara Marchetti, Dr. Florian Burkart and Dr. Andreas Walker. I would also like to thank Dr. Klaus Flötmann for insightful and fruitful discussions. The same goes for Dr. Timon Mehrling, whose thesis is also my personal bible of plasma acceleration.

My acknowledgements go also to Dr. Gennadiy Bagdasarov from the Keldysh Institute of Applied Mathematics, who kindly provided the data for plasma density profiles in realistic capillaries and even performed additional simulations.

I would like to express my deepest thanks to my family for their continuous support and understanding during this time. They all have been greatly missed. I am particularly grateful to my father, without whose dedication and sacrifice I would not have been able to finish this PhD.

Last but not least, my biggest recognition goes to Sonja for having shared this journey with me. Her constant dedication, patience and understanding, particularly during the final writing of this thesis, have been invaluable for me. I owe her countless experiences, trips I could have never dreamed of, as well as an empty count of vacation days.

This project has received funding from the European Union's Horizon 2020 research and innovation programme under Grant Agreement No. 653782.

List of publications

As first author

[FAM19] A. Ferran Pousa, R. Assmann and A. Martinez de la Ossa. "Wake-T: a fast particle tracking code for plasma-based accelerators". In: *J. Phys. Conf. Ser.* 1350 (Nov. 2019), p. 012056. DOI: 10.1088/1742-6596/1350/1/012056.

[Fer+19] A. Ferran Pousa et al. "Compact Multistage Plasma-Based Accelerator Design for Correlated Energy Spread Compensation". In: *Phys. Rev. Lett.* 123 (5 July 2019), p. 054801. DOI: 10.1103/PhysRevLett.123.054801.

[FMA19] A. Ferran Pousa, A. Martinez de la Ossa and R. W. Assmann. "Intrinsic energy spread and bunch length growth in plasma-based accelerators due to betatron motion". In: *Scientific Reports* 9.1 (2019), pp. 1–11. DOI: doi:10.1038/s41598-019-53887-8.

[FAM18] A. Ferran Pousa, R. Assmann and A. Martinez de la Ossa. "Beam Quality Limitations of Plasma-Based Accelerators". In: *Proc. 9th Int. Particle Accelerator Conf. (IPAC'18)* (Vancouver, BC, Canada). May 2018, pp. 607–611. DOI: 10.18429/JACoW-IPAC2018-TUXGBE4.

[FAM17] A. Ferran Pousa, R. W. Assmann and A. Martinez de la Ossa. "VisualPIC: A New Data Visualizer and Post-Processor for Particle-in-Cell Codes". In: *Proc. of 8th International Particle Accelerator Conference (IPAC'17)* (Copenhagen, Denmark). May 2017, pp. 1696–1698. DOI: 10.18429/JACoW-IPAC2017-TUPIK007.

[Fer+17] A. Ferran Pousa et al. "External injection into a laser-driven plasma accelerator with sub-femtosecond timing jitter". In: *J. Phys.: Conf. Ser.* 874.1 (2017), p. 012032. DOI: 10.1088/1742-6596/874/1/012032.

Other publications

[Mar+19a] A. Martinez de la Ossa et al. "Hybrid LWFA-PWFA staging as a beam energy and brightness transformer: conceptual design and simulations". In: *Philos. Trans. R. Soc. A* 377.2151 (2019). DOI: 10.1098/rsta.2018.0175.

[Ngh+19] P. A. P. Nghiem et al. “EuPRAXIA, A Step Toward A Plasma-Wakefield Based Accelerator With High Beam Quality”. In: *J. Phys. Conf. Ser.* 1350 (Nov. 2019), p. 012068. DOI: 10.1088/1742-6596/1350/1/012068.

[Wei+19a] M. K. Weikum et al. “Status of the Horizon 2020 EuPRAXIA conceptual design study”. In: *J. Phys. Conf. Ser.* 1350 (Nov. 2019), p. 012059. DOI: 10.1088/1742-6596/1350/1/012059.

[Wei+19b] M. K. Weikum et al. “EuPRAXIA – a compact, cost-efficient particle and radiation source”. In: *AIP Conference Proceedings* 2160.1 (2019), p. 040012. DOI: 10.1063/1.5127692.

[Svy+18] E. Svystun et al. “Beam quality preservation studies in a laser-plasma accelerator with external injection for EuPRAXIA”. In: *Nucl. Instrum. Methods Phys. Res. A* 909 (2018), pp. 90–94. DOI: 10.1016/j.nima.2018.02.060.

[Zhu+18] J. Zhu et al. “Simulation Study of an RF Injector for the LWFA Configuration at EuPRAXIA”. In: *Proc. 9th International Particle Accelerator Conference (IPAC'18)* (Vancouver, BC, Canada). 2018, pp. 3025–3028. DOI: 10.18429/JACoW-IPAC2018-THPAF032.

[Wei+17] M. Weikum et al. “Improved Electron Beam Quality from External Injection in Laser-Driven Plasma Acceleration at SINBAD”. In: *Proc. 8th International Particle Accelerator Conference (IPAC'17)* (Copenhagen, Denmark). May 2017, pp. 1707–1710. DOI: 10.18429/JACoW-IPAC2017-TUPIK013.

Eidesstattliche Versicherung

Hiermit versichere ich an Eides statt, die vorliegende Dissertationsschrift selbst verfasst und keine anderen als die angegebenen Hilfsmittel und Quellen benutzt zu haben.

Die eingereichte schriftliche Fassung entspricht der auf dem elektronischen Speichermedium.

Die Dissertation wurde in der vorgelegten oder einer ähnlichen Form nicht schon einmal in einem früheren Promotionsverfahren angenommen oder als ungenügend beurteilt.

Hamburg, den _____ Unterschrift: _____